# Ruthenium Polypridyl Complexes with Long Aliphatic Chains; Photophysics, Interfacial Assembly and Cell Imaging

**Stephen Finn B.Sc. (Hons.)**

**A Thesis presented at Dublin City University**

**for the Degree of Doctor of Philosophy**

**Supervisors**

**Prof. Tia E. Keyes**

**Prof. Robert J. Forster**

***School of Chemical Sciences***

***Dublin City University***

**July 2011**

## DECLARATION

*I hereby certify that this material, which I now submit for assessment on the programme of study leading to the award of doctor of philosophy is entirely my own work, that I have exercised reasonable care to ensure that the work is original, and does not to the best of my knowledge breach any law of copyright, and has not been taken from the work of others save and to the extent that such work has been cited and acknowledged within the text of my work.*

Signed: _____ ID No.: _____ Date: _____

**This thesis is dedicated to my parents**

## Acknowledgements

I would like to express my gratitude to my supervisor Prof. Tia E. Keyes for advice and support throughout my research. I would also like to express my gratitude to Prof. Robert J. Forster who also contributed to my research with advice and support.

I would like to thank all the members of our research group that I worked with throughout the years. I would also like to acknowledge the hard working technical staff of the NCSR, BDI and DCU school of chemical sciences who made working on my thesis a lot easier.

I would like to thank Frank Schramm and Mario Ruben who I collaborated with on the work with the $[Ru(L_{KET})_2]^{2+}$ complex.

I would like to thank Rozenn Le Parc who carried out the XPS surface analysis of the RuxD complexes for me.

I would also like to thank Roisin Moriarty who helped out immensely with the cell imaging studies

I wish to thank the technical staff of the NCSR, NBIPI and DCU School of Chemical Sciences who have helped me during my research.

I would like to thank the funding bodies IRCSET, SFI, NCSR and NBIPI that have contributed to my research. This work was part funded under PRTLI IV under Ireland's EU Structural Funds Programmes 20072013 co-funded by the Irish Government and the European Union.

I must extend a lot of gratitude to all my friends I met during my time in DCU. They include Colm Mallon, Bincy Jose, Anita Venkatanarayanan, Anitha Devadoss, Eoin Sheridan, Gavin Sewell, Nigel Brady, Andrea McNally, Yan Pellegrin, Rob Groarke, Lynn Dennany, Jamie Walsh, Aidan Fagan, Claudio Zuliani, Zoe Stack, Shane O'Carroll, Qiang Zeng, and Martina Lavelle.

A big special thank you to my BFF's Emmet O'Reilly, Lynda Cosgrave and of course Michele Kelly.

I'd like to thank all non academic friends who despite not knowing how to pronounce my thesis title managed to help me along the way by keeping me sane. Thanks Eamon Dolan, Shane Califf, Robert Kernan, Daniel Anderson, Brian Burns and Damien Callan.

I must thank my family as well who have stuck with me through the hard times. My brother Eric Finn who I know is proud of me despite calling me a nerd all the time. Also my parents Maureen and Christopher without whose support I wouldn't have been able to finish this PhD.

Last but not least I'd like to thank my girlfriend Sarah Lyons who managed to stick with me despite the fact that the worst boyfriend is one who is finishing their PhD!

## Table of Contents

## Glossary of Acronyms

| Acronym | - | Explanation |
|---|---|---|
| 6-ATAP | - | 5-Amido-1,10-phenanthroline-(6-acetylthio-hexanyl) |
| 8-ATAP | - | 5-Amido-1,10-phenanthroline-(8-acetylthio-octanyl) |
| 11-ATAP | - | 5-Amido-1,10-phenanthroline-(11-acetylthio-undecanyl) |
| 16-ATAP | - | 5-Amido-1,10-phenanthroline-(16-acetylthio-hexadecanyl) |
| x-ATAP | - | Term used to identify the family of complexes containing 6-ATAP, 8-ATAP, 11-ATAP and 16-ATAP |
| ACN | - | Acetonitrile |
| AFM | - | Atomic force microscopy |
| bpy | - | 2,2-bipyridine |
| BSA | - | Bovine Serum Albumin |
| CHO | - | Chinese hamster ovarian cells |
| CTAB | - | Cetyltrimethylammonium bromide |
| DCM | - | Dichloromethane |
| Dioc6 | - | 3-Hexyl-2-[3-(3-hexyl-2(3*H*)benzoxazolylidene)-1-propenyl]benzoxazolium iodide. Commercially available cellular stain that selectively stains the endoplasmic reticulum and mitochondria |
| DMSO | - | Dimethylsulfoxide |
| DMTMM | - | 4-(4,6-Dimethoxy-1,3,5-triazin-2-yl)-4-methylmorpholinium chloride |
| dpp | - | 4,7-diphenyl-1,10-phenanthroline |
| DRAQ7 | - | Commerically available fluorescent cellular stain that selectively stains the nuclei of cells with compromised cell membranes |
| EDC | - | ethyl(dimethylaminopropyl) carbodiimide |
| EEDQ | - | *N*-Ethoxycarbonyl-2-ethoxy-1,2-dihydroquinoline |
| FLIM | - | Fluorescence lifetime imaging microscopy |
| FRAP | - | Fluorescence recovery after photobleaching |
| HeLa | - | Cell line of human cervical carcinoma cells |
| HepG2 | - | Cell line of human liver carcinoma cells |
| $k_{nr}$ | - | Non-radiative decay rate |
| $k_r$ | - | Radiative decay rate |

| | | |
|---|---|---|
| LC | - | Ligand Centred transition |
| MLCT | - | Metal to Ligand charge transfer |
| $NH_2$phen | - | 5-amino-1,10-phenanthroline |
| NHS | - | *N*-hydroxysuccinimide |
| PBS | - | Phosphate buffer solution |
| phen | - | 1,10-phenanthroline |
| Ru6D | - | $[Ru(dpp)_2$(AmidoPhen-6-(acetylthio)-hexanyl)$](PF_6)_2$ |
| Ru8D | - | $[Ru(dpp)_2$(AmidoPhen-8-(acetylthio)-octanyl)$](PF_6)_2$ |
| Ru11D | - | $[Ru(dpp)_2$(AmidoPhen-11-(acetylthio)-undecanyl)$](PF_6)_2$ |
| Ru16D | - | $[Ru(dpp)_2$(AmidoPhen-16-(acetylthio)-hexadecanyl)$](PF_6)_2$ |
| RuxD | - | Term referring to the entire family of complexes consisting of Ru6D, Ru8D, Ru11D and Ru16D |
| SAMs | - | Self assembled monolayers |
| SEF | - | Surface enhanced fluorescence |
| SERS | - | Surface enhanced Raman spectroscopy |
| SERRS | - | Surface enhanced resonance Raman spectroscopy |
| SP2 myeloma | - | Mouse myeloma cell line |
| $TBAClO_4$ | - | Tetrabutylammonium perchlorate |
| TBATBF | - | Tetrabutylammonium tetrafluoroborate |
| TDDFT | - | Time-dependent density functional theory |
| tpy | - | 2,2';6',2''-terpyridine |
| $\lambda$ | - | Wavelength |
| $\tau$ | - | Lifetime |
| $\phi$ | - | Quantum yield |

# Abstract


**Ruthenium Polypyridyl Complexes with Long Aliphatic Chains; Photophysics, Interfacial Assembly and Cell Imaging**

A series of novel ruthenium polypyridyl complexes $[Ru(dpp)_2(x\text{-}ATAP)](PF_6)_2$ was synthesised and their photophysical and electrochemical properties are reported on, where x-ATAP is either 5-Amido-1,10-phenanthroline-(6-acetylthio-hexanyl), 5-Amido-1,10-phenanthroline-(8-acetylthio-octanyl), 5-Amido-1,10-phenanthroline-(11-acetylthio-undecanyl) or 5-Amido-1,10-phenanthroline-(16-acetylthio-hexadecanyl). These complexes exhibit bright emission. They are capable of self assembly on metallic surfaces. Furthermore, this series of complexes is capable of forming bilayer vesicle structures in aqueous conditions. Chapter 2 describes the synthesis, photophysics and solution phase electrochemistry of these complexes. The solvent dependence of the luminescence properties is also addressed along with the formation of bilayer vesicles of these compounds in aqueous conditions.

In chapter 3 self assembled monolayers of the $Ru(dpp)_2(x\text{-}ATAP)](PF_6)_2$ complexes were formed on platinum electrodes and these monolayers were characterized electrochemically. These monolayers were found to be somewhat unstable when analysed electrochemically even when backfilled with an appropriate length alkanethiol. Attempts to study the distance dependence of electron transfer reveal that these complexes when functionalized on metal surfaces lie flat on the surface as opposed to the ruthenium headgroup being raised above the surface. The photophysical properties of these monolayers on gold and platinum electrodes and gold nanoparticles are also reported. Despite the close proximity of the headgroup to the metal surface the monolayers remain luminescent and exhibit large SERS enhancement when absorbed on aggregated gold nanoparticle clusters.

Chapter 4 explores the interactions of the $Ru(dpp)_2(x\text{-}ATAP)](PF_6)_2$ complexes with monoclonal cells and their suitability as luminescence cell imaging probes. A CHO cell line (Chinese hamster ovary cell) was stained with the $Ru(dpp)_2(x\text{-}ATAP)](PF_6)_2$. This series of complexes was capable of crossing the cell membrane barrier and localizing in discrete

compartments of the cell. The stained cell line was imaged by FLIM (fluorescence lifetime imaging microscopy) and 3D z-stacked images of the cell were constructed. It was found that there was an alkyl chain length dependence on the localization of these complexes within the cell. Complexes with short alkyl chains stained throughout the cytoplasm and nucleus while the complexes with longer alkyl chains remain localized in endosomes.

Finally chapter 5 explores a novel ruthenium(II) bis-terpyridyl type complex, $[Ru^{II}(L_{Ket})_2].(PF_6)_2$. This complex was characterized photophysically and electrochemically. By extending the structure of the 2,2';6',2''-terpyridine (tpy) ligands with carbonyl bridging units the $[Ru^{II}(L_{Ket})_2].(PF_6)_2$ complex cage structure is much closer to perfect octahedral configuration compared to $[Ru^{II}(tpy)_2]^{2+}$. The photophysical performance in ambient conditions of $[Ru^{II}(L_{Ket})_2].(PF_6)_2$ is massively increased compared to $[Ru^{II}(tpy)_2]^{2+}$ or similar complexes and this complex displays the longest luminescence lifetime of any ruthenium complex at 298 K and in aerated conditions to our knowledge. The long term aims of this work are to modify this complex with a long chain alkane or peptide for cell imaging purposes.

# 1. Introduction

## 1.1 Introduction

The phrase supramolecular chemistry was first coined by Jean-Marie Lehn in 1978[1] and applied to the area of chemistry concerned with inter molecular interactions and interactions within molecular assemblies as opposed to the covalent bonding interactions within molecules. Supramolecular chemistry is a broad interdisciplinary domain covering a range of subjects including the miniaturization of devices and molecular recognition and catalysis. The underlying aim of supramolecular chemistry is the development of complex molecular constructs from molecules interacting by non-covalent intermolecular forces, such as Van Der Waals forces, hydrogen bonding and π-stacking. The organization and assembly of molecular assemblies through these interactions is highly important to their function. For example in biological systems the catalytic properties of enzyme are not only due to the enzymes' molecular components but also to the specific order in the spatial constructs.

It is not just the structure of these molecular assemblies that are of interest to the supramolecular chemist but also the interactions between components. Photoactive, and electroactive molecular arrays can be constructed that can pass information through electron or energy transfer between components thus functioning as molecular wires. Ionoactive molecular devices can transport ions through ion channels. These processes on the molecular level are the first step to building 'molecular machines' that are activated by external stimuli[2].

The manipulation of non-covalent forces between molecules is central in natural supramolecular assemblies such as cell membranes and proteins. One of the ultimate goals for supramolecular chemistry is the creation of molecular devices by self assembly. Self assembly provides a means to create technologically important devices from a 'bottom-up' process as opposed to the 'top-down' methods that are employed such as

photolithography. The benefits would be highly organized devices on the nanometer scale that overcome the size limitations of these top-down processes. The implicit possibilities of these devices on the nanometer scale are sensors with bio-recognition and chemical sensing of the nano-environment leading to new advances in disease diagnosis, environmental monitoring or drug delivery[3].

## 1.2 Photophysics and Photochemistry of Transition Metal Complexes

### *1.2.1 Photophysical Pathways and Processes*

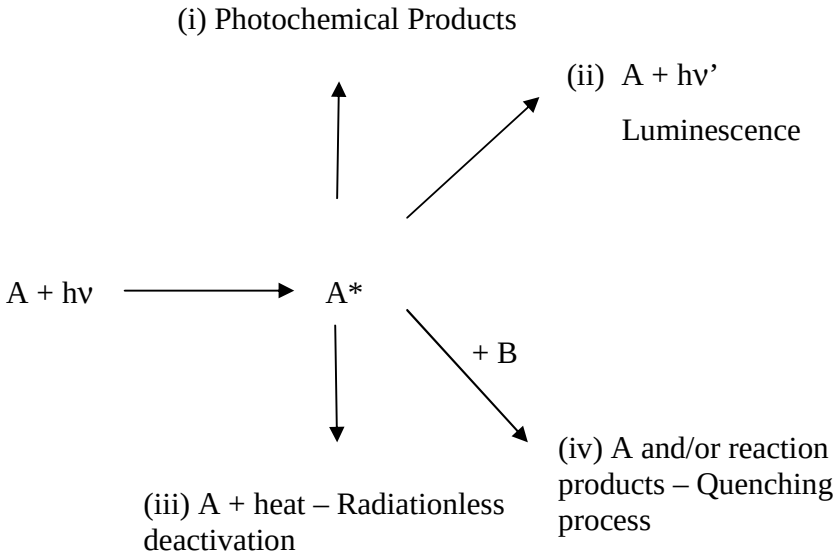


**Figure 1.2.1.1:** Deactivation pathways of an excited state molecule.

When a molecule absorbs a photon of light an excited state is formed. This high energy excited state is energetically unstable and must undergo deactivation back to the ground state. Fig 1.2.1.1 shows the processes through which deactivation of the excited state can occur.

(i) a photochemical reaction resulting in the disappearance of the original molecule and production of new products

(ii) Emission of light

(iii) Radiationless deactivation resulting in the degradation of the excess energy to heat and generation of the original molecule

(iv) A quenching process where the excited state interacts with some other species in solution.

The absorption and emission spectra properties of transition metal complexes come from the characteristics of the excited states involved and their spin quantum numbers. The Jablonski Diagram, Fig 1.2.1.2 shows the various deactivation processes involved in a photochemical process.

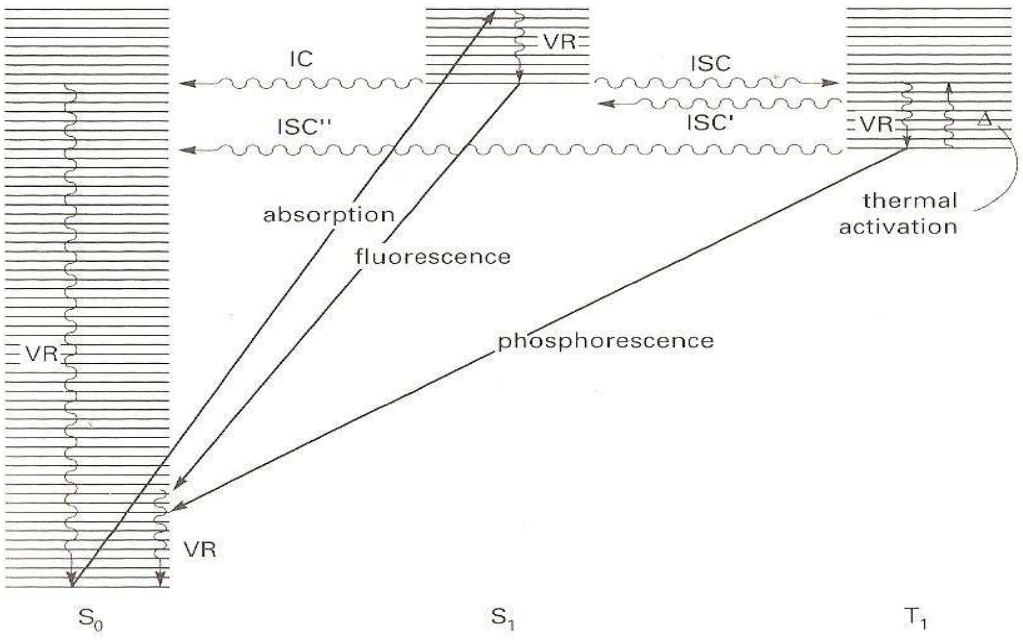


**Figure 1.2.1.2:** Jablonski diagram showing the typical photochemical activation and deactivation processes. Reproduced from ref [4].

A transition from the ground state to an excited state of the same spin quantum number is allowed, while transitions to excited states of different spin quantum numbers are spin forbidden. In most molecules the ground state is singlet. Photophysical

excitations from the $S_0$ ground state to the $S_1$ singlet excited state are allowed. The excited triplet state $T_1$ cannot be directly populated by photo excitation from $S_0$ to $T_1$ since this transition is spin forbidden. The triplet state can however be reached by deactivation of the higher singlet states.

A non-radiative deactivation between states of the same multiplicity is called internal conversion (IC) e.g. in the Jablonski diagram in Fig 1.2.1.2, relaxation from $S_1 \rightarrow S_0$. The excess energy is dissipated by vibrational relaxation such as by collisions with solvent molecules. Radiative transitions resulting in emission from states of the same multiplicity, e.g. $S_1 \rightarrow S_0$, are called fluorescence. Loss of energy through vibrational relaxation before emission leads to the $\lambda_{max}$ of emission being higher than the absorption.

Non-radiative crossover between states of different multiplicities, e.g. $T_1 \rightarrow S_0$, is referred to as intersystem crossing (ISC). ISC is a forbidden transition but spin orbit coupling can lead to a relaxing of this process. Phosphorescence comes from the de-excitation of an excited state to a ground state of different spin multiplicity, e.g. $T_1 \rightarrow S_0$. Intersystem crossing from S1 to T1 leaves the molecule with an excess of vibrational energy which is quickly dissipated in solution by collisions with solvent molecules, known as vibrational relaxation. In some molecules, including many heavy metal containing inorganic molecules, where there is a mixing of electronic excited states and the spin multiplicity of the emitting excited state cannot accurately be identified, emission is referred to as luminescence.

### *1.2.2 Kinetics of Photophysical Processes*

In the equation below a molecule in the ground state, M, is excited to an electronically excited state M* and decays back to M as a function of time.

$$M + h\nu \longrightarrow M^* \longrightarrow M + h\nu' \quad (1.2.1)$$

where hν‘ represents emission of lower energy than initially absorbed by the ground state. The decay of the excited state back to the ground state follows first order kinetics and can be represented by:

$$-\frac{d}{dt}[M*] = k_e^0[M*] \quad (1.2.2)$$

where $k_e^0$ is the natural emission rate coefficient. Integration of (1.2.2) yields:

$$[M*] = [M*]_0 e^{-k_e^0 t} \quad (1.2.3)$$

The natural emission lifetime, $\tau_e^0$, is the reciprocal of the emission radiative rate coefficient:

$$\tau_f^0 = \frac{1}{k_e^0} \quad (1.2.4)$$

From the above two equations we can see that at a time t = $\tau_e^0$, the concentration of M* will fall to 1/e of its initial concentration. In experimental conditions this equation does not take into account any de-excitation from non-radiative decay pathways. If emission is in direct competition with IC and ISC the rate of decay will still obey first order rate kinetics but with a rate coefficient of $k_e$:

$$[M^*] = [M^*]_0 e^{-k_e t}, \quad (1.2.5)$$

where $k_e = k_e^0 + k_{IC} + k_{ISC}$

The rate coefficient $k_e$ can include all deactivation pathways for the M* excited molecule. Therefore the measured emission lifetime can be calculated from the reciprocal of the summation of all the decay rate constants.[5] The measured lifetime is given by:

$$\tau_e = \frac{1}{k_e} = \frac{1}{k_e^0 + k_{IC} + k_{ISC}} \qquad (1.2.6)$$

Emission lifetimes are normally measured using a pulsed excitation source. The sample is excited with a short intense pulse, typically from a monochromatic excitation source, and a curve is constructed of the emission collected over time between pulses. A delay generator can be used to control a gated optical intensifier in front of the detector. The delay generator can be adjusted to change the time after the pulse that emission is detected and from this emission decay over time an exponential curve is built up. Another method is time correlated single photon counting (TCSPC). After the excitation pulse the time of arrival of single photons at the detector, normally a photo multiplier, is recorded and a histogram is built up over from additional pulses. The histogram is an exponential function from which the lifetime can be extracted.

### 1.3 Properties of Ruthenium Polypyridyl Complexes

The chemistry of polypyridyl ruthenium complexes has been heavily investigated since the discovery of the luminescence of $[Ru(bpy)_3]^{2+}$ in 1959 by Paris and Brandt[6]. $[Ru(bpy)_3]^{2+}$ and its derivatives have generated a lot of interest due to a combination of its chemical stability, luminescence emission and excited state lifetimes and chemical reactivity. This class of complexes has potential applications in the development of electron and energy transfer, luminescence and electrochemiluminscence sensors and solar energy conversion. The electrochemical and photophysical properties of $[Ru(bpy)_3]^{2+}$ are well documented and comparable to other ruthenium polypyridyl

complexes making it a good reference complex for other ruthenium (II) diimine complexes.

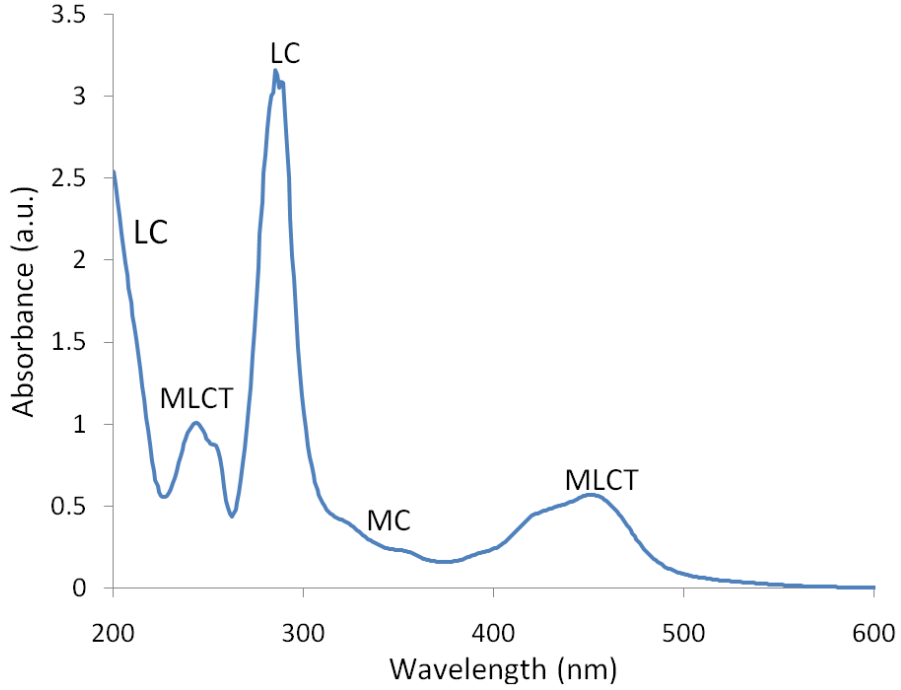


**Figure 1.3.1:** Electronic absorption spectrum of $[Ru(bpy)_3]^{2+}$.

The absorption spectrum for $[Ru(bpy)_3]^{2+}$ is shown in Fig 1.3.1**.** The bands at 185 nm and 285 nm are due to an LC $\pi \rightarrow \pi^*$ transition. The two intense bands at 240 nm and 450 nm have been assigned to MLCT $d \rightarrow \pi^*$ transitions. Two shoulders are present at 322 nm and 344 nm which are not incontrovertibly assigned but are thought to be due to MC $d \rightarrow d$ transitions. When absorption spectra are made in a 4: 1 methanol/ethanol glass at 77 K a shoulder at 550 nm is present that is thought to be due to the lowest spin forbidden $^3$MLCT state[7].

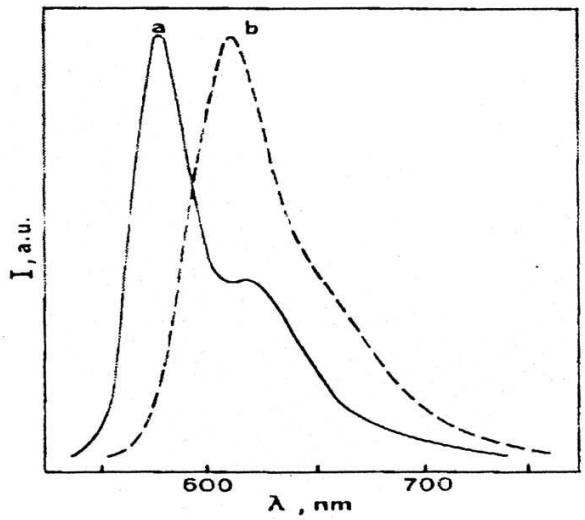


**Figure 1.3.2:** Emission spectrum of $[Ru(bpy)_3]^{2+}$ in alcoholic solution at (a) 77 K and (b) 298 K. Reproduced from Ref [7].

Excitation into any of the $[Ru(bpy)_3]^{2+}$ absorption bands leads to a single luminescence emission (see Fig 1.3.2). The intensity, lifetime and $\lambda_{max}$ of this luminescence emission show considerable temperature dependence. Detailed temperature dependence studies have been carried out and show that this luminescence originates from three closely spaced energy levels[8,9]. It is generally agreed that the energy levels involved in luminescence are MLCT is nature. Whether these levels can be described by spin quantum numbers or whether the promoted electron resides on a single ligand or a delocalized $\pi^*$ orbital are still under debate.

The emission lifetime of $[Ru(bpy)_3]^{2+}$ increases to ~5 μs and emission quantum yield to ~0.4 when measured in a solid 4 : 1 methanol/ethanol glass at 77 K[10]. The emission lifetime and quantum yield decrease with increasing temperature. This is thought to be due to a thermally populated upper lying $^3$MC state which undergoes fast non-radiative deactivation to the ground state[11]. The emission spectrum at 77 K shown in Fig 1.3.2 is highly structured compared to higher temperatures. The shoulder on the

emission spectrum at lower energy is due to *ν*(bpy) framework vibrations caused by distortions in the aromatic rings of the ligand on which the excited state resides[12, 13, 7].

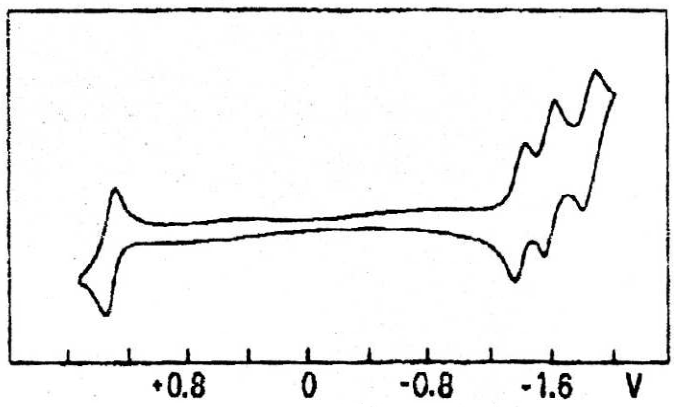


**Figure 1.3.3:** Cyclic voltammogram of $[Ru(bpy)_3]^{2+}$ in acetonitrile (potentials vs. AgCl electrode). Reproduced from Ref [7].

Fig 1.3.3 shows a cyclic voltammogram of $[Ru(bpy)_3]^{2+}$ in AcN. The single oxidation peak and three reduction peaks are all monoelectronic, reversible and independent of the solvent used. The single oxidation peak at 1.27 V is a metal centered oxidation. The three reduction peaks at -1.31 V, -1.50 V and -1.77 V represent bipyridine ligand based reductions.

The photophysical properties of $[Ru(bpy)_3]^{2+}$ arise from population of the $^3$MLCT state. Thermal population of the higher energy $^3$MC excited state leads to highly distorted geometry. The $^3$MC excited state undergoes fast radiationless deactivation to the ground state and can also lead to a cleavage of one of the Ru – N bonds forming a five coordinate square pyramidal species. If no coordinating ion is present, for instance in the case of the $PF_6^-$ salt, the complex returns to the $[Ru(bpy)_3]^{2+}$ configuration. If a coordinating anion is present, such as in the $Cl^-$ salt, a hexacoordinated monodentate bipyridyl intermediate is formed. This form can either undergo a 'self-annealing' process and return to $[Ru(bpy)_3]^{2+}$, or it can lose a ligand and form $[Ru(bpy)_2X_2]$[14].

This photodissociation of the ligand is a major problem to overcome when considering the applications of ruthenium polypyridyl complexes. Prevention of the population of the $^3$MC excited state and photodissociation after population of the $^3$MC state is very important. Avoiding working with coordinating ligands in solution can prevent ligand dissociation. Working at lower temperature prevents the thermal population of the $^3$MC state. Increasing the energy gap between the $^3$MLCT and $^3$MC states can also reduce the population of the $^3$MC state by changing the coordinating ligands.

The effect the ligands have on the $^3$MC and $^3$MLCT excited states of the ruthenium polypyridyl complexes depends on the σ–donor and π–acceptor properties of the ligand. Ligands with σ-donor properties donate electrons to the metal centre causing lower oxidation potentials and higher reduction potentials. Ligands with π-acceptor properties are more likely to accept electrons from the metal centre causing higher oxidation potentials and lower reduction potentials. Complexes with the bpy ligands replaced by ligands with better π–acceptor properties than bpy have lower lying $^3$MLCT states. In mixed ligand systems the excited state exists on the ligand with the lowest reduction potential. Complexes with ligands of better π-acceptor properties however are usually weaker σ-donors which reduces the energy of the $^3$MC excited state making it more accessible and increasing the probability of photodissociation occurring.

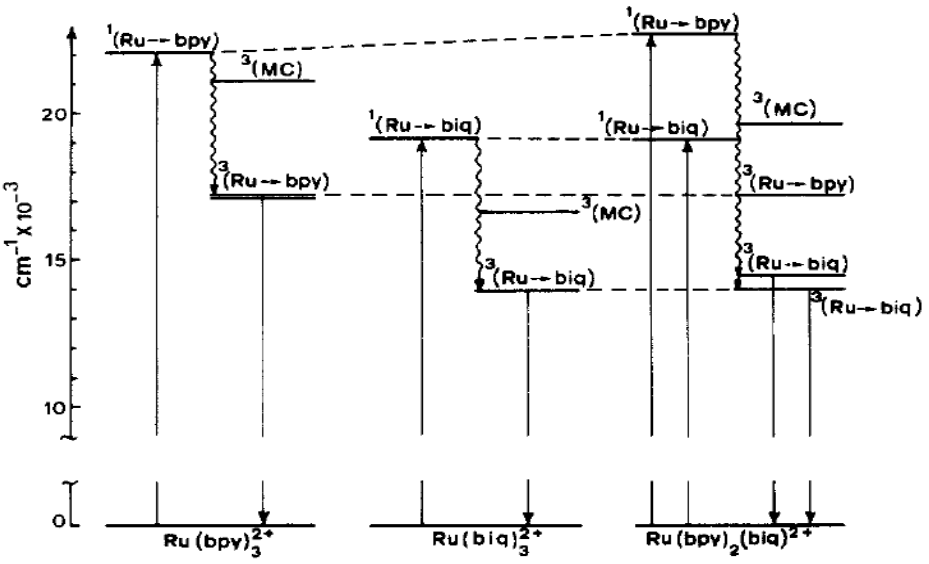


**Figure 1.3.4:** Energy level comparison of $[Ru(bpy)_3]^{2+}$, $[Ru(biq)_3]^{2+}$ and $[Ru(bpy)_2(biq)]^{2+}$. Reproduced from ref [15].

The photophysical properties of the ruthenium polypyridyl complex can be tuned by replacing one or more of the ligands in the system with a ligand with better σ–donor properties. This increases the energy gap between the lowest energy ligand centered $^3$MLCT state and the $^3$MC excited state by increasing the energy required to populate the $^3$MC excited state. The larger $^3$MLCT → $^3$MC energy gap leads to better photostability and quantum yield. This effect has been shown in many systems using biquinoline (biq)[15], bipyrazine and bipyrimidine[16]. Fig 1.3.4 shows a good example of energy level tuning of ruthenium polypyridyl complexes. Biquinoline has better π-acceptor properties than bpy. The $[Ru(biq)_3]^{2+}$ complex has a lower energy $^3$MLCT state but also a more easily accessible $^3$MC state. $[Ru(bpy)_2(biq)]^{2+}$ has two bpy ligands that are better σ–donors than biq. This leads to a lower energy emissive $^3$MLCT state on the biq ligand, since the emissive excited state resides on the most easily reduced ligand, and a larger energy gap between the $^3$MLCT and $^3$MC state.

The effect the choice of ligand has on the electrochemistry and photophysics of ruthenium complexes can be seen in the $[Ru(bpy)_3]^{2+}$ and $[Ru(biq)_3]^{2+}$ examples above. The ligand reduction potentials of the $[Ru(biq)_3]^{2+}$ complex are less negative than for

$[Ru(bpy)_3]^{2+}$ by about 0.67 V while the metal centered oxidation is more positive by about 0.2 V compared to $[Ru(bpy)_3]^{2+}$ [7]. The mixed ligand system $[Ru(bpy)_2(biq)]^{2+}$ has a metal oxidation potential of 1.33 V which falls between oxidation potentials of $[Ru(bpy)_3]^{2+}$ and $[Ru(biq)_3]^{2+}$ as expected due to the mixed ligand system. The first ligand reduction of $[Ru(bpy)_2(biq)]^{2+}$ appears at -0.905 V, closer to the first ligand reduction of $[Ru(biq)_3]^{2+}$, which appears at -0.73 V, than $[Ru(bpy)_3]^{2+}$, which appears at -1.340 V. This is as expected due to the π-acceptor properties of the biq ligand making it more easily reduced than bpy[15, 7]. In the absorption spectra $[Ru(biq)_3]^{2+}$ has a MLCT absorption band that is red shifted by 3000 $cm^{-1}$ compared to $[Ru(bpy)_3]^{2+}$ due to the lower energy $\pi^*$ acceptor orbitals of the biq ligand. The mixed ligand system $[Ru(bpy)_2(biq)]^{2+}$ displays two MLCT absorption bands centered at 439 nm and 525 nm corresponding to Ru → bpy and Ru → biq transitions respectively. The emission spectrum of $[Ru(biq)_3]^{2+}$ displays an emission band with a maximum of 718 nm, a red shift from the emission band of $[Ru(bpy)_3]^{2+}$ which has a maximum of 582 nm. This red shift of 3200 $cm^{-1}$ is comparable to the red shift of the MLCT absorption band and the lower energy ligand reduction potentials. The $[Ru(bpy)_2(biq)]^{2+}$ emission spectrum displays one emission maximum centered at 728 nm. No change in emission maximum is evident whether exciting in the 439 nm or 535 m absorption bands. This result shows that emission occurs from the lowest excited state of the complex, the Ru → biq transition, and that efficient conversion from the Ru → bpy to the Ru → biq excited state occurs[15].

## 1.4 Ruthenium Complexes in Supramolecular Structures and Interfacial Supramolecular Structures

### *1.4.1 An Introduction to Self Assembled Monolayers (SAMs).*

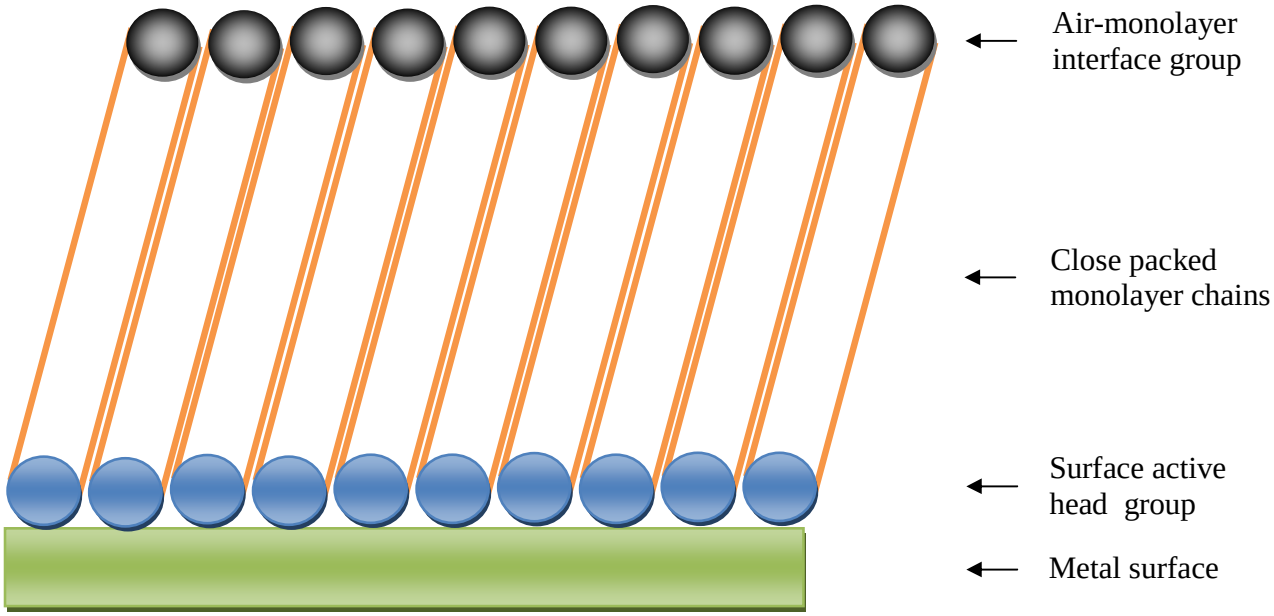


**Figure 1.4.1.1:** A simplified schematic of a spontaneously formed self assembled monolayer showing the surface active head group chemisorbed to the surface, close packing of the monolayer chains and the air-monolayer interface group that can give additional functionality to the monolayer surface.

Self-assembled monolayers are molecular aggregates that spontaneously form and organize into regular single molecule thick arrays on a surface. A simple representation of a self assembled monolayer is shown in Fig 1.4.1.1. The head group is typically a surface active species that binds to the substrate by a strong chemisorption interaction. This anchoring of the self assembling molecule brings the monolayer units close to its neighbours allowing short range lateral interaction with each other that facilitates the organization and packing of the monolayers[17,10].

The first phase of the formation of a monolayer, the initial attachment of the head groups to the surface, typically happens spontaneously over a short timescale. The second stage, the ordering and packing of the monolayer due to the Van der Waals and electrostatic static interactions between the monolayer units, happens over a timescale of hours, typically 24 hours or more. The surface coverage, conformation of individual monolayer units and defect density of the monolayer is dictated by the deposition time, concentration of the deposition solution, the nature and structure of the monolayer molecules and by the shape and roughness of the surface material[18].

Monolayer formation and structural studies have been carried out on a wide variety of surfaces and surface active head groups, for example, n-alkanoic acids on aluminium oxide surfaces[19] and alkyloxysilanes on silicon oxide surfaces[20]. However the vast majority of research has focused on monolayers of alkanethiols on metals such as gold, platinum, silver, palladium and mercury[21]. Alkanethiol monolayers on gold can provide relatively defect free monolayers on crystalline metals, although defects increase with surface roughness, decreasing alkyl chain length and vary with the thiol binding affinity with the surface. The large binding affinity of the thiol metal bond (418 kJ/mol and 234 kJ/mol for a thiolate on gold and platinum respectively) and interchain interactions, which can be comparable in energy to the surface binding, lead to very stable monolayer systems with a wide range of solvents and across a wide range of temperatures and potentials[22, 23].

Changing the group at the air-monolayer interface provides a means of varying the functionality of the surface. For example Gouget-Laemmel *et al.*[24] functionalized a crystalline silicon surface with 10-carboxydecyl monolayers. This created a monolayer with an air-monolayer interface composed of carboxylic acid functionalities. This carboxylic acid surface was further functionalized by the common EDC/NHS coupling reaction to create succinimidyl ester groups on the surface, creating a surface that is highly reactive with amide groups for further functionalisation. The wettability of the surface can be modified using monolayers. Ulman *et al.*[25] demonstrated that varying the concentrations of hydroxyl and methyl groups at the air-monolayer interface modified the

wettability of the surface to hexadecane in a nonlinear fashion with increasing concentration of OH groups at the air-monolayer interface.

In comparing complex structures with surface active thiols the thiol may need to be protected during the synthesis of the complex due to its highly reactive nature. Conversion from a thiol to an acetylthio functionality is a common method for protecting thiol groups. The acetylthio group can be converted back into a thiol by reacting it with a mild base base, such as $NH_4OH$ or low concentrations of NaOH. However the formation of M – S bonds and the formation of monolayers has been reported for the direct coupling of complexes containing acetylthio functionalities to metal surfaces. In the work by Bourgoin *et al*. a mixed monolayer of dodecanethiol and 2,5''-bis(acetylthio)-5,2'5',2''-terthienyl was created on a gold surface without the conversion of the acetylthio group to a thiol group with base[26]. Tour, Allara, *et al*. demonstrated the formation of monolayers on gold of numerous complexes with acetylthio functionalities with and without conversion of the acetylthio functional groups to thiols using a base. Higher concentrations of the acetylthio complexes were needed compared to the thiol or deacylated complex to form densely packed monolayers in the same time frame[27].

### *1.4.2 SAMs of Ruthenium Polypyridyl Complexes.*

Thin film devices constructed from surface active transition metal complexes have garnered much interest lately particularly on conducting surfaces. Interaction between the surface and the transition metal complex can influence the opto-electronic properties of the transition metal complex. Interactions involving electron or energy transfer from the transition metal complex to the surface provide an electronic connection to the processes occurring in the nanoscopic environment of the transition metal complex. Ruthenium polypyridyl complexes make good candidates for these thin film devices due to their light addressable functionality and favourable reversible electrochemistry of their oxidation states. The luminescence and redox electrochemistry can be used as a probe of the environment at the surface.

The photophysics of ruthenium polypyridyl complexes are affected by the closely packed and confined environment or a SAM and resemble the effect of rigidochromism at 77 K. Forster and Keyes[28] measured the emission of $[Ru(bpy)_2(Qbpy)]^{2+}$, where Qbpy is 2,2':4,4'':4'4''-quarterpyridyl, on a platinum microelectrode and compared it to the solution phase emission. These spectra are shown in Fig 1.4.2.1. The spontaneously formed monolayer emission is much broader with a shoulder on the lower energy side suggesting slower dipolar relaxation of the excited state. The red shift of the emission intensity is not as expected due to the less efficient solvation of the excited state in a monolayer and lower dielectric constant of the solvent. However this was attributed to stabilising interactions between the absorbates and the surface. The shape of the emission spectra of the monolayer with the broad shoulder on the low energy side of the emission band is similar to the shape of ruthenium polypyridyl complexes at 77 K which display broad low energy shoulders due to *v*(ligand) framework vibrations (see section 1.3). This change in emission spectrum shape when the complex is in a monolayer is due to the decreased vibrational and rotational relaxation experienced when the complex is in such a close packed structure, similar to the rigidochromic effect on emission when in a low temperature solvent glass (see section 1.3). The same effect was also seen by Pikramenou, Unwin, Forster *et al.*[29] for monolayers of $[Ru(bpy)_2(bpySH)](Pf_6)_2$ on platinum surfaces, where bpySH is 5,5'-bis(mercaptomethyl)-2,2'-bipyridine. Emission was red shifted 30 nm with a broad shoulder visible on the low energy side of the emission profile.

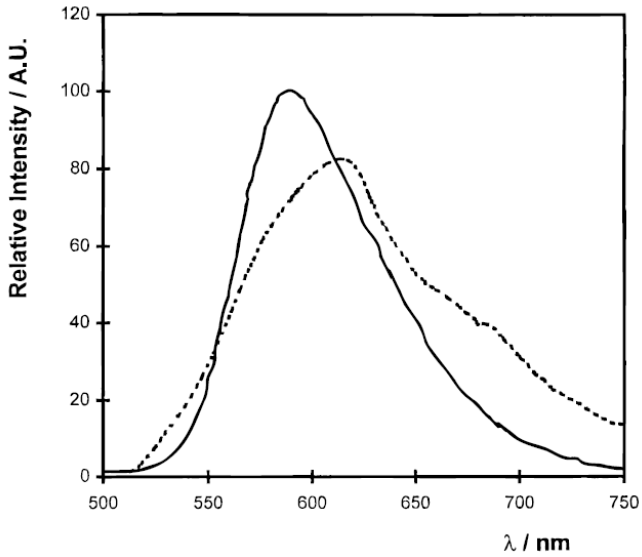


**Figure 1.4.2.1:** Emission spectra of $[Ru(bpy)_2(Qbpy)]^{2+}$. The solid line represents the complex in 4:1 methanol:ethanol while the broken line represents the complex as a spontaneously formed monolayer. The contact solvent for the monolayer was 4:1 methanol:ethanol. Reproduced from ref [28].

The emission remained evident from the $[Ru(bpy)_2(Qbpy)]^{2+}$ platinum microelectrodes despite being only 12 Å above the metal surface which shows that excited state quenching by the surface depends on the structure linking the ruthenium complex to the metal surface. If the luminescence excited state resides on a ligand further away from the metal surface then this can also reduce the rate of electron or energy transfer to the surface.

When the metal surface is roughened or patterned the SEF effect can be particularly prevalent as explained in section 1.5.3. Forster, Keyes, *et al.*[30] created gold surfaces patterned with nanocavities by electrochemically depositing gold on a tin oxide surface through monolayers of polystyrene spheres. The polystyrene spheres were dissolved leaving the patterned gold nanocavities. Monolayers of $[Ru(bpy)_2(Qbpy)]^{2+}$ were then formed on these nanocavity arrays. The emission enhancement factor within these cavities compared to the complex in solution was found to be approximately 4. Luminescence lifetimes were greatly reduced inside the nanocavities. The emission

enhancement of the monolayers was found to be less than the enhancement of the same cavities filled with a solution of $[Ru(bpy)_2(Qbpy)]^{2+}$ due to excited state quenching by the surface. Confocal emission lifetime images of the monolayer functionalized and solution filled nanocavities are shown in Fig 1.4.2.2. The suitability of these arrays as SERS substrates was investigated and it was found that the Raman enhancement factor was 5 x $10^7$ inside the cavities.

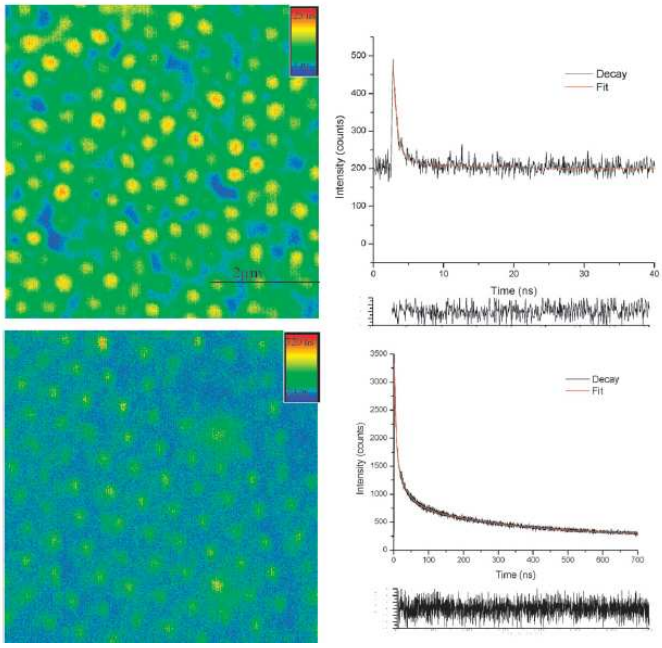


**Figure 1.4.2.2:** Confocal lifetime emission images (left) and emission lifetime decays (right) of gold nanocavity arrays. The top images represent the gold nanocavities functionalized with a $[Ru(bpy)_2(Qbpy)]^{2+}$ monolayer while the bottom images represent the gold nanocavities filled with a 80/29 v/v methanol/water solution of 1 mM $[Ru(bpy)_2(Qbpy)]^{2+}$. An excitation wavelength of 405 nm was used. Reproduced from ref [30].

Because of the high surface concentration of luminophores in a monolayer compared to solution lateral energy or electron transfer can occur leading to quenching of the excited state. Forster *et al.*[31] controlled the concentration of $Ru^{3+}$ in a monolayer of $[Ru(bpy)_2(Qbpy)]^{2+}$ on a platinum electrode by partially oxidizing the monolayer. It was

shown that $Ru^{3+}$ was an efficient quencher of $Ru^{2+}$*. Generation of $Ru^{3+}$ would lead to a decrease in luminescence due to the decrease in concentration of $Ru^{2+}$. A plot of $I/I_0$ vs. $Ru^{3+}$ concentration is shown in Fig 1.4.2.3. This plot was corrected for the change in $Ru^{2+}$ concentration due to the generation of $Ru^{3+}$. It was shown that the reduction of luminescence intensity was much greater than would be expected from loss of $Ru^{2+}$*. As an example the luminescence is reduced by 90% when only 10% of metal centres in the monolayer are oxidized.

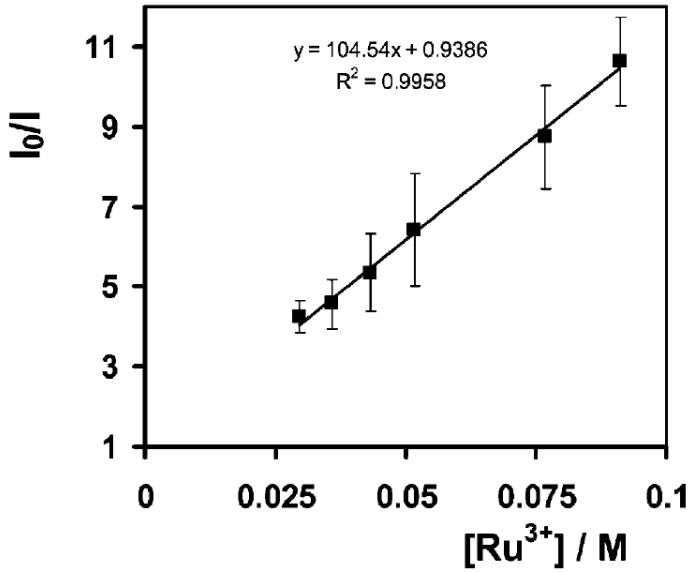


**Figure 1.4.2.3:** Dependence of $I/I_0$ on the concentration of $Ru^{3+}$ in a monolayer of $[Ru(bpy)_2(Qbpy)]^{2+}$ on a platinum electrode. Aqueous 0.1M $LiClO_4$ was the contact solvent. Intensities are corrected for the change in $Ru^{2+}$ concentration with $Ru^{3+}$ generation. Reproduced from ref [31].

A lot of interest has been generated lately in the development of photovoltaic devices and ultimately in the development of new solar cells, which is a key area to which interfacial luminescent SAMs will be applied. Yamada *et al.*[32] created a photovoltaic device based on monolayers of a two ruthenium surface active complexes on a transparent ITO electrode. The first complex was a ruthenium (II) tris(2,2'-bipyridine)-viologen linked thiol. The ruthenium polypyridyl head group and viologen linker act as a donor-acceptor electron transfer system. The other complex is a ruthenium (II) tris(2,2'-bipyridine)-alkane thiol. The structures of both of these complexes are shown in Fig

1.4.2.4. The complexes were synthesized as surface active disulphides. A schematic of the photovoltaic device and it's method of operation are shown in Fig 1.4.2.5. The photovoltaic device consisted of a modified ITO electrode and a bare ITO electrode with a filter paper in between filled with an electrolyte solution of a mixture of 0.03 M LiI and 0.001 M $I_2$ which would also serve as a sacrificial electron donor. The space between the electrodes was filled with a polyimide film to ensure electrical insulation and prevent evaporation of the electrolyte.

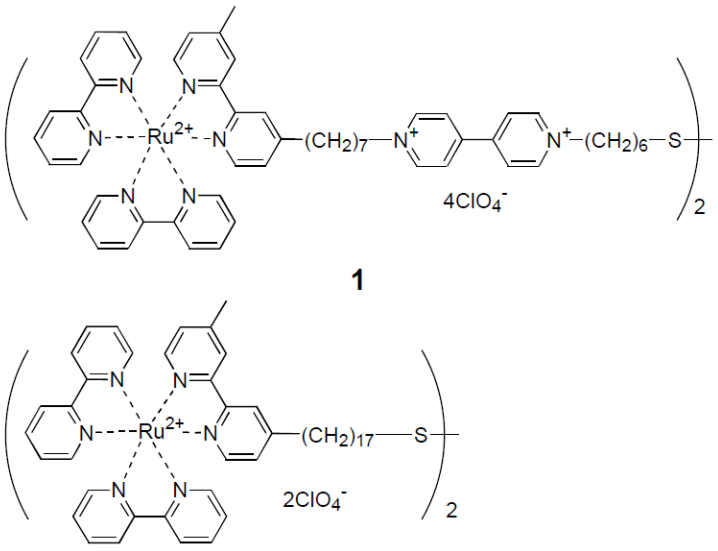


**Figure 1.4.2.4:** Structures of surface active ruthenium polypyridyl complexes from ref [32].

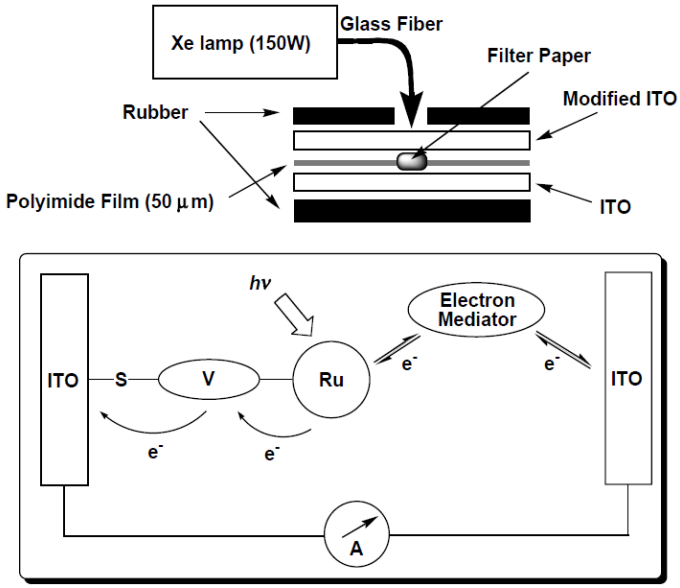


**Figure 1.4.2.5:** Schematic of the photovoltaic device and its basic principle of operation from ref [32].

It was shown that the complex with the viologen linker was far more efficient at producing a photocurrent response than the alkanethiol due to efficient electron transfer from the $Ru^{2+}$* state to the viologen followed by electron transfer from the viologen to the ITO surface. A comparison of the photovoltaic response compared to the absorption of the viologen linked complex is shown in Fig 1.4.2.6 below.

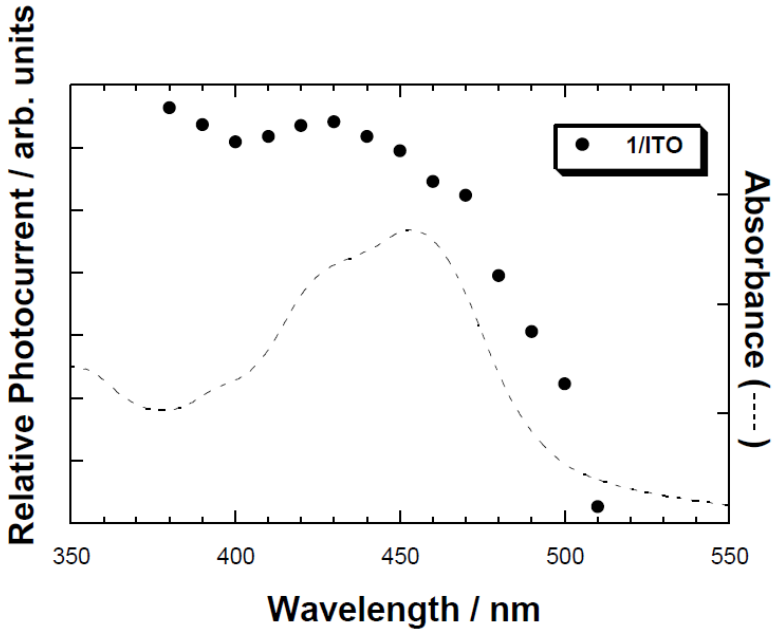


**Figure 1.4.2.6:** Photocurrent action of spectra of the viologen linked ruthenium complex 1 (dotted plot) and the absorption spectrum of the complex in acetonitrile. Reproduced from ref [32].

Surfaces modified with ruthenium polypyridyl complexes have also been used in sensor systems to accurately report on the environment experienced by the monolayer. Yam *et al.*[33] reported on a ruthenium polypyridyl complex attached to a glass substrate, the complex and reaction scheme are given in Fig 1.4.2.7. This complex showed highly efficient luminescence quenching by atmospheric oxygen. Varying the concentration of oxygen in the atmosphere around the sensor gave reproducible and measureable quenching of the luminescence proportional to the oxygen concentration.

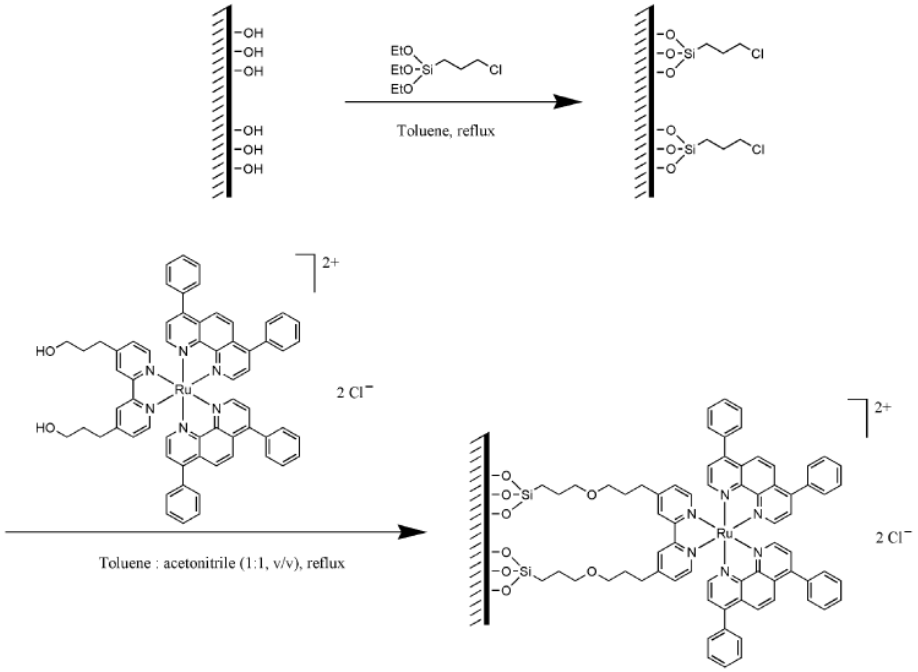


**Figure 1.4.2.7:** Formation scheme of $O_2$ sensing monolayer on glass substrate from ref [33].

Forster *et al.*[34] reported on the pH sensing ability of an ITO surface modified with a $[Ru(bpy)_2PIC](PF_6)_2$ monolayer, where PIC is 2-(4-carboxyphenyl)imidazo[4,5-f][1,10]phenanthroline, and this can be used as a pH probe. Ionization of the imidazo bridge by changing the pH will change the interfacial heterogeneous electron transfer rate and the luminescence of the monolayer. The ionization scheme of this complex as a monolayer is shown below in Fig 1.4.2.8. The heterogeneous electron transfer rate of the monolayer at an over potential of +50 mV increased from $0.7e^{-5}$ to $7e^{-5}$ $s^{-1}$ as the pH was changed from 1.7 to 9.3. A shift of the $\lambda_{max}$ of emission to higher energy was observed with protonation of the monolayer due to decreasing pH. A decrease in emission intensity was also observed with decreasing pH. The emission profile of the $[Ru(bpy)_2PIC](PF_6)_2$ complex in solution and as a monolayer on ITO is shown in Fig 1.4.2.9.

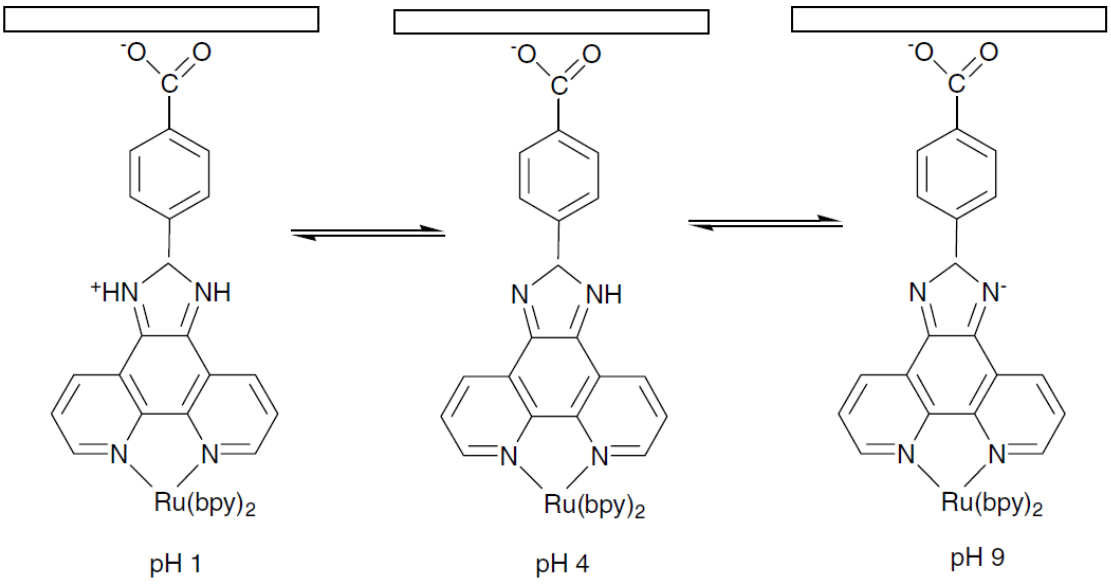


**Figure 1.4.2.8:** pH dependent ionazation of the imidazo bridge of $[Ru(bpy)_2PIC](PF_6)_2$. Reproduced from ref [34].

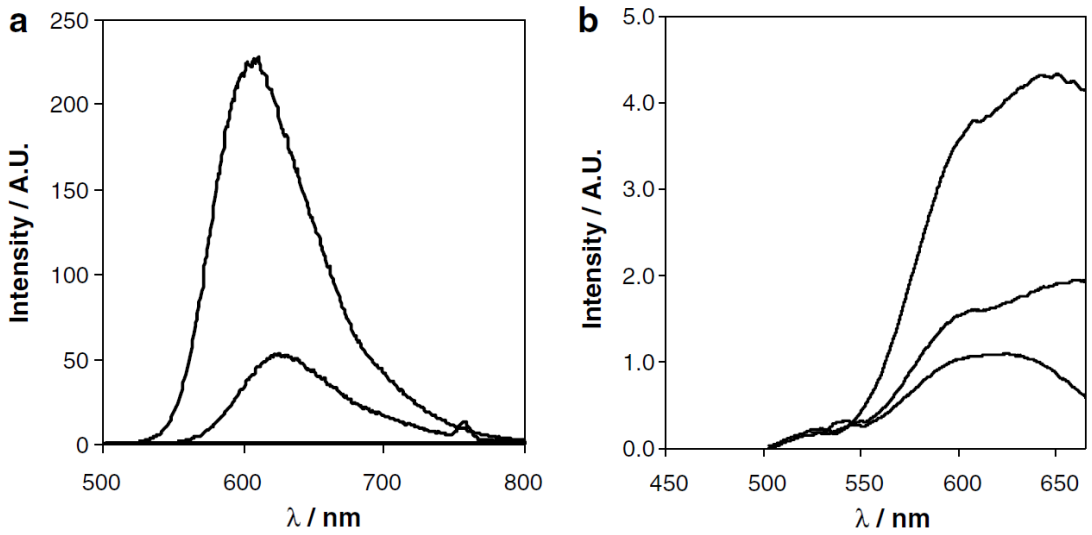


**Figure 1.4.2.9:** (a) Emission spectra of $[Ru(bpy)_2PIC](PF_6)_2$ in aqueous solution at pH 4 (upper curve) and pH 1 (lower curve). (b) Emission spectrum of $[Ru(bpy)_2PIC](PF_6)_2$ as a monolayer on ITO. From top to bottom the pH of the contacting solution is 4.0, 3.1 and 0.9. Reproduced from ref [34].

Thomas *et al*.[35] also saw lateral quenching of surface active ruthenium complexes when bound to gold nanoparticles. The ruthenium complexes were co-functionalised with a monothiol derivative of triethylene glycol on Au nanoparticles with average diameters of 4.5 nm. The structures of these functionalized monolayers and the complexes are shown in Fig 1.4.2.10. These functonalised nanoparticles had biexponential luminescence lifetimes consisting of a long component of 1.1µs and a short component of 4.3 ns in deaerated $CH_2Cl_2$. The long component was attributed to bound unquenched ruthenium complex while the short lifetime component is attributed to quenching of the $Ru^{2+}$* state through either energy or electron transfer. Transient absorption spectroscopy was used to identify and characterize the lateral electron transfer products $Ru^{+}$ and $Ru^{+}$. There was no experimental evidence to confirm the orientation of these ruthenium complexes on the gold nanoparticle surface.

Kamat, Thomas, *et al*. then modified Au nanorods with a $[Ru(bpy)_3]^{2+}$ complex with a pendant alkylthiol consisting of an alkyl chain five carbons long[36]. The Au nanorods were stabilised with a 1-dodecanethiol monolayer and functionalized with the ruthenium complex by a displacement reaction. Upon functionalisation the absorption spectrum of the nanorods changed suggesting morphological changes induced by the binding of the ruthenium complex. TEM imaging also suggests some aggregation of the nanorods occurred. These functionalized nanorods were emissive despite the close proximity of the ruthenium metal centres to the surface. The functionalized nanorods had a biexponential luminescence lifetime just like the functionalized nanoparticles in the previous publication. Again the long lifetime component was attributed to the unquenched bound ruthenium dye and the short lifetime component to quenching of the bound ruthenium complex. However for these nanorods transient absorption spectroscopy showed no evidence of the presence of $Ru^{+}$ or $Ru^{3+}$. This suggests that the quenching process is not an electron transfer process due to lateral quenching but an energy transfer process from the $Ru^{2+}$* to the metal surface. The low loading of the ruthenium complex was deemed responsible for the lack of electron transfer processes. Again just like the previous paper by Thomas *et al.*[35] there was no experimental evidence to confirm the

orientation of these ruthenium complexes on the gold nanoparticle surface. The schematic of this energy transfer process is shown below in Fig 1.4.2.10.

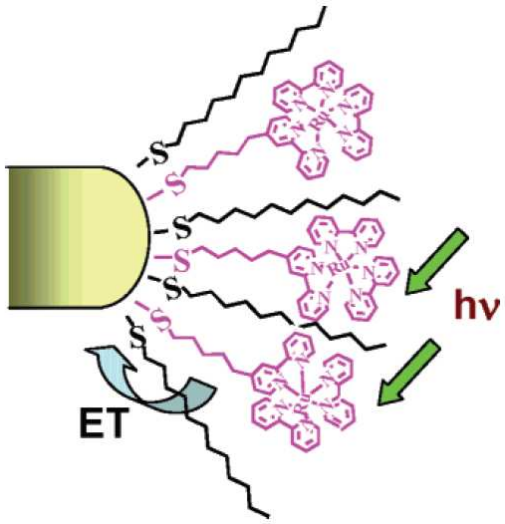


**Figure 1.4.2.10:** Schematic of the photo-induced energy transfer process occurring on the functionalized nanorods from ref [36.]

### *1.4.3 Ruthenium Polypyridyl Metallosurfactants*

Functionalising ruthenium polypyridyl complexes with pendant long chain hydrocarbon alkanes can create metallosurfactants with a polar transition metal head group and a hydrophobic alkyl chain tail group. A number of ruthenium metallosurfactants have been synthesized and reported in the literature that self assemble into micelles, bilayer vesicles or form bilayer films at the air/water interface. Due to the self assembly properties of these complexes metallosurfactants have applications in the creation of heterogeneous catalysts[37], thin film devices such as ECL or emission based immunoassays[38], surfactant membrane probes[39] or photosensitisers of semi-conducting surfaces[40].

De Cola *et al.*[39] reported on iridium and ruthenium polypyridyl metallosurfactant complexes the structures of which are shown in Fig 1.4.3.1. When solvated in water

below the CMC (crtitical micelle concentration) of 0.05mM the ruthenium complex has an emission lifetime of 360 ns, similar to the parent $[Ru(bpy)_3]^{2+}$ complex which has an emission lifetime of 390 ns. At concentrations above the CMC the ruthenium surfactant the emission intensity increased and emission lifetime decay becomes biexponential with a short and long lifetime component of 400 ns (20%) and 860 ns (80%). Micelles of CTAB were formed in aqueous solutions of the ruthenium surfactant and which led to an increase in emission intensity and biexponential emission decay with a short and long lifetime component of 380 ns (60%) and 650 ns (40%). It is thought that the short lifetime component in both systems is due to monomeric units of the complex in solution while the long lifetime component is due to the ruthenium surfactant in micelle form or, in the case of the CTAB micelles, integrated into the CTAB micellular structure. It was suggested that the longer lifetime component was due to lower oxygen diffusion in the micelle structure and a lowering of $k_{nr}$ due the close packing of the head groups reducing vibrational relaxation. In mixed micelles of the ruthenium and iridium surfactants and when both surfactants are dissolved in CTAB micelles efficient electron transfer from the iridium complex to the ruthenium complex is observed. When excited at 350 nm the characteristic emission of the iridium surfactant is not observed but the ruthenium emission at 645 nm is observed.

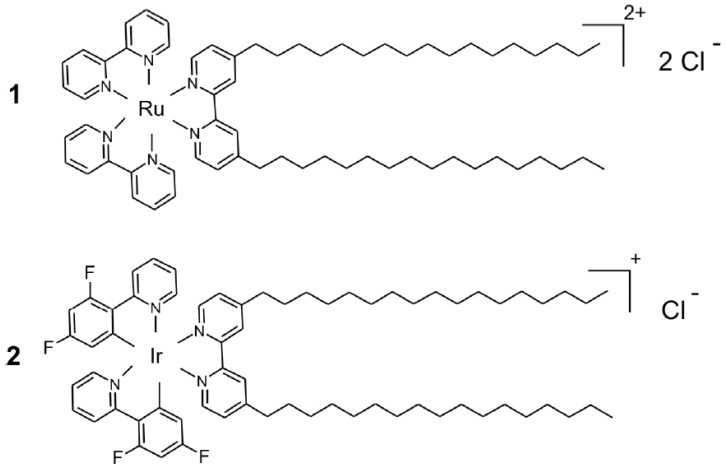


**Figure 1.4.3.1:** Structure of complexes from ref [39].

The biexponential emission lifetime of ruthenium metallosurfactant micelles and how the quenching rate can differ between monomers of the metallosurfactant in solution and the metallosurfactant in micellular form can be seen in the work by Schmehl *et al*.[40] In this communication the synthesis of a range of metallosurfactants based on the $[Ru(bpy)_3]^{2+}$ parent complex was reported. One of the bpy ligands was replaced with either a bpy ligand with two pendant alkyl chains or a bpy ligand with one alkl chain and a methyl group. [Ru(xCn)] was used to designate the type of complex, were x is either M (monoalkyl with a methyl group) or D (dialkyl) and n was the number of carbons in the alkyl chain. The structure of these ligands is given in Fig 1.4.3.2. At concentrations above and below the cmc for the [Ru(MC17)] complex in deaerated aqueous solution, effectively removing any quenching agents) the complex displayed single exponential emission lifetime decay. Addition of the quencher methyl viologen to the micellular solution produces a biexponential emission decay with a short and long lifetime component. An emission red shift was also observed of about 15 nm for all complexes upon micelle formation due to the more hydrophobic environment of the micelles.

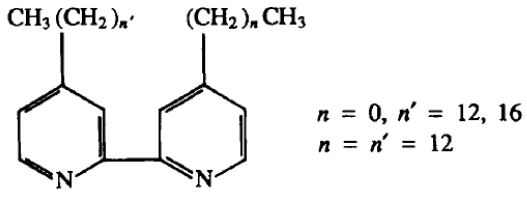


**Figure 1.4.3.2:** Structure of ligands synthesized in ref [40].

In many publications like the ones discussed above the size of the metallosurfactant aggregates is not discussed. The size of the aggregates can reveal important information about the structure of the metallosurfactant aggregates. Micelles typically have a diameter that is roughly the size of the length of two of the monomeric units. They are short lived and so far have proven to be impossible to isolate. Bilayer vesicles have much larger diameters and can be isolated by drying the solvent[41]. Bowers et. al[37] reported on a series of ruthenium metallosurfactants containing a bpy ligand

modified with two alkyl chains of varying lengths across the series, the structure of which is shown in Fig 1.4.3.3. These complexes were shown by small angle neutron scattering (SANS) to form small micelles with diameters between 10-20 Å depending on the complex. Single chained complexes possessed higher cmc concentrations than double chained complexes and the cmc concentration was lower with longer alkyl chains as expected.

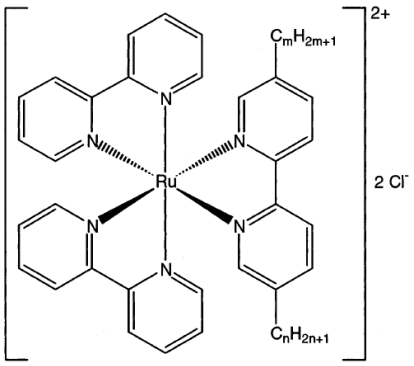


**Figure 1.4.3.3:** Structure of the ruthenium metallosurfactants in ref [37].

Fuhrhop *et al.*[41] synthesized a ruthenium complex with a malonate type ligand with two pendant alkyl chains. The structure of this complex is shown in Fig 1.4.3.4 below. It was found that this ruthenium metallosurfactant was insoluble in water with either $Cl_2$ or $(PF_6)_2$ as the counter-ions and both form surface monolayers. Upon sonication both ruthenium metallosurfactants dissolved in the aqueous solution. TEM of dried samples and cryo-TEM of the dichloride metallosurfactant dissolved in aqueous solution did not detect the formation of any vesicles although this publication did not rule out the formation of micelles. TEM and cryo-TEM or the aqueous solutions of the metallosurfactant with $PF_6$ counter-ions clearly showed the formation of multilaminar vesicles. Theses TEM images are shown in Fig 1.4.3.5.

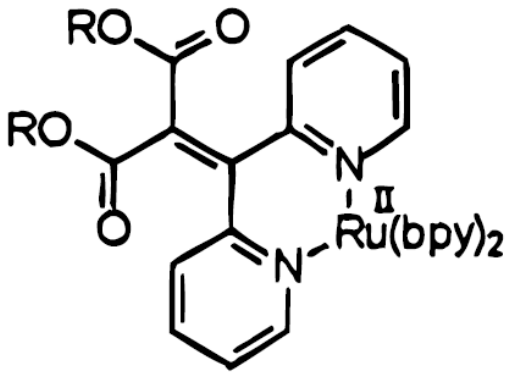


**Figure 1.4.3.4:** Structure of the ruthenium meallosurfactants from ref [41] where R is an alkyl chain 18 carbons in length.

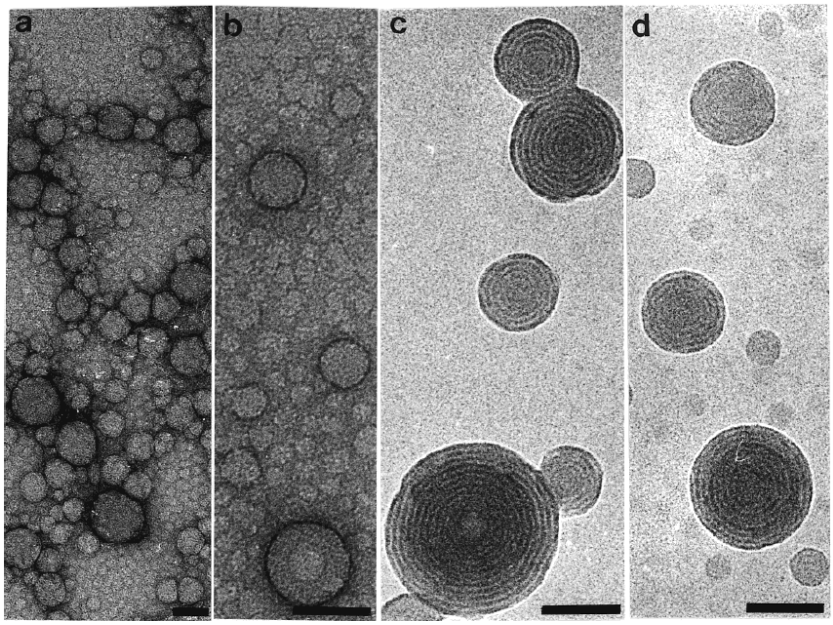


**Figure 1.4.3.5:** TEM micrographs of the multilaminar vesicles of the ruthenium metallosurfactant in ref[41]. (a) and (b) represent uranyl stained and unstained air dried samples respectively imaged at a high electron dose (1000 e/Å$^2$). (c) and (b) represent air dried and freeze dried samples respectively imaged at a low electron dose (100 e/Å$^2$). Images reproduced from ref [41].

In this thesis we investigate the properties of a series of novel ruthenium (II) polypyridyl complexes with pendant acetylthio alkanes of varying lengths and the supramolecular structures of these complexes. These complexes are capable of forming SAMs on metallic surfaces and spontaneously form micellular structures when in aqueous solution.

## 1.5 Raman Spectroscopy and Surface Plasmon Effects.

### *1.5.1 An Introduction to Raman Spectroscopy*

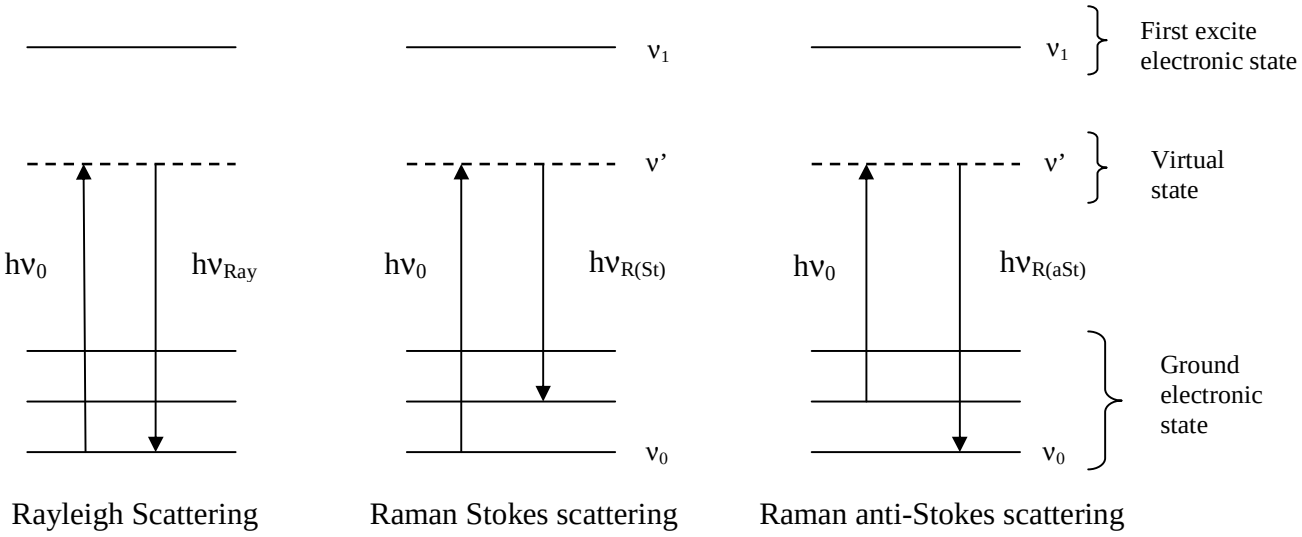


**Figure 1.5.1.1:** Diagram showing the different types of light scattering expected from a molecule, where $\nu_0$ represents the ground electronic state, $\nu_1$ the first excited electronic state and $\nu$' the non-stationary 'virtual' vibrational state.

Scattering of radiation occurs when a photon interacts with a molecule and this photon does not have enough energy to correspond to a difference between any two stationary energy levels in the molecule. Since the photon does not have the energy to excite the molecule to a natural energy state it instead excites the molecule to a 'virtual' energy state. A virtual energy state is a non-stationary energy state lower in energy but in

close proximity to a natural energy state which will decay rapidly due to its low stability. Fig 1.5.1.1 shows the types of scattering that can occur after this type of excitation. The majority of scattering proceeds without any change in the frequency of the incident photon and is called Rayleigh or elastic scattering. Rayleigh scattering gives no information on the vibrational structure of the sample.

Scattered photons with a different frequency to the incident photons are also emitted and are known as Raman scattering. Stokes scattering occurs when the molecule is excited from the ground vibrational state to the virtual state and decays to a higher energy vibrational state. Anti-Stokes scattering occurs when the molecule is excited from the first vibrational excited state to the virtual state and then decays to a vibrational state of lower energy than the incident photons[42].

The Raman spectrum is given by the Raman shift calculated by subtracting the frequency of the scattered light from the frequency of the incident light ($\nu - \nu'$). Boltzmann's law states that only a small portion of molecules will exist in the first excited vibrational state at room temperature meaning the Stokes scattering is more intense than anti-Stokes scattering. Therefore Raman spectroscopy usually involves measuring the Stoke bands. Anti-Stokes bands will increase in intensity with increasing temperature[43]. All molecules including diatomic molecules are Raman scatterers making it a very valuable spectroscopy.

Raman spectroscopy differs from infrared spectroscopy in that Raman active molecular vibrations or rotations cause a change in the molecular polarizability, while IR active vibrations and rotations cause a change in molecular dipole. In typical Rayleigh scattering an oscillating dipole when excited by a beam of radiation with a frequency of $\nu$ undergoes oscillations with a frequency of $\nu$. This type of dipole emits radiation with a frequency of $\nu$. However if the molecule undergoes some internal motion such as a vibration or rotation of frequency $\nu_{vib}$ which changes the polarizability we get the Raman scattering. This oscillating dipole will have a frequency of $\nu \pm \nu_{vib}$ and will emit radiation with this frequency despite an excitation frequency of $\nu$[44].

### *1.5.2 Resonance Raman*

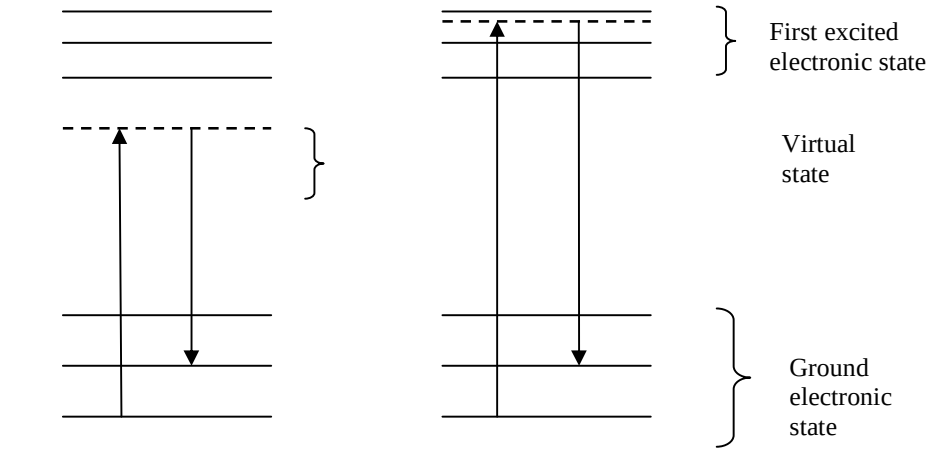


**Figure 1.5.2.1:** Comparison of Raman Stokes scattering with Resonance Raman Stokes scattering.

A comparison of Raman and resonance Raman processes is shown in Fig 1.5.2.1. Non- resonance Raman scattering techniques require high concentration samples in the molar range to give good quality spectra. When a sample is excited with excitation radiation close to or equal to the frequency of absorption of the sample the intensities of certain Raman bands can be greatly increased. Resonance Raman leads to simplified Raman spectra since only vibrational transitions coupled with the electronic transition which is excited will be enhanced and tend to swamp non-enhanced Raman bands. This can be useful for identifying and characterizing vibrational transitions involved in the electronic spectrum. Resonance Raman can give enhancements of several orders of magnitude compared to non-resonance Raman and can give good quality spectra in the mM to μM range[11].

### *1.5.3 Surface Plasmons*

A surface plasmon is an oscillation of the conducting electrons at the metal dielectric interface of a rough metal surface. This creates surface electromagnetic waves that propagate parallel to the metal dielectric interface[45]. This surface plasmon can be excited by irradiation with photons with the same frequency and momentum as the surface plasmon oscillations. This coupling of the surface plasmon with a photon creates a quasiparticle called a polariton and is known as surface plasmon resonance (SPR)[46].

Two types of surface plasmon resonance are used in sensors (a) propagating surface plasmon resonances and (b) localized surface plasmon resonances. The differences between them are illustrated in Fig 1.5.3.1 below.

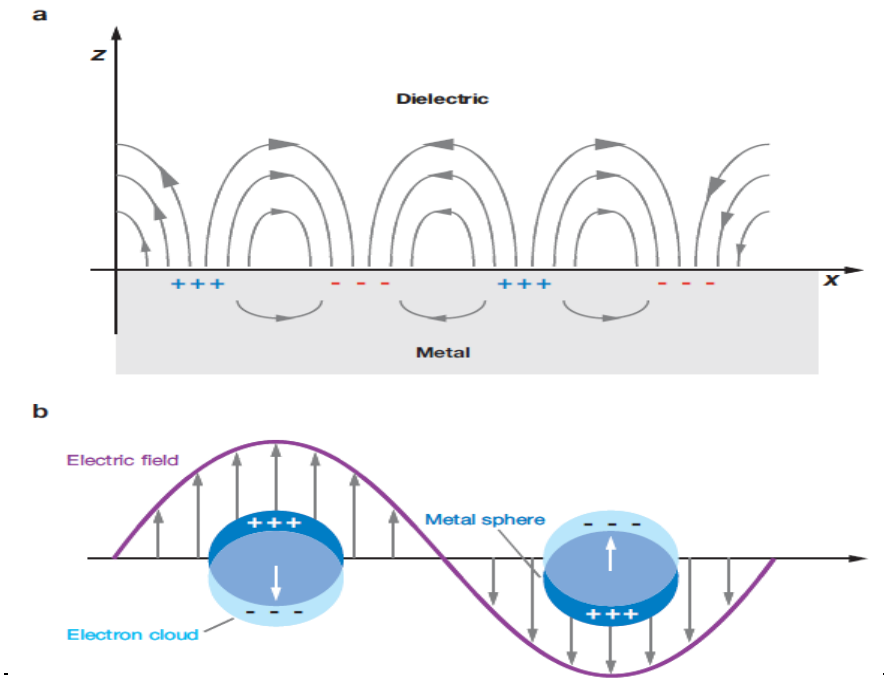


**Figure: 1.5.3.1** Diagram illustrating (a) propagating surface plasmon resonances (SPR) and (b) localized surface plasmon resonances (LSPR). Diagram reproduced from ref [47].

Propagating surface plasmon resonance occurs when the frequency of the incident light couples with the frequency of oscillation of the electrons at the metal surface and creates an electron resonance. These plasmons propagate along the metal surface in the x and y plane in order of 10-100 μm with an associated electric field that decays in the z direction exponentially from the surface. SPR has been used in many biosensing applications such as Biacore. Small changes in the refractive index above the metal surface, such as those caused by the binding of a low molecular weight molecule, cause a shift in the plasmon resonance condition that can be measured by intensity, wavelength or angle shifts[16,48].

For localized surface plasmon resonance to occur light interacts with particles that are much smaller than the wavelength of the incident light. This creates an oscillating electric field that causes the conduction electrons to oscillate coherently. The electron cloud becomes displaced with regard to the nuclei. A restoring force due to the Coulombic attraction between nuclei and electrons sets up oscillations of the electron cloud relative to the nuclei[17,49]. This results in strong light scattering and the appearance of strong surface plasmon absorbance bands. This is represented in Fig 1.5.3.1.

The unique properties of materials that support surface plasmon resonance has enabled the techniques of surface enhanced Raman spectroscopy (SERS) and surface enhanced fluorescence (SEF), amongst others. LSPR is very attractive for SERS and SEF methods since advances in the fabrication and lithographic techniques for the manufacture of sub-wavelength sized nanoparticles allows researchers to tune the LSPR wavelength through changing the size shape and material of the nanoparticles[50,18]. Au and Ag nanoparticles are popular since they exhibit strong plasmonic absorbance in the visible region.

### *1.5.4 Surface Enhanced Fluorescence*

Although plasmonic enhancement of emission has been known for some time[51,52,53] surface enhanced fluorescence has only relatively recently generated interest as an analytical technique. At distances of around < 5 nm fluorescence can be readily quenched by metal surfaces by Förster energy transfer from the excited state to the metal surface[54,55,56]. However at longer distances of around 5-200 nm the fluorophore can interact with the surface plasmons of the metal due to a through space near field interaction. Lakowicz reported enhancement of fluorescence intensity as radiative decay engineering (RDE)[24].

This enhanced fluorescence is due to an increase in the radiative decay rate of the excited state induced by the electronic field of the plasmon. The quantum yield of the fluorophore increases and the lifetime decreases. The mechanism for SEF is not yet fully understood or proven. The most reasonable explanation for SEF effects is due to the scattering component of the metal surface. When the metal surface absorbs light the excess energy is either non-radiatively lost as heat or radiatively lost through elastic scattering from the induced plasmons. SEF occurs when the absorption and/or emission bands overlap with the scattering wavelength of the metal[57]. Either the incident light induces an oscillating dipole in the metal surface that interacts with the fluorophore or the excited fluorophores oscillating dipole can induce a dipole in the metal surface that interacts with the fluorophore[24].

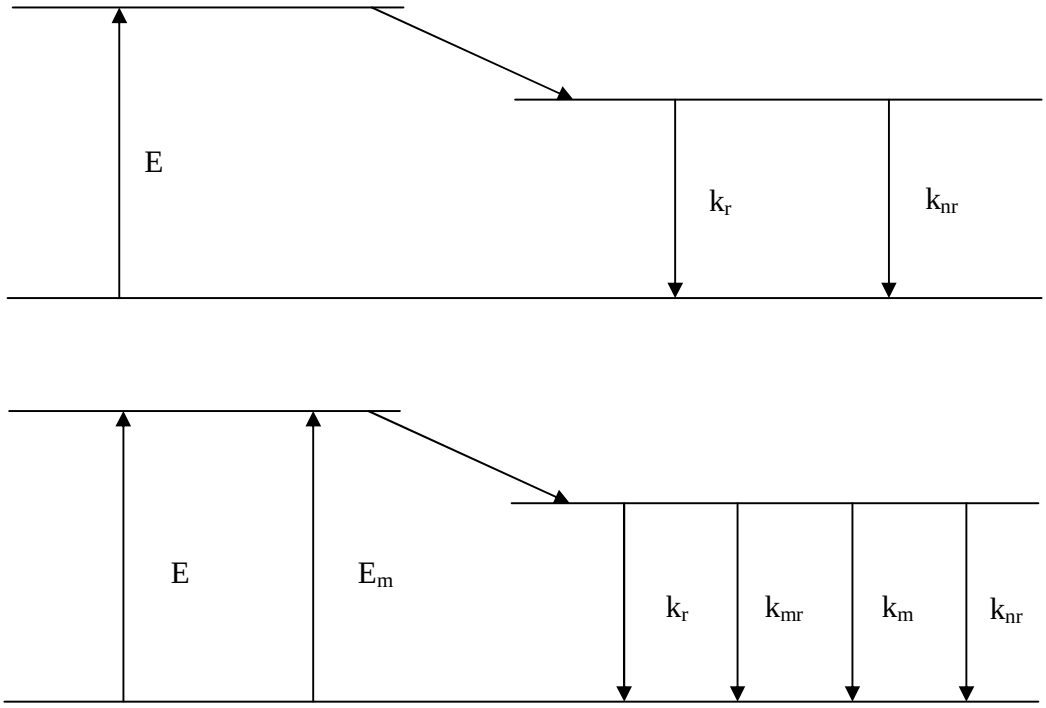


**Figure 1.5.4.1:** Jablonski diagram showing the modification of the radiative decay rate of a fluorophore by a metal surface. Reproduced from ref [55].

Fig 1.5.4.1 shows a Jablonski diagram explaining how a metal surface can modify the radiative decay rate of a nearby fluorophore. In the absence of any other quenching interactions the quantum yield ($\phi_0$) of a fluorophore is given by;

$$\phi_0 = k_r/(k_r + k_{nr})$$

And the natural lifetime ($\tau_0$) by;

$$\tau_0 = 1/(k_r + k_{nr})$$

Where $k_r$ is the radiative decay rate and $k_{nr}$ is the non-radiative decay rate. The presence of a nearby metal modifies these equations by adding another radiative decay pathway $k_{mr}$. The quantum yield and lifetime near the surface ($\phi_m$ and $\tau_m$ respectively) now become;

$$\phi_m = k_r + k_{mr}/(k_r + k_{mr} + k_{nr})$$

$$\tau_m = 1/(k_r + k_{mr} + k_{nr})$$

As can be seen from these equations as $k_{mr}$ increases the quantum yield will increase while the lifetime will decrease. SEF will have a much larger enhancement effect on fluorophores with low quantum yields since an increase in $k_{mr}$ will have no effect on the quantum yield if it is already 1[58]. To keep these equations simple the decay rate due to metal quenching, $k_m$, has not been included. At short distances from the metal surface where $k_m$ is large there will be significant competition between quenching of fluorescence and enhancement.

The use of silver and gold colloids and silver islands has shown to give large increases in quantum yield of molecules that usually have a weak intrinsic quantum yield. Lakowicz *et al*. showed that the normally weak intrinsic fluorescence of DNA can be enhanced to a level that would allow the detection of DNA without the use of fluorescent labels[59]. SEF has also been used to significantly increase the quantum yields of molecules with much higher quantum yields[60,61].

### *1.5.5 Surface Enhanced Raman Spectroscopy (SERS)*

SERS was first observed by Fleischmann *et al*.[62] in 1974 from adsorbed pyridine on a roughened silver electrode surface. The aim of this experiment was to roughen the electrode to increase the surface area and the number of available molecules for study. However Jeanmaire and Van Duyne[63] and Albrecht and Creighton[64] recognised that the increase in Raman band intensities could not be accounted for simply by the increase in available molecules on the surface. They proposed that the increase in Raman band intensity was caused by a resonant Raman effect caused by the adsorbed pyridine interacting with the surface plasmon.

By its nature Raman spectroscopy is a very low sensitive spectroscopy. Only 1 in 10 million photons scattered by a molecule will be Raman scattering. Even with high

powered lasers good spectra can only be obtained from solid samples or highly concentrated solutions. SERS provides a method of gaining very high sensitivity from what is usually a very low sensitivity spectroscopy. Typical Raman enhancement factors on the order of $10^4$-$10^6$ are reported for SERS experiments with some enhancement factors reportedly as high as $10^8$-$10^{14}$ and can be high enough to be capable of single molecule detection [65, 66].

There are two commonly accepted mechanisms that are thought to both contribute to the overall SERS effect. The electromagnetic enhancement (EM) effect is caused by the excitation of the surface plasmons of a conducting metal that are excited by an incident beam of light. Surface morphology, roughness and curvature are very important for the SERS effect since the electric field of the surface plasmon must lie perpendicular to the surface in order to be scattering. Such a large enhancement of Raman scattering is observed due to two mechanisms. The oscillating dipole of the surface plasmon when in resonance with the frequency of the incident light has the effect of enhancing the incident light and increasing the amount absorbed radiation and therefore Raman scatter. The Raman scattered light is also enhanced by the same enhancement effect as the incident light. Raman scatter that is shifted further away from the frequency of the surface plasmon dipole oscillations is enhanced less than Raman scatter that is only slightly shifted due to the resonance enhancement effect[67].

The EM effect contributes the most to the SERS enhancement factor but it cannot fully account for the enhancement seen in systems chemisorbed to the conducting metal surface. Enhancement due to what is known as chemical enhancement (CM) accounts for the rest of the enhancement by SERS in these systems. A graphical representation of the chemical enhancement effect is shown in Fig. 1.5.5.1 below. In many cases the energy of the highest occupied molecular orbital (HOMO) and the lowest unoccupied molecular orbital (LUMO) falls symmetrically about the Fermi level of the metal surface. In the case of a Raman active molecule chemisorbed to a conducting metal the Fermi level can act as a charge transfer intermediate. Charge transfer excitations can then occur at around half the energy of the intramolecular excitation of the chemisorbed molecule. Most

complexes that are studied by SERS have their lowest lying excitations in the near UV region meaning by this model the charge transfer excitations can be instigated by light in the visible region, such as the wavelengths of light commonly used in SERS experiments.

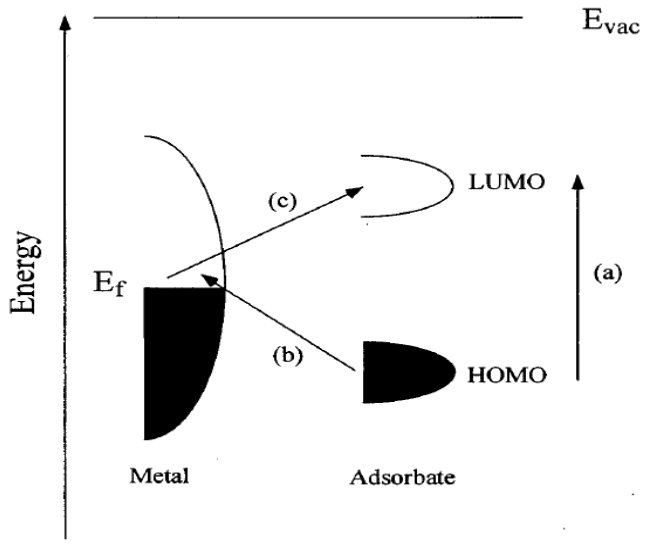


**Figure 1.5.5.1:** Energy level diagram for a molecule chemisorbed to a metal surface showing the chemical enhancement mechanism. Reproduced from ref [67].

## 1.6 Fluorescence Imaging Microscopy

Fluorescence imaging microscopy is a central tool in cell biology as a minimally invasive procedure for imaging tissues and cells. Combining fluorescence microscopy techniques with confocal laser scanning microscopy fluorescence makes it possible to obtain high resolution fluorescence images with little interference from out of focus light which can be reduced by the use of a pinhole or two photon excitation[68]. The laser is focused on a confocal point on the sample and rastered over the sample. The image is built up from the measured emission at each point. Confocal laser scanning microscopy

also allows true 3D imaging. The focus of the laser can be changed in the z-axis and a z-stack of images created from which a 3D image can be formed.

The contrast of fluorescence images can be generated by a variety of parameters such as, emission wavelength, intensity or polarization for example[69]. Fluorescence lifetime imaging microscopy (FLIM), where the contrast of the image is generated from variations in the measured emission lifetimes, has emerged as a very powerful imaging technique particularly for biomedical applications. FLIM imaging is independent of concentration, light scattering, light path length and laser excitation power. The inherent auto-fluorescence of the cell has been used to generate FLIM images[70, 71, 72]. A variety of fluorescent probes can be used to stain the cell and give a wide range of information about the cell or tissue, for example a variety of luminescence probes have been used to give FLIM images mapping $O_2$ concentration or pH differences in the cell[73, 74, 75, 76, 77]. The discovery and isolation of the Green Fluorescence Protein (GFP) has lead to the engineering of new fluorescence proteins that do not interfere with biological processes for use as FLIM probes for Förster Resonance Energy Transfer (FRET) imaging[78].

Lately there has been much interest in the development of improved fluorescence cell imaging probes for emission spectroscopy and FLIM. Ideally a fluorescence imaging probe should be soluble and stable in aqueous buffers. It should be non-toxic over the course of the experiment for live cell imaging. It should be readily taken up by the cell and preferably without any additional chemical agents such as ethanol or DMSO to aid uptake. The excitation and emission wavelengths of the probe should be transparent to the sample. Red wavelengths are preferred for tissue samples due to its relative transparency to biological cells. However red light at around 600 nm can stimulate cellular autofluorescence. An excitation and emission wavelength in the 650-900 nm range is ideal for tissue samples. This is less important for single cell imaging due to the transparency of the sample. Therefore for single cell imaging lower wavelength excitation and emission is ideal to avoid interference from autofluorescence. UV radiation should be avoided since it can lead to cellular damage as should infrared wavelengths which cause heating of the sample. The imaging probe should have a large

stokes shift to prevent self quenching and distinguish the emission from the excitation source and from autofluorescence. A long lifetime that is distinguishable from cellular autofluorescence is important for FLIM imaging[81].

The majority of available organic fluorophores are based on a series of fused aromatic rings. These organic fluorophores and fluorescent proteins have high extinction coefficients and quantum yields. These fluorescence probes however suffer from many disadvantages. They have small Stokes shifts leading to an overlap of excitation and emission spectra resulting in reduced sensitivity due to excitation source interference and self quenching. They are susceptible to photobleaching making them unsuitable for experiments requiring prolonged exposure to an excitation source. They have short lifetimes, typically 2-4 ns which are hard to distinguish from cellular autofluorescence which is typically < 10 ns which is a problem for FLIM imaging [79, 80, 81]. To overcome these deficiencies new classes of cellular imaging probes are being developed.

A number of lanthanide complexes with 4f electronic configurations have been used as luminescence imaging probes. These complexes have very long lived lifetimes in the ms range and display sharp almost spectral emission bands. Some emit in the NIR range although they tend to have reduced lifetimes in the µs range[82]. Due to the shielding by the ligands of the metal based inner sphere partially filled 4f orbitals where the excited state lies they are relatively insensitive to environmental conditions such as quenching from $O_2$ [3 82]. The free ion lanthanides are however highly toxic to cells thus requiring the synthesis of large macrocyclic ligands to stabilize the complex and prevent free ion formation. Direct excitation of the lanthanide is very difficult and requires an additional chromophore 'antenna' on the complex to absorb the excitation radiation and transfer energy from the excited state to the metal centre. Lanthanide complexes usually need excitation from UV light which can cause photo damage to biological samples[83]. Despite the limitations lanthanide luminescence imaging probes are quite advanced[84, 85].

Quantum dots have also been used as luminescence cellular probes. Quantum dots are nanoparticles of semiconducting materials. They possess longer lifetimes than organic

fluorophores and have good quantum yields. They offer excellent control over their photophysical properties since they can be controlled as a function of their size and constitution. They are very resistant to photobleaching. However the semiconducting materials used to make up quantum dots such as cadmium are highly toxic to cells. A coating of organic molecules is therefore required to stabilize the particles and make them soluble in aqueous media and biocompatible. These coatings are broken down easily over time which can lead to issues with toxicity for long experiments[86].

## 1.7 Heavy Metal $d^6$ Complexes as Luminescence Biological Imaging Agents

Heavy metal $d^6$ complexes have emerged only very recently as potentially valuable luminescent cellular imaging agents. Research has focused on polypyridyl complexes of Ir (III), Re (I) and Ru (II). These complexes have many advantages over organic fluorophores, lanthanides and quantum dots for imaging purposes. Polypyridyl $d^6$ metal complexes have low rates of ligand exchange. The heavy metal free ions can be toxic to cells but the low rate of formation of free ions leads to the low cytotoxicity of these complexes. They display long lived luminescence lifetimes (100 ns – ms) that are distinct from cellular autofluorescence. Many of their complexes have large Stokes shifts making self quenching negligible and reducing interference from the excitation source. They possess a broad excitation spectrum allowing them to be excited over a wide range of excitation wavelengths. Even if the excitation maximum is in the UV region the complex may still be excitable by wavelengths in the visible region. They are highly photostable compared to organic fluorophores and fluorescent proteins. Compared to lanthanides they have higher excitation coefficients as their excited state transitions are charge transfer allowed therefore making them easily excited without the need for energy transfer from an 'antenna' component due to allowed MLCT $\pi$-$\pi^*$ excitation transitions. Quantum yields in ambient conditions are higher than lanthanide complexes but lower than those of organic fluorophores and fluorescent proteins. The chemistry of $d^6$ heavy metal complexes means that a wide variety of ligands are available for tailoring the

properties of these complexes, from photophysical properties, cellular uptake properties, their sensitivity to environmental influences or localization within biological samples.

Unlike lanthanides where the excited emissive state is localized on the metal centre, $d^6$ polypyridyl complexes have the emissive excited state localized on the ligand. The lack of shielding makes the excited state very susceptible to environmental quenching, in particular quenching by $O_2{}^3$. Variations in luminescence intensity and lifetime of these complexes can be a good indication of the local environment. Ruthenium polypyridyl complexes have been used successfully to map $O_2$ concentrations in the cell by FLIM[87, 88, 89]. The use of these complexes as oxygen sensors or as $O_2$ mapping agents in cells and tissues has many advantages over the traditional method for measuring $O_2$ levels in biological systems, the Clark electrode. The Clark electrode is an invasive technique as opposed to FLIM imaging. Not only is it invasive but it also consumes oxygen during measurements and has poor reproducibility. FLIM imaging of biological samples with oxygen sensitive heavy metal complexes can give full oxygen concentration mapping across the sample with high resolution as opposed to the Clark electrode which is only capable of point measurements[88]. The quenching of the luminescence lifetimes of ruthenium diimine complexes by $O_2{}^3$ can be described accurately by a stern-volmer equation as a dynamic quenching process[75, 87]. $[Ru(bpy)_3]^{2+}$ and $[Ru(phen)_3]^{2+}$ have been investigated as $O_2$ cellular probes using FLIM mapping. More advanced probes are discussed later[90, 87].

For a complex to be used as a cellular imaging agent it must be readily taken up by the cell. The first barrier it must cross is the cell membrane which consists of a phospholipid bilayer. Embedded in this bilayer are a variety of other complexes including proteins that act as channels and pumps for molecules into and out of the cell. The cell membrane maintains the electric potential of the cell and has a net negative charge on its external surface. Cellular uptake of imaging agents depends on a number of factors including, charge, size, hydrophobicity, lipophilicity and any substituent groups.

Cell permeabilising agents have been used to aid the uptake of heavy metal $d^6$ imaging agents, in most cases DMSO and short chain alcohols[83]. DMSO used in concentrations of 1% v/v makes the membrane 'floppy' to enhance the cell membranes permeability. It has been used in topical transdermal drug delivery due to its permeabilising properties. DMSO molecules have amphiphilic properties and insert themselves between the phospholipid units of the membrane and open water pores in the cell membrane allowing easier access to the cytoplasm for imaging agents[91]. Short chain alcohols, also amphiphilic complexes, have been predicted to operate in the same manner[91]. It is important to keep the concentration of these cell permeabilising agents low to avoid rupturing the cell membrane and killing the cell. Since the use of cell permeabilising agents adds an external influence to the cell imaging experiment the use of these permeabilising agents should be avoided where possible.

An important factor for cellular uptake is the charge of the luminescence imaging agent. Due to the negatively charged exterior surface of the cell membrane positively charged complexes are favoured by the cell for uptake into the cytoplasm. Cationic molecules can interact with the negatively charged membrane facilitating uptake while anionic molecules are repulsed. Some cationic low molecular weight ruthenium and Iridium complexes have been shown to enter the cytoplasm[92, 93, 94] although a 1 : 49 solution of DMSO : PBS pH 7 buffer was employed to aid uptake in all referenced cases. The introduction of a negative charge to the complex can greatly reduce uptake by the cell as can be seen in the case of zwitterionic iridium complexes[95]. Again a 1 : 49 solution of DMSO : PBS pH7 buffer was employed to aid uptake.

The addition of a hydrophobic or lipophilic group to the cell imaging agent can also aid uptake into the cytoplasm. Due to the aqueous medium needed for cells it's important that the complex remains water soluble despite the addition of the hydrophobic group. Hydrophobic groups have a high affinity for the hydrophobic cell membrane and lipophilic groups such as alkyl chains can interact with the cell membrane by embedding themselves in the phospholipid bilayer thus facilitating diffusion into the cytoplasm. In the case of $d^6$ heavy metal luminescence imaging agents the addition of more

hydrophobic ligands can increase the rate of uptake into the cell as shown by Barton *et al.*[93] where a series of Ruthenium complexes containing one dipyridophenazine (dppz) ligand the most lipophilic complex (measured as a function of log *P* were *P* is the octanol/$H_2O$ partition coefficient) with two dpp (dpp = 4,7-diphenyl-1,10-phenanthroline) ligands showed the greatest cellular uptake. Huang *et al.*[95] showed with a series of Iridium complexes that show increasing cellular uptake with increasing lipophilicity of the complex. Coogan *et al.* [96] demonstrated a series of rhenium luminescence imaging complexes with pendent alkyl group that are readily taken up by the cell. Fluorescence microscopy showed that the complex mainly associated with the internal cell membranes. Of note is that the more highly lipophilic complexes at higher concentrations were cytotoxic. Disruption of the cell membrane but the highly lipophilic pendent groups was thought to be the cause of the observed cytotoxicity.

Lo *et al.*[97] have shown that the choice chain length of the pendent alkyl chain is very important when considering the cytotoxicity of the complex. A series of iridium complexes shown in Fig 1.7.1 were synthesized with varying length alkyl chains as luminescence cell imaging agents. For the n = 2 complexes the cytotoxicity was relatively non-toxic, about the same cytotoxicity as cisplatin or better when comparing $IC_{50}$ values for HeLa cells. The n = 10 complexes were the most cytotoxic with $IC_{50}$ values 10 times higher than cisplatin. The n = 18 complexes had $IC_{50}$ values lower but comparable to cisplatin. Cytotoxicity did not follow a trend with increasing chain length or lipophilicity. Uptake of the complex also did not follow a chain length or lipophilicity trend with cellular uptake for complex 3 increasing from for chain lengths n = 2, n = 18 to n = 10. It is thought that low solubility and formation of aggregates of the n = 18 complex are the cause of the surprisingly low cellular uptake. Cellular uptake is therefore not entirely dependent on lipophilicity and the chain length used for any cell imaging agent should be chosen carefully.

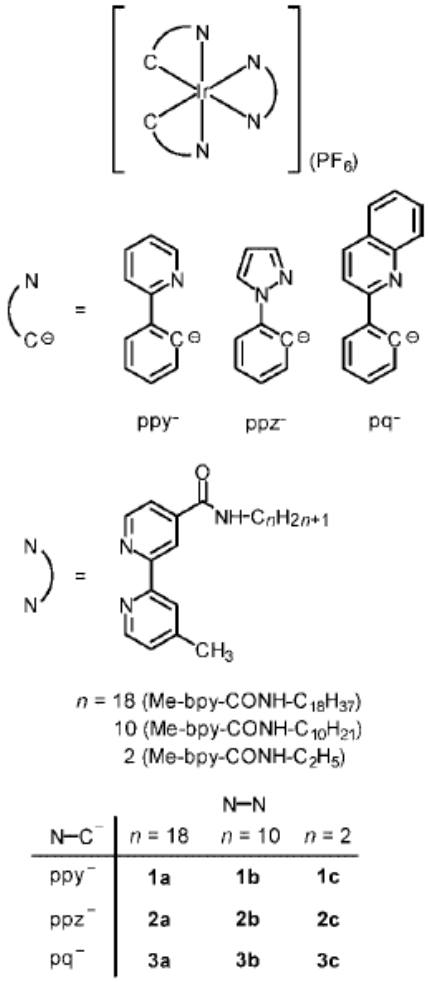


| N–C⁻ | N–N *n* = 18 | *n* = 10 | *n* = 2 |
|---|---|---|---|
| ppy⁻ | **1a** | **1b** | **1c** |
| ppz⁻ | **2a** | **2b** | **2c** |
| pq⁻ | **3a** | **3b** | **3c** |

**Figure 1.7.1:** Structure of complexes from Lo *et al*. Reproduced from ref [97].

Here in this thesis we investigate the cellular uptake of a novel series of ruthenium (II) polypyridyl with pendent acetlylthio alkane chains of varying length. The lipophilicity of the alkane chains aids the uptake of the complex into the cell cytoplasm. 0.9% DMSO was used to solvate the complex and aid the uptake of the complex into the cell cytoplasm. The suitability of the complex as an emission intensity and FLIM imaging agent was also investigated. The sensitivity of the emission of these complexes to oxygen concentrations and the polarity of its environment gave detailed information on the areas within the cell in which the complex was localized.

Bioconjugation of heavy metal $d^6$ complexes to biological molecular transporters is a new method for creating luminescence imaging agents with good cell uptake and reduced cytotoxicity compared to alkyl chains due to the biocompatibility of bioconjugates. A variety of bioconjugates attached to heavy metal $d^6$ complexes have already been explored. Lo *et al*. reported on the suitability of a series of Ru complexes bioconjugated to estradiol as luminescence cellular imaging probes[98]. The structures are shown in Fig 1.7.2. These complexes displayed good lipophilicity and cellular uptake. In particular the two complexes with two dpp ligands showed the highest lipophilicity and cellular uptake due to the hydrophobicity of these ligands. In addition these complexes showed substantially lower cytotoxicity than cisplatin, with $IC_{50}$ values from around two to five times larger than cisplatin for HeLa cells. Luminescence intensity microscopy images of cells stained with the $[Ru(Ph_2\text{-phen})_2(bpy\text{-ph-est})](PF_6)_2$ complex showed that the complex is localized in the cell cytoplasm with no nuclear uptake. The complex appears to reside in the perinuclear region suggesting strong hydrophobic association with hydrophobic organelle structures such as the endoplasmic reticulum and Golgi apparatus.

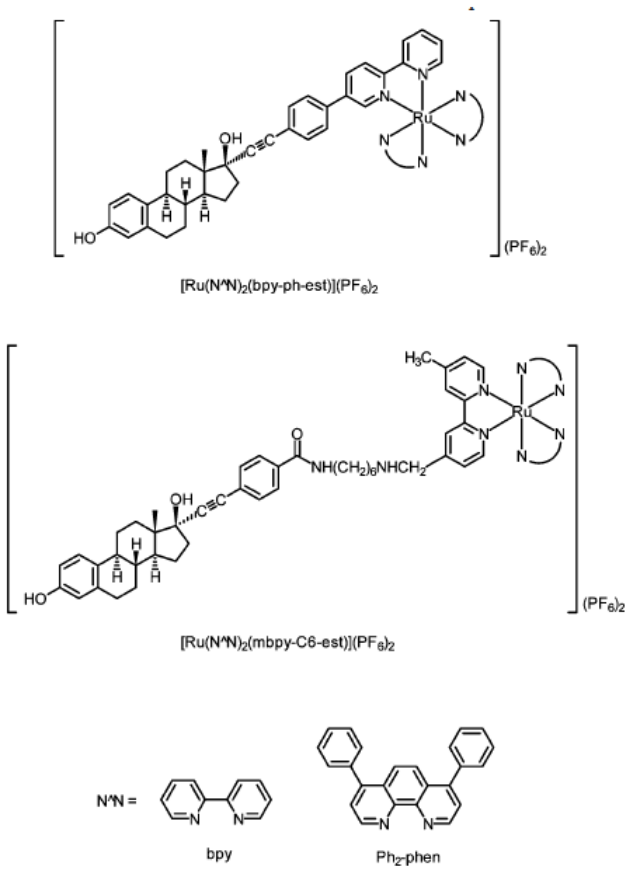


**Figure 1.7.2:** Structure of complexes from Lo *et al*. Reproduced from ref [98].

Pegylation represents another form of bioconjugation for heavy metal $d^6$ luminescence imaging probes that possess both good cellular uptake and are biocompatible. Pegylation involves the conjugation of polyethylene glycol (PEG) chains to a complex. The use of PEG has already been approved by the FDA for use in products such as food, pharmaceuticals and cosmetics. Pegylation can aid the uptake of complexes with little to no alteration of the complexes properties. Pegylation can also make complexes soluble in aqueous medium that are insoluble in their non-pegylated form. PEG complexes display a lack of non-specific binding to extracellular proteins leading to no immunogenic or antigenic cellular response reducing the cytotoxicity of complexes it is conjugated to[99,100].

Lo et.al. have demonstrated a series of iridium complexes conjugated to PEG chains for use as luminescence cell imaging agents[101]. Structures are shown in Fig 1.7.3.

Pegylation greatly improved the solubility of these Ir(III) complexes in aqueous media, before pegylation these complexes were relatively insoluble. Cellular uptake was not markedly improved but was comparable to the unpegylated 1c and 2c complex and other reported Ir(III) cell imaging complexes possibly due to the slow uptake of long chain pegylated complexes. The unpegylated complexes 1c and 2c are quite cytotoxic to HeLa cells, 1c has a comparable $IC_{50}$ value to cisplatin while 2c is more cytotoxic with a lower $IC_{50}$ value than cisplatin. Pegylation of the complexes greatly decreases the cytotoxicity of these complexes and they display $IC_{50}$ values for HeLa cells 1-2 orders of magnitude higher than cisplatin. These values are also much higher than reported for the previous iridium complexes conjugated to estradiol[98]. This result coupled with the comparable uptake of the pegylated and unpegylated complexes shows that conjugation of the PEG units is responsible for the lowered cytotoxicity. Only complex 2a was used to stain HeLa cells for luminescence intensity microscopy imaging, these images are shown in Fig 1.7.4 The complex should punctuated staining of the cytoplasm with no nuclear staining detected. It is likely that the punctuated staining of the cytoplasm is due to the complex binding favorably to hydrophobic organelle structures such as the Golgi apparatus and endoplasmic reticulum.

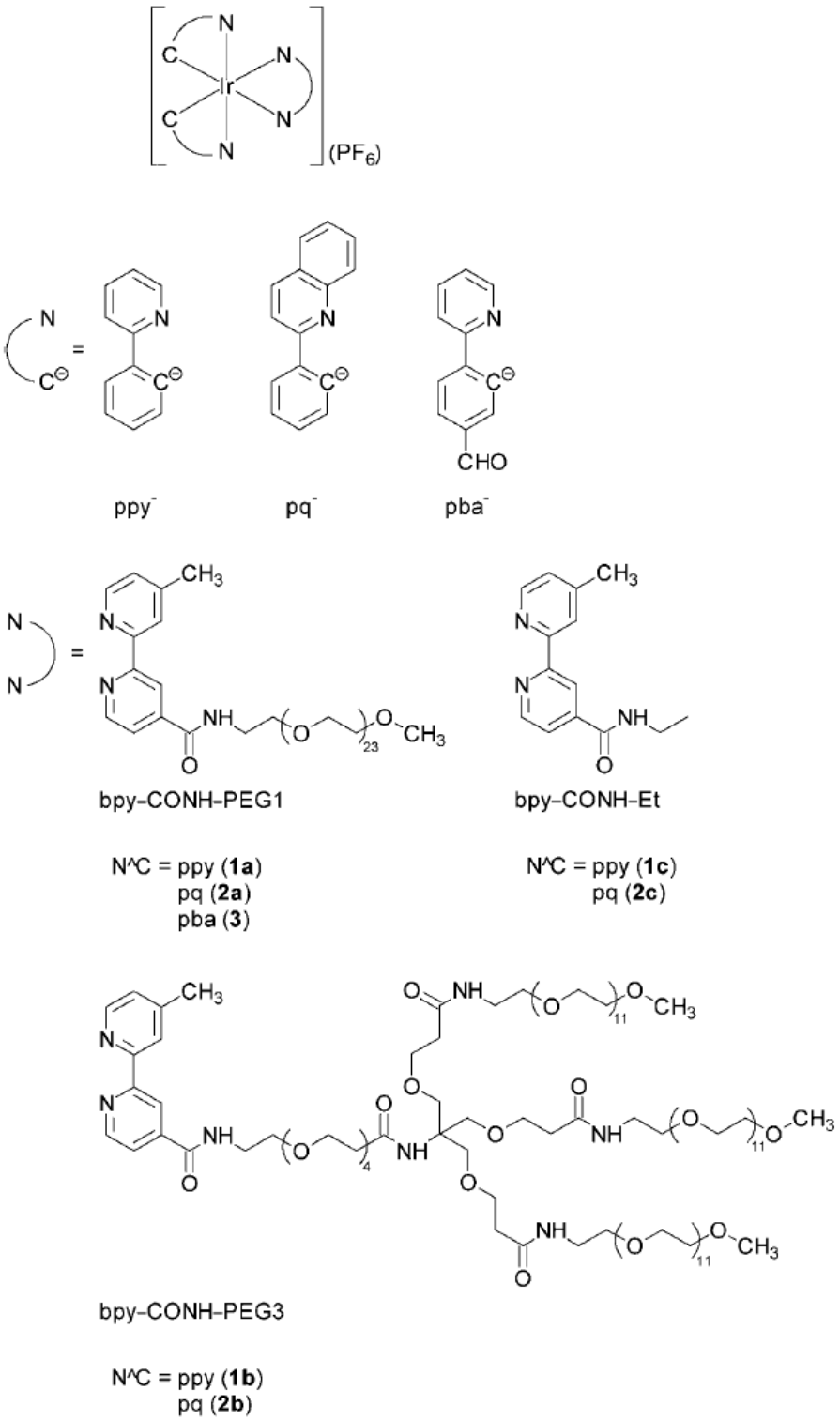


**Figure 1.7.3:** Structure of complexes from Lo *et al*. Reproduced from ref [101].

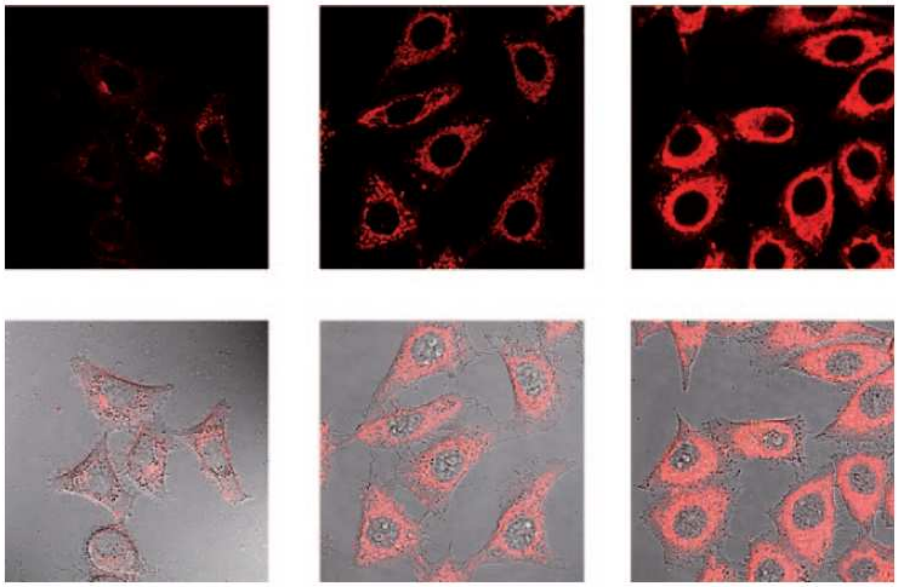

**Figure 1.7.4:** Images of HeLa cells stained with complex 2a. The top images are confocal fluorescence intensity images while the bottom images are a combination of the confocal fluorescence intensity images and white light images. From left to right the HeLa cells were incubated with 10 µm 2a for 1h, 100 µm 2a for 1 h and 200 µm 2a for 2 h at 37 $^{o}$C. Image reproduced from ref [101].

The discovery of cell penetrating proteins (CPP's) has opened another avenue for the design of bioconjugated heavy metal $d^6$ luminescence imaging probes. The protein HIV-1 Tat has been shown to cross the cells plasma membrane. This protein can be shortened to the sequence of 9 amino acids responsible of cellular uptake, $Tat_{49-57}$, and still retain its cell penetrating properties. Attachment of the $Tat_{49-57}$ peptide to proteins has allows these proteins to be delivering into the cells. New CPP's structurally related to the HIV $Tat_{49-57}$ peptide have been developed with even greater cell penetrating properties. One of these CPP's is polyarginine, which consists of a peptide of seven to nine Arginine amino acids[102]. Bioconjugation of polyarginine peptides to ruthenium polypyridyl complexes can be used as a method for transporting ruthenium complexes across the cell membrane barrier into the cytoplasm.

Keyes *et al*. have reported on two supramolecular ruthenium polypyridyl complexes with pendent polyarginine groups, one containing five arginines and the other eight, Ru-Ahx-$R_5$ and Ru-Ahx-$R_8$ respectively[103]. The structure is shown in Fig 1.7.5. The parent complex $[Ru(bpy)_2(picH_2)]^{2+}$ does not penetrate the cell membrane and after 20 minutes incubation with myeloma cells no emission due to this complex is observed in the cytoplasm. Incubation of a myeloma cell for 20 minutes with Ru-Ahx-$R_5$ also shows no detectible luminescence from the complex inside the cell cytoplasm. Fluorescence intensity and FLIM images of myeloma cells incubated with Ru-Ahx-$R_8$ are shown in Fig 1.7.6 which shows luminescence due to the complex throughout the cytoplasm and in the cell membrane with luminescence lifetimes varying in different compartments of the cell. Cellular uptake is heavily dependent on the number of arginine amino acids in the peptide chain. This complex could have applications as a luminescence $O_2$ mapping agent. The complex displays a shorter luminescence lifetime in the cell membrane than in the cytoplasm which corresponds to the higher solubility of $O_2$ in the cell membrane.

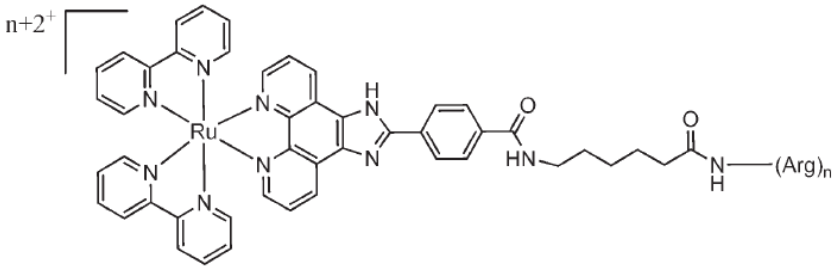


**Figure 1.7.5:** Structure of complex Ru-Ahx-$R_n$ (n is 5 or 8). Reproduced from ref [103].

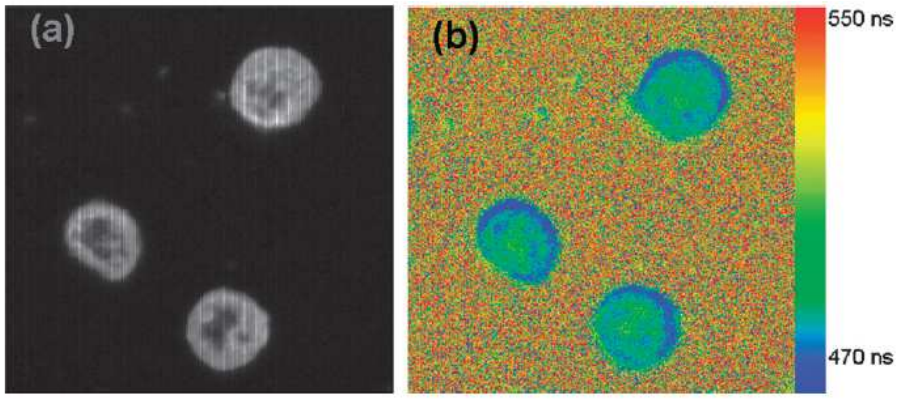


**Figure 1.7.6:** (a) Emission intensity image and (b) false colour FLIM (fast FLIM) image of myeloma cells incubated with Ru-Ahx-$R_8$ for 15 minutes. Image reproduced from ref [103].

Keyes *et al*. applied these octa-arginine bioconjugation to another ruthenium luminescence imaging agent[104]. The structure is shown in Fig 1.7.7 This complex contains two dppz ligands which makes the excited state easily quenched by aqueous environments. Confocal luminescence images of SP2 Myeloma stained with this complex is shown in Fig 1.7.8 The complex is selectively luminescent when bound to hydrophobic structures like the cell membrane, nuclear membrane and cell organelle membranes. The parent complex $[Ru(dppz)_2PIC\text{-}Arg_8]^{2+}$ does not penetrate the cell and only displays luminescence where it accumulated on the exterior cell membrane. Resonance Raman mapping was employed to show that the dye had distributed throughout the cell and is not just localized in hydrophobic cell structures. Resonance Raman mapping of SP2 Myeloma cells stained with the parent $[Ru(dppz)_2PIC\text{-}Arg_8]^{2+}$ showed no evidence of having penetrated the cell. These resonance Raman mapping images are shown in Fig 1.7.9.

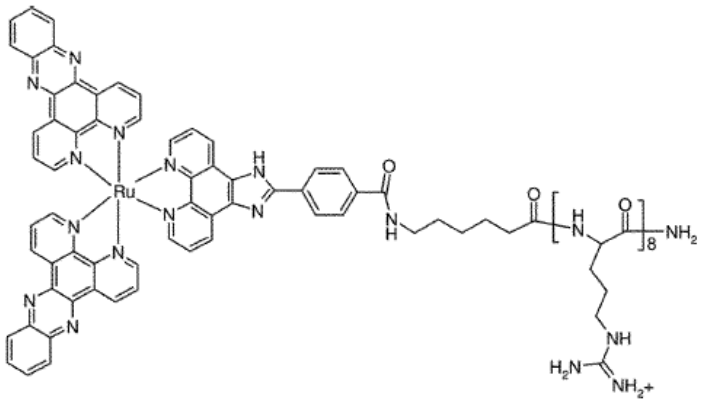

**Figure 1.7.7:** Structure of complex $[Ru(dppz)_2PIC\text{-}Arg_8]^{2+}$. Reproduced from ref [104].

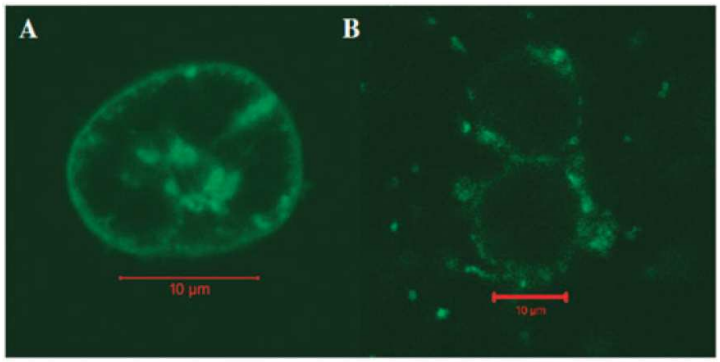


**Figure 1.7.8:** Confocal luminescence intensity images of live SP2 myeloma cells incubated with (A) $[Ru(dppz)_2PIC\text{-}Arg_8]^{2+}$ and (B) $[Ru(dppz)_2PIC]^{2+}$ for 48 hours at 37 $^{o}$C. Reproduced from ref [104].

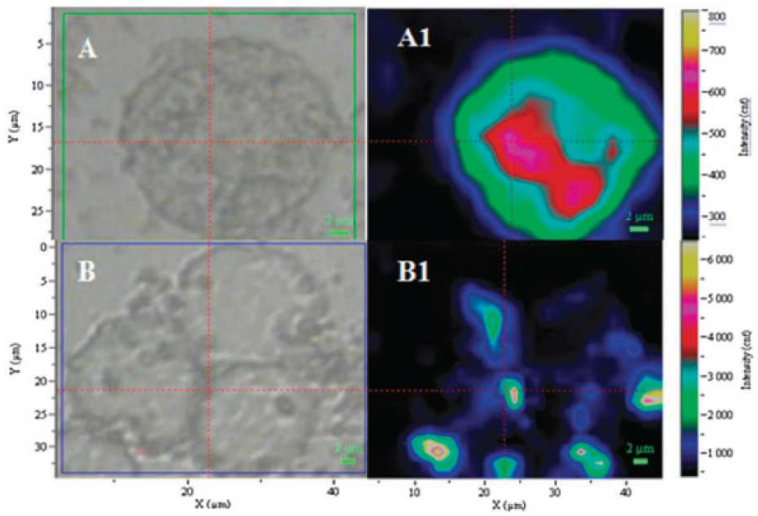


**Figure 1.7.9:** Resonance Raman inensity map of live SP2 myeloma cell after incubation with $[Ru(dppz)_2PIC\text{-}Arg_8]^{2+}$ (A1) and $[Ru(dppz)_2PIC]^{2+}$ (B1). And excitation wavelength of 458 nm was used. Images A and B are the corresponding white light images. Reproduced from ref [104].

## 1.8 Conclusions

The first part of this literature review gives an overview of the properties and photophysical pathways of ruthenium polypyridyl complexes. This is followed by an overview of the literature published on the properties of ruthenium polypyridyl complexes in supramolecular assemblies of micelle and vesicle structures and interfacial supramolecular structures of ruthenium (II) polypyridyl complexes, both examples of self assembled supramolecular systems. Despite the many ruthenium polypyridyl based metallosurfactants described in the literature, their unique properties are not being fully exploited. Most show luminescence excited state sensitivity to they are in vesicle/micelle form or solvated. The lipophilicity of these complexes makes these complexes suitable for use as cell imaging or cell membrane probes. Again despite some examples of monolayers of ruthenium (II) polypyridyl complexes on metallic surfaces there are surprisingly few practical applications of these monolayers. The potential of these monolayers for use in solar energy conversion systems has been explored by relatively few publications. The use of roughened and patterned metallic surfaces to enhance emission quantum yield and Raman signal intensity of ruthenium (II) polypyridyl monolayers is relatively new and has major future applications for the improvement of sensor devices.

The third part of this literature survey focuses on the use of heavy metal $d^6$ complexes as luminescence live cell imaging agents, including ruthenium (II) polypyridyl complexes. These complexes offer advantages over the commercially available organic cell imaging fluorescent dyes commonly used. The use of heavy metal $d^6$ complexes for luminescence cell imaging is still a relatively new area. Most of the literature so far has focused on the uptake of these complexes into cells and the functionalisation of these complexes to improve cell uptake for live cell imaging. However due to the relative insolubility of these complexes low concentrations of DMSO are employed to solubilise the complex and also aid in the uptake of the complex. The use of DMSO aids in the uptake of the complex into the cell and is often ignored by these publications. Of greater importance is the localization of these complexes in discrete compartments within the

cell, the sensitivity of the luminescence of the complex to the intracellular environment and therefore what information can be obtained about the processes and changing environment within these cell compartments from the luminescence intensity or lifetime of these complexes.

# References


[1] Lehn, J. M.; *Pure Appl. Chem.*, 50, **1978**, 871-872

[2] Lehn, J-M.; *Rep. Prog. Phys.*, 67, **2004**, 249-265

[3] Nguyen, S. T.; Gin, D. L.; Hupp, J. T. and Zhang, X.; *Proc. Natl. Acad. Sci, USA*, 98, **2001**, 11849-11850

[4] Gilbert, A. and Baggott, J.; Essentials of Molecular Photochemistry, Blackwell Scientific Publications, **1991**

[5] Valeur, B.; Molecular Fluorescence, Principles and Applications, Wiley-VCH, **2002**

[6] Paris, J.P. and Brandt, W.W.; *J. Am. Chem. Soc.,* 81, **1959**, 5001-5002

[7] Juris, A. and Balvani, V.; *Coord. Chem. Rev.*, 85, **1988**, 85-277

[8] R.W. Harrigan, R.W. and Crosby, G.A.; *J. Chem. Phys,* 59, **1973**, 3468-3476

[9] Hipps, K.W. and Crosby, G.A.; *J. Am. Chem. Soc.,* 97, **1975**, 7042-7048

[10] Demas, J.N. and Crosby, G.A.; *J. Am. Chem. Soc.,* 93, **1971**, 2841-2847

[11] Van Houten, J. and Watts, R.J.; *J. Am. Chem Soc.,* 98, **1976**, 4853-4858

[12] Klassen, D. M. and Crosby, G. A.; *J. Phys. Chem.*, 48, **1968**, 1853-1858

[13] Caspar, J. V. and Meyer, T. J.; *Inorg. Chem.*, 22, **1983**, 2444-2453

[14] Durham, B.; Caspar, J.V.; Nagle, J.K. and Meyer, T.J.; *J. Am. Chem. Soc.*, 104, **1982**, 4803- 4810

[15] Barigelletti, F.; Juris, A,; Balzani, V.; Belser, P. and Zelewsky, A.; *Inorg. Chem.,* 22, **1983**, 3335-3339

[16] Allen, G.H.; White, R.P.; Rillema, D.P. and Meyer, T.J.; *J. Am. Chem. Soc.,* 106, **1984**, 2613-2620

[17] Ulman, A,; *Chem. Rev.*, 96, **1996**, 1533-1554

[18] Forster, R. J.; Keyes, T.E. and Vos, J.G.; Interfacial Supramolecular Assemblies, Wiley, **2003**

[19] Allara, D. L. and Nuzzo, R. G.; *Langmuir,* 1, **1985**, 45.

[20] Sagiv, J.; *J. Am. Chem. Soc.*, 102, **1980***,* 92.

[21] Love, J.C.; Estroff, L.A.; Kriebel. J.K.; Nuzzo, R.G. and Whitesides J.M.; *Chem. Rev*., 105, **2005**, 1103-1169

[22] Dubois, L.H.; Zegarski, B.R. and Nuzzo, R.G.; *Proc. Natl. Acad, Sci. USA*, 84, **1987**, 4739-4742

[23] Sellers, H.; Ulman, A.; Shnidman, Y. and Eilers J.E.; *J. Am. Chem. Soc.,* 115, **1993**, 9389-9401

[24] Touahir, L.; Chazalviel, J-N.; Sam, S.; Moraillon, A.; Henry de Villeneuve, C.; Allongue, P.; Ozanam, F. and Gouget-Laemmel, A.C.; *J. Chem. Phys. C*, 115, **2011**, 6782-6787

[25] Ulman, A.; Evans, S. D.; Shnidman, Y.; Sharma, R.; Eilers, J. E. and Chang, J. C.; *J. Am. Chem. Soc.*, 113, **1991**, 1499-1506

[26] Patrone, L.; Palacin, S.; Bourgoin, J. P.; Lagoute, J.; Zambelli, T. and Gauthier, S.; *Chem. Phys.*, 281, **2002**, 325-332

[27] Tour, J. M.; Jones, L.; Pearson, D. L.; Lamba, J. J. S.; Burgin, T. P.; Whiteside, G. M.; Allara, D. L.; Parikh, A. N. and Sundar, V. A.; *J. Am. Chem. Soc.*, 117, **1995**, 9529-9534

[28] Forster, R. J. and Keyes, T. E.; *J. Phys. Chem. B.*, 102, **1998**, 10004-10012

[29] Bertoncello, P.; Kefalas, E. T.; Pikramenou, Z.; Unwin, P. R. and Forster, R. J.; *J. Phys. Chem. B.*, 110, **2006**, 10063-10069

[30] Jose, B.; Steffen, R.; Neugebauer, U.; Sheridan, E.; Marthi, R.; Forster, R. J. and Keyes, T. E.; *Phys. Chem. Chem. Phys.*, 11, **2009**, 10923-10933

[31] Brennan, J. L.; Keyes, T. E. and Forster, R. J.; *Langmuir*, 22, **2006**, 10754-10761

[32] Akiyama, T.; Inoue, M.; Kuwahara, Y. and Yamada, S.; *Jpn. J. Appl. Phys.*, 41, **2002**, 4737-4728

[33] Chu, B. W-K. and Yam, V. W-W.; *Langmuir*, 22, **2006**, 7437-7443

[34] Forster, R. J.; Pellegrin, Y. and Keyes, T. E.; *Electrochem. Comm.*, 9, **2007**, 1899-1906

[35] Pramod, P.; Sudeep, P. K.; Thomas, K. G. and Kamat, P. V.; *J. Phys. Chem. B. Letts.*, 110, **2006**, 20737-20741

[36] Jebb, M.; Sudeep, P. K.; Pramod, P.; Thomas, K. G. and Kamat, P. V.; *J. Phys. Chem. B.*, 111, **2007**, 6839-6844

[37] Bowers, J.; Danks, M. J. and Bruce, D. W.; *Langmuir*, 19, **2003**, 292-298

[38] Barbante, G. J.; Hogan, C. F.; Wilson, D. J. D.; Lewcenko, N. A.; Pfeffer, F. M.; Barnett, N. W. and Francis, P. S.; *Analyst*, 136, **2011**, 1329-1338

[39] Guerrero-Martinz, A.; Vida, Y.; Dominguez-Gutierrez, D.; Alburquerque, R. Q. and De Cola, L.; *Inorg. Chem.*, 47, **2008**, 9131-9133

[40] Torki, F. M. and Schmehl, R. H.; *J. Chem. Soc., Faraday Trans.*, 85, **1989**, 349-362

[41] Draeger, C.; Bottcher, C.; Messerschmidt, C.; Schulz, A.; Ruhlmann, L.; Siggel, U.; Hammarström, L.; Berglund-Baudin, H.; and Fuhrhop, J. *Langmuir*, 16, **2000**, 2068-2077

[42] Gardiner, D.J.; Graves, P.R. and Bowley, H.J.; Practical Raman Spectroscopy, Springer-Verlag, **1989**

[43] Baranska, H.; Labudzinska, A. and Terpinska, J.; Laser Raman Spectroscopy, Ellis Horwood Limited, **1987**

[44] Banwell, C.N.; Fundamentals of Molecular Spectroscopy, McGraw-Hill Book Company (UK) Limited, **1994**, Chapter 4

[45] Brockman, J.M.; Nelson, B.P. and Corn, R.M.; *Annu. Rev. Phys. Chem.*, 51, **2000**, 41-63

[46] Van Duyne, R.P.; *Phys.,* 306, **2004**, 985-986

[47] Willets, K.A. and Van Duyne, R.P.; *Annu. Rev. Phys. Chem.*, 58, **2007**, 267-197

[48] Stewart, M.E.; Anderton, C.R.;Thompson, L.B.; Maria, J.; Gray, S.K.; Rogers, J.A. and Nuzzo, R.G.; *Chem. Rev.,* 108, **2008**, 494-521

[49] Kelly, K.L.; Coronado, E.; Zhao, L.L. and Schatz, G.C.; *J. Phys. Chem. B.*, 107, **2003**, 668-677

[50] Sherry, L.J.; Chang, S.H.; Schatz, G.C. and Van Duyne, R.P.; *Nano Lett.,* 5, **2005**, 2034–38

[51] Gersten, J. and Nitzan, A.; *J. Chem. Phys.,*75, **1981**, 1139-1151

[52] Chew, H.; *J. Phys. Chem.*, 87, **1987**, 1355-1359

[53] Weitz, D.A.; Garoff, S.; Gersten, J.I. and Nitzan, A.; *J. Phys. Chem.,* 78, **1983**, 5324-5338

[54] Gu, T.; Whitesell, J.K. and Fox, M.A.; *Chem. Mater.*, 15 (6), **2003**, 1358-1366

[55] Lakowicz, J.R.; *Anal. Biochem.*, 298, **2001**, 1–24

[56] Fan, C.; Wang, S.; Hong, J.W.; Bazan, G.C.; Plaxco, K.W. and Heeger, A.J.; *Proc. Natl. Acad. Sci. US,* 100, **2003**, 6297-6301

[57] Lakowicz, J.R.; *Plasmonics*, 1, **2006**, 5–33

[58] Aslan, K.; Gryczynski, I.; Malicka, J.; Matveeva, E.; Lakowicz, J.R. and Geddes, C.D.; *Current Opinion in Biotechnology*, 16, **2005**, 55–62

[59] Lakowicz, J.R.; Shen, B.; Gryczynski, Z.; D'Auria, S. and Gryczynski, I.; *Biochem. Biophys. Res. Comm.* 286*,* **2001**, 875–879

[60] Iosin, M.; Baldeck,P. and Astilean, S.; *Nuc. Instrum. Meth. Phys. Res. B*, 267, **2009**, 403–405

[61] Gryczynski, I.; Malicka, J.; Holder, E.; DiCesare, N. and Lakowicz, J.R., *Chem. Phys. Lett.*, 372, **2003**, 409–414

[62] Fleischmann, M.; Hendra, P.J. and McQuillan, A.J. *Chem. Phys. Lett.*, 26, **1974**, 163.

[63] Jeanmaire, D.L. and Van Duyne, R.P.; *J. Electroanal. Chem.*, 84, **1977**, 1.

[64] Albrecht, M.G. and Creighton, J.A.; *J. Am. Chem. Soc.*, 99, **1977**, 5215.

[65] Nie, S. and Emory, S.R.; *Science*, 275, **1997**, 1102.

[66] Emory, S.R. and Nie, S.; *Anal. Chem.*, 69, **1997**, 2631.

[67] Campion, A. and Kambhampati, P.; *Chem. Rev. Soc.,* 27, **1998,** 241-250

[68] Ploem, J. S.; *Applied Optics*, 26, **1987**, 3226-3231

[69] Levitt, J. A.; Matthews, D. R.; Ameer-Beg, S. M. and Suhling, K.; *Current Opinion in Biotech.*, 20, **2009**, 28-36

[70] Schneckenburger, H.; Wagner, M.; Weber, P.; Strauss, W. S. L. and Sailer, R.; *J. Fluor.*, 14, **2004**, 649-654

[71] Konig, K. and Riemann, I.; *J. Biomed. Optics.*, 8, **2003**, 432-439

[72] Ghukasyan, V.V. and Kao, F.J.; *J. Phys. Chem. C.*, 113, **2009**, 11532-11540

[73] Neugebauer, U.; Pellegrin, Devocelle, M.; Forster, R.J.; Signac, W.; Moran, N. and Keyes, T.E.; *Chem. Comm.,* **2008**, 5305-5309

[74] Lin, H. J., Herman, P. and Lakowicz, J.R.; *Cytometry Part A*, 52A, **2003**, 77-89

[75] Zhong, W.; Urayama, P. and Mycek, M.A.; *J. Phys. D.: Appl. Phys.*, 36, **2003**, 1689-1695

[76] Ji, J.; Rosenzweig, N.; Jones, I. and Rosenzweig, Z.; *J. Biomed. Optics*, 7, **2002**, 404-409

[77] Carlsson, K.; Liljebourg, A.; Andersson, R.M. and Brismar, H.; *J. Microsp.*, 199, **2000**, 106-114

[78] Tsien, R. Y.; *Angew. Chem. Int. Ed.*, 48, **2009**, 5612-5626

[79] Dimitrow, E.; Riemann, I.; Ehlers, A.; Koehler, M. J.; Norgauer, J., Elsner, P.; Konig, K. and Kaatz, M.; *Experimental Dermatology*, 18, **2009**, 509-515

[80] Wang, H. W.; Gukassyan, V.; Chen, C. T.; Wei, Y. H.; Guo, H. W.; Yu, Y. S. and Kao, F. J.; *J. Biomed. Optics*, 13, **2008**, 054011-1 – 054011-9

[81] Fernandez-Moreira, V.; Thorp-Greenwood, F. L. and Coogan, M. P.; *Chem. Comm.*, 46, **2010**, 186-202

[82] Faulkner, S.; Pope, S. J. A. and Burton-Pye, B. P.; *App. Spectro. Rev.*, 40, **2005**, 1-31

[83] Zhao, Q.; Huang, C. and Li, F.; *Chem. Soc. Rev.*, 40, **2011**, 2508-2524

[84] Montgomery, C. P.; Murray, B. S. New, E. J.; Pal, R.; and Parker, D.; *Acc, Chem, Res.*, 42, **2009**, 925-937

[85] Song, B.; Vandevyver, C. D. B.; Chauvin, A. S. and Bunzli, J. C. G.; *Org. Biomol. Chem.*, 6, **2008**, 4125-4133

[86] Michalet, X.; Pinaurd, F. F.; Bentolila, J. M.; Tsay, J. M.; Doose, S.; Li, J. J.; Sundaresan, G.; Wu, A. M.; Gambhir, S. S. and Weiss, S.; *Science*, 307, **2005**, 538-544

[87] Gerritsen, H. C.; Draaijer, A.; Ince, C. and Levine, Y. K.; *J. Fluorescence*, 7, **1997**, 11-15

[88] Stucker, M.; Schulze, L.; Pott, G.; Hartmann, P.; Lubber, D.; Rochling, A. and Altmeyer, P.; *Sensors and Actuators*, 51, **1998**, 171-175

[89] Zhong, W.; Urayama, P. and Mycek, M. A.; *J. Phys. D: Appl. Phys.*, 36, **2003**, 1689-1695

[90] Dobrucki, J. W.; *J. Photochem. Photobiol. B.: Bio.* 65, **2001**, 136-144

[91] Notman, R.,; Noro, M.; O'Malley, B. and Anwar, J.; *J. Am. Chem. Soc.*, 128, **2008**, 13982-13983

[92] Zhao, Q.; Yu, M.; Shi, L.; Liu, S.; Li, C.; Shi, M.; Zhou, Z.; Huang, C. and Li, F.; *Organometallics*, 29, **2010**, 1085-1091

[93] Puckett, C. A. and Barton, J. K.; *J. Am. Chem. Soc.*, 129, **2007**, 46-47

[94] Puckett, C. A. and Barton, J. K.; *Biochem.*, 47, **2008**, 11711-11716

[95] Jiang, W.; Gao, Y.; Sun, Y.; Ding, F.; Xu, Y.; Bian, Z.; Li, F.; Bian, J. and Huang, C.; *Inorg. Chem.*, 49, **2010**, 3252-3260

[96] Amoroso, A. J.; Coogan, M. P.; Dunne, J. E.; Fernandez-Moreira, V.; Hess, J. B.; Hayes, A. J.; Llyod, D.; Millet, C.; Pope, S. J. A. and Williams, C.; *Chem. Comm.*, **2007**, 3066-3068

[97] Lo, K. K. W.; Lee, P. K. and Lau, S. Y.; *Organometallics,* 27, **2008**, 2998-3006

[98] Lo, K. K. W.; Lee, T. K. M.; Lau, J. S. Y.; Poon, W. L. and Cheng, S. H.; *Inorg. Chem.*, 47, **2008**, 200-208

[99] Harris, J. M. and Chess, R. B.; *Nature Rev. Drug Discovery*, 2, **2003**, 214-221

[100] Bailon, P. and Berthold, W.; *Pharma. Sci. Tech. Today*, 1, **1998**, 352-356

[101] Li, S. P. Y.; Liu, H. W.; Zhang, K. Y. and Lo, K. K. W.; *Chem. Eur. J.*, 16, **2010**, 8329-8339

[102] Wender, P. A.; Mitchell, D. J.; Pattabiraman, K.; Pelkey, E. T.; Steinman, L. and Rothbard, J. B.; *Biochem*, 97, **2000**, 13003-13008

[103] Neugebauer, U.; Pellegrin, Y.; Devocelle, M.; Forster, R. J.; Signac, W.; Moran, N. and Keyes, T. E.; *Chem. Comm.*, **2008**, 5307-5309

[104] Cosgrave, L.; Devocelle, M.; Forster, R. J. and Keyes, T. E.; *Chem. Comm.*, 46, **2010**, 103-105

# 2. Synthesis and characterization of a Novel Family of $[Ru(dpp)_2(x\text{-}ATAP)]^{2+}$ complexes

## 2.1 Introduction

Ruthenium polypyridyl complexes remain the focus of intense research across a diverse array of areas such as solar cells[1,2], artificial photosynthesis and photocatalytic systems[3] and as charge transfer mediators for supramolecular devices[4] to name a few. The versatility of ruthenium polypyridyl complexes is due to the ease with which they can be synthesised with a wide variety of ligands to modify their excited state properties or with additional functionality, such as surface active groups. Recently surface active ruthenium polypyridyl complexes have been used to investigate the mechanisms of SERS. The strong absorbance of these complexes makes them good candidates for SERRS studies. Recent contributions have used surface active ruthenium polypyridyl complexes to try and elucidate contribution to the SERS effect from the electromagnetic and chemical mechanisms[5, 6].

Replacement of ligands in the synthesis of ruthenium complexes rarely proceeds directly. The more common mechanism is an anation reaction involving solvent participation, for example, when a nucleophile like $H_2O$ is present in concentrations 10% v/v. An example of an anation reaction is shown below:

$$[L_nMX] + H_2O \rightarrow [L_nM(H_2O)] + X$$

$$[L_nM(H_2O)] + Y \rightarrow [L_nMY] + H_2O$$

When heated in a nucleophilic solvent such as $H_2O$ the X ligand is replaced by a $H_2O$. The $H_2O$ ligands can then leave forming an intermediate ion that has a long enough lifetime to distinguish between the various ligands in solution. This intermediate ion is then attacked by the ligand Y forming the desired complex[7]. $RuCl_3 \bullet 3H_2O$ is the starting point for the synthesis of most ruthenium complexes and is used in the synthesis of the $[Ru(dpp)_2(x\text{-}ATAP)]^{2+}$

complexes in this chapter. The $[Ru(dpp)_2(x\text{-}ATAP)]^{2+}$ complexes in this chapter are formed by the same reaction mechanism described here.

For the synthesis of the complexes presented in this chapter phenanthroline derivatives were used due to the advantages ruthenium polypyridyl complexes with phenanthroline derivative ligands confer over ruthenium complexes with bpy ligands in terms of their photophysics. The benzene ring structure between the pyridine rings of phenanthroline provides greater rigidity compared to bypridine and reduces excited state distortion of the ligand. This stabilizes the excited state by reducing the rate of non-radiative decay, $k_{nr}$, resulting in greater luminescent lifetimes and quantum yields[8]. The 5-amino-1,10-phenanthroline used as the heteroligand has an amino group that can be easily functionalized by the creation of a peptide bond to further increase the functionality of the complex. The additional phenyl rings in the 4,7-diphenyl-1,10-phenanthroline (dpp) ligand stabilize the excited state further due to greater delocalization of the excited state electron density over a larger molecular framework compared to the unsubstituted complex 1,10-phenanthroline. The use of phenyl substituted ligands in ruthenium polypyridyl complexes lowers the energy gap between the singlet state and the emitting triplet state in comparison to complexes with unsubstituted ligands due to the increased π-acceptor properties of the phenyl substituted ligands[8, 9]. A smaller energy gap difference would lead to reduced lifetimes but due to the greater delocalization which reduces $k_{nr}$ of the excited state across the ligand in the case of ruthenium complexes using dpp there is only a slight reduction in lifetime compared to a similar complex using unsubstituted ligands[9]. The excellent sensitivity of the lifetimes and quantum yields of ruthenium complexes with dpp ligands to the presence of oxygen has prompted their use in many sensor applications[10, 11, 12]. Although it was originally thought that the phenyl groups would sterically shield the excited state from quenchers it is now known that the excited state is delocalized across the phenanthroline portion and phenyl rings of the ligand and thus the ruthenium complexes are more susceptible to quenching by quenchers such as $O_2$[13, 9].

In this chapter a series of novel ruthenium (II) complexes with aliphatic chains of increasing length peptide bonded to phenanthroline are reported. The synthesis and structural characterization of x-ATAP, where x-ATAP is either 5-amido-1,10-phenanthroline-(6-acetylthio-hexanyl), 5-amido-1,10-phenanthroline-(8-acetylthio-octanyl), 5-amido-1,10-

phenanthroline-(11-acetylthio-undecanyl) or 5-amido-1,10-phenanthroline-(16-acetylthio-hexadecanyl) and x represents the number of carbons in the ligands aliphatic chain is reported. Also reported is the synthesis, structural, electrochemical and photophysical characterization of a novel polypyridyl ruthenium complex, $Ru(ddp)_2$(x-ATAP), where dpp is 4,7-diphenyl-1,10-phenanthroline. The reaction scheme and structure of the complexes is shown in Fig 2.1. This series of complexes is surface active due to the availability of a thioacetate functionality which can spontaneously form covalent bonds between the sulphur group and a noble metal surface. The range of alkyl chain lengths was designed to control the distance that the ruthenium centre is held from the surface allowing investigation of the distance dependence of surface plasmon effects on a variety of planar, roughened and nanoparticle noble metal surfaces. The alkyl chain also provides a means for the ruthenium polypyridyl complex to interact with lipid membranes such as the phospholipid bilayer of eukaryotic cells.

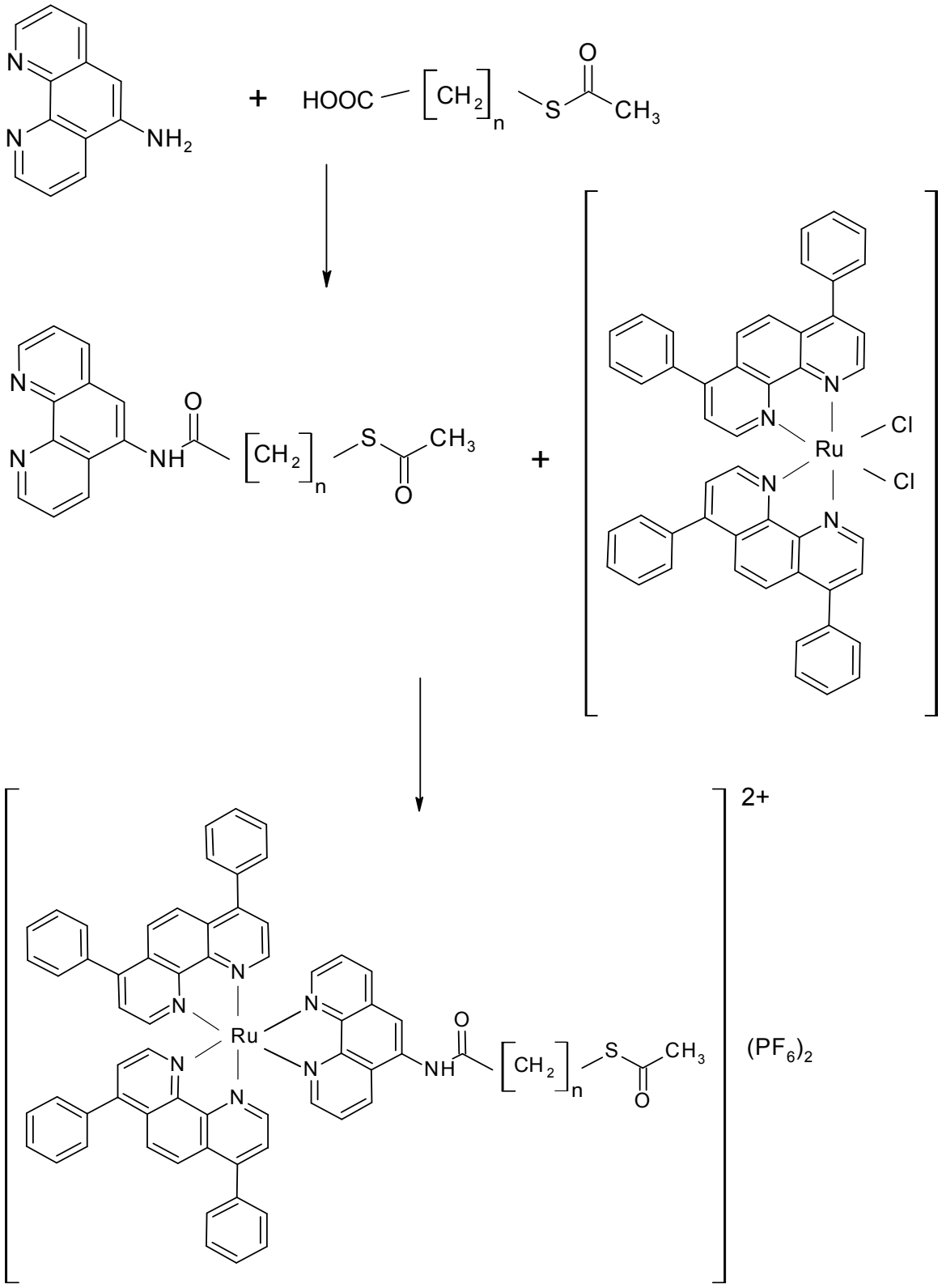


**Figure 2.1** Reaction scheme for the formation of $[Ru(dpp)_2(x\text{-}ATAP)](PF_6)_2$ where x is the number of carbons in the aliphatic chain.

## 2.2 Experimental and Synthesis

### *2.2.1 Materials and Methods*

All reagents used in synthesis were analytical grade. Absorption and emission spectroscopy were carried out in spectroscopic grade acetonitrile. Solution phase electrochemistry was carried out in spectroscopic grade acetonitrile. Water was purified using a MilliQplus – 185 Millipore system. Chemicals purchased from Sigma-Aldrich were used as received.

### *2.2.2 Synthesis of 4-(4,6-Dimethoxy-1,3,5-triazin-2-yl)-4-methyl-morpholinium (DMTMM)*

2-Chloro-4,6-dimethoxy-1,3,5-triazine (0.0483 g, 2.5 x $10^{-4}$ mol) was dissolved in 1ml THF. N-methylmorpholine (0.0253 g, 2.5x $10^{-4}$ mol) was added to this stirring solution. This solution was stirred for 30 minutes at room temperature. The white precipitate was collected by vacuum filtration and washed with THF before collecting the dried product. Structure and purity was analysed by $^{1}$H NMR analysis. $^{1}$H NMR in deuterated DMSO. 4.35 (d, 2H), 4.1 (s, 6H), 3.98 (d, 2H), 3.9 (t, 2H), 3.77 (t, 2H), 3.47 (s, 3H).

### *2.2.3 Synthesis of 6-(acetylthio)-hexanoic acid*

800 mg potassium thioacetate was added to a stirred solution of 6-bromohexanoic acid (0.468 g, 2.4 mmol) in 16 ml anhydrous DMF at $0^{o}$ C. The solution was stirred at room temperature for 30 minutes, diluted with 40 ml $CH_2Cl_2$ and washed 3 times with water. The organic solution was dried with $MgSO_4$ and the solvent was removed by rotary evaporation. A yellow oil was collected. 0.1414 g (31 % yield) of 6-(acetylthio)-hexanoic acid was recovered. Structure and purity was confirmed by $^{1}$H NMR analysis. $^{1}$H NMR in deuterated $CDCl_3$. 2.86 (t, 2H), 2.35 (t, 2H), 2.32 (s, 3H), 1.62 (m, 4H), 1.42 (m, 2H).

### *2.2.4 Synthesis of 8-(acetylthio)-octanoic acid*

400 mg potassium thioacetate was added to a stirred solution of 8-bromooctanoic acid (0.267 g, 1.2 mmol) in 8 ml anhydrous DMF at $0^{o}$ C. The solution was stirred at room temperature for 30 minutes, diluted with 20 ml $CH_2Cl_2$ and washed 3 times with water. The organic solution was dried with $MgSO_4$ and the solvent was removed by rotary evaporation. A yellow oil that solidified on standing was collected. 0.1355 g (51.7 % yield) of 8-(acetylthio)-octanoic acid was recovered. Structure and purity was confirmed by $^{1}$H NMR analysis. $^{1}$H NMR in deuterated $CDCl_3$. 2.86 (t, 2H), 2.35 (t, 2H), 2.32 (s, 3H), 1.63 (m, 2H), 1.56 (m, 2H), 1.33 (m, 6H)

### *2.2.5 Synthesis of 11-(acetylthio)-undecanoic acid*

11-Mercaptoundecanoic acid (0.1899 g, 0.87 mmol) was dissolved in 3 ml of dichloromethane and 3 ml of acetic acid. 0.5 g zinc powder was then added to the stirred solution. The solution was then stirred for 20 minutes. After this time the reaction solution was cooled to $0^{o}$ C and 1.2 ml (17 mmol) of acetyl chloride was added. When production of hydrogen gas ceased, after about 20 minutes, the reaction solution was allowed to reach room temperature. After 10 minutes the zinc powder was removed by filtering the reaction solution through celite. The reaction solution was then washed with HCl (0.1 M, 25 ml) and mixed with ice twice, each time collecting the organic phase. The solvent was then removed and was purified by flash chromatography through silica. This was repeated twice, the first time using toluene/ethyl acetate 100:1 as the mobile phase and the second time using toluene/ethyl acetate 10:1. $^{1}$H NMR data showed no difference in product purity after purification with flash chromatography so this step was left out in subsequent reactions. 0.1648 g (72 % yield) of 11-(acetylthio)-undecanoic acid was recovered. $^{1}$H NMR in deuterated $CDCl_3$. 2.86 (t, 2H), 2.36 (t, 2H), 2.33 (s, 3H), 1.63 (m, 2H), 1.56 (m, 2H), 1.27 (m, 12H)

### *2.2.6 Synthesis of 16-(acetylthio)-hexadecanoic acid*

16-mercaptohexadecanoic acid (0.5 g, 1.74 mmol) was dissolved in 6 ml of dichloromethane and 6 ml of acetic acid. 1 g zinc powder was then added to the stirred solution. The solution was then stirred for 20 minutes. After this time the reaction solution

was cooled to $0^{o}$ C and 2.4 ml (17 mmol) of acetyl chloride was added. When production of hydrogen gas ceased after about 20 minutes the reaction solution was allowed to reach room temperature. After 10 minutes the zinc powder was removed by filtering the reaction solution through a celite column. The reaction solution was then washed with HCl (0.1 M, 50 ml) mixed with ice twice, each time collecting the organic phase. The organic phase was rotary evaporated to dryness and collected. 0.5355 g (93.1 % yield) of 16-(acetylthio)-hexadecanoic acid was recovered. Structure and purity was confirmed by $^{1}$H NMR analysis. $^{1}$H NMR in deuterated $CDCl_3$. 2.86 (t, 2H), 2.35 (t, 2H), 2.32 (s, 3H), 1.63 (m, 2H), 1.56 (m, 2H), 1.25 (m, 22H)

### *2.2.7 Synthesis of $[Ru(dpp)_2]Cl_2$*

0.1181 g ($4.52 \times 10^{-4}$ mol) $RuCl_3.3(H_2O)$ was dissolved in 15 ml of DMF and stirred. 0.2 g of LiCl was added to the stirring solution. The solution was then brought to reflux under a nitrogen atmosphere. 0.3 g ($9.04 \times 10^{-4}$ mol) of bathophenanthroline was then added slowly to the refluxing solution over 20 minutes. The solution was refluxed under a nitrogen atmosphere for 8 hours. After this time the reaction was cooled and added to 250 ml of acetone and kept in a freezer for 16 hours. The precipitate that had formed was collected by vacuum filtration. The precipitate was then washed with water, to remove any $[Ru(dpp)_3]Cl_2$, until the water ran clear. The precipitate was dried with a small amount of diethyl ether. Structure and purity was confirmed by HPLC and $^{1}$H NMR analysis. 0.1020 g (27 % yield) of $[Ru(dpp)_2]Cl_2$ was recovered. $^{1}$H NMR in deuterated DMSO. 10.44 (d, 2H), 8.26 (dd, 4H), 8.06 (dd, 4H), 7.85 (d, 4H), 7.74, (t, 4H), 7.72 (t, 2H), 7.56 (m, 10H), 7.42 (d, 2H)

### *2.2.8 Synthesis of 5-amino-1,10-phenanthroline*

1.5 g ($6.6 \times 10^{-3}$ mol) of 5-nitro-1,10 phenanthroline was dissolved in 30 ml of EtOH. 0.3 g of 5 % Pd/C catalyst was added to the solution and the solution was heated to $70^{o}$ C under an $N_2$ atmosphere. 1.55 g of hydrazine monohyrdrate was added dropwise to the solution over 30 minutes. The solution was then stirred for 5 hours at 70 $^{o}$C. The solution was then cooled to room temperature and filtered over celite to remove the catalyst which was washed with EtOH to remove any residual product. The filtrate was rotary evaporated until the first yellow crystals formed. The solution was then diluted with just enough EtOH to

redissolve the crystals. The solution was filtered to remove the grey impurity and left over night to crystallize. The precipitate that formed was filtered off and washed with water and a small amount of diethyl ether. 0.7071 g (55 % yield) of 5-amino-1,10-phenanthroline was collected. Purity was confirmed with $^{1}$H NMR analysis. $^{1}$H NMR in deuterated DMSO. 9.04 (quintet, 1H), 8.66 (quintet, 2H), 8.03 (dd, 1H), 7.73 (quintet, 1H), 7.75 (quintet, 1H), 6.86 (s, 1H), 6.1 (s, 2H)

### *2.2.9 Synthesis of 5-Amido-1,10-phenanthroline-(6-acetylthio-hexanyl)*

220 mg (1.132 mmol) of $NH_2$phen and 195 mg (1.029 mmol) of 6-(acetylthio)-hexanoic acid were dissolved in 15ml anhydrous DMF and stirred for 30 minutes. 2 equivalents (0.5695 g, 2.058 mmol) DMTMM was added to the reaction which was then stirred for 18 hrs. When the reaction was completed the solution volume was reduced to about 5 ml by rotary evaporation and then added to 100 ml $H_2O$. The resulting precipitate was collected by vacuum filtration and washed with plenty of water and diethyl ether. The crude solid was sonicated in 50 ml acetone and the undissolved material was removed by vacuum filtration. This was carried out multiple times on the precipitate until the product was found to be sufficiently pure as confirmed by $^{1}$H NMR analysis. 55.4 mg was recovered (13.3 % yield). Structure and purity was confirmed by $^{1}$H NMR analysis. The $^{1}$H NMR numbering scheme is shown in Fig 3.3.3.1. $^{1}$H NMR in deuterated DMSO. 10.12 ($1H^{5}$, s, NH), 9.13 ($1H^{8}$, dd, C-H), 9.03 ($1H^{1}$, dd, C-H), 8.60 ($1H^{6}$, dd, C-H), 8.44 ($1H^{3}$, dd, C-H), 8.17 ($1H^{4}$, s, C-H), 7.83 ($1H^{7}$, dd, C-H), 7.74 ($1H^{2}$, dd, C-H), 2.87 ($2H^{17-18}$, t, $CH_2$), ~2.5 obscured by solvent peak ($2H^{9-10}$, t, $CH_2$), 2.3 ($3H^{19-21}$, s, $CH_3$), 1.69 ($2H^{15-16}$, quintet, $CH_2$), 1.58 ($2H^{11-12}$, quintet, $CH_2$), 1.44 ($2H^{13-14}$, quintet, $CH_2$).

### *2.2.10 Synthesis of 5-Amido-1,10-phenanthroline-(8-acetylthio-octanyl)*

220 mg (1.132 mmol) of $NH_2$phen and 223.9 mg (1.029 mmol) of 8-(acetylthio)-octanoic acid were dissolved in 15 ml anhydrous DMF and stirred for 30 minutes. 2 equivalents (0.5695 g, 2.058 mmol) DMTMM was added to the reaction which was then stirred for 18 hrs. When the reaction was completed the solution was added to 100 ml $H_2O$ and the resulting precipitate was collected by vacuum filtration and washed with plenty of water and diethyl ether. The crude solid was sonicated in 50 ml acetone and the undissolved

material was removed by vacuum filtration. This was carried out multiple times on the precipitate until the product was found to be sufficiently pure as confirmed by $^{1}$H NMR analysis. 0.1562 g was recovered (34.9 % yield). GC-MS: 418.2 ($M^{+}$, +23). Structure and purity was confirmed by $^{1}$H NMR analysis. $^{1}$H NMR in deuterated DMSO. 10.12 (1H, s, NH), 9.12 (1H, dd, C-H), 9.03 (1H, dd, C-H), 8.60 (1H, dd, C-H), 8.44 (1H, dd, C-H), 8.17 (1H, s, C-H), 7.83 (1H, dd, C-H), 7.74 (1H, dd, C-H), 2.84 (2H, t, $CH_2$), ~2.5 obscured by solvent peak (2H, t, $CH_2$), 2.31 (3H, s, $CH_3$), 1.68 (2H, quintet, $CH_2$), 1.52 (2H, quintet, $CH_2$), 1.4-1.2 (6H, m, three $CH_2$).

### *2.2.11 Synthesis of 5-Amido-1,10-phenanthroline-(11-acetylthio-undecanyl)*

220 mg (1.132 mmol) of $NH_2$phen and 266.7 mg (1.029 mmol) of 11-(acetylthio)-undecanoic acid were dissolved in 15 ml anhydrous DMF and stirred for 30 minutes. 2 equivalents (0.5695 g, 2.058 mmol) DMTMM was added to the reaction which was then stirred for 18 hrs. When the reaction was completed the solution was added to 100 ml $H_2O$ and the resulting precipitate was collected by vacuum filtration and washed with plenty of water and diethyl ether. The crude solid was sonicated in 50 ml acetone and the undissolved material was removed by vacuum filtration. This was carried out multiple times on the precipitate until the product was found to be sufficiently pure as confirmed by $^{1}$H NMR analysis. 0.1079 g was recovered (21.8 % yield). Structure and purity was confirmed by $^{1}$H NMR analysis. $^{1}$H NMR in deuterated DMSO. 10.12 (1H, s, NH), 9.12 (1H, dd, C-H), 9.03 (1H, dd, C-H), 8.60 (1H, dd, C-H), 8.44 (1H, dd, C-H), 8.17 (1H, s, C-H), 7.83 (1H, dd, C-H), 7.74 (1H, dd, C-H), 2.80 (2H, t, $CH_2$), ~2.5 obscured by solvent peak (2H, t, $CH_2$), 2.3 (3H, s, $CH_3$), 1.69 (2H, quintet, $CH_2$), 1.48 (2H, quintet, $CH_2$), 1.4-1.2 (12H, m, six $CH_2$).

### *2.2.12 Synthesis of 5-Amido-1,10-phenanthroline-(16-acetylthio-hexadecanyl)*

220 mg (1.132 mmol) of $NH_2$phen and 340 mg (1.029 mmol) of 16-(acetylthio)-hexadecanoic acid were dissolved in 15 ml anhydrous DMF and stirred for 30 minutes. 2 equivalents (0.5695 g, 2.058 mmol) DMTMM was added to the reaction which was then stirred for 18 hrs. When the reaction was completed the solution was added to 100 ml $H_2O$ and the resulting precipitate was collected by vacuum filtration and washed with plenty of water and diethyl ether. The crude solid was sonicated in 50 ml acetone and the undissolved

material was removed by vacuum filtration. This was carried out multiple times on the precipitate until the product was found to be sufficiently pure as confirmed by $^1$H NMR analysis. 0.1213 g was recovered (21.1 % yield). Structure and purity was confirmed by $^1$H NMR analysis. $^1$H NMR in deuterated DMSO. 10.12 (1H, s, NH), 9.12 (1H, dd, C-H), 9.03 (1H, dd, C-H), 8.60 (1H, dd, C-H), 8.44 (1H, dd, C-H), 8.17 (1H, s, C-H), 7.83 (1H, dd, C-H), 7.74 (1H, dd, C-H), 2.80 (2H, t, $CH_2$), ~2.5 obscured by solvent peak (2H, t, $CH_2$), 2.3 (3H, s, $CH_3$), 1.69 (2H, quintet, $CH_2$), 1.47 (2H, quintet, $CH_2$), 1.4-1.2 (22H, m, eleven $CH_2$).

### *2.2.13 Synthesis of [Ru(dpp)$_2$(AmidoPhen-6-(acetylthio)-hexanyl)](PF$_6$)$_2$*

0.0554 g ($1.5065 \times 10^{-4}$ mol) Amidophenanthroline-6-(acetylthio)-hexanyl and 0.1315 g $[Ru(dpp)_2]Cl_2$ were dissolved in 50 ml 80 : 20 EtOH : $H_20$. This solution was refluxed for 16 hrs and then the reaction mixture was rotary evaporated down to about 15 ml. Ammonium hexafluorophosphate was used to precipitate the product as a $PF_6$ salt. The orange product was collected by vacuum filtration and washed with water and diethyl ether. 0.1485 g was recovered (69 % yield). Structure and purity was confirmed by $^1$H NMR analysis. GC-MS: 1278 ($M^+$, -145). $^1$H NMR in deuterated DMSO. 10.46 (1H, s, N-H), 8.92 (1H, d, C-H), 8.79 (1H, d, C-H), 8.67 (1H, s, C-H), 8.35 (1H, d, C-H), 8.32 (1H, d, C-H), 8.27 (5H, m, C-H), 8.20 (2H, m, C-H), 8.14 (1H, t, C-H), 7.90 (1H, m, C-H), 7.82 (3H, m, C-H), 7.8 (2H, m, C-H), 7.7-7.5 (20H, m, C-H), 2.86 (2H, t, $CH_2$), 2.60 (2H, t, $CH_2$), 2.30 (3H, s, $CH_3$), 1.67 (2H, quintet, $CH_2$), 1.59 (2H, quintet, $CH_2$), 1.44 (2H, quintet, $CH_2$). Elemental analysis: C 57.38 % (56.96 %), H 3.75 % (3.58 %), N 6.89 % (6.68 %). Calculated values are in brackets.

### *2.2.14 Synthesis of [Ru(dpp)$_2$(AmidoPhen-8-(acetylthio)-octanyl)](PF$_6$)$_2$*

75 mg ($1.898 \times 10^{-4}$ mol) Amidophenanthroline-8-(acetylthio)-octanyl and 0.1657 g $[Ru(dpp)_2]Cl_2$ were dissolved in 50 ml 80 : 20 EtOH : $H_20$. This solution was refluxed for 16 hrs and then the reaction mixture rotary evaporated down to about 15 ml. Ammonium hexafluorphosphate was used to precipitate the product as a $PF_6$ salt. The orange product was collected by vacuum filtration and washed with water and diethyl ether. 0.242 g was recovered (87.8 % yield). Structure and purity was confirmed by $^1$H NMR analysis. GC-MS: 1305.8 ($M^+$, -145). $^1$H NMR in deuterated DMSO. 10.46 (1H, s, N-H), 8.91 (1H, d, C-H), 8.78 (1H, d, C-H), 8.66 (1H, s, C-H), 8.35 (1H, d, C-H), 8.32 (1H, d, C-H), 8.28 (5H, m, C-

H), 8.20 (2H, m, C-H), 8.14 (1H, t, C-H), 7.90 (1H, m, C-H), 7.82 (3H, m, C-H), 7.8 (2H, m, C-H), 7.7-7.5 (20H, m, C-H), 2.83 (2H, t, $CH_2$), 2.59 (2H, t, $CH_2$), 2.30 (3H, s, $CH_3$), 1.69 (2H, quintet, $CH_2$), 1.51 (2H, quintet, $CH_2$), 1.45-1.2 (6H, m, $CH_2$). Elemental analysis: C 57.93 % (57.62 %), H 3.96 % (3.76 %), N 6.76 % (6.56 %). Calculated values are in brackets.

### *2.2.15 Synthesis of $[Ru(dpp)_2$(AmidoPhen-11-(acetylthio)-undecanyl)$](PF_6)_2$*

53 mg ($1.288x10^{-4}$ mol) Amidophenanthroline-11-(acetylthio)-undecanyl and 0.1123 g $[Ru(dpp)_2]Cl_2$ were dissolved in 50 ml 80 : 20 EtOH : $H_20$. This solution was refluxed for 16 hrs and then the reaction mixture was rotary evaporated down to about 15 ml. Ammonium hexafluorophosphate was used to precipitate the product as a $PF_6$ salt. The orange product was collected by vacuum filtration and washed with water and diethyl ether. 0.1666 g was recovered (86.7 % yield). Structure and purity was confirmed by $^1$H NMR analysis. GC-MS: 1348 ($M^+$, -145). $^1$H NMR in deuterated DMSO. 10.58 (1H, s, N-H), 8.91 (1H, d, C-H), 8.78 (1H, d, C-H), 8.67 (1H, s, C-H), 8.35 (1H, d, C-H), 8.32 (1H, d, C-H), 8.27 (5H, m, C-H), 8.20 (2H, m, C-H), 8.14 (1H, t, C-H), 7.90 (1H, m, C-H), 7.82 (3H, m, C-H), 7.8 (2H, m, C-H), 7.7-7.5 (20H, m, C-H), 2.79 (2H, t, $CH_2$), 2.63 (2H, t, $CH_2$), 2.29 (3H, s, $CH_3$), 1.70 (2H, quintet, $CH_2$), 1.46 (2H, quintet, $CH_2$), 1.45-1.2 (12H, quintet, $CH_2$). Elemental analysis: C 58.71 % (56.15 %), H 4.25 % (3.89 %), N 6.57 % (6.03 %). Calculated values are in brackets.

### *2.2.16 Synthesis of $[Ru(dpp)_2$(AmidoPhen-16-(acetylthio)-hexadecanyl)$](PF_6)_2$*

55.1 mg ($1.084x10^{-4}$ mol) Amidophenanthroline-16-(acetylthio)-hexadecanyl and 94.6 mg $[Ru(dpp)_2]Cl_2$ were dissolved in 50 ml 80 : 20 EtOH : $H_20$. This solution was refluxed for 16 hrs and then the reaction mixture was rotary evaporated down to about 15 ml. Ammonium hexafluorophosphate was used to precipitate the product as a $PF_6$ salt. The orange product was collected by vacuum filtration and washed with water and diethyl ether. 0.1475 g was recovered (87 % yield). Structure and purity was confirmed by $^1$H NMR analysis. GC-MS: 1418 ($M^+$, -145). $^1$H NMR in deuterated DMSO. 10.45 (1H, s, N-H), 8.91 (1H, d, C-H), 8.78 (1H, d, C-H), 8.68 (1H, s, C-H), 8.35 (1H, d, C-H), 8.32 (1H, d, C-H), 8.26 (5H, m, C-H), 8.20 (2H, m, C-H), 8.14 (1H, t, C-H), 7.90 (1H, m, C-H), 7.82 (3H, m, C-H), 7.8 (2H, m, C-H), 7.7-7.5 (20H, m, C-H), 2.78 (2H, t, $CH_2$), 2.67 (2H, t, $CH_2$), 2.29 (3H, s, $CH_3$), 1.70 (2H, quintet, $CH_2$), 1.46 (2H, quintet, $CH_2$), 1.44 (22H, quintet, $CH_2$).

Elemental analysis: C 57.38 % (56.96 %), H 3.75 % (3.58 %) N 6.89 % (6.68 %). Calculated values are in brackets. Elemental analysis: C 59.92 % (58.96 %), H 4.71 % (4.44 %), N 6.27 % (5.84 %). Calculated values are in brackets.

### *2.2.17 Synthesis of $[Ru(dpp)_2(NH_2phen)].(PF_6)_2$*

0.0779 g of ($8.9 \times 10^{-5}$ mol) of $[Ru(dpp)_2].Cl_2$ and 0.0182 g ($8.9 \times 10^{-5}$ M) of $NH_2$phen were dissolved in 50 ml of 80 : 20 EtOH : $H_2O$. This solution was refluxed for 16 hrs and then the reaction mixture was rotary evaporated down to dryness. The orange product was collected. 0.086 g was recovered (90 % yield). This dichloride product was converted to a $(PF_6)_2$ salt by dissolving $[Ru(dpp)_2(NH_2phen)].(Cl)_2$ in a saturated solution of ammonium hexafluorophosphate and collecting the resulting precipitate by vacuum filtration. $^1$H NMR in deuterated DMSO. $^1$H NMR in deuterated DMSO. 9.01 (d, 1H), 8.35 (m, 3H), 8.26 (s, 4H), 8.19 (m, 3H), 7.79 (m, 5H), 7.47 (d, 1H), 7.66 (m, 21H), 7.14 (s, 1H), 7.05 (s, 2H)

## 2.3 Results and Discussion

### *2.3.1 Synthesis and Structural Characterization*

For the remainder of this report the $[Ru(dpp)_2(6\text{-ATAP})]^{2+}$, $[Ru(dpp)_2(8\text{-ATAP})]^{2+}$, $[Ru(dpp)_2(11\text{-ATAP})]^{2+}$ and $[Ru(dpp)_2(16\text{-ATAP})]^{2+}$ will be referred to as Ru6D, Ru8D, Ru11D and Ru16D respectively, where dpp is 4,7-diphenylphenanthroline and 6-ATAP, 8-ATAP, 11-ATAP and 16-ATAP are 5-Amido-1,10-phenanthroline-(6-acetylthio-hexanyl), 5-Amido-1,10-phenanthroline-(8-acetylthio-octanyl), 5-Amido-1,10-phenanthroline-(11-acetylthio-undecanyl) and 5-Amido-1,10-phenanthroline-(16-acetylthio-hexadecanyl) respectively. The entire family of complexes will be referred to as RuxD.

Synthesis of the RuxD complexes was initially attempted by reaction of $[Ru(dpp)_2(5\text{-amino-1,10-phenanthroline})]^{2+}$ with the corresponding carboxylic acid terminated alkane thiol using the DMTMM dehydration reaction procedure described above. The reaction

scheme for this reaction is shown in Fig 2.3.1.1. This reaction was unsuccessful none of the desired products being formed and NMR analysis indicating that the starting materials remained unreacted. This reaction was repeated with other amide bond forming agents such as EEDQ (2-ethoxy-1-ethoxycarbonyl-1,2-dihydroquinoline) and EDC NHS (1-Ethyl-3-(3-dimethylaminopropyl)-carbodiimide and *N*-Hydroxysuccinimide) as well as varying the temperature of the reaction and reaction time. NMR analysis indicated that the starting products still remained unreacted. The reaction was carried out again with the corresponding carboxylic acid terminated alkane acetylthio complexes. It was thought that the highly reactive thiol group was interfering with the reaction and that an acetyl protecting group would protect the reactants from the thiol group. Two methods were employed to add acetylthio functionalities to long chain carboxylic acids. The first method was to replace a bromo group with an acetyl thio functionality by reaction with potassium thioacetate. The electron withdrawing bromo group allowed attack of the adjacent carbon by the nucleophilic tioacetate. The second method was by reduction of the thiol group of a long chain mercapto carboxylic acid by zinc. The reduced thiol was attacked by an acetyl chloride, forming the acetylthio functionality. However this reaction was also unsuccessful. The method described in sections 2.2.9 – 2.2.16 was finally used and found to be successful. Acetyl groups were used to protect the reactive thiol functional group during the reaction although later experiments have shown that this reaction goes to completion when an acetyl protection group is not used (see NMR in Appendix Fig A-6). The failure of the previous synthetic methods has been attributed to the electrophilic properties of the ruthenium metal upon complexation. Amide bond catalysts such as EDC/NHS, EEDQ and DMTMM work by forming an activated ester with the carboxylic acids that reacts readily with nuleophiles such as amines. It is theorized that the electrophilic properties of the ruthenium centre draws electron density in the phenanthroline structure away from the $NH_2$ moiety. This decrease in electron density in the phenanthroline $\pi$ system and the electron withdrawing effect of the aromatic phenanthroline system itself reduces the nucleophilicity of the $NH_2$ group of the 5-amino-1,10-phenanthroline to such a degree that nucleophilic attack on the activated ester is unfavourable. Steric hinderance from the bulky $[Ru(dpp)_2(NH_2phen)]^{2+}$ could also have been a factor. The synthesis that was finally successful involved first synthesizing the x-ATAP ligand first by a DMTMM reaction of $NH_2$phen and the acetyltio-alkane carboxylic acid. The ligand was then complexed with $[Ru(dpp)_2]^{2+}$ to give the final complex.

Literature shows that the use of the acetylthio functionality does not interfere with the complexes ability to bind to metal surfaces. Acetylthio groups will spontaneously form thiol bonds with a metal surface without the need of acid cleavage of the acetyl group[14, 15]. Therefore it was decided to proceed with a protected acetylthio complex.

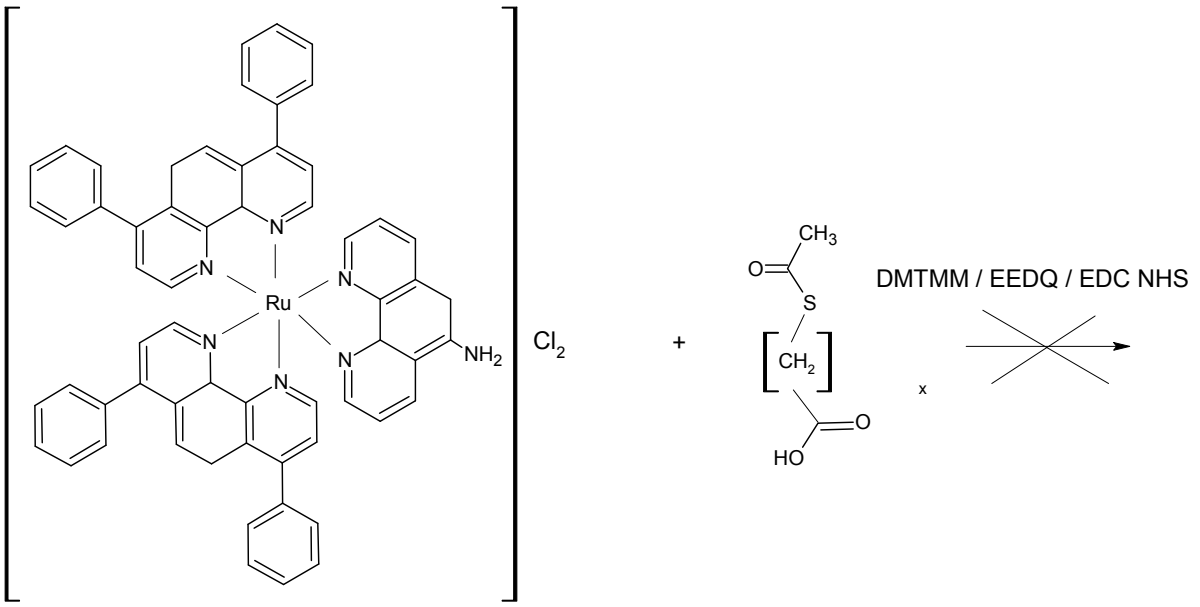


**Figure 2.3.1.1:** Reaction scheme of failed RuxD synthesis.

$^{1}$H NMR and C, H, N elemental analysis were very useful in confirming that the synthesis had been successful. Elemental analysis showed the ratios of C, H and N agreed favourably with the calculated values for the complex, to within 1 % with the calculated values. The $^{1}$H NMR spectra of all the x-ATAP ligands are very similar. Table 2.1 contains the $^{1}$H NMR data for the x-ATAP series of ligands and the NMR spectra of all x-ATAP ligands are shown in Fig 2.3.1.3 – 2.3.1.6. A proton numbering scheme for 6-ATAP is shown in Fig 2.3.1.2. In the case of 6-(ATAP) after formation of the amide bond the $NH_2$ doublet at 6.2 ppm from the 5-amino-1,10-phenanthroline is replaced by a singlet at 10.1 ppm from the amide group. This is a useful marker indicating that the reaction has been successful. The singlet from $^{4}$H adjacent to the NH of the amide bond is shifted downfield from 6.9 ppm to 8.1 ppm. All other protons from the aromatic phenanthroline have been shifted slightly downfield after the amide bond formation due to deshielding by the highly electronegative amide. In the aliphatic chain contributions from protons $^{11\text{-}16}$H remain relatively unchanged with only slight downfield shifts of less than 0.2 ppm in comparison to the parent 6-

acetylthio-hexanoic acid complex. In 8-(ATAP), 11-(ATAP) and 16-(ATAP) the most upfield multiplets in the 0-2 ppm range represent the protons from the middle of the aliphatic chain. Protons $^{17\text{-}18}$H remain unshifted in comparison to 6-acetylthio-hexanoic acid and remain around 2.9 ppm. The $^{9\text{-}10}$H protons shift downfield from 2.3 ppm to around 2.5 ppm (obscured by DMSO solvent peak) after the amide bond formation in comparison to 6-acetlythio-undecanoic acid. These downfield shifts of the aliphatic protons are due to deshielding from the electronegative carbonyl of the amide bond.

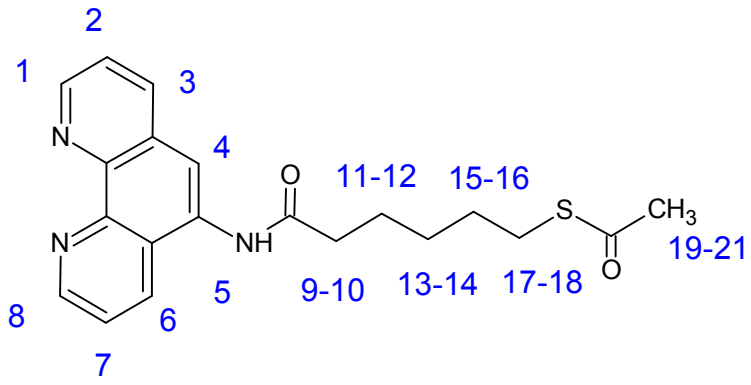


**Figure 2.3.1.2** NMR numbering scheme of amidophenanthroline-6-(acetylthio)-hexanyl

Upon complexation of the ligand with $[Ru(dpp)_2]^{2+}$, protons $^{1}$H and $^{8}$H experience an upfield shift of 0.2 ppm due to disruption of the polarization of the π system of the pyridine moieties. In a hetroaromatic system with a coordinating nitrogen, such as in pyridine and phenanthroline, the nucleophilic N causes a decrease in electron density at the carbons. This is disrupted upon complexation with the ruthenium centre which increases electron density to the carbons . A $^{1}$H COSY NMR spectrum of Ru6D was taken and is presented in Fig 2.3.11 In the aliphatic region of the 6-ATAP ligand $^{17\text{-}18}$H shows coupling with the quintet at 1.61 ppm indicating that these protons relate to $^{15\text{-}16}$H protons in the 6-ATAP ligand. The protons obscured by the solvent peak at around 2.5 ppm relating to $^{9\text{-}10}$H couple with the quintet at 1.7 ppm indicating that this quintet relates to protons $^{11\text{-}12}$H in the 6-ATAP ligand. The large peak at 7.6 ppm that integrates for about 20 protons only couples with itself indicating that these protons relate to the pendant phenyl rings of the diphenylphenanthroline. The two quintets at 8.9 and 8.8 ppm seem to relate to the $^{1}$H and $^{8}$H protons of the 6-ATAP ligand since they integrate for 1 proton each and are in similar positions to the uncoordinated ligand.

Mass spec analysis of the co-ordinated RuxD complexes, shown in Appendix A-2 to A-5, gives a molecular ion with the molecular weight of the $[M\text{-}PF_6]^+$ ion. The molecular ion has a complex isotopic pattern indicative of a ruthenium complex due to the 7 stable isotopes of ruthenium.

| | Protons (ppm) | | | | | | | |
|---|---|---|---|---|---|---|---|---|
| **Ligand** | $^{1}$H | $^{2}$H | $^{3}$H | $^{4}$H | $^{5}$H | $^{6}$H | $^{7}$H | $^{8}$H |
| 6-ATAP | 9.13 (dd) | 7.74 (quartet) | 8.59 (dd) | 8.17 (s) | 10.11 (s) | 8.45 (dd) | 7.83 (quartet) | 9.03 (dd) |
| | $^{1}$H | $^{2}$H | $^{3}$H | $^{4}$H | $^{5}$H | $^{6}$H | $^{7}$H | $^{8}$H |
| 8-ATAP | 9.13 (dd) | 7.74 (quartet) | 8.59 (dd) | 8.17 (s) | 10.11 (s) | 8.45 (dd) | 7.83 (quartet) | 9.03 (dd) |
| | $^{1}$H | $^{2}$H | $^{3}$H | $^{4}$H | $^{5}$H | $^{6}$H | $^{7}$H | $^{8}$H |
| 11-ATAP | 9.12 (dd) | 7.74 (quartet) | 8.59 (dd) | 8.17 (s) | 10.11 (s) | 8.45 (dd) | 7.82 (quartet) | 9.03 (dd) |
| | $^{1}$H | $^{2}$H | $^{3}$H | $^{4}$H | $^{5}$H | $^{6}$H | $^{7}$H | $^{8}$H |
| 16-ATAP | 9.12 (dd) | 7.74 (quartet) | 8.59 (dd) | 8.17 (s) | 10.11 (s) | 8.44 (dd) | 7.82 (quartet) | 9.03 (dd) |

| **Ligand** | $^{9\text{-}10}$H | $^{11\text{-}12}$H | $^{13\text{-}14}$H | $^{15\text{-}16}$H | $^{17\text{-}18}$H | $^{19\text{-}21}$H |
|---|---|---|---|---|---|---|
| 6-ATAP | ~ 2.5 (t) | 1.70 (quintet) | 1.45 (quintet) | 1.62 (quintet) | 2.88 (t) | 2.32 (s) |
| | $^{9\text{-}10}$H | $^{11\text{-}12}$H | $^{13\text{-}18}$H | $^{19\text{-}20}$H | $^{21\text{-}22}$H | $^{23\text{-}25}$H |
| 8-ATAP | ~ 2.5 (t) | 1.68 (quintet) | 1.37 (m) | 1.54 (quintet) | 2.84 (t) | 2.31 (s) |
| | $^{9\text{-}10}$H | $^{11\text{-}12}$H | $^{13\text{-}24}$H | $^{25\text{-}27}$H | $^{27\text{-}28}$H | $^{29\text{-}31}$H |
| 11-ATAP | ~2.5 (t) | 1.68 (quintet) | 1.29 (m) | 1.54 (quintet) | 2.80 (t) | 2.31 (s) |
| | $^{9\text{-}10}$H | $^{11\text{-}12}$H | $^{13\text{-}34}$H | $^{35\text{-}36}$H | $^{37\text{-}38}$H | $^{39\text{-}41}$H |
| 16-ATAP | ~ 2.5 (t) | 1.69 (quintet) | 1.23 (m) | 1.47 (quintet) | 2.80 (t) | 2.31 (s) |

**Table 2.1:** Proton NMR data (δ scale) for x-ATAP ligands in $(CD_3)_2SO$

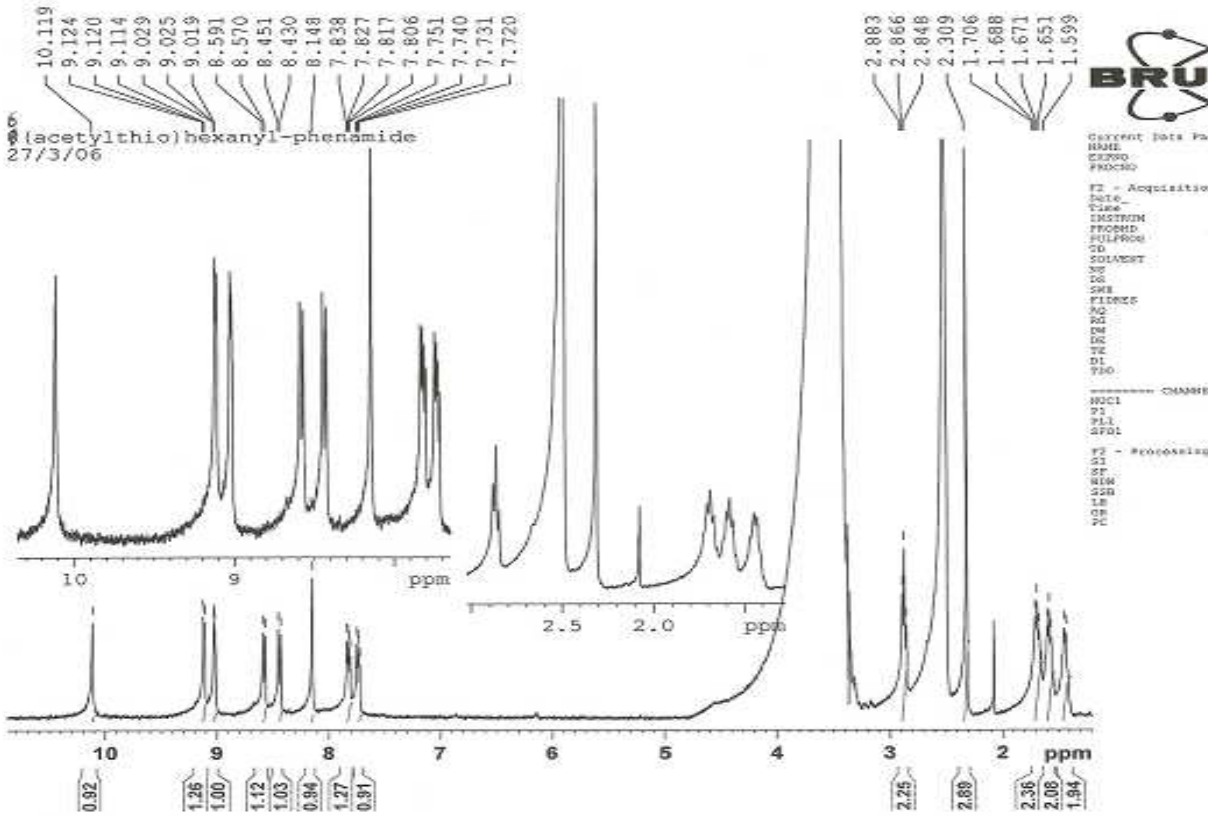


**Figure 2.3.1.3:** $^{1}$H NMR of amidophenanthroline-6-(acetylthio)-hexanyl in $(CD_3)_2SO$.

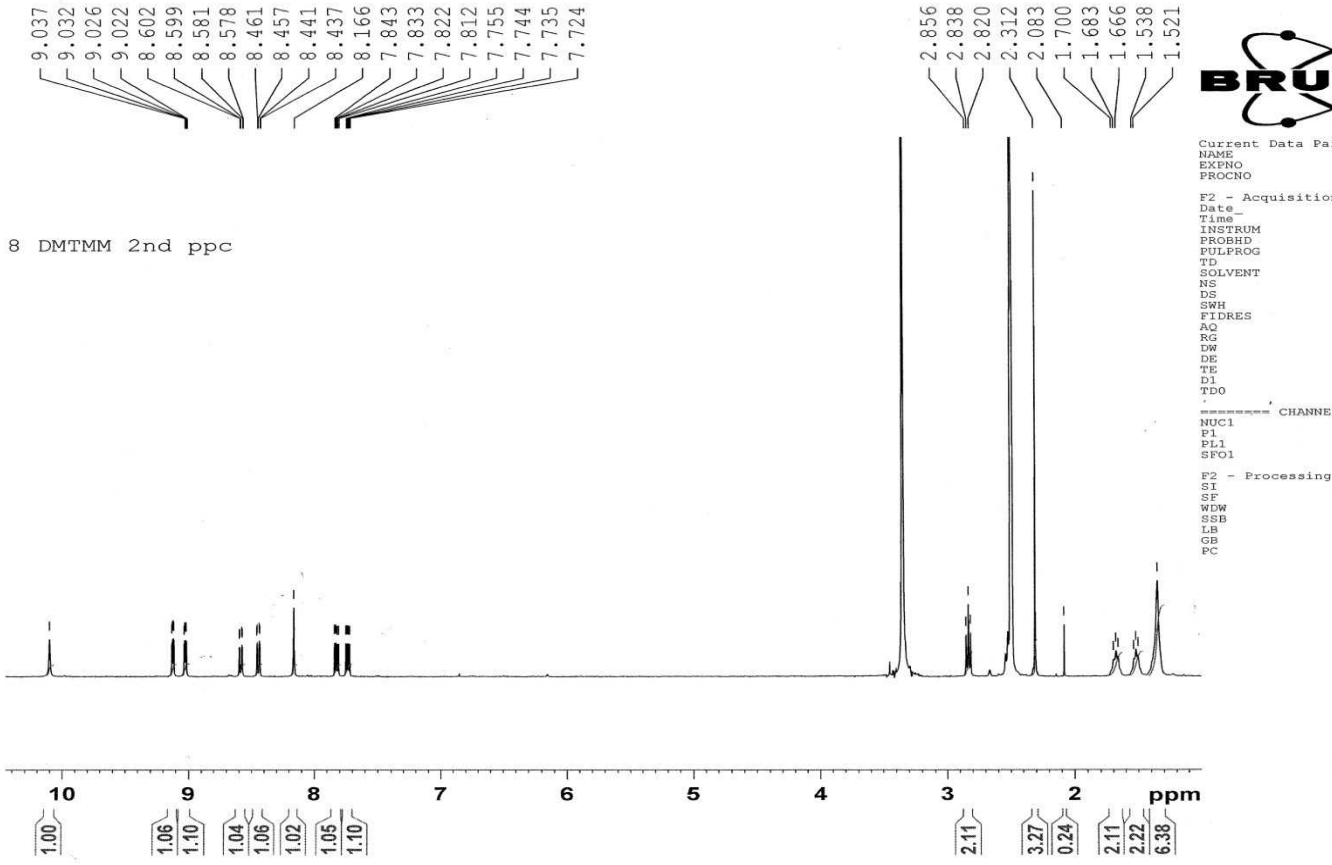


**Figure 2.3.1.4:** $^{1}$H NMR of amidophenanthroline-8-(acetylthio)-octanyl in $(CD_3)_2SO$

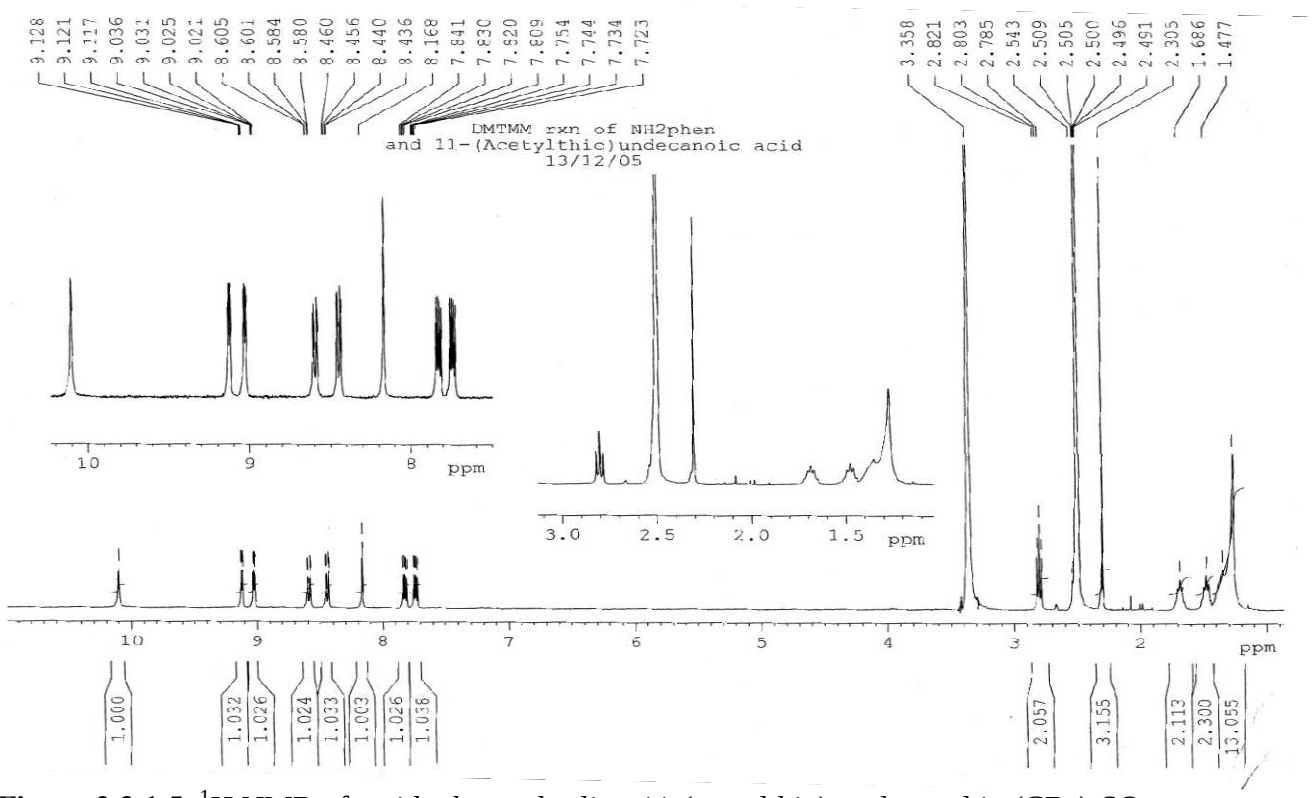


**Figure 2.3.1.5:** $^{1}$H NMR of amidophenanthroline-11-(acetylthio)-undecanyl in $(CD_3)_2SO$.

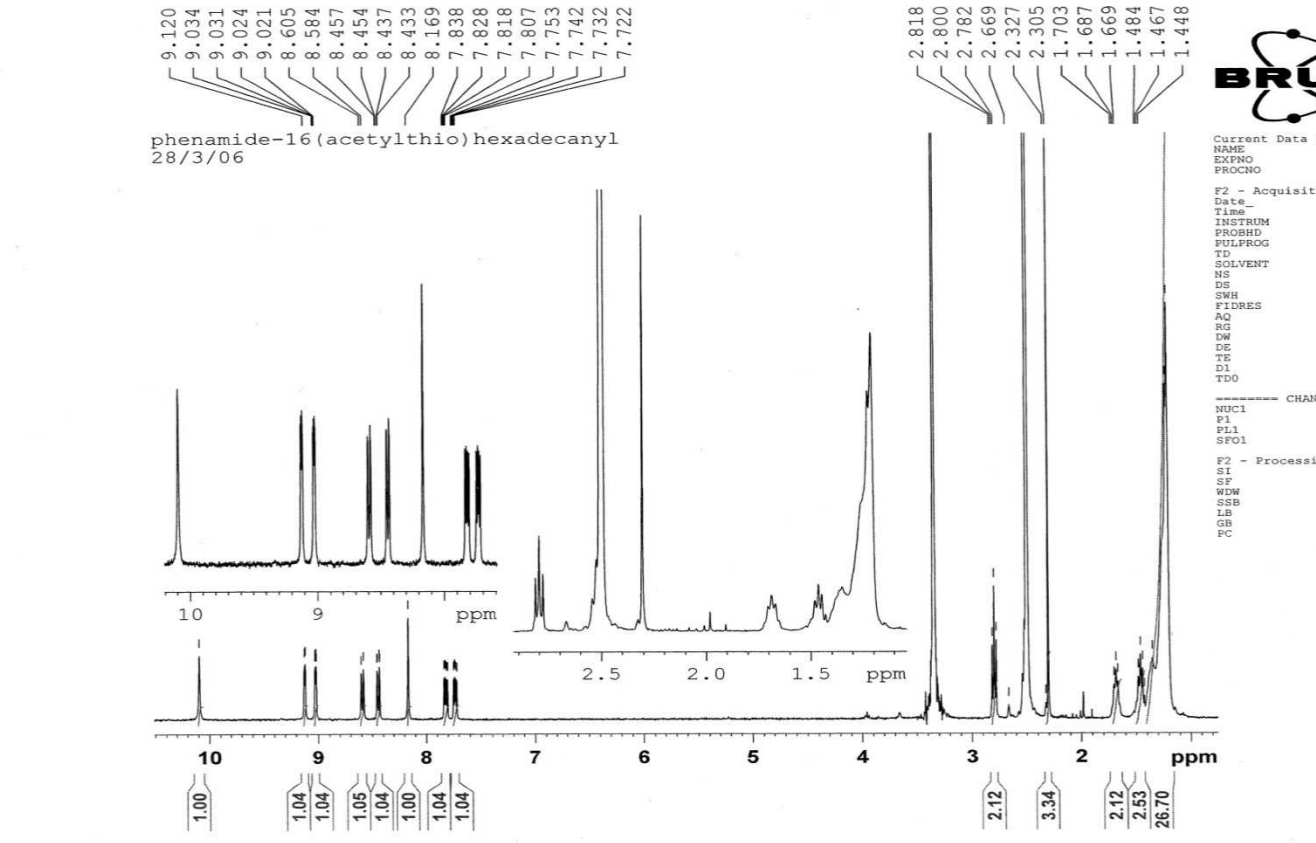


**Figure 2.3.1.6:** $^{1}$H NMR of amidophenanthroline-16-(acetylthio)-hexadecanyl in $(CD_3)_2SO$.

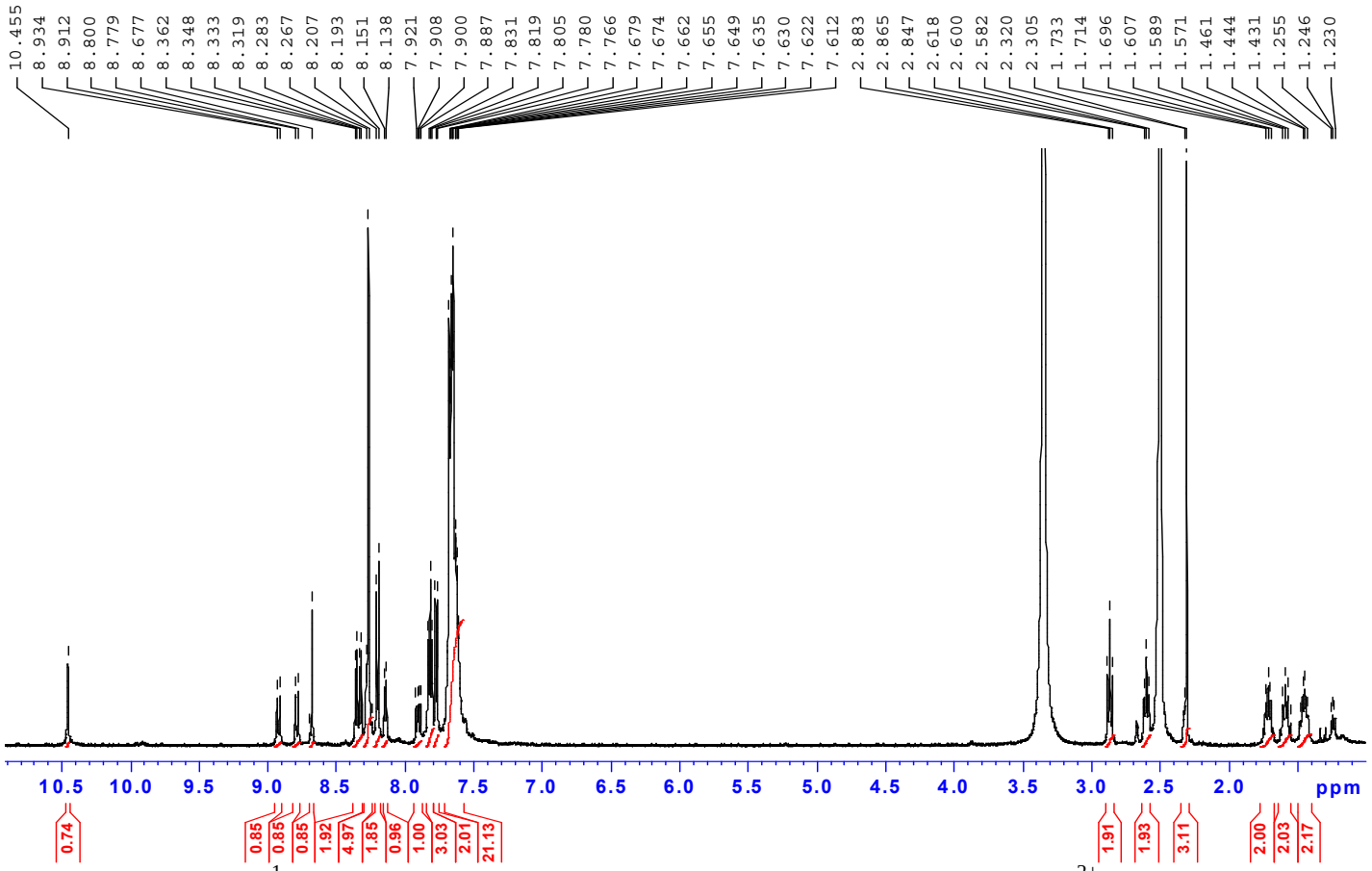

**Figure 2.3.1.7:** $^{1}$H NMR of $[Ru(dpp)_2(amidoPhen\text{-}6\text{-}(acetylthio)\text{-}hexanyl)(PF_6)_2]^{2+}$ in $(CD_3)_2SO$.

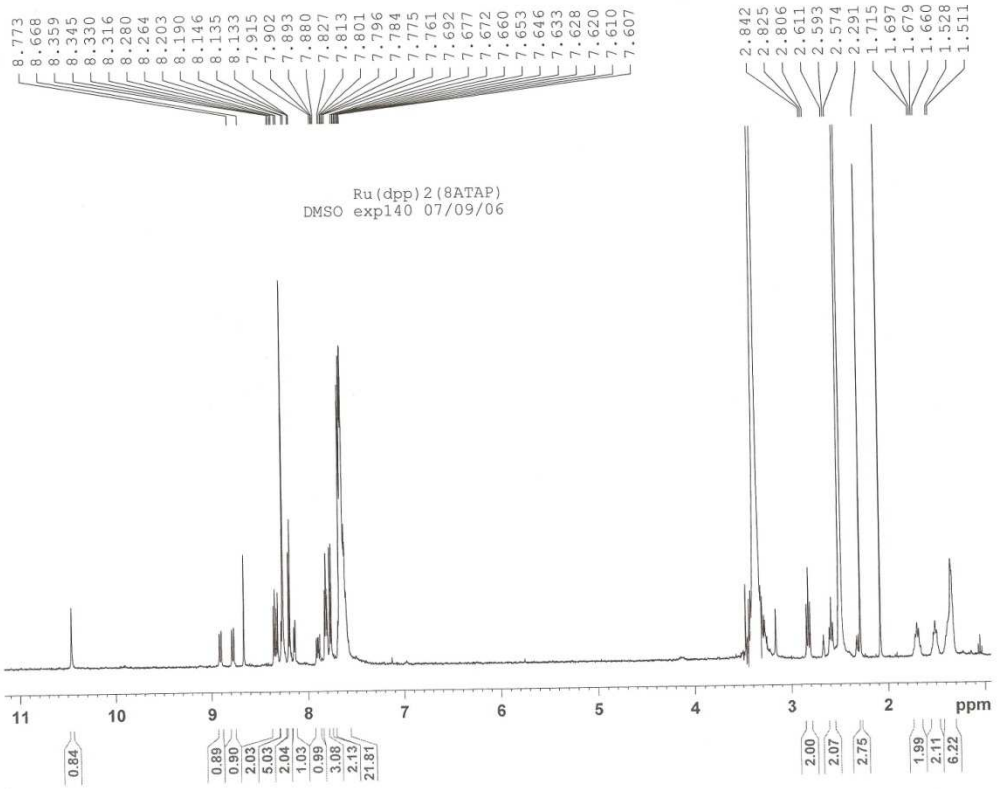


**Fig 2.3.1.8:** $^{1}$H NMR of $[Ru(dpp)_2(amidoPhen\text{-}8\text{-}(acetylthio)\text{-}octanyl)(PF_6)_2]^{2+}$ in $(CD_3)_2SO$.

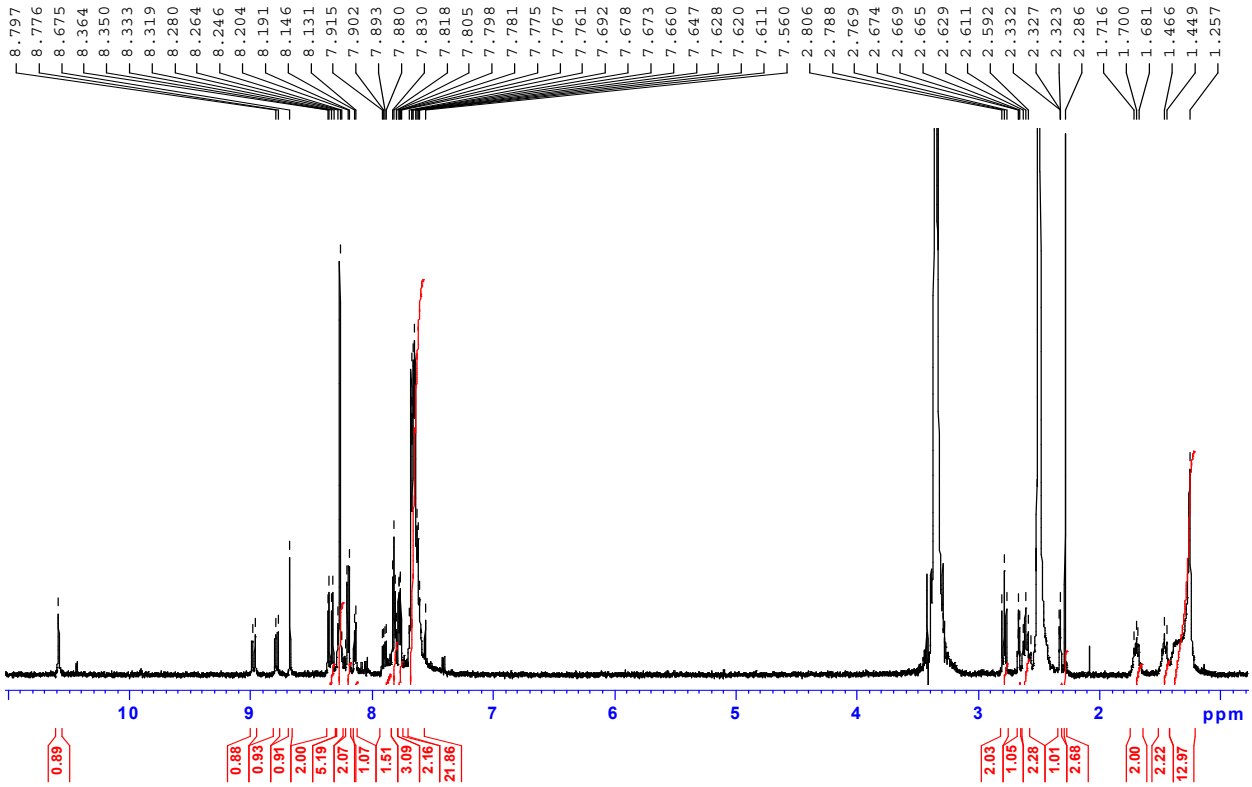


**Figure 2.3.1.9:** $^{1}$H NMR of $[Ru(dpp)_2(amidoPhen\text{-}11\text{-}(acetylthio)\text{-}undecanyl)(PF_6)_2]^{2+}$ in $(CD_3)_2SO$

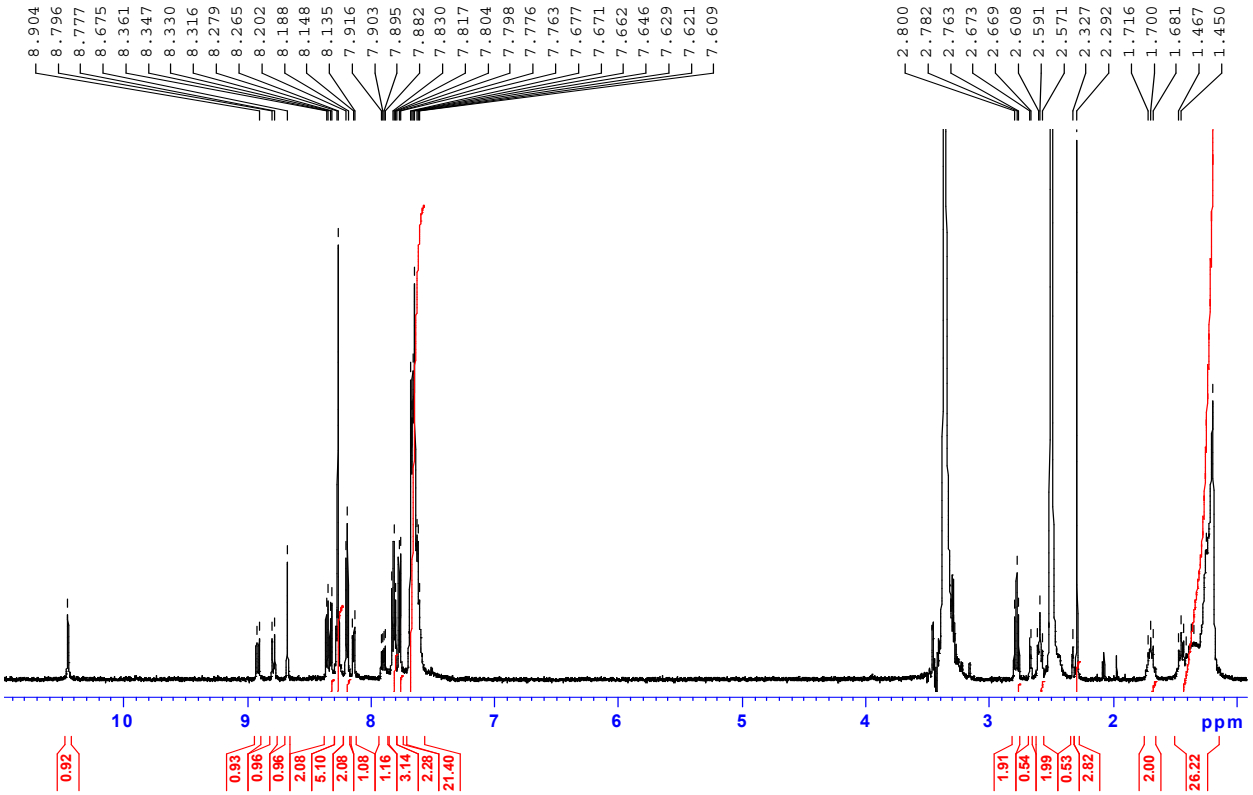


**Figure 2.3.1.10:** $^{1}$H NMR of $[Ru(dpp)_2(amidoPhen\text{-}16\text{-}(acetylthio)\text{-}hexadecanyl)(PF_6)_2]^{2+}$ in $(CD_3)_2SO$

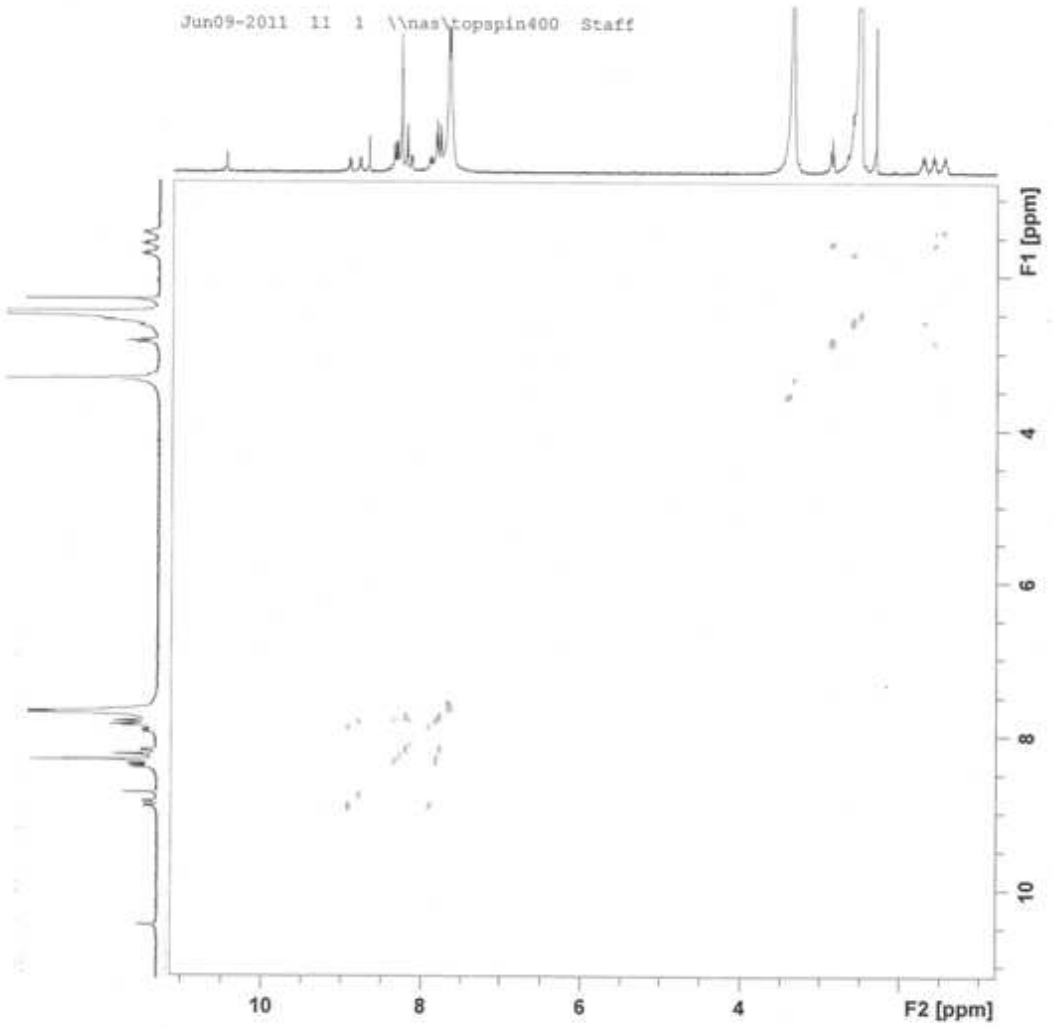


**Figure: 2.3.1.11:** $^{1}$H NMR COSY of $[Ru(dpp)_2(amidoPhen\text{-}6\text{-}(acetylthio)\text{-}hexanyl)(PF_6)_2]^{2+}$ in $(CD_3)_2SO$

### *2.3.2 Absorption and Emission Spectroscopy*

The photophysical properties of the RuxD series of complexes are detailed in Table 2.2. The UV-vis absorbance spectra of all 4 RuxD complexes in acetonitrile are shown in Fig 2.3.2.1. The electronic absorption spectra of the RuxD complexes are comparable to the electronic absorption spectra of $[Ru(bpy)_3]^{2+}$ and other similar Ru polypyridyl complexes. The absorbance at ~200 nm (cut off in this spectrum) is attributed to a LC $\pi \rightarrow \pi^*$ transition. The shoulder at ~222 nm is attributed to an MLCT $d \rightarrow \pi^*$ transition. The strong absorbance with a $\lambda_{max}$ of 276 nm is attributed to LC $\pi - \pi^*$ intraligand transitions. The slight shoulder at ~315 nm is probably due to a MC $d \rightarrow d$ transition although this has not been comfirmed yet for this class of ruthenium polypyridyl complexes[16]. By comparison with other ruthenium polypyridyl complexes the broad absorption peak with a $\lambda_{max}$ of 454 nm can be classified as a $^1$MLCT Ru (II) $\rightarrow$ (ligand) transition. The shape and position of this band is in good agreement with phenanthroline and diphenylphenanthroline containing Ru polypyridyl complexes. These bands were assigned by comparison with 4,7-diphenyl-1,10-phenanthroline and 5-amino-1,10-phenanthroline containing ruthenium polypyridyl comlexes[17, 18, 19, 20]. The presence and length of the aliphatic chain has no noticable effect on the UV-vis spectrum.

The emission spectra of all RuxD complexes are shown in Fig 2.3.2.2 absorbance matched under aerated conditions. All four complexes exhibit intense emission at $\lambda_{em}$ = 608 nm which is independent of the excitation wavelength. There is no noticeable change in the emission intensity with alkyl chain length within experimental error. The Stokes shift, the energy gap between the lowest energy absorption and the emission maximum, was calculated to be 154 nm which is slightly greater than the Stokes shift for $[Ru(bpy)_3]^{2+}$. The deaerated emission spectra are shown in Fig 2.3.2.3. The slight variation in fluorescent intensity of the different RuxD complexes is due to the lack of absorbance matching because of the loss of solvent during the degassing process. Emission in deaerated solvent shows a large increase in the emission intensity compared with aerated samples with no shift in the $\lambda_{max}$ of the emission as expected. The solvent was degassed by bubbling $N_2$ through the solvent for 20 minutes.

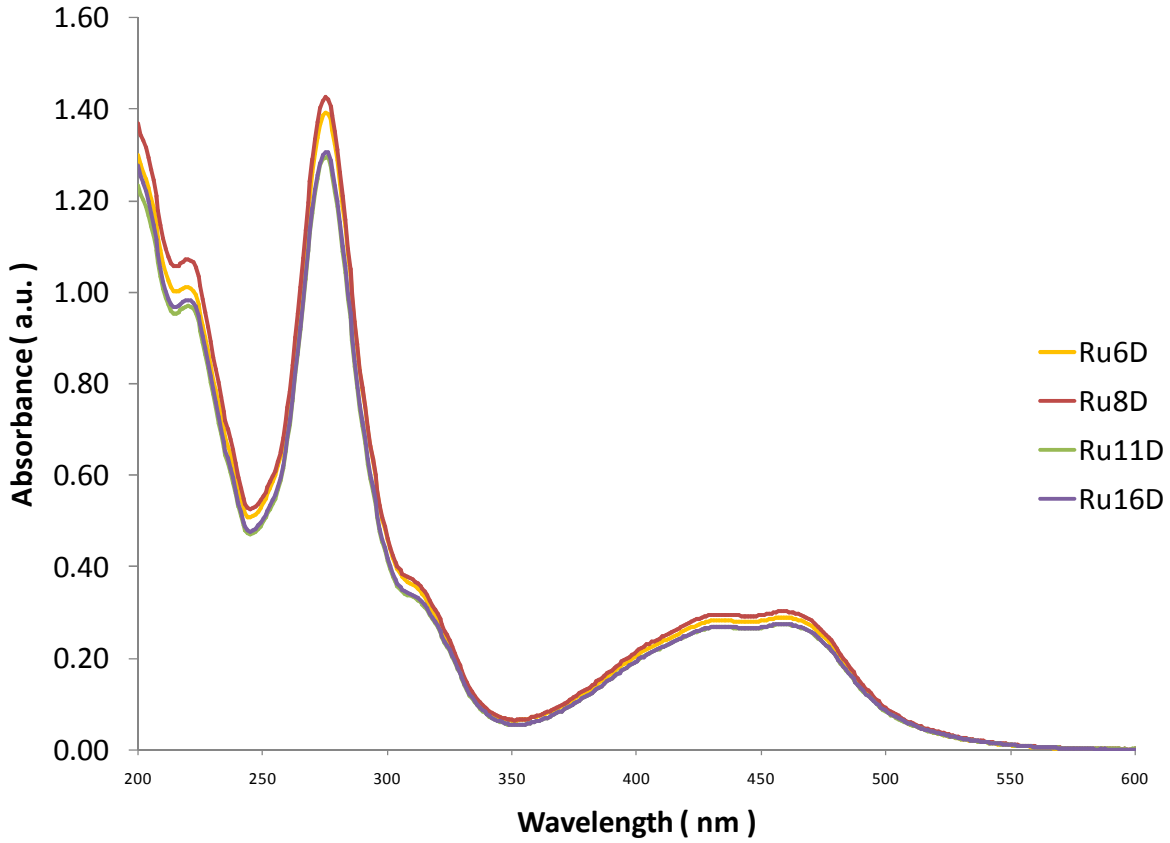


**Figure 2.3.2.1:** UV-vis spectra of RuxD complexes. All spectra are absorbance matched at 454 nm and made up in ACN.

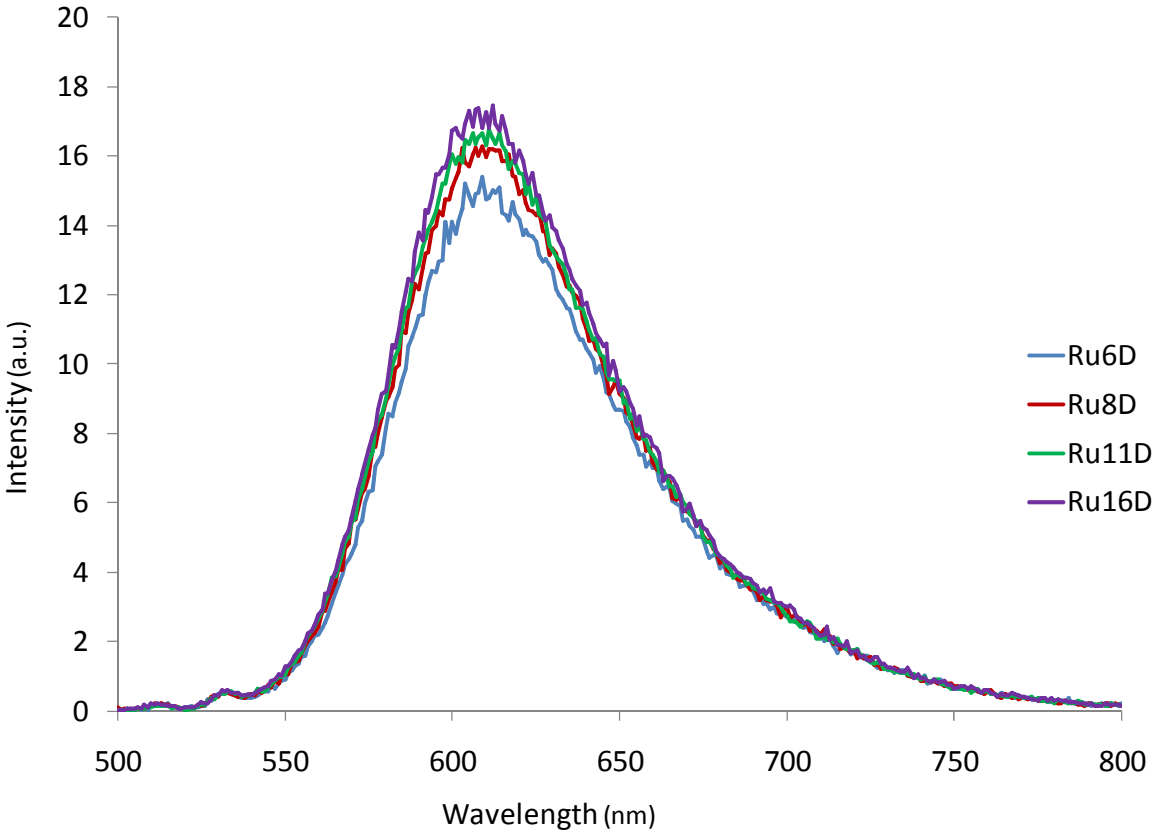


**Figure: 2.3.2.2:** Emission spectra of RuxD complexes at room temperature. All spectra are taken from ~1μM solutions in aerated ACN absorbance matched at 454 nm and excited at 454 nm.

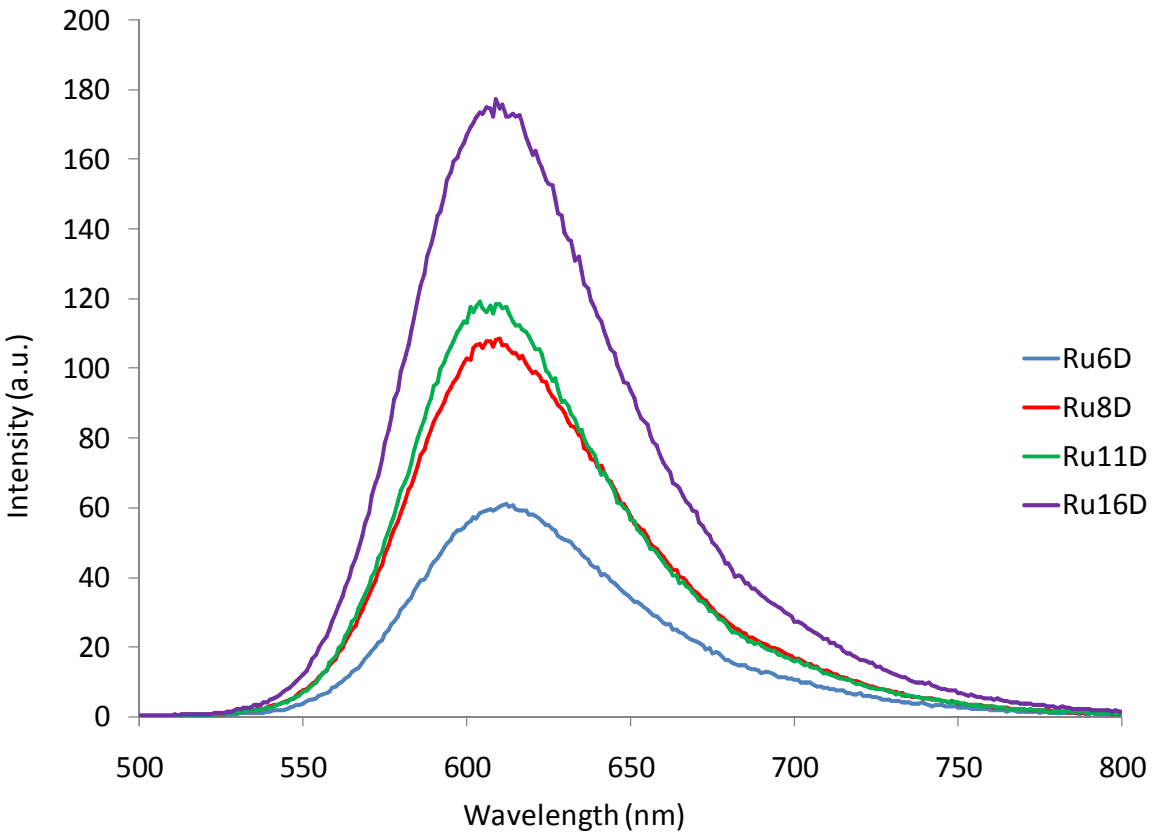


**Figure 2.3.2.3:** Emission spectra of RuxD complexes at room temperature in deaerated ACN. Solutions were degassed by purging with $N_2$ gas for 20 minutes prior to analysis. Samples were excited at 454 nm. Solutions were not absorance matched.

The lifetimes of the RuxD complexes were all found to be ~180 ns in aerated conditions with no appreciable difference due to alkyl chain length within experimental error. This is comparable to the luminescence lifetime of $[Ru(bpy)_3]^{2+}$ of 172 ns under the same conditions[21]. The aerated quantum yield of ~0.011 is lower than the quantum yield of $[Ru(bpy)_3]^{2+}$ which is 0.016 in the same conditions. This is probably due to the increased oxygen sensitivity of the RuxD complexes in comparision. In deaerated solvent purged with $N_2$ the lifetime increases to ~0.8 μs. These values are comparable to $[Ru(bpy)_3]^{2+}$ under the same conditions[22]. This luminescence lifetime is greater than the lifetime of $[Ru(phen)_3]^{2+}$ which is 0.5 μs under the same conditions[22]. Luminescence quantum yields of RuxD in deaerated conditions are also significantly higher than $[Ru(phen)_3]^{2+}$, ~0.13 as opposed to 0.28 respectively[22]. These low aerated emission quantum yields and short emission lifetimes are probably caused by π-acceptor properties of both ligands surrounding the metal center. As mentioned in section 1.3 a mixture of π-acceptor and σ-donor ligands in a ruthenium

polypyridyl complex is preferable. Solution phase electrochemistry of the RuxD complexes in section 2.3.5 also indicates the π-acceptor properties of the dpp and x-ATAP ligands in the RuxD complex. The $k_r$ and $k_{nr}$ values are the same as $[Ru(dpp)_2(NH_2phen)]^{2+}$ within experimental error.

The radiative and non-radiative decay rates, $k_r$ and $k_{nr}$ respectively were calculated using the relationship[8];

$$k_r = \frac{\Phi_{\mathrm{em}}}{\tau_{em}}$$

$$k_{nr} = \frac{1}{\tau_{em}} - k_r$$

where $\Phi_{em}$ and $\tau_{em}$ are the deaerated luminescence quantum yield and lifetime respectively. Compared to $[Ru(dpp)_3]^{2+}$, which has a $k_r$ and $k_{nr}$ value of 5.7 x $10^4$ $s^{-1}$ and 9.9 x $10^4$ $s^{-1}$ respectively[22], the RuxD complexes have much higher rates of radiative and non-radiative decay, which have $k_r$ and $k_{nr}$ values of about 3 x $10^5$ $s^{-1}$ and 9 x$10^5$ $s^{-1}$. However RuxD complexes have lower $k_{nr}$ than $[Ru(phen)_3]^{2+}$, which has a $k_r$ and $k_{nr}$ of 6 x $10^4$ and 2.1x $10^6$ respectively. This attributed to delocalisation of the excited state effect since dpp ligands have a greater area of delocalisation than phen ligands. The faster $k_{nr}$ confirms that population of the $^3$MC is far more likely due to a smaller energy gap between the $^3$MLCT and $^3$MC states.

The high sensitivity of luminescence lifetime and quantum yield of RuxD complexes to $O_2$ is not unexpected considering that various publications have shown that ruthenium complexes with phen and dpp ligands show excellent sensitivity of their luminescence intensities and lifetimes to $O_2$ concentration and $[Ru(dpp)_3]^{2+}$ has been used in highly senstive oxygen sensing devices[11, 13]. Ruthenium polypridyl complexes containing dpp and phenanthroline ligands have been shown to have a large Stern-Volmer $[O_2]$ quenching constant in comparison to most ruthenium polypridyl complexes[13]. This high sensitivity of the luminescense lifetime and quantum yield to $[O_2]$ makes the RuxD complexes good

candidates for $O_2$ concentration probes and as markers for $O_2$ concentration mapping in complex matrices such as cells, which is one of the reasons they are explored here.

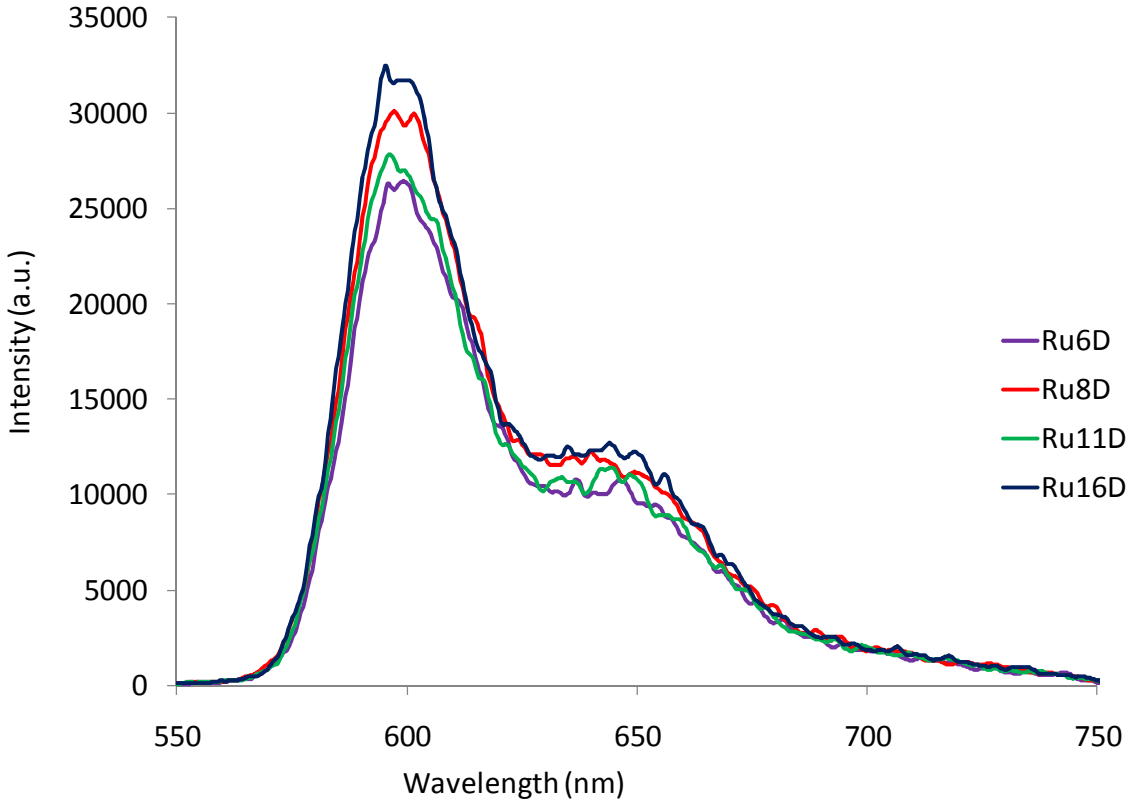


**Figure 2.3.2.4:** Emission spectra at 77K of the RuxD series excited at 355nm in propionitrile : butryonitrile (4:5 v/v) glass. Samples were absorbance matched at 355 nm.

Emission spectra for the RuxD complexes taken in an aerated 4:1 butyronitrile:propionitrile glass at 77 K are shown in Fig 2.3.2.4. Extra vibrational fine structure compared to measurements at 298 K were observed. Again there is no observable difference in emission intensity with chain length across the RuxD complexes. The $\lambda_{max}$ of emission has blue shifted by 9 nm to 599 nm as is expected in 77 K measurements of ruthenium polypyridyl complexes[23]. This shift of 9 nm in the $\lambda_{max}$ of emission is comparable to a similar complex such as $[Ru(bpy)(dpp)_2]^{2+}$, which displays a blue shift of 11 nm in a ethanol: methanol (4:1 v/v) glass at 77 K compared to solution phase measurements at room temperature[18]. These blue shifts are due to a rigidochromism effect. Excitation to the $^3$MLCT excited state results in a change in dipole and electron density distrubution compared to the ground state. This excited state is destabilised with respect to the complex geometry and solvent orientation. In a fluid system the solvent molecules can reorientate and stabilise this

excited state within the time frame of the excited state. In a rigid system the solvent molecules cannot reorientate within the time frame of the excited state lifetime resulting in a higher energy destabilised $^3$MLCT and a blue shift in emission[24,25]. The shape of the emission including the pronounced shoulder at 640 nm are due to ν(ligand) framework vibrations from comparison to similar comlexes[26].

Luminescent lifetimes at 77 K in a 4:1 butyronitrile:propionitrile glass are around 10 μs for all RuxD complexes. Quantum yields of the RuxD series are dramatically increased to around 0.60 for all RuxD complexes when measured under the same conditions. This value is comparabe to similar ruthenium polypyridyl complexes such as $[Ru(bpy)_2(dpp)]^{2+}$, $[Ru(bpy)(phen)_2]^{2+}$ and $[Ru(dpp)_3]^{2+}$ under these conditions[22]. The dramatic increase in emissive lifetime and quantum yield values at 77K is due to a lower probability of thermal population of the $^3$MC state at lower temperatures which can lead to radiationless deactivation of the excited state.

The addition of an alkyl acetylthio chain to the 5-amino-1,10-phenanthroline affects the photophysical properties of the full RuxD complex. The shorter luminescence lifetimes and lower quantum yields of this complex compared to similar class of complexes, such as $[Ru(dpp)_2(NH_2phen)]^{2+}$, $[Ru(bpy)(dpp)_2]^{2+}$ and $[Ru(dpp)_2(phen)]^{2+}$ at ambient temperature and oxygen concentrations indicates that the excited state has been sensitised to deactivation by thermal and quenching mechanisms possibly due to increased π-acceptor characteristics of the x-ATAP ligands. Luminescence lifetimes and quantum yields at 77 K and in deaerated solutions are comparable to these complexes due to the elimination of $O_2$ quenching and thermal population of the $^3$MC state respectively.

| | $\varepsilon_{454nm}$ ($mol^{-1}$ $cm^{-1}$) | λmax aerated @298K (nm) [a] | λmax deaerated @298K (nm) [a] | $\phi_{em}$ aerated (298K) [a] | $\phi_{em}$ deaerated (298K) [a] |
|---|---|---|---|---|---|
| $Ru[(dpp)_2(NH_2phen)]^{2+}.(PF_6)_2$ [a] | $2.2x10^4 \pm 5x10^2$ | 617 | 617 | 0.0094 ± 0.0004 | 0.13 ±0.02 |
| Ru6d | $2.9x10^4 \pm 4x10^2$ | 608 | 608 | 0.0114 ± 0.0002 | 0.13 ± 0.01 |
| Ru8D | $3x10^4 \pm 4x10^2$ | 608 | 608 | 0.0113 ± 0.0002 | 0.12 ± 0.02 |
| Ru11D | $2.8x10^4 \pm 3x10^2$ | 608 | 608 | 0.0114 ± 0.0002 | 0.12 ± 0.02 |
| Ru16D | $2.8x10^4 \pm 4x10^2$ | 608 | 608 | 0.0114 ± 0.0002 | 0.15 ± 0.005 |
| $[Ru(dpp)_3]^{2+}$ [a] | $2.86 \times 10^4$ (@ 463 nm) | | 618 | | 0.366 |

| | $\tau_{em}$ aerated @298K (s) [b] | $\tau_{em}$ deaerated @298K (s) [b] | $k_r$ ($s^{-1}$) | $k_{nr}$ ($s^{-1}$) | λmax @ 77K (nm) [c] | $\phi_{em}$ 77K [c] | $\tau_{em}$ @ 77K(s) [c] |
|---|---|---|---|---|---|---|---|
| $Ru[(dpp)_2(NH_2phen)]^{2+}.(PF_6)_2$ | 1.62E-07 ± 1.7E-08 | 1.04E-06 ± 2.6E-08 | 1.25E+05 ± 1.9E+04 | 8.37E+05 ± 3E+04 | n/a | n/a | n/a |
| Ru6d | 1.75E-07 ± 2.2E-08 | 9.42E-07 ± 3.1E-08 | 1.38E+05 ± 1.1E+04 | 9.24E+05 ± 3.7E+04 | 599 | 0.55 ± 0.05 | 9.96E-06 ± 3.5E-06 |
| Ru8D | 1.73E-07 ± 3.3E-08 | 8.86E-07 ± 3.7E-08 | 1.35E+05 ± 2.3E+04 | 9.93E+05 ± 5.2E+04 | 599 | 0.63 ± 0.01 | 1.14E-05 ± 2.1E-06 |
| Ru11D | 1.82E-07 ± 2.3E-08 | 9.99E-06 ± 3.3E-08 | 1.2E+05 ± 2E+04 | 8.81E+05 ± 3.9E+04 | 599 | 0.58 ± 0.04 | 1.1E-05 ± 3.4E-06 |
| Ru16D | 1.85E-07 ± 2.6E-08 | 1.02E-06 ± 4.2E-08 | 1.47E+05 ± 5E+03 | 8.33E+05 ± 4.1E+04 | 599 | 0.67 ± 0.02 | 1.0E-05 ± 4.1E-06 |
| $[Ru(dpp)_3]^{2+}$ [a] | | 6.4E-06 | | | 595 | 0.682 | 9.58E-6 |

**Table 2.2:** Photophysical properties of RuxD complexes. Deaerated samples were deaerated by purging with $N_2$ for 20 minutes.$[Ru(dpp)_2(NH_2phen)]^{2+}$ data included as comparison [a]Absorbance matched and excited at 454nm in ACN. [b]Absorbance matched and excited at 355nm in ACN. [c]Absorbance matched and excited at 355nm in Butyronitrile: Propionitrile (4:1 v/v). [a] $[Ru(dpp)_3]^{2+}$ values are included as a comparison. Values are from $[Ru(dpp)_3]^{2+}$ in MeOH:EtOH 4:1 (v/v) solution. Values are taken from ref[22].

### *2.3.3 Photophysical Solvent Dependence and Nanoscale Vesicle Formation*

The solvent used to dissolve a ruthenium polypyridyl complex can have significant influence over its photophysical properties. Interactions of the complex with the solvent in the ground state and the excited state can influence the absorption and emission properties of the complex greatly. Tazuke *et al*. showed that photophysical properties of $[Ru(phen)_2(CN)_2]^{2+}$ were dependent on Gutmann's acceptor number (AN) of the solvent. An electron accepting solvent would interact with the cyano decreasing the σ-donating ability of the ligand while a more electron donating ligand will increase the σ-donating ability[27, 28]. Turro *et al*. demonstrated that the polarity of the solvent affected energy of the excited state of $[Ru(bpy)_n(dppp2)_{3-n}]^{2+}$, were n = 0-2 and dppp2 is pyrido-[2',3':5,6]pyrazino[2,3-*f*][1,10]phenanthroline. Due to the increased polarity of the excited state of the complex the polar solvents efficiently reorganize around the excited state, stabilising it and reducing its energy[29].

The photophysical properties of the RuxD series were compared in ACN, DCM and $H_2O$. A summary of the photophysical properties of the RuxD complexes are detailed in Table 2.3. The absorption spectra of the RuxD complexes in various solvents are presented in Fig 2.3.3.1 - 2.3.3.4. To solvate the RuxD complexes in water 1% acetonitrile was used. Overall the absorption spectra of the RuxD complexes are not strongly influenced by the solvent. Comparison of the MLCT absorption band of the RuxD complexes in ACN and DCM shows no change in the absorption peak shape. A slight red shift of the $\lambda_{max}$ of absorption in DCM compared to ACN suggests a more stable and lower energy $t_{2g}$ ground state. The RuxD complexes are relatively non-polar due to the two dpp ligands, pendant alkyl chain and the two $PF_6$ counterions. DCM is less polar than ACN therefore solvation of the RuxD complex in DCM would be expected to stabilize the RuxD ground state more so than solvation in ACN and reduce the energy of the ground state. In water the MLCT absorption band changes shape more significantly and has a blue shifted $\lambda_{max}$ of absorption at 438 nm. These large changes are attributed to the formation micelles of RuxD in aqueous solution, which is discussed in more detail is subsequent sections. For the aqueous solutions the RuxD complexes where dissolved in 20 µL of acetonitrile before being made up to 2 mL in $H_2O$ due to the insolubility of the complexes in $H_2O$.

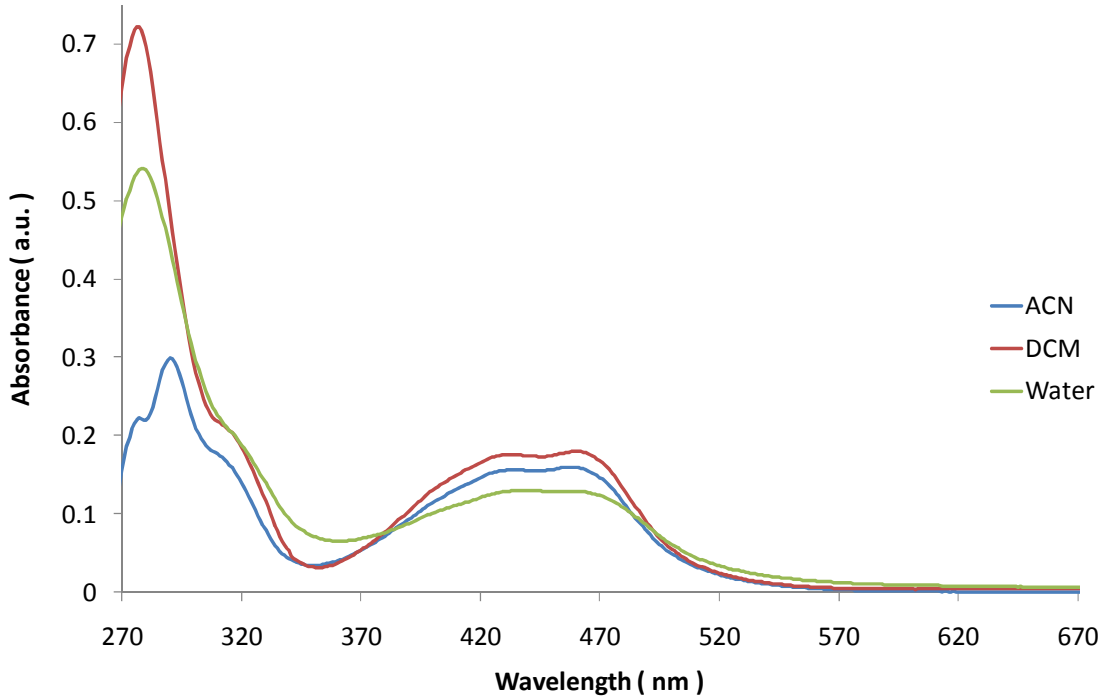


**Figure 2.3.3.1:** Absorption spectra of Ru6D in ACN, DCM and $H_2O$. Concentration of Ru6D is 5 x $10^{-6}$ M in all solvents. For the results in water are in 99 : 1 (v/v) water : acetonitrile.

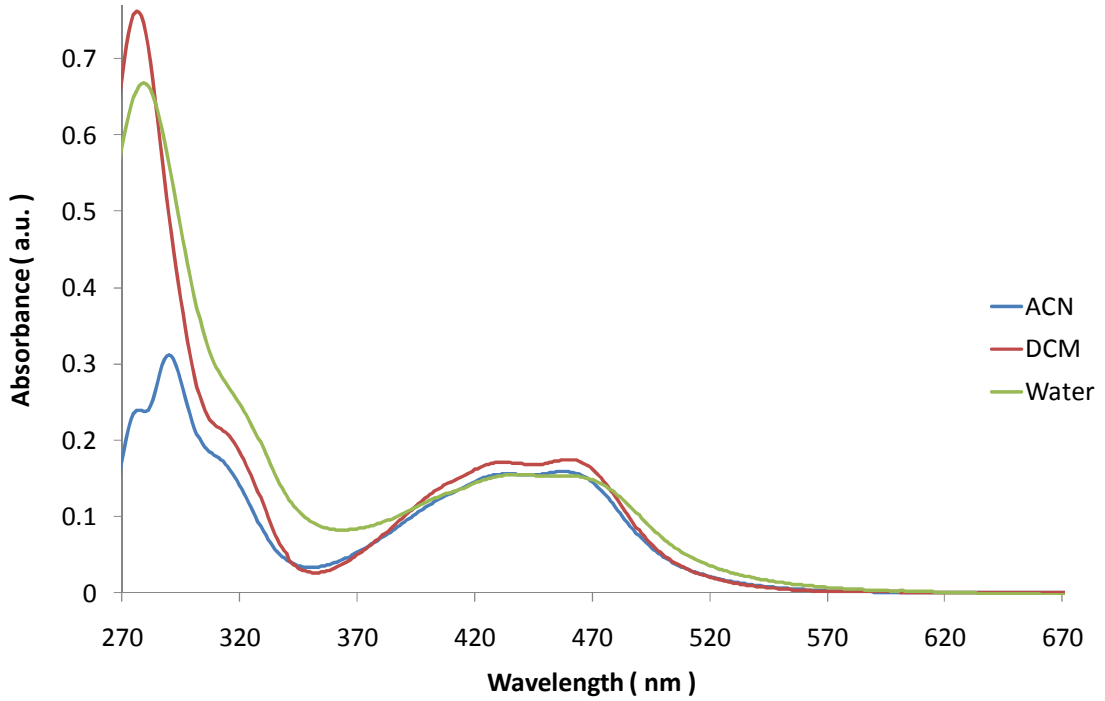


**Figure 2.3.3.2:** Absorption spectra of Ru8D in ACN, DCM and $H_2O$. Concentration of Ru8D is 5 x $10^{-6}$ M in all solvents. For the results in water are in 99 : 1 (v/v) water : acetonitrile.

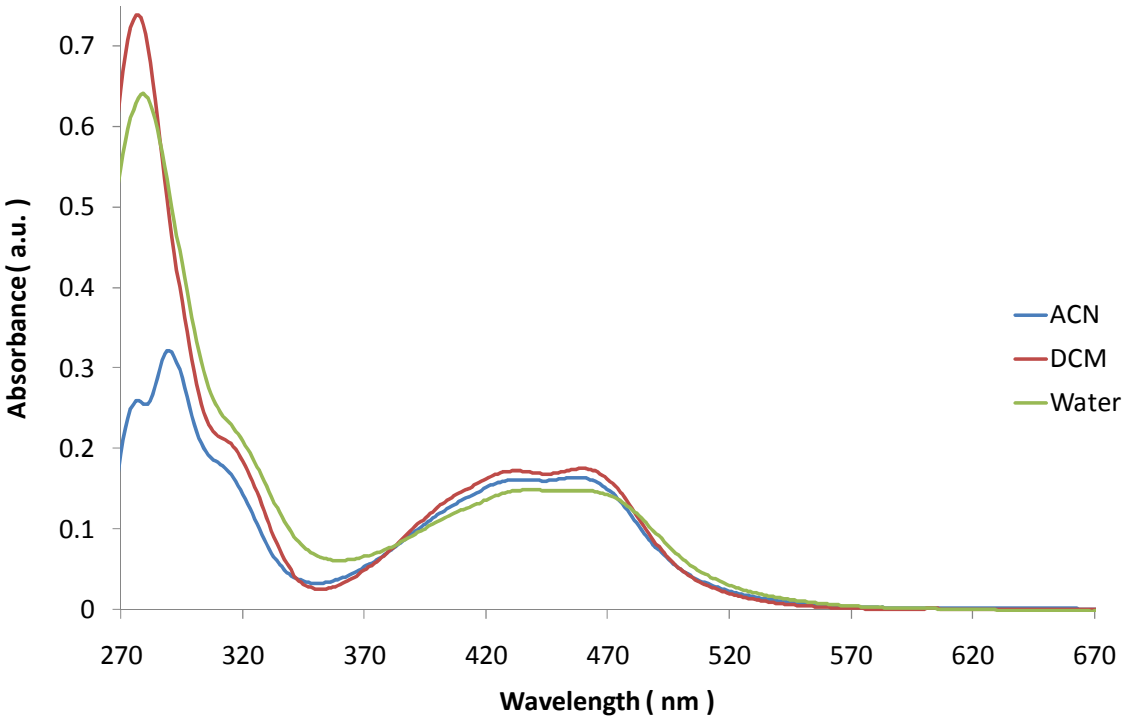


**Figure 2.3.3.3:** Absorption spectra of Ru11D in ACN, DCM and $H_2O$. Concentration of Ru11D is 5 x $10^{-6}$ M in all solvents. For the results in water are in 99 : 1 (v/v) water : acetonitrile.

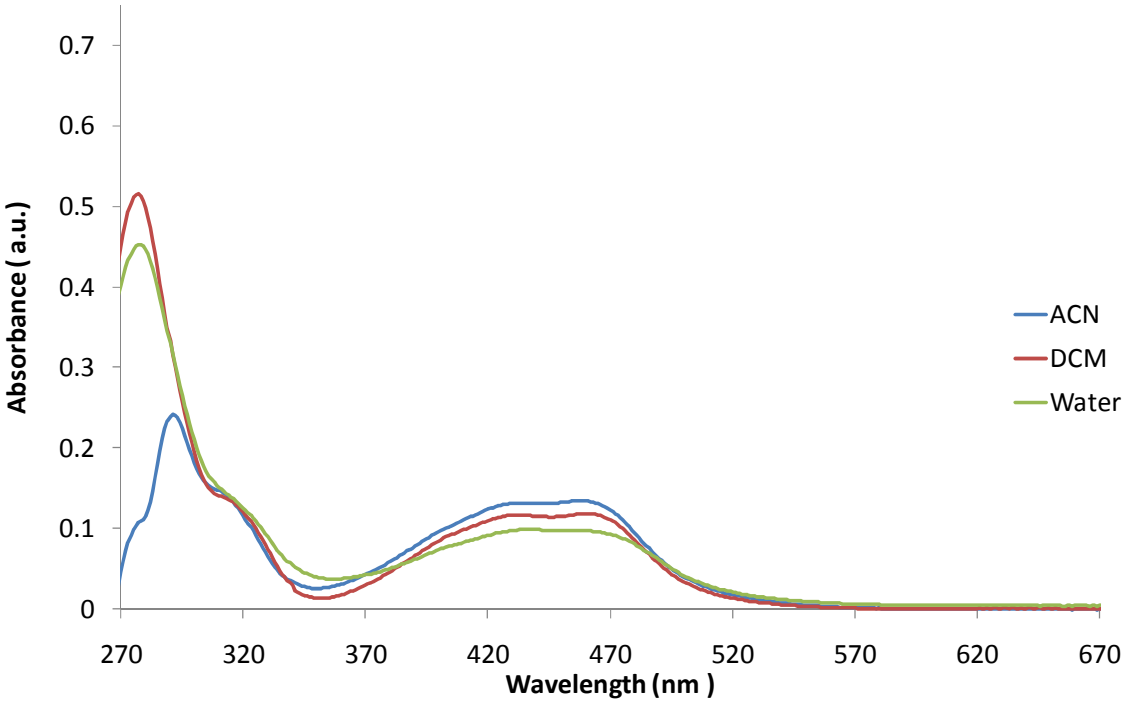


**Figure 2.3.3.4:** Absorption spectra of Ru16D in ACN, DCM and $H_2O$. Concentration of Ru16D is 5 x $10^{-6}$ M in all solvents. For the results in water are in 99 : 1 (v/v) water : acetonitrile.

A comparison of the emission spectra of the RuxD complexes in DCM, acetonitrile and water are provided in Figs 2.3.3.6 – 2.3.3.9. The emission lifetimes of the RuxD complexes in these solvents can be found in Table 2.3. All values are quoted for aerated solvent. The influence of solvent on emission is considerably greater than absorption. The $\lambda_{max}$ of emission for the RuxD complexes in DCM is blue shifted to 596 nm compared to 608 nm in acetonitrile. The quantum yield of emission increases significantly in DCM compared to acetonitrile. The emission lifetime also increases remarkably in DCM compared acetonitrile, ~640 ns in DCM compared to ~180 ns in acetonitrile for all RuxD. These large changes in the emission properties of RuxD complexes in different solvents is due to stabilisation of the excited state by solvent reorganisation. Promotion of an electron from the metal orbitals to the ligand orbitals to form the excited state creates a large change in dipole with the excited state species in the case of RuxD being far more polar than the ground state complex. In a polar solvent such as acetonitrile the solvent will reorganise around the excited state within the excited states lifetime and stabilise it lowering it's energy leading to a red shifed emission. For a non-polar solvent such as DCM no re-organisation and stabilisation of the excited state will occur leading to higher energy emission. The energy gap law states that ln $k_{nr}$ will decrease linearly as the energy released through non-radiative decay increases[30]. This may account for the large increase in emission quantum yield and lifetime of RuxD in DCM compared to acetonitrile due to the increase in energy between the ground state and emitting excited state. This solvatochromic effect was also seen in $[Ru(bpy)_n(dppp2)_{3-n}]^{2+}$ reported by Turro *et al*. which also has an extended π-system on the dppp2 ligands where the excited state is localized, similar to the extended π-system on the dpp ligands of RuxD[29]. For example $[Ru(bpy)_2(dppp2)]^{2+}$ exhibits a blue shift in emission of about 100 nm and an increase in luminescence lifetime from 35 ns to 273 ns when dissolved in DCM compared to when dissolved in acetonitrile. The structure of the dppp2 ligand is given in Fig 2.3.3.5 below.

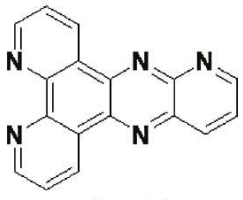

dppp2

**Fig 2.3.3.5:** Structure of dppp2 ligand. Image reproduced from Ref[29].

The emission spectrum of the RuxD complex in water changes significantly, where it exhibits a very broad emission spectrum with a red shifted $\lambda_{max}$ compared to DCM and acetonitrile. The formation of RuxD micellular bilayers would mean that the environment experienced by the RuxD complex in these bilayers would vary in polarity leading to this difference in emission $\lambda_{max}$. Interestingly the emission lifetime for all RuxD complexes in water is biexpontential consisting of a long lifetime component of about 800 ns and a short lifetime component of about 130 ns. The short lifetime component has a fractional intensity of about 10 % and is attributed to fully solvated RuxD. The short lifetime of the free coplex in water is attributed to the highly polar water very efficiently stabilising the RuxD excited state and efficiently promoting non-radiative pathways due to high frequency H-O oscillations. The long lifetime component has a fractional intensity of about 90 % and is attributed to RuxD in vesicle bilayers, *vide infra*. The less polar environment of the bilayer system, its rigidity and the extra protection this provides from oxygen quenching is responsible for the longer lived emission lifetime. Biexponential lifetimes of ruthenium complexes in micellular environments has been reported on in the literature, for example De Cola *et al*. who reported the biexponential lifetimes of dialkyl ruthenium complexes that form micelles which have a long and short emission lifetime component was attributed to micellular and solvated ruthenium complex respectively[31]. A bilayer vesicle structure of the RuxD aggregates in water is the most likely due to the presence of a biexponential lifetime. The multi-vesicular structures of ruthenium complexes with long alkyl chains reported by Fuhrhop *et al*. displayed tri-exponential lifetimes[32].

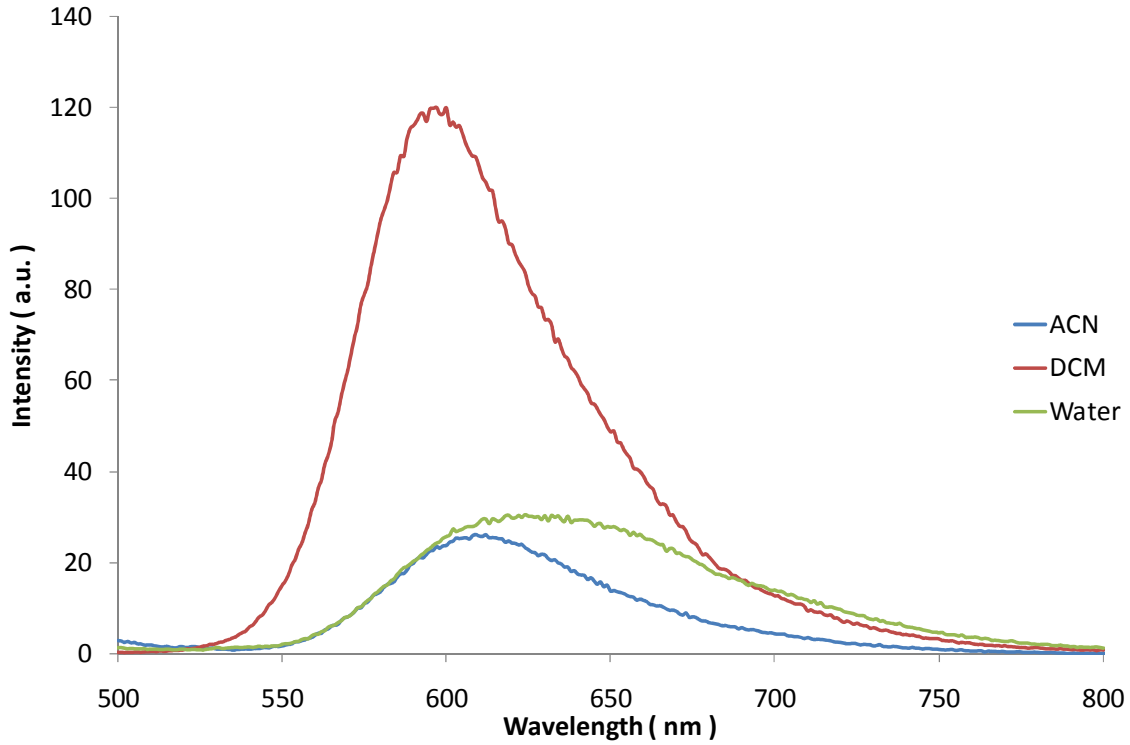


**Figure 2.3.3.6:** Emission spectra of Ru6D in ACN, DCM and $H_2O$. Concentration of Ru6D is 5 x $10^{-6}$ M in all solvents. An excitation wavelenght was 454 nm. For the results in water are in 99 : 1 (v/v) water : acetonitrile.

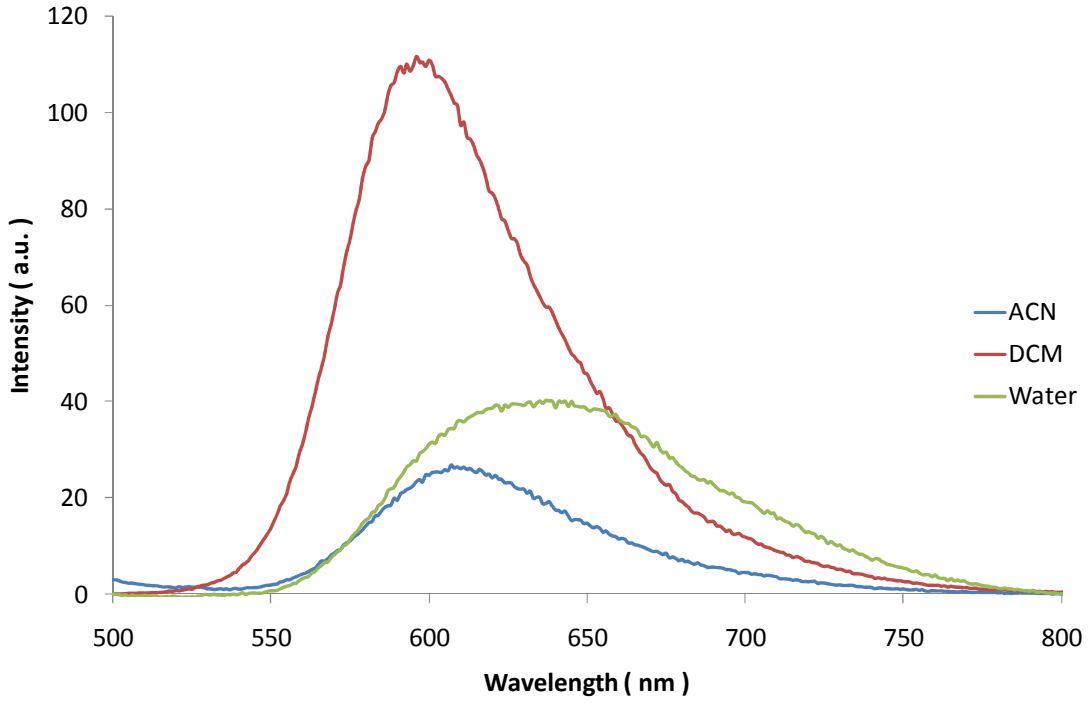


**Figure 2.3.3.7:** Emission spectra of Ru8D in ACN, DCM and $H_2O$. Concentration of Ru8D is 5 x $10^{-6}$ M in all solvents. An excitation wavelenght was 454 nm. For the results in water are in 99 : 1 (v/v) water : acetonitrile.

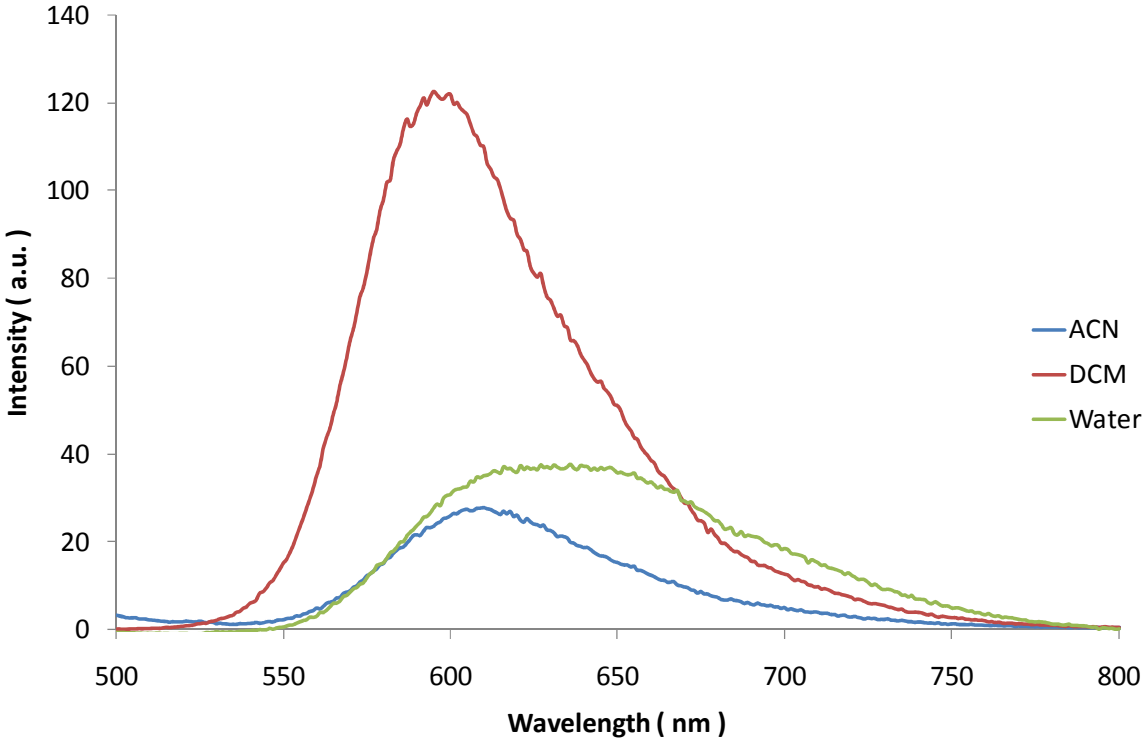


**Figure 2.3.3.8:** Emission spectra of Ru11D in ACN, DCM and $H_2O$. Concentration of Ru11D is 5 x $10^{-6}$ M in all solvents. An excitation wavelenght was 454 nm. For the results in water are in 99 : 1 (v/v) water : acetonitrile.

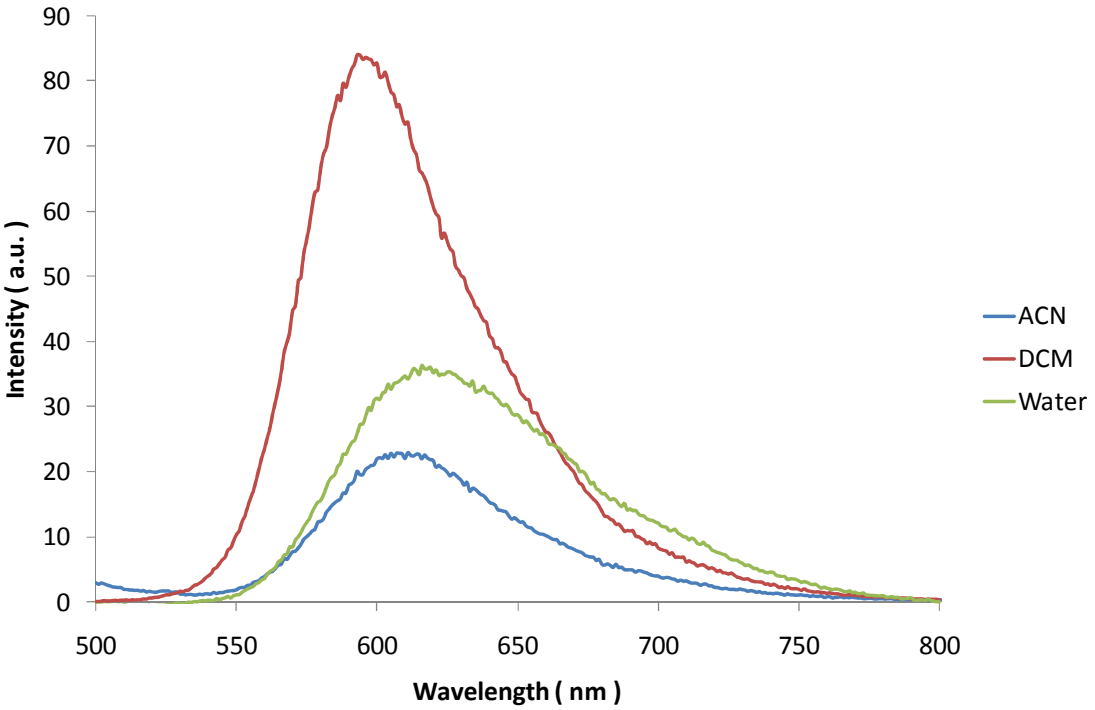


**Figure 2.3.3.9:** Emission spectra of Ru16D in ACN, DCM and $H_2O$. Concentration of Ru16D is 5 x $10^{-6}$ M in all solvents. An excitation wavelenght was 454 nm. For the results in water are in 99 : 1 (v/v) water : acetonitrile.

| | Abs $\lambda_{max}$ (nm) | | | Emission $\lambda_{max}$ (nm) | | |
|---|---|---|---|---|---|---|
| | ACN | DCM | $H_2O$ | ACN | DCM | $H_2O$ |
| Ru6D | 454 | 459 | 438 | 608 | 596 | 628 |
| Ru8D | 454 | 459 | 438 | 608 | 596 | 636 |
| Ru11D | 454 | 459 | 438 | 608 | 596 | 636 |
| Ru16D | 454 | 459 | 438 | 608 | 596 | 618 |

| | Lifetime (ns) Fractional intensities in brackets. | | | |
|---|---|---|---|---|
| | ACN | DCM | $H_2O$ (biexponential) | |
| Ru6D | 1.75E-07 ± 2.2E-08 | 6.46E-07 ± 3.8 E-09 | 7.38E-07 ± 2.3E-09 (91 %) | 1.05E-07 ± 1E-09 (9 %) |
| Ru8D | 1.73E-07 ± 1E-08 | 6.39E-07 ± 8E-09 | 8.29E-07 ± 2.5E-10 (90 %) | 1.35E-07 ± 2.5E-10 (10 %) |
| Ru11D | 1.82E-07 ± 2.3E-08 | 6.42E-07 ± 4.8E-09 | 8.06E-07 ± 1E-09 (89 %) | 1.37E-07 ± 1.8E-09 (11 %) |
| Ru16D | 1.85E-07 ± 2.6E-08 | 6.39E-07 ± 1.28E-08 | 9.19E-07 ± 7.5E-09 (90 %) | 1.38E-07 ± 4E-09 (10 %) |

**Table 2.3:** Photophysical properties of the RuxD complexes in various solvents in aerated conditions at 298 K. In all cases the concentration of RuxD was 5 x $10^{-6}$ M.

The formation of micelles for the two extremes of alkyl chain length studied, Ru6D and Ru16D, was confirmed using dynamic light scatter (DLS), the results of which are tabulated in Table 2.4. Aqueous 5 x $10^{-6}$ M solutions of Ru6D and Ru16D in $H_2O$ gave a strong scattering signal indicating the formation of large particles while solutions of Ru6D and Ru16D in acetonitrile and dichloromethane gave no scattering signal. DLS measurements showed that the diameter of the micelles was 189 nm and 135 nm for 5 x $10^{-6}$ M aqueous solutions of Ru16D and Ru6D respectively. Polydispersity indexes were close to 0.1 indicating fairly monodisperse size distributions of micelles. The large size of these structures confirms that they are bilayer vesicles and not micellular. Micellular structures would typically have a diameter a little greater than twice the length of the complex. The size of the Ru6D and Ru16D structures have a diameter far greater than twice the length of their respective structures. A representation of the size difference between a micelle and a bilayer

vesicle is displayed in Fig 2.3.3.10. The small size of these bilayer vesicles means they could not be imaged by microscopy.

| | Diameter (nm) | Polydispersity Index |
|---|---|---|
| Ru16D | 188.9 ± 1.4 | 0.125 ± 0.016 |
| Ru6D | 135.3 ± 0.8 | 0.122 ± 0.023 |

**Table 2.4:** Diameter and polydispersity index of Ru6D and Ru16D micelles in aqueous solution. Solutions of Ru6D and Ru16D were 5 x $10^{-6}$ M in $H_2O$.

(a)

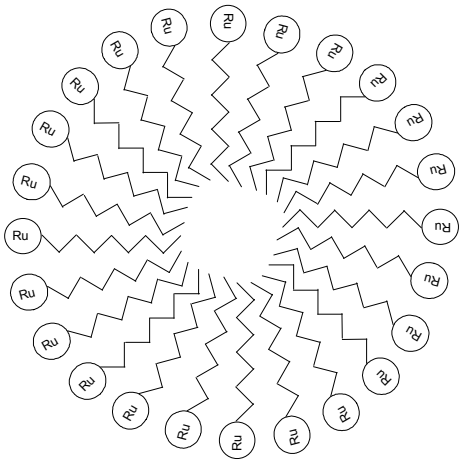


(b)

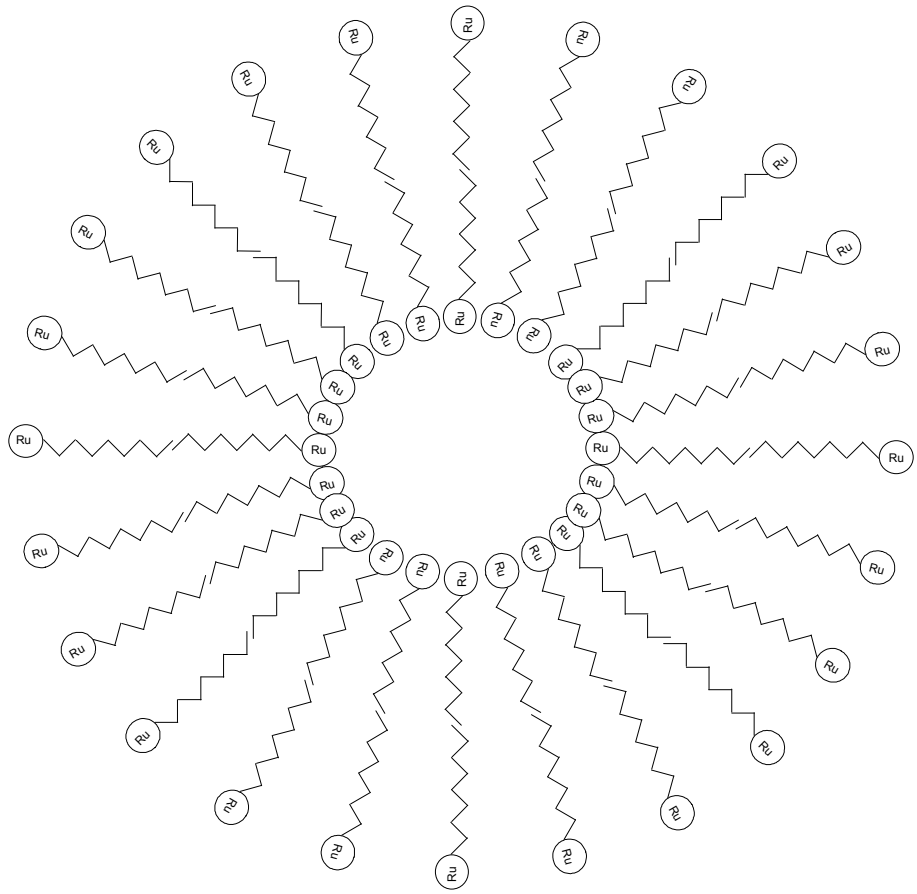


**Figure 2.3.3.10:** Graphical representation of the size difference between a micelle and a bilayer vesicle, where (a) represents a micelle and (b) represents a bilayer vesicle.

### *2.3.4 Resonance Raman Spectrocopy*

Resonance Raman is a very useful technique that can be used in a mixed ligand system to assign which ligands are involved in the MLCT transition, which can lead to insights into which ligands the emissive state is likely to be localised on. In mixed ligand systems exciting into the Ru$\rightarrow\pi^*$(ligand) transition will give a resonance enhancement up to four orders of magnitude of the symmetrical stretching modes of the ligand where the excited state is localised. Fig 2.3.4.1 and 2.3.4.2 show the resonance Raman spectra of the RuxD complexes in KBR discs excited and in solution at 458 nm. 458 nm excitation was provided by an Argon ion laser source. As expected no differece in band postion or intensity was found between the RuxD complexes. Table 2.5 details the Raman modes present in the resonance Raman spectra of RuxD in solution and as a solid KBr disc with resonance Raman modes of $[Ru(phen)_3]^{2+}$ and $[Ru(dpp)_3]^{2+}$ as a comparison. The vibration assignment was estimated by comparison of the data with normal mode coordinate analysis of $[Ru(bpy)_3]^{2+}$.[33] The resonance Raman spectrum shows large enhanced modes characteristic of both the phen and dpp ligands[18, 25, 34]. These results indicate that the origin of the observed MLCT optical transition is due to both Ru $\rightarrow$ dpp and Ru $\rightarrow$ phen transitions. Both transtitions are resonant with the MLCT $\lambda_{max}$ at 458 nm.

Further evidence that both the phen and dpp ligands are responsible for the MLCT absorption was revealed when comparing the resonance Raman spectra of the RuxD complexes at 458 nm and the Raman spectra at 785 nm. From comparison with the resonance Raman spectra of $[Ru(dpp)_3]^{2+}$ and $[Ru(phen)_3]^{2+}$ the Raman bands at 1582, 1402 and 1265 $cm^{-1}$ are exclusive to 1,10-phenanthroline while the bands at 1556, 1516, 1442 and 1315 $cm^{-1}$ are exclusive to 4,7-diphenyl-1,10-phenanthroline. Comparison of the non-resonance Raman spectra of RuxD complexes at 785 nm and the resonance Raman spectra at 458 nm shows that both the exclusive phenanthroline and the exclusive diphenyl phenanthroline Raman bands are enhanced in the resonance Raman spectrum with the exception of the band at 1315 $cm^{-1}$ which remains weak in both the resonance and non resonance Raman spectra. A comparison of the resonance Raman and nonresonance Raman of Ru6D is shown in Fig 2.3.4.3.

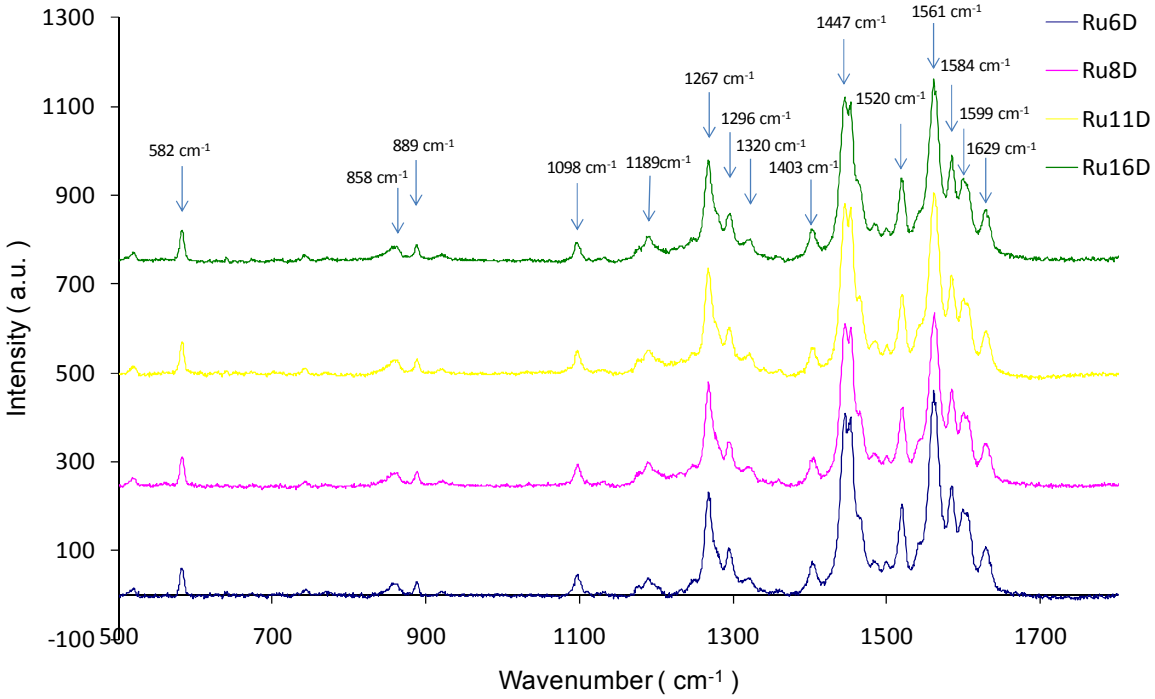


**Figure 2.3.4.1** Resonance Raman spectra of (a) Ru6D, (b) Ru8D, (c) Ru11D and (d) Ru16D. All samples were 10% w/w in KBr discs. An excitation wavelength of 458 nm was used.

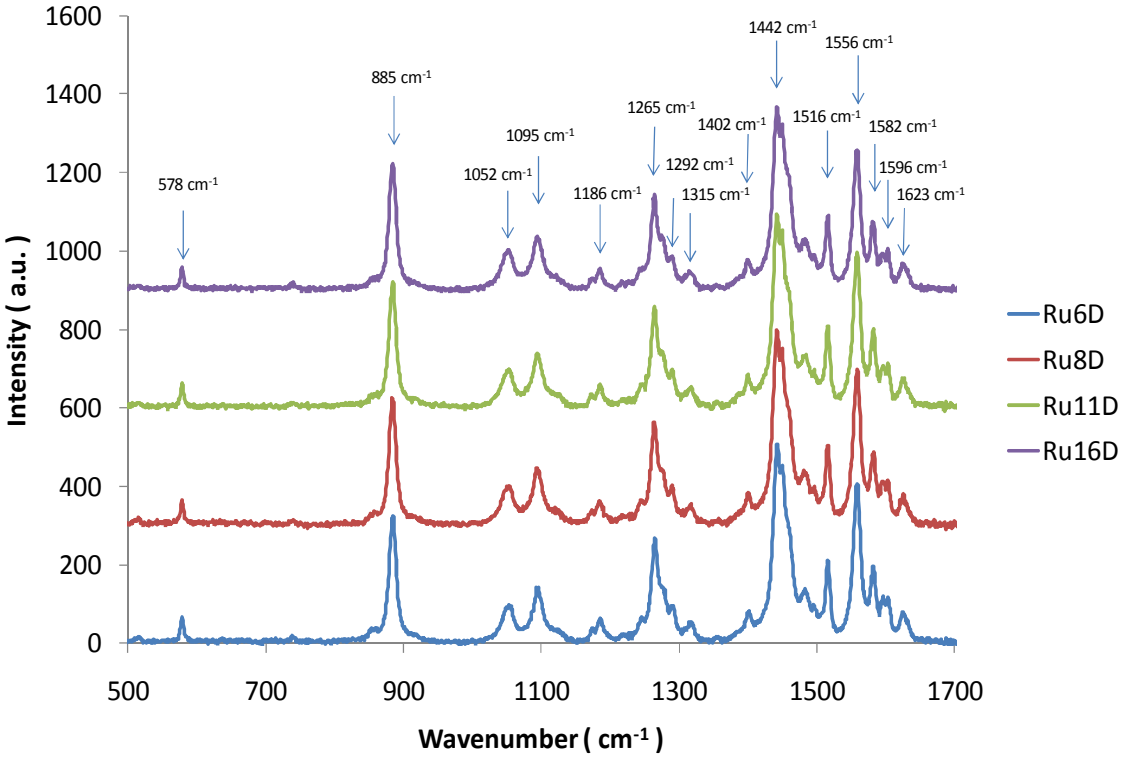


**Figure 2.3.4.2:** Solution phase resonance Raman of RuxD complexes. Samples were were $5e^{-5}$ M in ACN and excited at 457 nm.

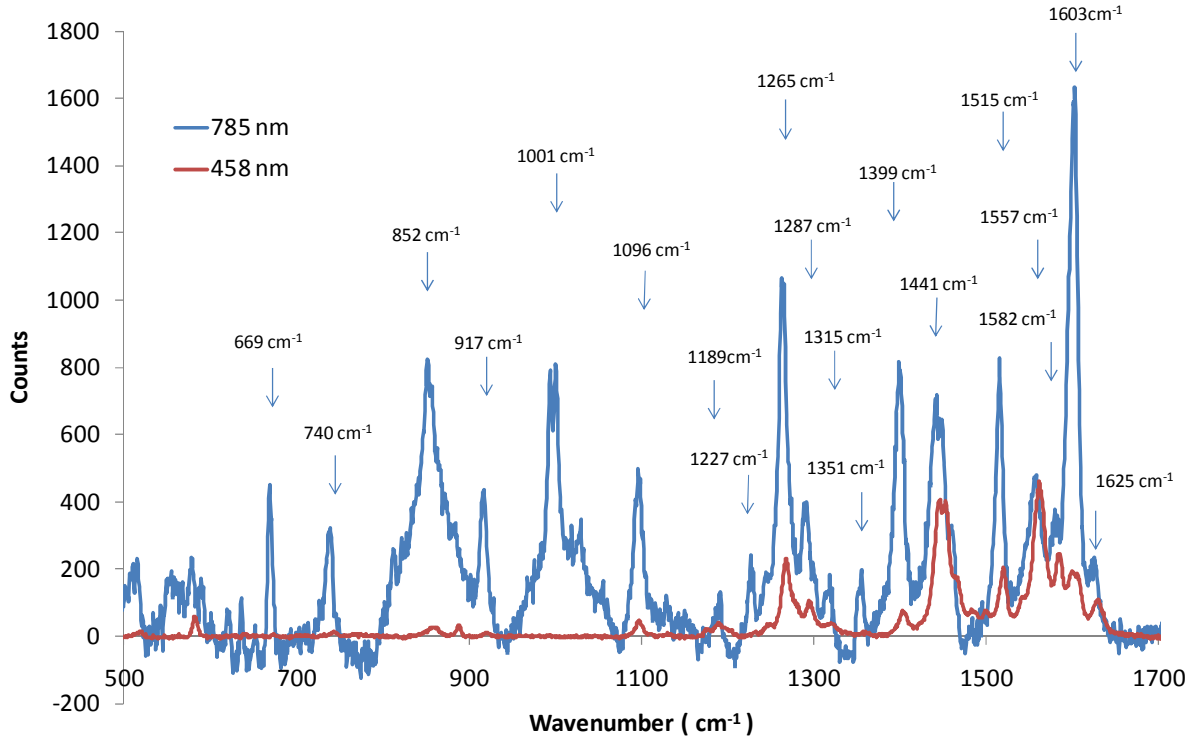


**Figure 2.3.4.3:** Raman spectra of Ru6D. All samples were 10% w/w in KBr discs. The red trace represents a resonance Raman spectrum of Ru6D excited at 458 nm while the blue trace represents a Raman spectrum of Ru6D at 785 nm excitation.

| RuxD @458 nm | | Ru6D @785 nm [a] ( $cm^{-1}$ ) | $[Ru(dpp)_3]^{2+}$ ( $cm^{-1}$ ) [b] | $[Ru(phen)_3]^{2+}$ ( $cm^{-1}$ ) [b] | Vibration assignment |
|---|---|---|---|---|---|
| Solid ( $cm^{-1}$ ) | Solution ( $cm^{-1}$ ) | | | | |
| 1629 | 1625 | 1625 | 1626 | 1629 | C-C ring stretch |
| 1599 | 1596 | 1603 | 1594 | 1584 | C-C ring stretch |
| 1584 | 1582 | 1582 | | 1579 | C-C ring stretch |
| 1561 | 1556 | 1557 | 1556 | | C-C ring stretch |
| 1520 | 1516 | 1515 | | 1515 | C-C ring stretch |
| 1447 | 1442 | 1441 | 1440 | 1451 | C-C ring stretch |
| | | | | 1435 | |
| 1403 | 1402 | 1399 | 1404 | | C-H bend |
| | | 1351 | | | |
| 1320 | 1315 | 1315 | | 1312 | C-H bend |
| 1296 | 1292 | 1287 | 1288 | 1291 | Ring stretch |
| 1267 | 1265 | 1265 | 1264 | | Ring stretch |
| | | 1227 | | | |
| 1189 | 1186 | 1189 | | | C-H bend |
| | | | | 1145 | |
| 1098 | 1095 | 1096 | | | C-H bend |
| | 1052 | | | | Ring breathing |
| | | 1001 | | | |
| 889 | 885 | 917 | 889 | | Ring bend |
| 858 | | 852 | | | Ring bend |
| | | 740 | | | |
| 578 | 582 | 669 | | | Ring bend |

**Table 2.5:** Table detailing the wavenumber assignments for the Resonance Raman bands of the RuxD series of complexes. An excitation wavelenght of 458 nm from an argon ion laser was used with the exception of [a] where a 785 nm excitation from a diode laser was used. [b] Resonance Raman bands for $[Ru(dpp)_3]^{2+}$ and $[Ru(phen)_3]^{2+}$ are shown for comparison and are taken from Ref[34] where an excitation wavelength of 354 nm and 441.6 nm were used.

### *2.3.5 Solution Phase Electrochemistry*

In order to understand the molecular orbital structure of the RuxD complexes and for comparison with the interfacial layers of RuxD (see Chapter 3) the solution phase electrochemistry of the RuxD coplexes was studied by cyclic voltammetry. Table 2.6 summarises the solution phase electrochemical properties of the four RuxD complexes. Solution phase CVs for the RuxD complexes are shown in Fig. 2.3.5.1 – 2.3.5.4. All solution phase electrochemistry was carried out with 1 mM solutions of complex in ACN with 0.1 mM $TBATBF_4$ as the supporting electrolyte and a glassy carbon electrode as the working electrode. All potentials are quoted vs. $Ag/AgNO_3$ electrode. For all four complexes fully reversible one electron oxidation with an $E_{1/2}$ value of +0.92 V is observed. $\Delta E_p$ for the $Ru^{2+/3+}$ redox process is about 83 mV, quite close to 59 mV expected for an ideal solution phase fully reversible redox process. This is attributed to the $Ru^{2+/3+}$ couple. A ligand based, reversible reduction is observed with an $E_{1/2}$ value of ~ -1.7 V. This ligand based reduction seems to result from 3 separate and poorly resolved one electron ligand reductions since the integrated area under this reduction is three times the size of the integrated area of the metal based oxidation which is a one electron process.

The potential of the $Ru^{2+/3+}$ redox couple of the complexes RuxD at +0.92 V is more positive than the $Ru^{2+/3+}$ redox couple of $[Ru(bpy)_3]^{2+}$, which appears at +0.85 V in ACN using the ferrocene Fc+/Fc couple as a standard[16]. This is as expected for a ruthenium polypyridyl complex with ligands with greater π-acceptor properties than bpy. Again the slightly more positive ligand reduction at -1.7 V compared to the ligand reduction at -1.76 V of the first ligand reduction of $[Ru(bpy)_3]^{2+}$ can be explained by the π-acceptor properties of the dpp and x-ATAP ligands. The nature of the ligands surrounding the metal center greatly affects the redox properties of the complex. Ligands with strong π-acceptor properties will increase electron density at the metal centre, increasing the energy of the Ru ($t_2g$) orbital making the metal centre harder to oxidise and decreasing the energy required to reduce the ligands. This is consistent with the spectroscopy results that show photophysical behavior consistent with a ruthenium polypyridyl complex with π-acceptor ligands. An electron withdrawing group on the ligand, such as the amide bond in the x-ATAP ligands, can have an effect on the electrochemistry of the complex. Francis, Hogan, *et al*. showed that the effect of an electron withdrawing amide and carboxylate functionality on a bpy ligand can

significantly shift the first ligand reduction and the $Ru^{2+/3+}$ redox couple to more positive potentials compared to $[Ru(bpy)_3]^{2+}$ [35]. A large irreversible peak, which is very narrow, appears in the CVs of all RuxD complexes at -2.1V. Based on its shape it is thought that this is an adsorption peak as a result of the RuxD complex adsorbing to the carbon electrode surface. This is not unexpected as these complexes are surface active and lay flat on the surface, as demonstrated in Chapter 3, due to ligand interaction with the metal surface. Adsorption of $[Ru(bpy)_3]^{2+}$ has been demonstrated by Sereno *et al.*[36] on a glassy carbon electrode that had been modified electrochemically by cycling the electrode from -500 and 1860 mV in 1M $H_2SO_4$. It was believed that adsorption was due to π-stacking of the bipyridine ligands and the aromatic ribbon carbons in the electrode surface. It is believe that the same π-stacking effect between the ligands of RuxD and the aromatic ribbon carbons are what cause absorption of the RuxD complexes to the carbon electrode surface.

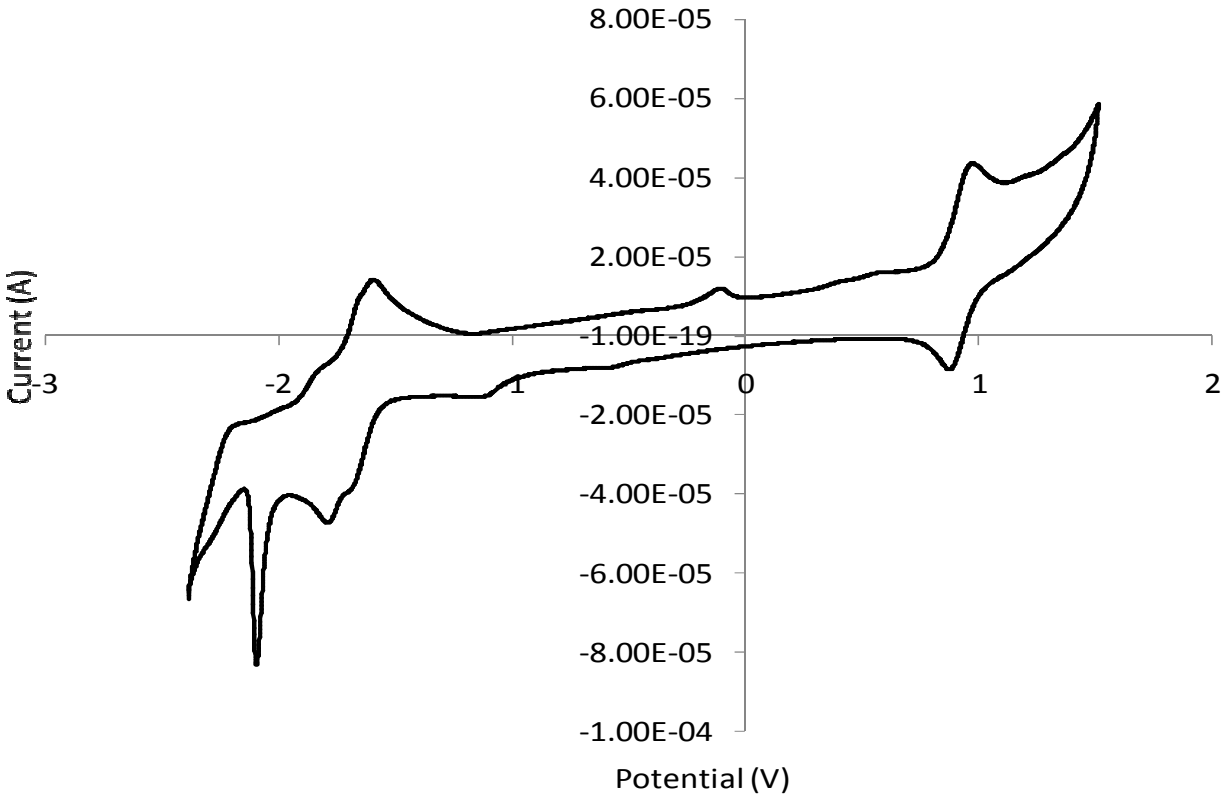


**Figure 2.3.5.1:** Cyclic Voltammagram of Ru6D in 0.1M TBATBF acetonitrile solution. A scan rate of 0.1 V/s was used. A glassy carbon working electrode was employed with a platinum wire as the counter electrode and a $Ag/AgNO_3$ reference electrode.

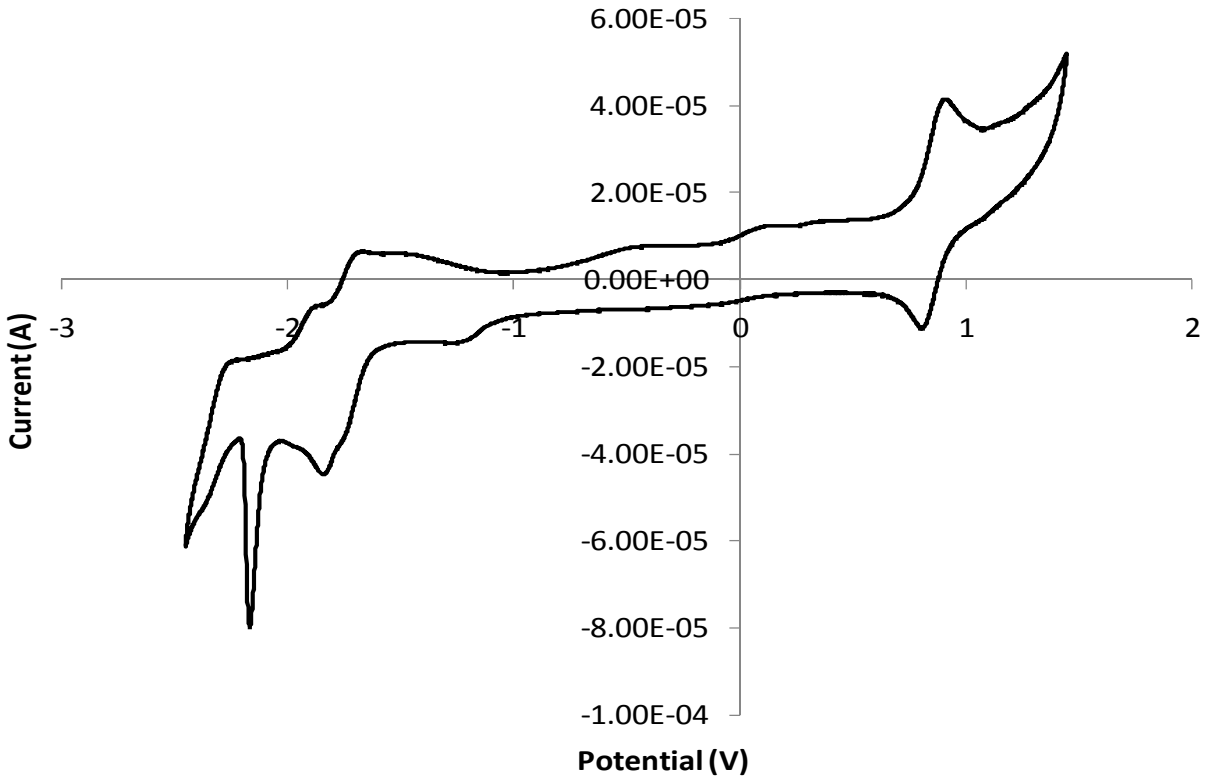


**Figure 2.3.5.2:** Cyclic Voltammagram of Ru8D in 0.1M TBATBF acetonitrile solution. A scan rate of 0.1 V/s was used. A glassy carbon working electrode was employed with a platinum wire as the counter electrode and a $Ag/AgNO_3$ reference electrode.

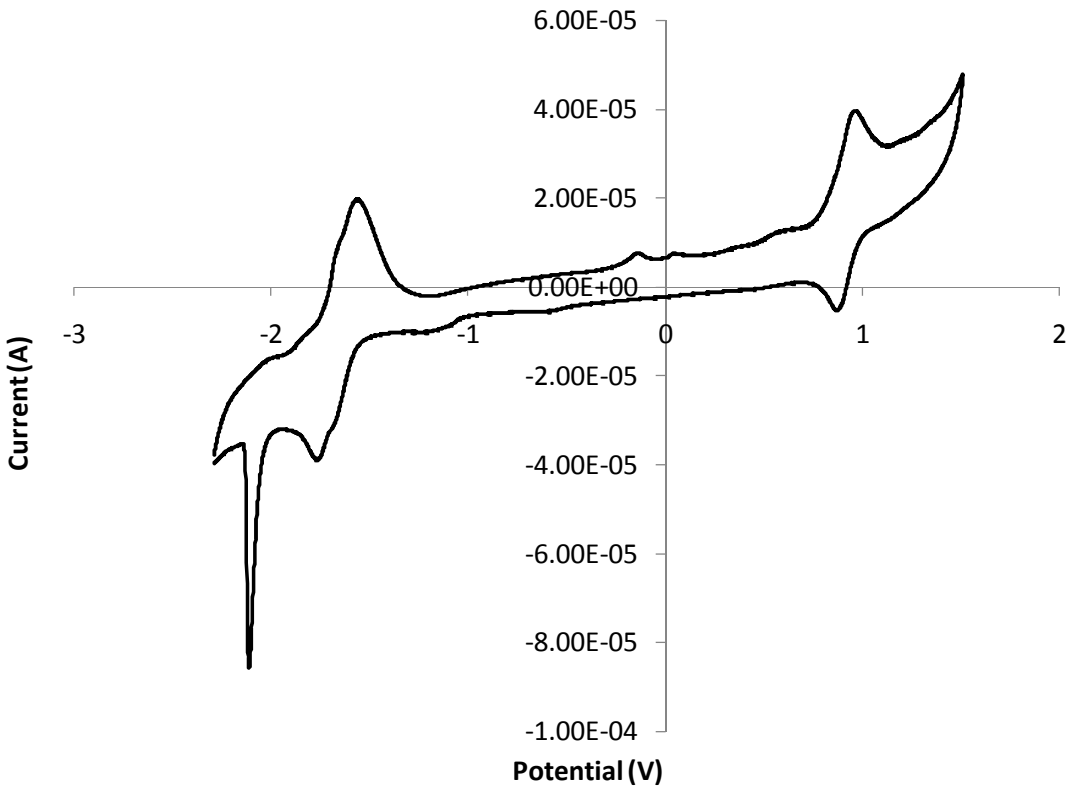


**Figure 2.3.5.3:** Cyclic Voltammagram of Ru11D in 0.1M TBATBF acetonitrile solution. A scan rate of 0.1 V/s was used. A glassy carbon working electrode was employed with a platinum wire as the counter electrode and a $Ag/AgNO_3$ reference electrode.

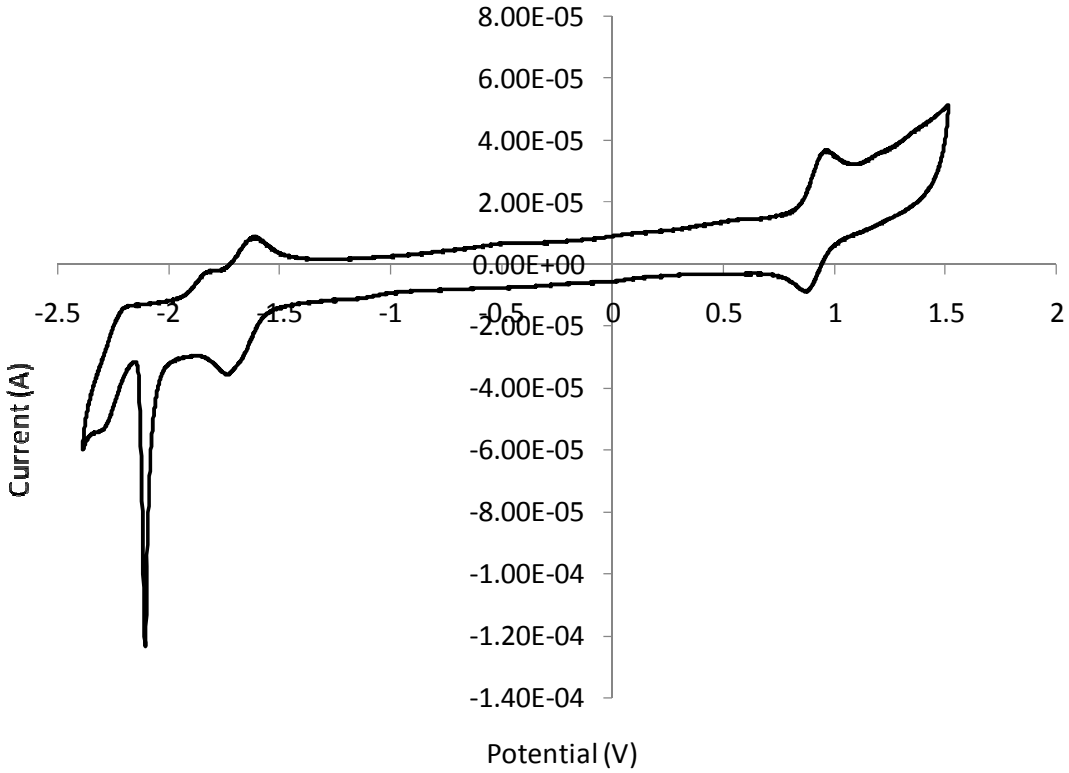


**Figure 2.3.5.4:** Cyclic Voltammagram of Ru16D in 0.1M TBATBF acetonitrile solution. A scan rate of 0.1 V/s was used. A glassy carbon working electrode was employed with a platinum wire as the counter electrode and a $Ag/AgNO_3$ reference electrode.

A plot of $i_p$ vs. (scan rate)$^{1/2}$ is shown in Fig 2.3.5.5. All four RuxD complexes give linear $i_p$ vs. $v^{1/2}$ relationships with $R^2$ values exceeding 99.7%. The linear sweep voltammetry relationship for a reversible system is;

$$i_p = (2.69 \times 10^5) n^{3/2} A C_O^* D_O^{1/2} v^{1/2}$$

where $i_p$ is the peak current in A, n is the number of electrons involved in the redox process, A is the area of the electrode in $cm^2$, $C_o^*$ is the bulk concentration in $mol/cm^3$, $D_o$ is the diffusion coefficient in $cm^2/s$ and $v$ is the scan rate in V/s. A plot of $i_p$ vs. $v^{1/2}$ should give a linear plot if in good agreement with reversible solution phase electrochemistry[37]. The peak splitting of the metal centred redox shows fully reversible solution phase behavior. The area under the oxidation and reduction is identical and the peak splitting, $\Delta E_p$, is about 0.08 V,

which is in good agreement with the peak splitting calculated for a fully reversible solution phase system of 0.059 V[37].

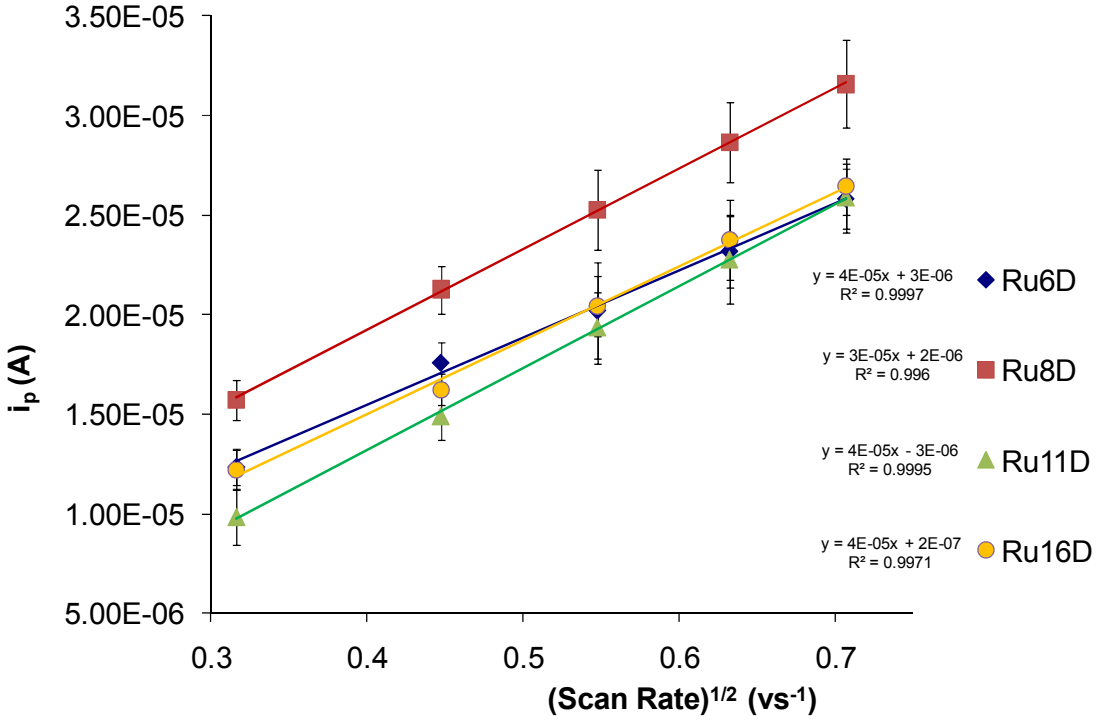


**Figure 2.3.5.5:** Scan rate dependence of RuxD complexes in solution. Electrochemistry was carried out with 1 mM solutions of complex in ACN with 0.1 mM $TBATBF_4$ as the supporting electrolyte and a glassy carbon electrode as the working electrode. All potentials are vs. $Ag/AgNO_3$ electrode.

The equation for linear sweep voltammetry for a reversible system relationship above was used to calculate the diffusion coefficients of the RuxD complexes in solution. When rearranged this equation becomes:

$$D_o^{1/2} = \frac{i_p}{(2.69 \times 10^5) n^{3/2} C_o^* v^{1/2}}$$

which simplifies to;

$$D_o^{1/2} = \frac{m}{(2.69 \times 10^5) n^{3/2} C_o^*}$$

where m is the slope of the $i_p$ vs. $v^{1/2}$ plot. The diffusion coefficients are given in Table 2.5 are slightly slower compared to $[Ru(bpy)_3]^{2+}$, which has a $D_o$ of 5.6 x $10^{-6}$ $cm^2s^{-1}$, due to the bulkier nature of the complexes resulting in slower migration to the electrode surface[38]. Similar complexes with pendant alkyl chain groups were reported by Francis, Hogan, *et al*. which had $D_o$ values similar to but lower than $[Ru(bpy)_3]^{2+}$ [35]. No trend within experimental error was observed with increasing alkyl chain length.

The standard rate constants for electron transfer were calculated for all RuxD complexes using the method of Nicholson[39], which relates the standard rate constant with the peak splitting of a redox process. Nicholson gives the relationship;

$$\psi = \gamma^{\alpha} k / \sqrt{\pi a D_o}$$

where

$$a = nFv/RT$$

and $$\gamma = \left(\frac{D_o}{D_R}\right)^{1/2}$$

For a fully reversible redox reaction $\gamma$ is simplified to 1. The equation is then simplified to;

$$k = \psi / \sqrt{\pi (nFv/RT) D_o}$$

where *k* is the standard rate constant for electron transfer, n is the number of electrons involved in the redox process, *v* is the scan rate in V/s and $D_o$ is the diffusion coefficient. $\psi$ is a term that is variable with $\Delta E_p$ and has been calculated numerically for various values of $\Delta E_p$ in Nicholsons publication[39]. k values for the RuxD complexes were about $7e^{-3}$ which is expected for a ruthenium polypyridyl complex complex with a $\Delta E_p$ of about 0.8 [40]V. The

standard rate constant for electron transfer is lower for RuxD than $[Ru(bpy)_3]^{2+}$, which is 2.9 x $10^{-3}$, but within the same order of magnitude.

| | $E_{1/2}{}^{red}{}_{ligand}$ | $E_{1/2}{}^{ox}{}_{Ru}{}^{2+/3+}$ | $\Delta E_p{}^{ox}{}_{Ru}{}^{2+/3+}$ | $D_o$ ($cm^2\ s^{-1}$) | k ($cm.s^{-1}$) |
|---|---|---|---|---|---|
| Ru6D | -1.7 V | +0.92 V | 0.08 V | 3.14E-06 ± 2.4E-07 | 0.0062 ± 4.8E-04 |
| Ru8D | -1.7 V | +0.92 V | 0.085 V | 4.54E-06 ± 3.1E-07 | 0.0075 ± 5.1E-04 |
| Ru11D | -1.67 V | +0.92 V | 0.081 V | 4.69E-06 ± 4.5E-07 | 0.0076 ± 7.2E-04 |
| Ru16D | -1.67 V | +0.92 V | 0.081 V | 3.8E-06 ± 2.6E-07 | 0.0068 ± 4.7E-04 |

**Table 2.6:** Solution phase electrochemistry data of RuxD complexes with diffusion coefficients and electron transfer rate constants. All solution phase electrochemistry was carried out with 1 mM solutions of complex in ACN with 0.1 mM $TBATBF_4$ as the supporting electrolyte and a glassy carbon electrode. All potentials are vs. $Ag/AgNO_3$ electrode.

## 2.4 Conclusions

The synthesis and structural characterization of a new family of 4 ligands, x-ATAP, has been reported in this chapter. The synthesis and structural, photophysical and electrochemical characterization of the family of four ruthenium polypyridyl complexes RuxD, with two dpp ligands and an x-ATAP ligand are also reported in this chapter. The addition of a ligand functionalised with an acetylthio terminated alkyl chain renders the complexes surface active and allows interaction with phospholipid bilayers.

Photophysical performance of the RuxD complexes was weaker than comparable ruthenium polypyridyl complexes containing dpp and phen ligands at ambient temperature under aerated and deaerated conditions. Luminescent lifetimes and quantum yields were only slightly better than $[Ru(bpy)_3]^{2+}$ and significantly smaller than complexes with similar ligands $[Ru(dpp)_2(phen)]^{2+}$. Photophysical measurements at 77K in glassy 4:1 butyronitrile : propionitrile showed an increase in the quantum yield and luminescent lifetime of the complex compareable to similar ruthenium complexes containing dpp and phen ligands. The addition of the alkyl chain to the phenanthroline ligand seems to affect the excited state of the complex making it more sensitive to thermal deactivation and $O_2$ quenching under ambient conditions than similar ruthenium polypyridyl complexes as a result of the amide bond on the x-ATAP ligand. Resonance Raman spectra indicates that the excited state exists on both the x-ATAP and dpp ligands. Solution phase cyclic voltammetry revealed that the RuxD complexes had comparable but smaller diffusion constants and slower rates of electron transfer than comparable ruthenium complexes such as $[Ru(bpy)_3]^{2+}$ due to their bulkier size. It was also revealed that these complexes adsorp to the surface of glassy carbon electrodes which had implications for the interfacial surface electrochemistry of Chapter 3.

Finally, it was shown that the RuxD series of complexes spontaneously forms bilayer vesicles when solvated in water. These vesicles had a size between 130 – 190 nm depending on the RuxD complex. The luminescence lifetimes of these complexes increased to about 800-900 ns when in vesicle form due to the rigidity of the environment. These results demonstrate the lipophilic nature of the complexes. This lipophilicity and the sensitivity of the luminescence lifetime of the RuxD complexes to rigid environments such as lipid bilayers has implications in their suitability for use as luminescence cell imaging agents.

# References


[1] Haque, S.A.; Tachibane, Y.; Willis, R.L.; Moser, J.E.; Gratzel, M.; Klug, D.R. and Durrant, J.R.; *J. Phys. Chem.*, 104, **2000**, 538-547

[2] Kalyanasundaram, K. and Gratzel, M.; *Coord. Chem. Rev.*, 77, **1998**, 347-414

[3] Lombard, J.; Boulaouche, R.; Jose, D. A.; Chauvin, J.; Collomb, M. N. and Deronizer, A.; *inorg. Chim. Acta.*, 363, **2010**, 234-242

[4] Santoni, M. P.; Medlycott, E. A.; Hanan, G. S.; Hasenknopf, B.; Proust, A.; Nastasi, F.; Campagna, S.; Chioboli, C.; Argazzi, R. and Scandola, F.; *Dalton Trans.*, 20, **2009**, 3964-3970

[5] Alexander, B.D. and Dines, T.J.; *J. Phys. Chem. B.*, 109, **2005**, 3310-3318

[6] Zhao, J.; Dieringer, J.A.; Zhang, X.; Schatz, G.C. and Duyne, P. V.; *J. Phys. Chem. C.*, 112, **2008**, 19302-19310

[7] Cotton, F.A. and Wilkinson, G.; Advanced Inorganic Chemistry: Fourth Edition, Wiley Interscience Publications, **1980**

[8] Treadway, J.A.; Loeb, B.; Lopez, R.; Anderson, P.A.; Keene, R.F. and Meyer T.J.; *Inorg. Chem.*, 35, **1996**, 2242-2246

[9] Watts, R.J. and Crosby, G.A.; *J. Am. Chem. Soc.*, 94, **1972**, 2606-2614

[10] Bacon, J.R. and Demas, J.N.; *Anal. Chem.*, 59, **1987**, 2780-2785

[11] Carraway, E.R.; Demas, J.N.; DeGraff, B.A. and Bacon, J.R.; *Anal. Chem.*, 63, **1991**, 337-342

[12] Draxler, S.; Lippitsch, M.E.; Klimant, I.; Kraus, H. and Wolfbeis, O.S.; *J. Phys. Chem.*, 99, **1995**, 3162-3167

[13] Demas, J.P.; Harris, E.W. and McBride, R.P.; *J. Am. Chem. Soc.*, 99, **1977**, 3547-3551

[14] Patronea, L.; Palacina, S.; Bourgoina, J.P.; Lagouteb, J.; Zambellib, T. and Gauthierb, S.; *Chem. Phys.,* 281, **2002**, 325–332

[15] Tour, J.M.; Jones II, L.; Pearson, D.L.; Lamba, J.J.S.; Burgin, T.P.; Whitesides, G.M.; Allara, D.L.; Parikh, A.N. and Atr, S.V.; *J. Am. Chem. Soc.,* 117, **1995***,* 9529-9534

[16] Juris, A.; Balzani, V.; Barigelletti, F.; Campagna, S.; Belser, P. and Zelewsky, V.; *Coord. Chem. Rev.*, 84, **1988**, 85-277

[17] Kim, H-K.; Lincoln, P.; Nord´en, B. and Tuite, E.; *Chem. Comm.,* 24, **1997,** 2375-2376

[18] Mongey, K.F.; Vos, J.G.; MacCraith, B.D.; McDonagh, C.M.; Coates, C. and McGarvey, J.J.; *J. Mater. Chem.*, 7, **1997**, 1473-1479

[19] Crosby, G.A.; Perkins, W.G. and Klassen, D.M.; *J. Chem. Phys.*, 43, **1965**, 1498-1503

[20] Bachas, L.G.; Cullen, L.; Hutchins, R.S. and Scott, D.L.; *J. Chem. Soc., Dalton Trans.*, 9, **1997**, 1571-1577

[21] Issberner, J.; Vogtle, F.; De Cola, L. and Balzani, V.; *Chem. Eur. J.*, 5, **1997**, 706-712

[22] Juris, A. and Balvani, V.; *Coord. Chem. Rev.*, 48, **1988**, 85-277

[23] Hage, R.; Prins, R.; Haasnoot, J.G.; Reedijk, J. and Vos, J. G.; *J. Chem. Soc. Dalton. Trans.*, 6, **1987**, 1389-1395

[24] Leasure, R. M.; Sacksteder, L. A.; Nesselrodt, D.; Reitz, G. A.; Demas, J. N. and DeGraff, B. A.; *Inorg. Chem.*, 30, **1991**, 3722-3728

[25] Milder, S. J.; Gold, J. S. and Kilger, D. S.; *J. Phys. Chem.*, 90, **1996**, 548-550

[26] Caspar, J.V. and Meyer, T.J.; *Inorg. Chem.*, 22,**1983**, 2444-2453

[27] Benniston, A. C.; Mackie, P. R.; Farrugia, L. J.; Smith, G.; Teat, S. J. and McLean, A. J.; *New J. Chem.*, 25, **2001**, 458-464

[28] Kitamura, N.; Sato, M.; Kim, H-B.; Obata, R. and Tazuke, S.; *Inorg. Chem.*, 27, **1988**, 651-658

[29] Sun, Y. and Turro, C.; *Inorg. Chem.*, 49, **2010**, 5025-5032

[30] Caspar, J. V. and Meyer, T. J.; *J. Phys. Chem.*, 87, **1983**, 952-957

[31] Guerrero-Martinez, A.; Vida, Y.; Dominguez-Gutierrez, D.; Albuquerque, R. Q. and De Cola, L.; *Inorg. Chem.*, 47, **2008**, 9131-9133

[32] Draeger, C.; Bottcher, C.; Messerschmidt, C.; Schulz, A.; Ruhlmann, L.; Siggel, U.; Hammarstrom, L.; Berglund-Baudin, H. and Fuhrhop, J-H.; *Langmuir*, 16, **2000**, 2068-2077

[33] Strommen, D. P.; Mallick, P. K.; Danzer, G. D.; Lumpkin, R. S. and Kincaid, J. R.; *J. Phys. Chem.*, 94, **1990**, 1357-1366

[34] Kumar, C.V.; Barton, J.K.; Turro, N.J. and Gould, I.R.; *Inorganic Chemistry,* 26, **1987***,* 1455-1457

[35] Barbante, G. J; Hogan, C. F.; Wilson, D. J. D.; Lewcenko, N. A.; Pfeffer, F. M.; Barnett, N. W. and Francis, P. S.; *Analsyt*, 136, **2011**, 1329-1338

[36] Barbero, C.; Silber, J. J. and Sereno, L.; *J. Electroanal. Chem.*, 248, **1988**, 321-340

[37] Bard, A. J. and Faulkner, L. R.; Electrochemical Methods: Fundamentals and Applications Second Edition, John Wiley & Sons, Inc., **2001**

[38] Yan, X.; Li, H.; Xu, Z. and Li, W.; *Bioelectrochemistry,* 74, **2009**, 310-314

[39] Nicholson, R. S.; *Analytical Chemistry.,* 11, **1965**, 1351-1355

[40] Kanoufi, F. and Bard, A. J.; *J. Phys. Chem. B.*, 103, **1999**, 10469-10480

# 3. Interfacial Assembly of $[Ru(dpp)_2(x\text{-}ATAP)]^{2+}$

## 3.1 Introduction

Since the formation of alkanethiol SAMs on gold surfaces from dilute solutions of di-n-alkyl disulphides was first demonstrated by Nuzzo and Allara, alkanethiol monolayers on gold surfaces have become the most studied self assembled monolayer (SAM) system[1]. Depending on chain length alkanethiol SAMs can be highly ordered and can be modified at both the chain and terminal groups to modify the properties of the surface. Self assembling surfactant monolayer units are composed of three parts. The first part is the headgroup with provides the molecule with the means to interact with the substrate surface, the thiol $S^-$ group in the case of alkanethiols. Disulphide and acetylthio groups ($S\text{-}COCH_3$) have also been shown to spontaneously form monolayers with transition metal surfaces through S-Au bonds[23,4]. The binding of the headgroups to the substrate brings the molecules close enough together to allow short range dispersive interactions between the second part of the self assembling surfactant molecules, the organic moiety. In alkanethiols the organic moiety is the alkyl chain. The 2D ordering and packing of the monolayer is facilitated by short range interactions (Van der Waals, steric, electrostatic interactions etc.) between the organic moieties[5, 6]. The terminal group at the end of the SAM monolayer unit can be varied to engineer the monolayer units for a variety of purposes, such as adding functional groups for binding interactions. Ulman *et al.*[7] showed that varying the concentration of hydroxyl and methyl groups at the air-monolayer interface can change the wettability of a monolayer surface of hexadecance while Gouget-Laemmel *et al.*[8] demonstrated how a monolayer with amine groups at the air-monolayer interface could be easily modified through amide bonds using the well known EDC/NHS reaction. Although gold is the most common substrate for alkanethiols other metals such as platinum can be as a monolayer substrate. Although the Pt-S bond enthalpy is lower than that of Au-S, 234 and 418 kJ/mol respectively, typically alkanethiol monolayers form with much higher surface coverages on platinum than on gold. For example Petrovykh *et al.*[39] reported on the surface coverage of a hexanethiol monolayer on a Pt surface to be $5.5 \times 10^{14}$ molecules/cm$^2$ while for the same monolayer on a Au surface

was reported as 4.5 x $10^{`14}$ molecules/$cm^2$. Platinum is a more suitable surface than gold on which to carry out electrochemistry of monolayers of complexes with very positive redox potentials, such as ruthenium polypyridyl complexes, since platinum has a much higher oxidation potential than gold in non-aqueous solvents

Interrogation of the properties and structure of interfacial assemblies is problematic by conventional techniques such as mass spectroscopy, NMR etc. These techniques are typically too insensitive to analyse such thin films and are not suited to the analysis of samples consisting of a thin, often one molecule thick film on a solid substrate support. Vibrational spectroscopic techniques have proven to be very valuable in the characterisation of interfacial assemblies. Techniques such as FTIR (Fourier Transform Infra Red), reflectance spectroscopy and diffuse reflectance UV-vis spectroscopy are particularly suited to the analysis of interfacial assemblies and provide the sensitivity lacking in other forms of analysis. Of particular note is the analysis of interfacial assemblies is Raman spectroscopy which due to plasmonic effects can provide excellent sensitivity for the analysis of interfacial assemblies on metallic surfaces. Raman spectroscopy is a powerful analytical tool that can give information on molecular structure, intermolecular interactions and molecular dynamics based on changes in the frequency of scattered light. However Raman spectroscopy is an inherently insensitive technique with a cross section of ~$10^{-30}$ $cm^2$, nearly 15 orders of magnitude lower than standard fluorescence techniques[9]. Fleischmann *et al.*[10] reported an increase in Raman spectra intensity from pyridine absorbed on a roughened silver electrode. However it was Jeanmarie and Van Duyne[11], and Alrecht and Creighton[12] that recognised that the increase in sensitivity of these pyridine monolayers on roughened silver surfaces was too large to be due to surface area increases alone and proposed that there must be a surface enhancement effect from the roughened silver surface. SERS transforms the relatively insensitive Raman technique into one that has been demonstrated to be capable of single molecule detection when combined with resonance enhancement (surface enhanced resonance Raman spectroscopy, SERRS)[13,14].

The SERS effect occurs when the analyte is in close proximity to a surface that supports a localised plasmon, such as roughened metal surfaces and metallic nanoparticles. The electrons on the surface of these materials when excited into their resonant vibrational

mode by incident radiation oscillate generating an EM (electromagnetic) field, or surface polariton, thus enhancing the EM field experienced by the analyte, the so called EM effect[9]. The EM effect however cannot account for the full extent of the Raman enhancement in some systems where the analyte is chemisorbed to the conducting metal surface. A chemical enhancement mechanism (CM) in addition to the EM effect are thought to be responsible for the Raman enhancement in these cases. In systems where the analyte is chemisorbed to a conducting metal surface the Fermi level of the metal can act as a charge transfer intermediate. Charge transfer excitations can therefore occur at around half the energy of intramolecular charge transfer excitations[15]. SERS has become one of the most sensitive methods for monitoring the adsorption, formation and structural properties of SAMs.

Using a SERS active surface that has been modified with alkanethiols has many uses and advantages. As mentioned SAM monolayer units can be designed to give excellent control over the formation, orientation and structure of the surface and the terminal group can be chosen to control the properties to the surface. Interaction of many molecules including biological units like proteins and some aromatic molecules with the bare transition metal surface of the SERS substrate can alter the structure of the molecule, sometimes irreversibly, destroying the chemical identity of the species and altering Raman shifts of the complex. The use of an intervening SAM can block direct surface interactions to permit the retention of the chemical identity of the analyte under study[16,17]. SERS enhancement through the long range electromagnetic mechanism (EM) effect will still affect the analyte giving enhancement. Significant enhancement of the Raman signal is still observed since the EM contributes far more to the enhancement factor than the chemical mechanism (CM) [18,19,20].

The full potential of using SERS in sensor or analytical applications has not yet been fully realised due to a lack of control over the enhancement factor. Non-uniformity of the SERS substrate can greatly affect enhancement factors. A reliable distance dependence enhancement factor is also important to quantify, for example, in the study of protein structures[19]. A distance dependence study of the enhancement factor using SAMs of varying thickness could help calculate distance dependence enhancement factors leading to the development of reliable SERS based sensors[16,19].

Recent publications show that luminophores are not completely quenched by close proximity to metal surfaces and cases of surface enhanced fluorescence (SEF) have been reported[21, 22, 23]. Although not yet fully understood, SEF has been demonstrated. An increase in the radiative decay rate of the luminophore is induced by the electric field of the plasmon of the metal surface. This has the effect of increasing quantum yields and reducing luminescence lifetime of the luminophore[24]. SEF has only relatively recently generated interest in its use in applications such as sensor systems, for example the SEF cavity platforms reported by Keyes *et al*[25].

In this chapter the properties of the RuxD series of complexes are investigated on gold and platinum surfaces. The surface coverage, orientation and conformation of the monolayers are investigated by electrochemistry and Raman methods. The photophysical properties of Au nanoparticles functionalised with monolayers of RuxD were also investigated. The effect of the metallic surface being in such close proximity to the Ruthenium redox centre on photophysical properties is of great interest.

## 3.2 Experimental

### *3.2.1 Materials and Methods*

All reagents and solvents used were analytical grade. Solution phase electrochemistry was carried out in spectroscopic grade acetonitrile. Water was purified using a MilliQ plus – 185 Millipore system. Chemicals purchased from Sigma-Aldrich were used as received. 50 nm Gold Nanoparticles were purchased from British Biocell International.

### *3.2.2 Electrochemical Cleaning of Gold Electrodes*

The gold disk electrodes were first polished with 1 µm, 0.3 µm and 0.05 µm alumina powder consecutively, washing between each polishing cycle with water and sonicating the

electrode in water for 5 minutes, to ensure a smooth electrode surface. The gold disk electrodes were electrochemically cleaned in an aqueous solution of 0.1 M $H_2SO_4$ using a platinum wire as the counter electrode and a Ag/AgCl aqueous reference electrode. The reference electrode was separated from the bulk solution using a salt bridge to prevent $Cl^-$ leakage that interferes with the cleaning process. The electrode was repetitively scanned from -0.2 V to 1.45 V at 0.1 V/s for 16 scans. The presence of only the gold oxidation features of a clean gold electrode cyclic voltammagram signified a successfully cleaned electrode. The surface area of the electrode was calculated by integrating the gold oxidation peak to get the charge in coulombs. This was divided by the standard reference charge of polycrystalline gold, which is 390 $\mu C/cm^2$.

### *3.2.3 Electrochemical Cleaning of Platinum Electrodes*

The platinum disk electrodes were first polished with 1 µm, 0.3 µm and 0.05 µm alumina powder consecutively, washing between each polishing cycle with water and sonicating the electrode in water for 5 minutes, to ensure a smooth electrode surface. The platinum disk electrodes were electrochemically cleaning in an aqueous solution of 0.1 M $H_2SO_4$ using a platinum wire as the counter electrode and an Ag/AgCl aqueous reference electrode. The reference electrode was separated from the bulk solution using a salt bridge to prevent $Cl^-$ leakage that interferes with the cleaning process. The electrode was repetitively scanned from -0.2 V to 1.5 V at 0.1 V/s for 20 scans. The presence of only the platinum oxidation and hydrogen adsorption/desorption features of a clean platinum electrode cyclic voltammagram signified a successfully cleaned electrode. The cleaned electrode was then held at 0.3 V for 30 seconds to desorb any adsorbed hydrogen. The surface area of the electrode was calculated by integrating the platinum oxidation peak to get the charge in coulombs. This was divided by the standard reference charge of polycrystalline platinum, which is 420 $\mu C/cm^2$.

### *3.2.4 Electrochemical Roughening of Gold Electrodes*

Electrochemically cleaned gold electrodes were electrochemically roughened in an aqueous solution of 0.1 M KCl using a using a platinum wire as the counter electrode and a Ag/AgCl aqueous reference electrode. The electrode was repetitively scanned from -0.3 V to

1.2 V at a scan rate of 0.1 V/s each time holding the negative potential at for 10 seconds and the positive potential for 3 seconds until a stable CV was obtained.

### *3.2.5 Modification of Gold and Platinum Electrodes with RuxD monolayers*

The electrochemically cleaned gold or platinum electrodes were immersed in a 0.2 mM ethanolic solution of the RuxD complexes. The electrodes were left immersed for 96 hours to ensure the formation of stable well ordered monolayers. Afterwards the electrodes were washed with ethanol and sonicated for 2 minutes in ethanol to remove any loosely bound physisorbed material. If backfilling was required the monolayers were backfilled with 1-hexanethiol for Ru6D, 1-octanethiol for Ru8D, 1-undecanethiol for Ru11D or 1-hexadecanethiol for Ru16D monolayers, wherein the electrodes modified with RuxD monolayers were immersed in an ethanolic 0.1 mM solution of the respective alkanethiol for 24 hours. The electrodes were then washed with ethanol and sonicated in ethanol for 2 minutes to remove any loosely bound physisorbed material.

### *3.2.6 Modified RuxD 50 nm gold nanoparticles*

1 mL of a 0.2 mM RuxD solution in EtOH was added to 3 mL of commercial 50 nm in diameter citrate stabilized gold nanoparticles and left for 24 hours. The solution was sonicated for 5 mins and the nanoparticles were removed, centrifuged and resuspended in 50:50 EtOH : $H_2O$ multiple times to remove any unbound material. The nanoparticles were then sonicated between each of the centrifugation steps to remove any loosely bound or physisorbed RuxD material. Purification by centrifugation had to be carried out quickly to stop the nanoparticles irreversibly adhering to the sides of the vessels. If the nanoparticles adhered to the sides the solution was gently heated to about $50^{o}$ C and while sonicating vigorously until a colloidal suspension was reformed. The purified nanoparticles can be stabilised with 0.5 mL of 1 mM $NaSO_4$ per 3 mL nanoparticle solution to stop them adhering to the sides of the container. This however caused the nanoparticles to agglomerate and precipitate out after some time. Sonication of the solution for 5 minutes resuspends the nanoparticles. Suspensions of these functionalized nanoparticles were a deep purple colour compared to the red colour of the unfunctionalised nanoparticles. These functionalized nanoparticles will degrade over a period of time by adhering irreversibly to the sides of any

container they are held in. Therefore, any analysis carried out on these functionalised nanoparticles must be carried out shortly after purification.

### *3.2.8 Particle Sizing*

Particle sizing was carried out using a Delsa Nano C Submicron Particle Size and Zeta Potential Particle Analyzer with the standard size cell accessory.

### *3.2.9 Raman Spectroscopy*

Raman spectra were collected on a Jobin Yvon Horiba HR800 UV raman spectrometer using a HeNe and Argon ion laser. Available excitation lines were 458nm, 488nm, 514nm and 632nm. A backscattering geometry was used to collect scattered light with an air cooled CCD array using either 1800 lines/mm or 600 lines/mm gratings. The wavenumber axis was calibrated before measurements with the silicon line at 521cm$^{-1}$. Laser intensity was kept at 100%.

## 3.3 Results and Discussion

### *3.3.1 Electrochemical Characterisation of Nonbackfilled RuxD Monolayers on Platinum Surfaces*

Fig 3.3.1.1 shows the voltammetric response of the nonbackfilled monolayers of RuxD complexes on 3 mm diameter platinum electrodes when cycled in 0.1 M $TBAClO_4$ ACN solution. All nonbackfilled monolayers exhibited a formal potential, $E^{0'}$, of approximately +0.92 V corresponding to the metal centred oxidation as detailed in Table 3.3.1. This is the same formal potential as the complex in acetonitrile solution (see Chapter 2). This is as expected for this monolayer system. Faulkner *et al.*[31] saw only minor shifts of 10-20 mV in $E^{0'}$ for monolayers of $[Os(bpy)_2Cl(pNp)]^+$ on platinum compared to solution, where p*N*p is 4,4'-bipyridyl, 1,2-bis(4-pyridyl)ethane or 4,4'-trimethylenedipyridine. The surface coverage of all 4 RuxD monolayers on platinum is very low, less than one third of the

coverage of comparable $[Ru(bpy)_2Qbpy]^{2+}$ monolayers[26], making it unlikely that a uniformly well structured monolayer is formed in this scenario.

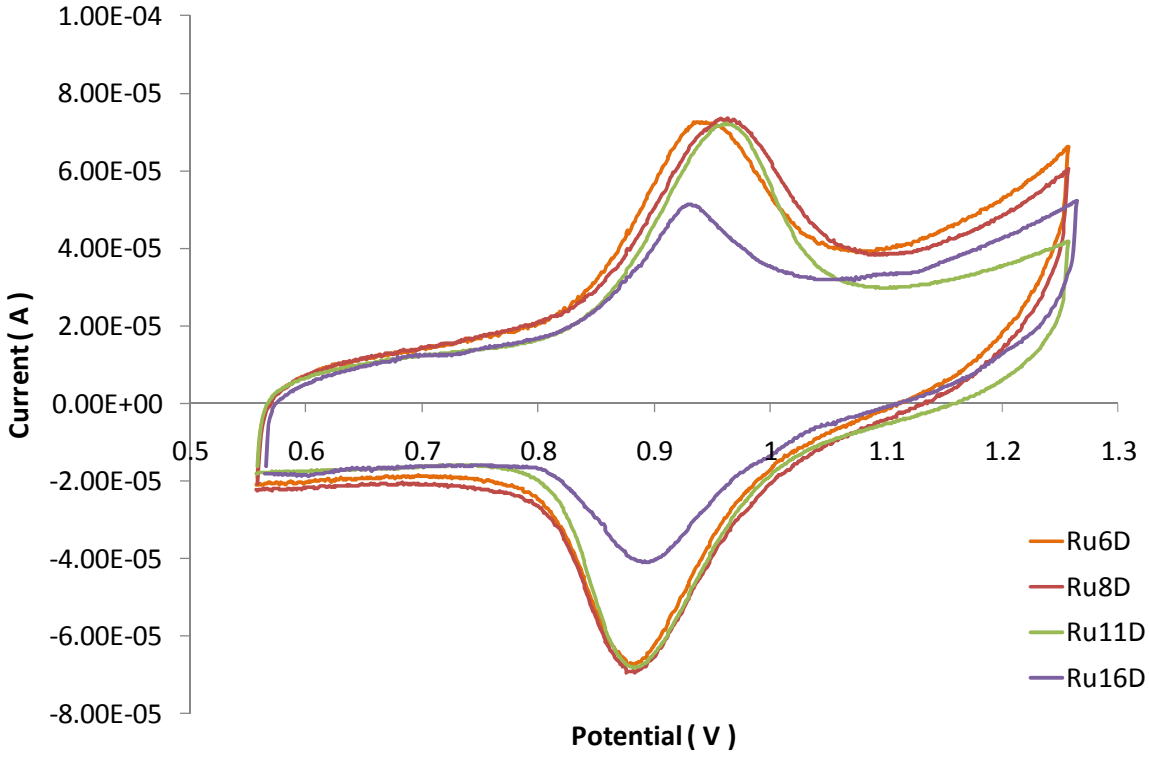


**Figure 3.3.1.1:** Cyclic voltammagrams of nonbackfilled monolayers of RuxD on a 3 mm diameter Platinum electrodes. All electrochemistry was carried out in ACN with 0.1 mM TBA $ClO_4$ as the supporting electrolyte. All potentials are vs. $Ag/AgNO_3$ electrode and corrected against ferrocene. A scan rate of 20 V/s was used.

Fig 3.3.1.2 shows the scan rate dependence of the current density, J, for each of the nonbackfilled RuxD monolayers. Since the concentration of RuxD varies with the surface area of the electrode J is used as a means to normalise the peak current $I_p$ and is the peak current $I_p$ divided by the electrochemically measured surface area of the electrode. In a surface confined system $I_p$, or in this case J, will vary linearly with increasing scan rate. As can be seen, in the case of all nonbackfilled monolayers J varies linearly with increasing scan rate therefore suggesting ideal reversible surface confined electrochemistry for the RuxD monolayers. $\Delta E^{0}$'p values for the nonbackfilled RuxD monolayers are about < 30 mV at 1 V/s scan rates which is close to $\Delta E_p$ for an ideal surface confined system which is 0 mV. Faulkner *et al.*[31] reported $\Delta E_p$ values for monolayers of $[Os(bpy)_2Cl(pNp)]^+$ on platinum

electrodes to be < 35 mV. FWHM values of the $Ru^{2+/3+}$ redox process were between 95-110 mV, again quite close to the expected FWHM of an ideal surface confined system which is 90.6 mV. Faulkner *et. al.*[31] reported similar FWHM values of 90-110 mV for their surface confined $[Os(bpy)_2Cl(pNp)]^+$ system.

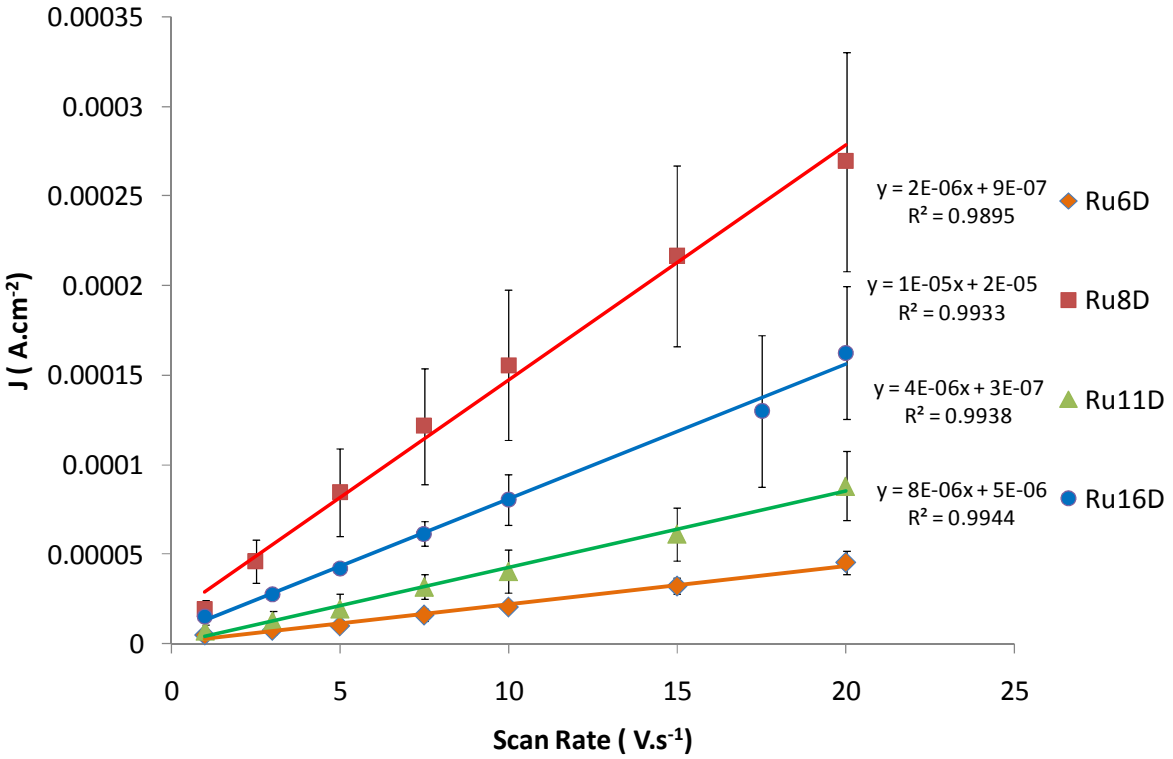


**Figure 3.3.1.2:** Scan rate dependence of nonbackfilled RuxD monolayers on 3 mm diameter platinum electrodes. All measurements were in ACN with 0.1 M $TBATBF_4$ as the supporting electrolyte and with a platinum wire counter electrode.

The electrochemical properties of platinum electrodes modified with RuxD complexes are as expected for surface confined redox complexes. As already mentioned the peak current of the ruthenium redox process increases linearly with increasing scan rate, as expected in a surface confined system. Peak to peak separation $\Delta E_p$ is as close to 0 mV within experimental error and does not vary at low scan rates. However at scan rates of about 100 V/s, $\Delta E_p$ values increase significantly indicating limitations in the charge transfer process. The scan rate has become so fast that the kinetic redox process has not completed before the scan has moved to a higher potential. This increase in the $\Delta E_p$ with scan rate can

be used to calculate the standard rate constants for electron transfer ($k^o$). The $k^o$ values for nonbackfilled RuxD monolayers are presented in Table 3.3.1. The classic method derived by Laviron[27] was used to calculate $k^o$ by the variation of the anodic and cathodic $\Delta E_p$ with scan rate. Laviron plots for the nonbackfilled RuxD monolayers on Pt electrodes are presented in Fig. 3.3.1.3 - 3.3.1.6. All peak potential values have been corrected against ferrocene. Potentials were also corrected for ohmic drop by measuring the resistance at $E^0_{anodic}$ and $E^0_{cathodic}$ of the $Ru^{2+/3+}$ process after each measurement. The resistance was multiplied by the peak current to obtain the extent of ohmic drop in volts. The anodic and cathodic peak potentials were then corrected by this amount. Resistance was small, about 140-200 Ω and had no significant effect on $\Delta E_p$ until fast scan rates above 20 V/s.

Laviron plots can be used to estimate $k^o$ in diffusionless systems such as these RuxD monolayers where the redox centre is fully reversible and irreversibly adsorbed to the surface of the electrode. Under these circumstances at low scan rates, before the electron transfer process is rate limited, $\Delta E_p$ should remain constant, in the case of a one electron reversible surface confined process $\Delta E_p$ should be zero or close to zero. When the scan rate becomes fast enough the electron transfer process becomes rate limited and the electrochemical system tends towards the behaviour of a totally irreversible system leading to an increase in $\Delta E_p$, with $\Delta E_p$ increasing proportionally with $\log_{10}$ scan rate. At high enough scan rates a plot of $E_{p\ anodic}$ and $E_{p\ cathodic}$ against the log of the scan rate will be linear with slopes of 2.3RT / (1-α) $n$F and – 2.3 RT / α$n$F for anodic and cathodic respectively, where α is the transfer coefficient and $n$ is the number of electrons involved in the charge transfer process. The transfer coefficient α is a dimensionless measure of the symmetry of the energy barrier to the formation of the reactant and product. The point where these two lines intersect on the midline gives log ($\nu_s$), the log of the scan rate where the electron transfer process becomes rate limited. $k^o$ can then be calculated from using this formula:

$$k^o = \alpha n F \nu_s / RT$$

A one electron fully reversible redox system is expected to have an α of around 0.5 so in this case an estimated value of 0.5 was used. The relative error in calculating $k^o$ when α is estimated at 0.5 for a surface confined 1 electron redox system is very small, it was calculated to be at most 6% in Laviron's paper[27].

The rate constant for electron charge transfer in the nonbackfilled RuxD monolayers was between about 1000 $s^{-1}$ and 1400 $s^{-1}$. Interestingly and unexpectedly the scan rate follows no trend with increasing chain length. These experiments were repeated twice to obtain the experimental error. At such fast electron transfer rates the experimental error becomes quite large since even a small changes in $\nu_s$ can result in a large change in the calculation of $k^o$. The electron transfer rate constants of the RuxD monolayer systems are much faster than other comparable monolayers systems with ruthenium redox centres separated from the metal surface by an alkanethiol spacer layer where electron transfer is a through space interaction[28,29,30]. For example Finklea *et al.*[30] reported the rate constants for electron charge transfer in monolayers of alkanethiols with pendant $[Ru(NH_3)_5(py)]^{2+}$ groups, where py = pyridine. For nonbackfilled well organised monolayers $k^o$ was reported to be 1-3 $s^{-1}$ for complexes with an alkanethiol group 15 carbons in length and 130 – 220 $s^{-1}$ for the complexes with an alkanethiol group 10 carbons in length. Monolayers were formed on a gold surface and 1 M aqueous $NaSO_4$ was used as the supporting electrolyte. The electron transfer rates are closer to those reprted by Faulkner *et al.*[31] who reported the rate constants for electron transfer in monolayers of $[Os(bpy)_2(pNp)Cl]^+$, where pNp is either 4,4'-bipyridyl (p0p), 1,2-bis(4-pyridyl)-Ethane (p2p), or 4,4'-trimethylenedipyridine (p3p). $k_s$ was reported to be >70$e^{-4}$, 11$e^{-4}$ and 1.80$e^{-4}$ $s^{-1}$ for monolayers of $[Os(bpy)_2(pNp)Cl]^+$, where pNp is either p0p, p2p and p3p respectively. Monolayers were on platinum microelectrode with 0.1 M perchlorate in acetonitrile as the supporting electrolyte. In this case the metal centre and the metal surface were separated by a very short distance by an aromatic ligand.

The fast electron transfer rates of these nonbackfilled RuxD monolayer systems suggest that there is direct electron transfer from the ruthenium head group over a very short distance to the metal surface. Taking into account the very fast electron transfer rates, the chain length independence of the electron transfer rate and poor surface coverage and it would seem that in these nonbackfilled monolayers the RuxD complexes are lying down on the electrode surface with the Ruthenium redox centre is direct contact with the metal surface. Due to the RuxD monolayer systems lying flat on the metal surface and the lack of distance dependence, no β distance dependence values, where β is the change in $k_s$ per unit length, could be calculated. The solution phase chemistry of the RuxD complexes in Chapter 3 showed the presence of adsorption isotherms. It has been theorised that the RuxD

complexes are lying flat on the metal surface due to attraction between the aromatic rings of the dpp ligands and the metal surface. This affect has been reported on for pyridine on gold and platinum by Wieckowski *et al.*[32, 33] where at low concentrations pyridine is adsorbed to the metal surface in a horizontal configuration.

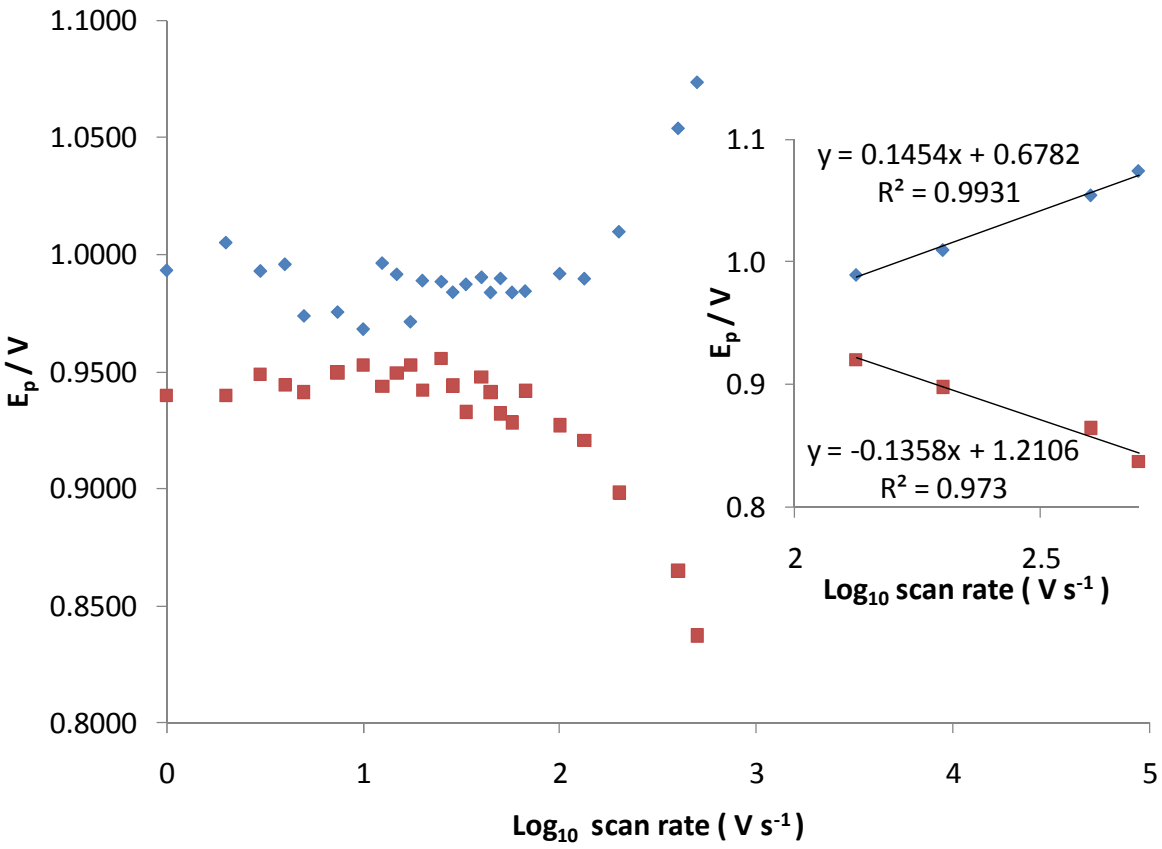


**Fig 3.3.1.3:** Laviron plot showing the dependence of the peak potential on the logarithm of scan rate for a nonbackfilled Ru6D monolayer on a 3 mm diameter platinum. The inset shows the linear segments of the Laviron plots. All peak potentials were corrected for ohmic drop. All electrochemistry was carried out in ACN with 0.1 mM $TBAClO_4$ as the supporting electrolyte. All potentials are vs. $Ag/AgNO_3$ electrode and corrected against ferrocene. Values for $k^o$ were an average of two separate experiments.

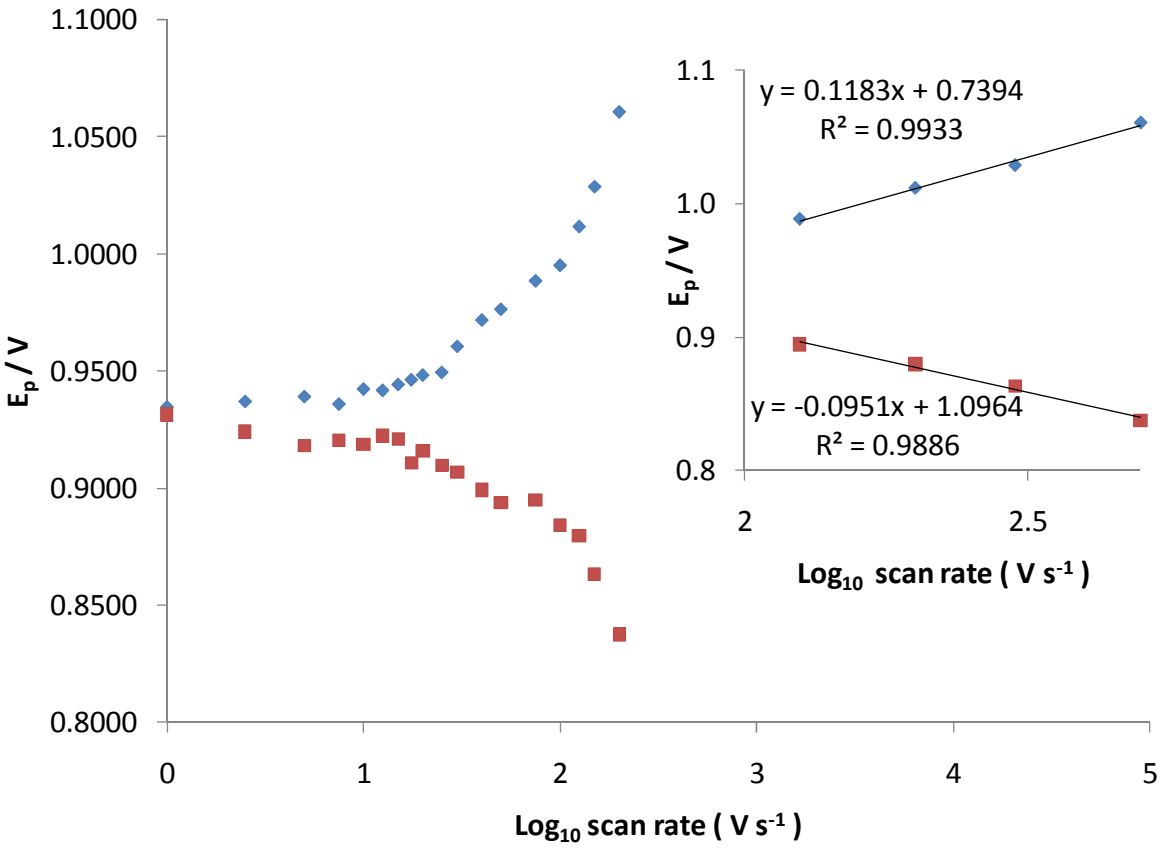


**Fig 3.3.1.4:** Laviron plot showing the dependence of the peak potential on the logarithm of scan rate for a nonbackfilled Ru8D monolayer on a 3 mm diameter platinum. The inset shows the linear segments of the Laviron plots. All peak potentials were corrected for ohmic drop. All electrochemistry was carried out in ACN with 0.1 mM $TBAClO_4$ as the supporting electrolyte. All potentials are vs. $Ag/AgNO_3$ electrode and corrected against ferrocene. Values for $k^o$ were an average of two separate experiments.

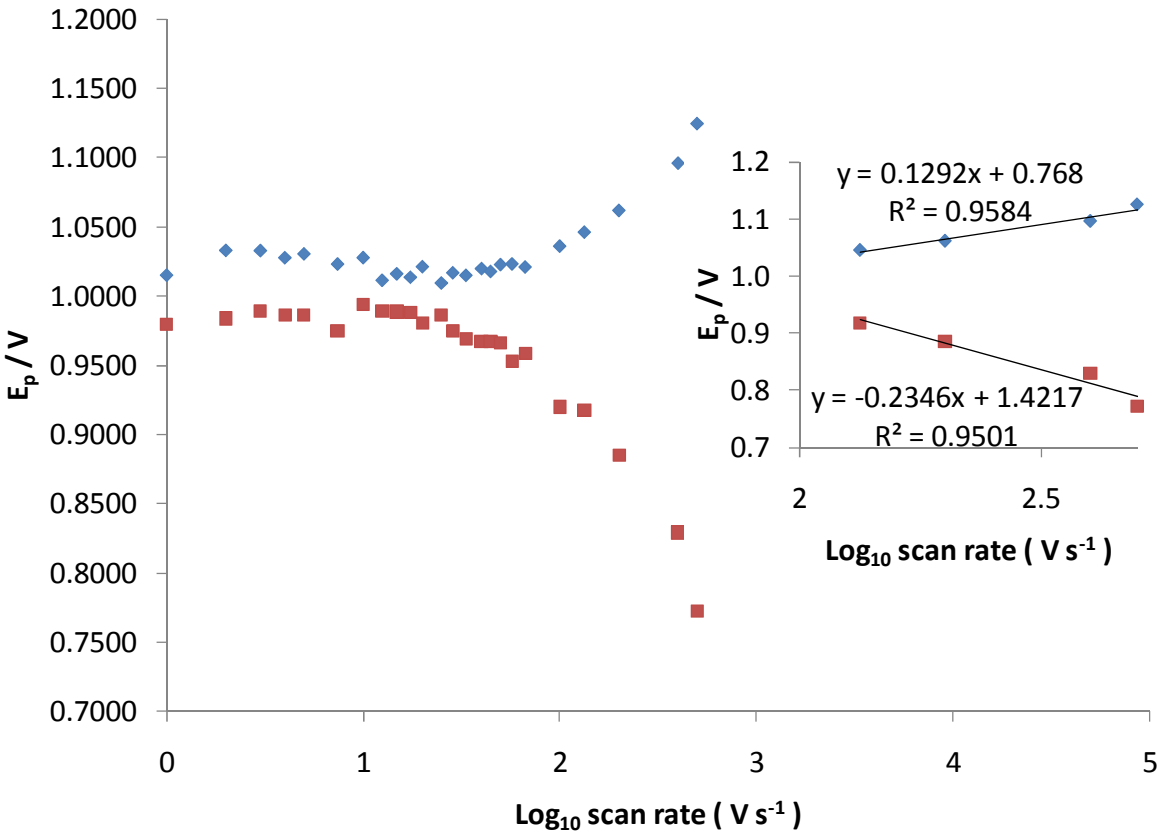


**Fig 3.3.1.5:** Laviron plot showing the dependence of the peak potential on the logarithm of scan rate for a nonbackfilled Ru11D monolayer on a 3 mm diameter platinum. The inset shows the linear segments of the Laviron plots. All peak potentials were corrected for ohmic drop. All electrochemistry was carried out in ACN with 0.1 mM $TBAClO_4$ as the supporting electrolyte. All potentials are vs. $Ag/AgNO_3$ electrode and corrected against ferrocene. Values for $k^o$ were an average of two separate experiments.

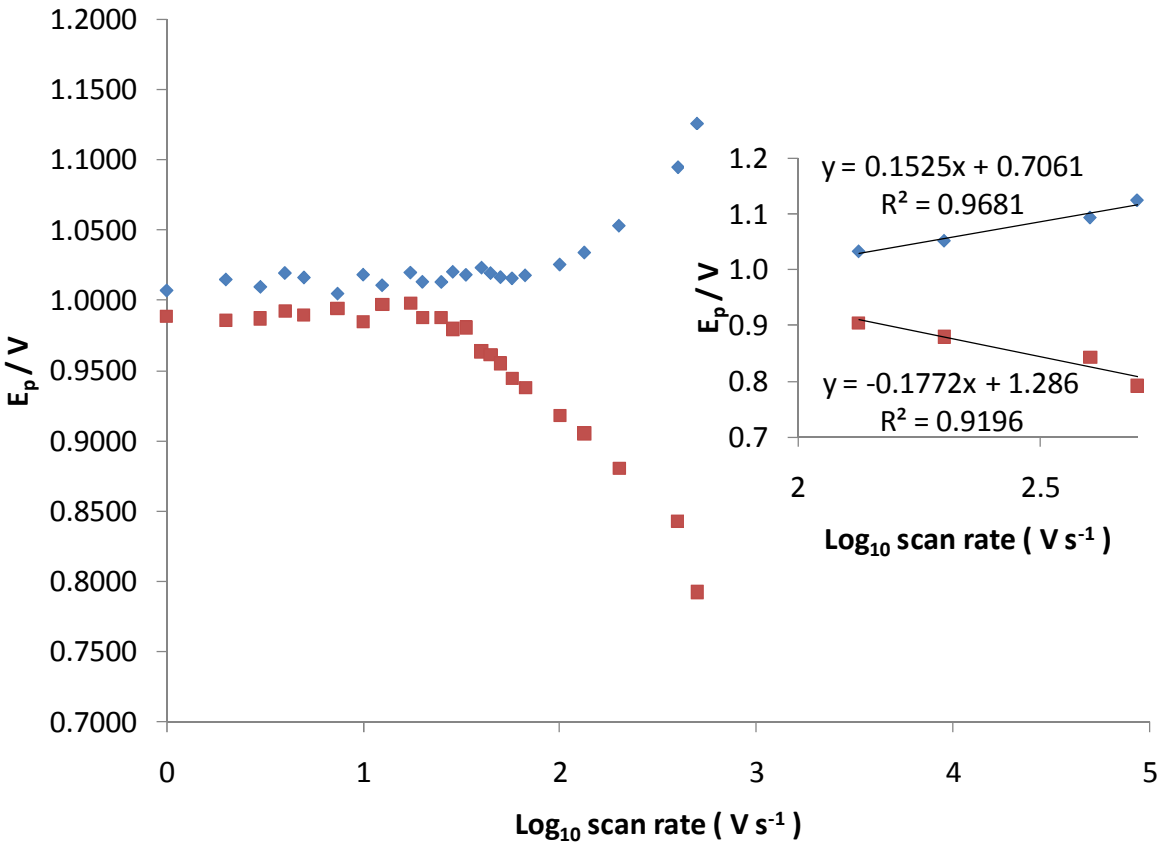


**Fig 3.3.1.6:** Laviron plot showing the dependence of the peak potential on the logarithm of scan rate for a nonbackfilled Ru16D monolayer on a 3 mm diameter platinum. The inset shows the linear segments of the Laviron plots. All peak potentials were corrected for ohmic drop. All electrochemistry was carried out in ACN with 0.1 mM $TBAClO_4$ as the supporting electrolyte. All potentials are vs. $Ag/AgNO_3$ electrode and corrected against ferrocene. Values for $k^o$ were an average of two separate experiments.

### *3.3.2 Electrochemical Characterisation of Backfilled RuxD Monolayers on Platinum Surfaces*

In an effort to force a change in the surface conformation in orientation of the RuxD monolayers on the surface – coadsorption with alkanethiols of comparable length to the RuxD alkyl chain was employed. Fig 3.3.2.1 shows the voltammetric response of the backfilled monolayers of RuxD complexes on 3 mm diameter platinum electrodes when cycled in ACN solution containing 0.1 M $TBAClO_4$. The Ru6D, Ru8D, Ru11D and Ru16D monolayers were backfilled with 1-hexanethiol, 1-octanethiol, 1-undecanetiol and 1-hexadecanethiol respectively. As detailed in Table 3.3.1 backfilling the monolayers with an alkanethiol of the same length as the alkane chain of the RuxD complex results in a positive $E^{0'}$ shift compared to the nonbackfilled monolayers of RuxD and RuxD in solution. An $E^{0'}$ shift of about +0.025 V (± 0.012 V) is observed for monolayers of Ru6D, Ru8D and Ru11D after backfilling. An even greater positive $E^{0'}$ shift of about + 0.04 V (± 0.008 V) is observed in Ru16D monolayers following backfilling. This is unexpected as just like the monolayers of $[Os(bpy)_2(pNp)Cl]^+$ reported by Faulkner *et. al.*[31] very little change in $E^{0'}$ is expected between the complex as a monolayer and in solution. However an explanation for these positive shifts in $E^{0'}$ is if the RuxD complex is buried in the alkanethiol backfilled monolayer while in a lying down configuration. A positive shift in $E^{0'}$ has been reported for monolayers of ferrocene complexes with pendent alkanethiols that are buried in alkanethiol backfilled layers by Creager *et al.*[34, 35] It was proposed that this effect was due to the more no-polar the ferrocene complex is in when buried in an alkanethiol. The formation of the charged oxidation product ferrocenium is unfavourable in the non-polar environment. Also ions from the electrolyte solution that can stabilise the ferrocenium state are slower to diffuse to the ferrocene moiety due to a blocking effect of the alkanethiol layer. It is thought that the same affect causes the positive shifts in $E^{0'}$ for the backfilled monolayers of RuxD. This would also explain the chain length dependence on this positive $E^{0'}$ for the backfilled monolayer of Ru16D since the ruthenium head group would experience an even more non-polar environment than the other RuxD complexes.

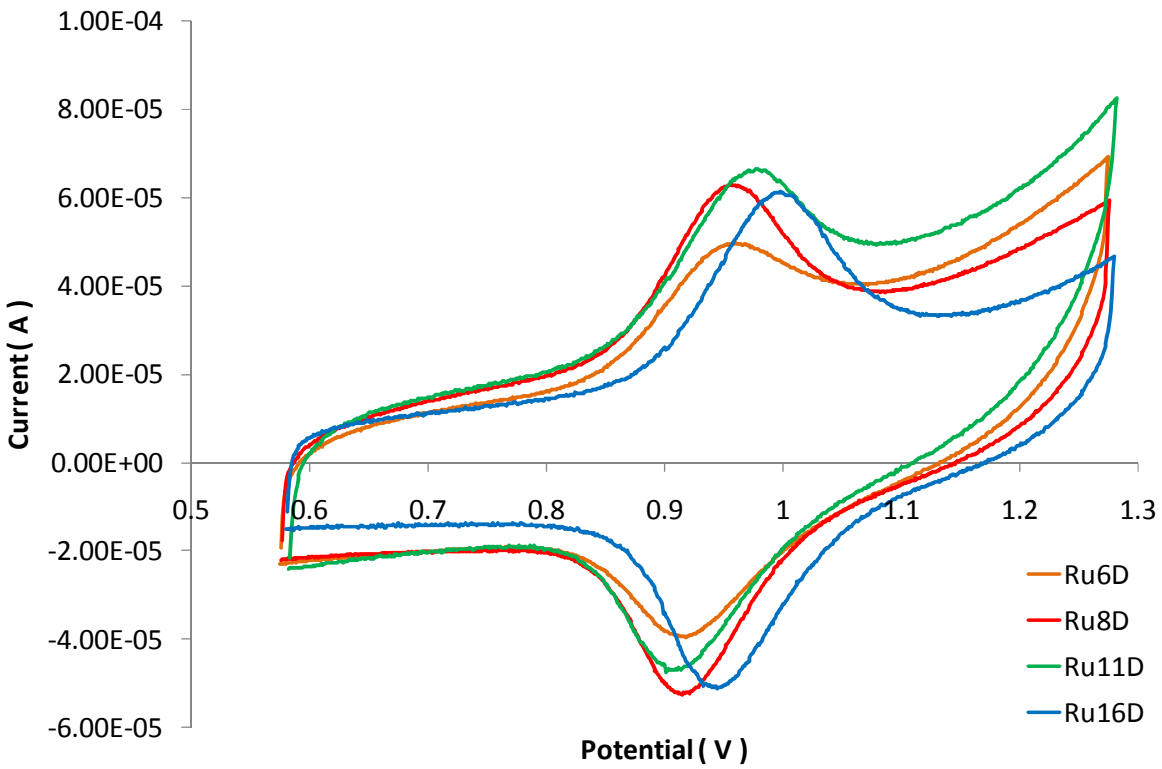


**Figure 3.3.2.1:** Cyclic voltammagrams of backfilled monolayers of RuxD on Platinum electrodes. The Ru6D, Ru8D, Ru11D and Ru16D monolayers were backfilled with 1-hexanethiol, 1-octanethiol, 1-undecanetiol and 1-hexadecanethiol respectively. All electrochemistry was carried out in ACN with 0.1 mM $TBAClO_4$ as the supporting electrolyte and with a platinum wire counter electrode. All potentials are vs. $Ag/AgNO_3$ electrode and corrected against ferrocene. A scan rate of 20 V/s was used.

Fig 3.3.2.2 shows the scan rate dependence of J for each of the backfilled RuxD monolayers. As with the nonbackfilled RuxD monolayers in the case of the backfilled RuxD monolayers J varies linearly with increasing scan rate and therefore exhibits ideal reversible surface confined electrochemistry. $\Delta E_p$ and FWHM values for the $Ru^{2+/3+}$ process are also close to ideal for all backfilled RuxD monolayers, between 95-110 mV for $\Delta E_p$ and ~110mVfor FWHM. As detailed in table 3.3.1 the surface coverage of the backfilled monolayers of about $1.8e^{-11}$ mol $cm^{-2}$ was even lower than the nonbackfilled monolayers. Surface coverage was measure from the charge measured under the $Ru^{2+/3+}$ redox process using the following equation:

$$surface\ coverage = \frac{Q}{\mathrm{F.A}}$$

where Q is the measured charge under the $Ru^{2+/3+}$ anodic or cathodic peak in coulombs, F is faradays constant and A is the area of the electrode in $cm^{-2}$. This gives a surface coverage in mol $cm^{-2}$.

Displacement of some of the RuxD moieties by alkanethiols during the backfilling process is the likely cause. Replacement of bulkier monolayer units by alkanethiols has been reported in the literature. For example, Weiss, Crespi *et al*.[36] reported on the complete displacement of 1-adamantanethiolate by n-dodecanethiol while Fox *et al*.[37] reported that when a mixed monolayer of 1-hexadecanethiol and 16-(ferrocenylcarbonyloxy)hexadecanethiol is immersed in an ethanolic solution of 1 mM 1-hexadecanethiol, a loss of around one third of the 16-(ferrocenylcarbonyloxy)hexadecanethiol from the surface is observed.

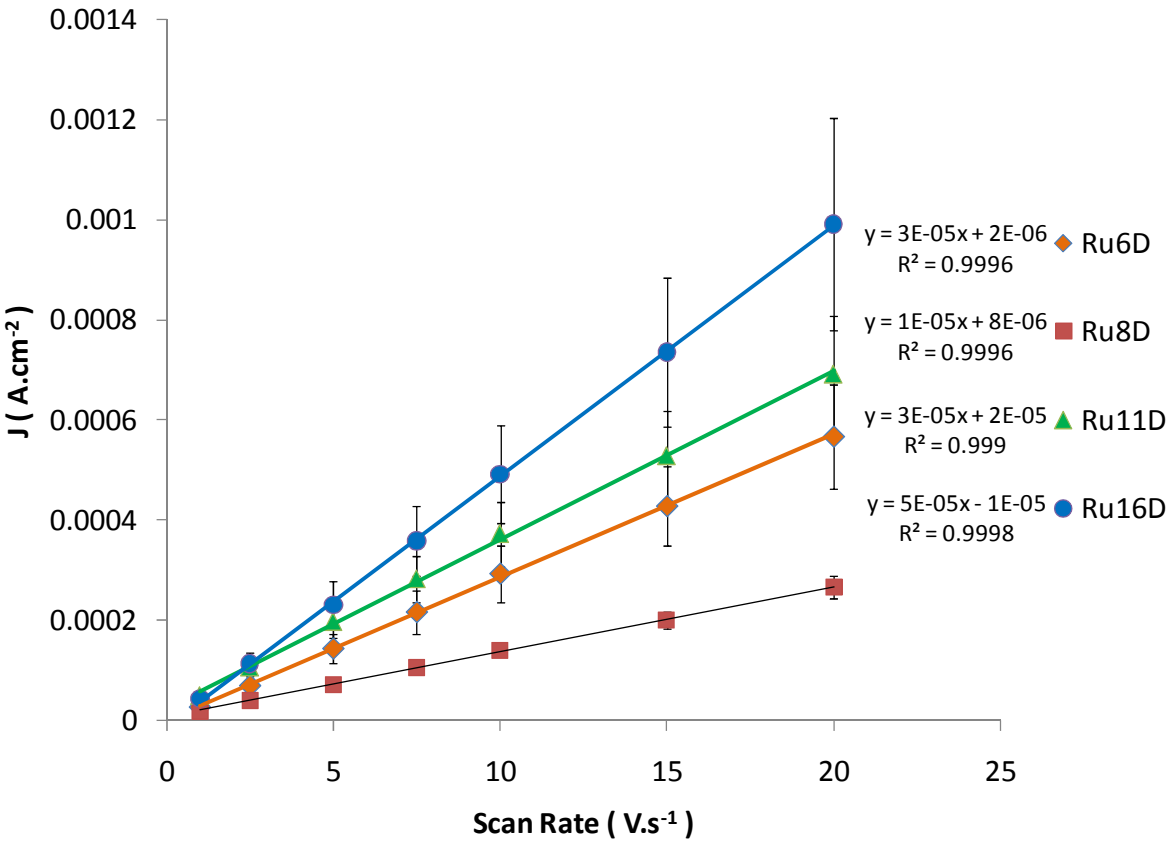


**Figure 3.3.2.2:** Scan rate dependence of backfilled RuxD monolayers on 3 mm diameter platinum electrodes. The Ru6D, Ru8D, Ru11D and Ru16D monolayers were backfilled with 1-hexanethiol, 1-octanethiol, 1-undecanetiol and 1-hexadecanethiol, respectively. All measurements were in ACN with 0.1 M $TBATBF_4$ as the supporting electrolyte and with a platinum wire counter electrode.

Ideally in these backfilled RuxD monolayer systems the ruthenium redox centre should be lying exposed on top of the alkanethiol monolayer. However the positive shift in $E^{o'}$ as mentioned is evidence for the other possibility of the ruthenium redox centre being buried in the alkanethiol layer. These two scenarios are illustrated in Figs 3.3.2.3 and 3.3.2.4.

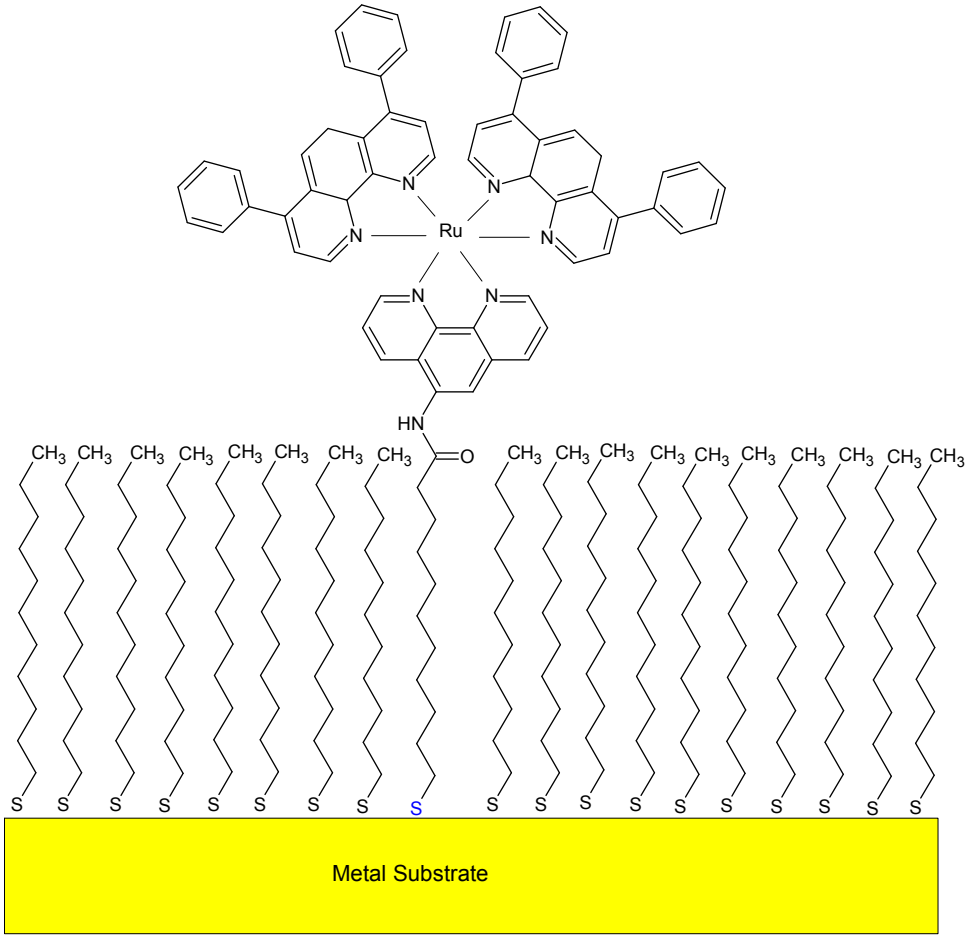


**Fig 3.3.2.3:** Scenario where the ruthenium centre of the Ru11D complex lies exposed on top of a 1-undecanethiol backfilling monolayer.

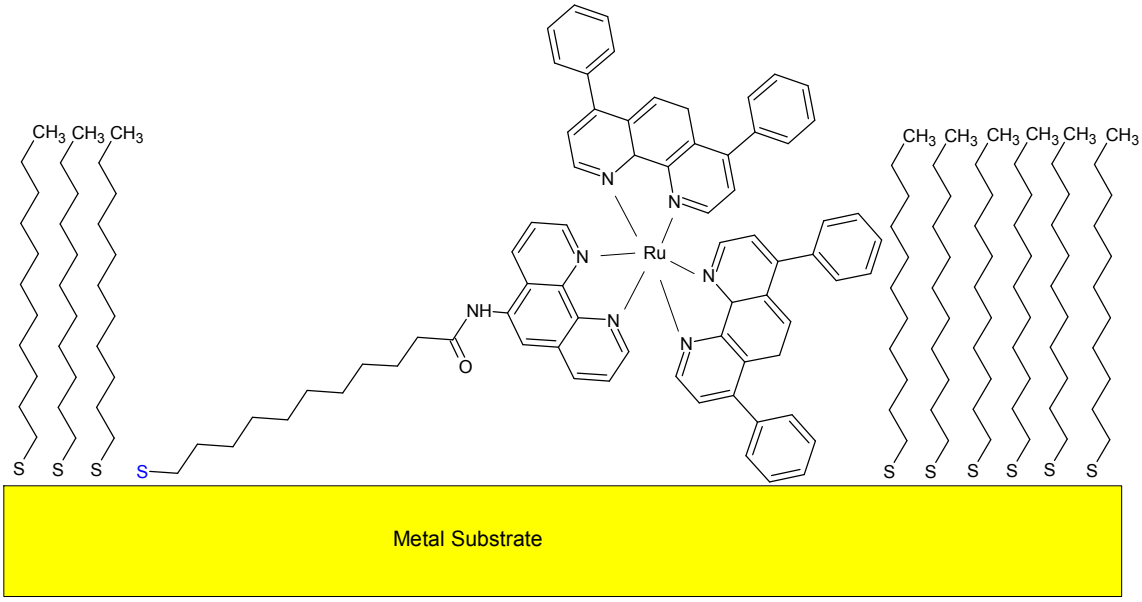


**Fig 3.3.2.4:** Scenario where Ru11D moiety is lying flat on the electrode surface buried in the 1-undecanethiol backfilling monolayer.

To elucidate which of these scenarios is correct for the backfilled monolayers of RuxD the method of Laviron was again employed to calculate $k^o$ the rate constant for electron charge transfer. If the scenario presented in Fig 3.3.2.3 is correct then $k^o$ will be much slower than calculated for the nonbackfilled RuxD monolayers, which have a configuration similar to the one presented in Fig 3.3.2.4. . Laviron plots for the nonbackfilled RuxD monolayers on Pt electrodes are presented in Fig. 3.3.2.5 - 3.3.2.8. All peak potential values have been corrected against ferrocene and also corrected for ohmic drop as describe previously in Section 3.3.1. As detailed in table 3.3.1 the electron transfer rate is extremely fast with $k^o$ values between 1000 and 1400 $s^{-1}$, comparable to the nonbackfilled RuxD monolayers. Again there is no progression in $k^o$ with increasing alkyl chain length. Taking these results into account it would appear that just like the nonbackfilled RuxD monolayers, the backfilled RuxD monolayers are lying flat on the surface of the electrode buried in the alkanethiol backfilling monolayer. Unfortunately again a β value and any information on electron tunnelling with increasing distance from the electrode surface was impossible to obtain.

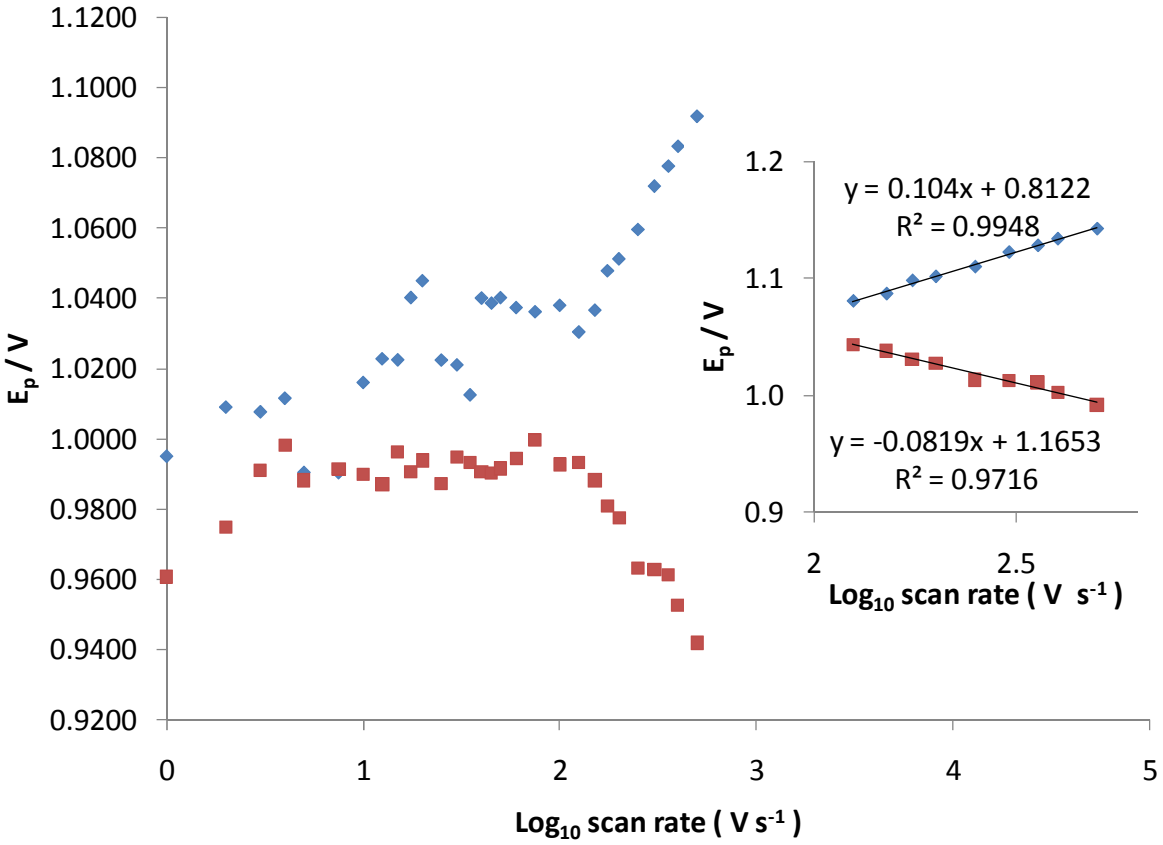


**Fig 3.3.2.5:** Laviron plot showing the dependence of the peak potential on the logarithm of scan rate for a Ru6D monolayer backfilled with 1-hexanethiol on a 3 mm diameter platinum. The inset shows the linear segments of the Laviron plots. All peak potentials were corrected for ohmic drop. All electrochemistry was carried out in ACN with 0.1 mM $TBAClO_4$ as the supporting electrolyte. All potentials are vs. $Ag/AgNO_3$ electrode and corrected against ferrocene. Values for $k^o$ were an average of two separate experiments.

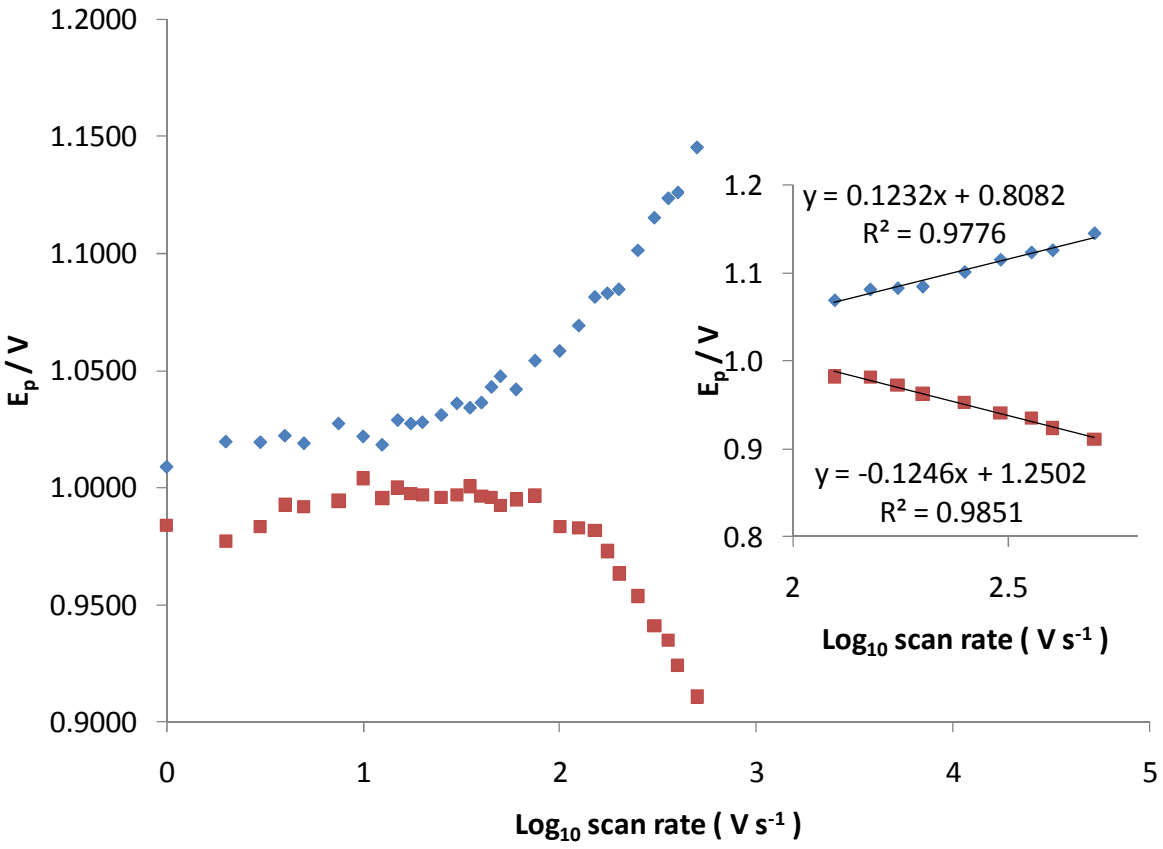


**Fig 3.3.2.6:** Laviron plot showing the dependence of the peak potential on the logarithm of scan rate for a Ru8D monolayer backfilled with 1-octanethiol on a 3 mm diameter platinum. The inset shows the linear segments of the Laviron plots. All peak potentials were corrected for ohmic drop. All electrochemistry was carried out in ACN with 0.1 mM $TBAClO_4$ as the supporting electrolyte. All potentials are vs. $Ag/AgNO_3$ electrode and corrected against ferrocene. Values for $k^o$ were an average of two separate experiments.

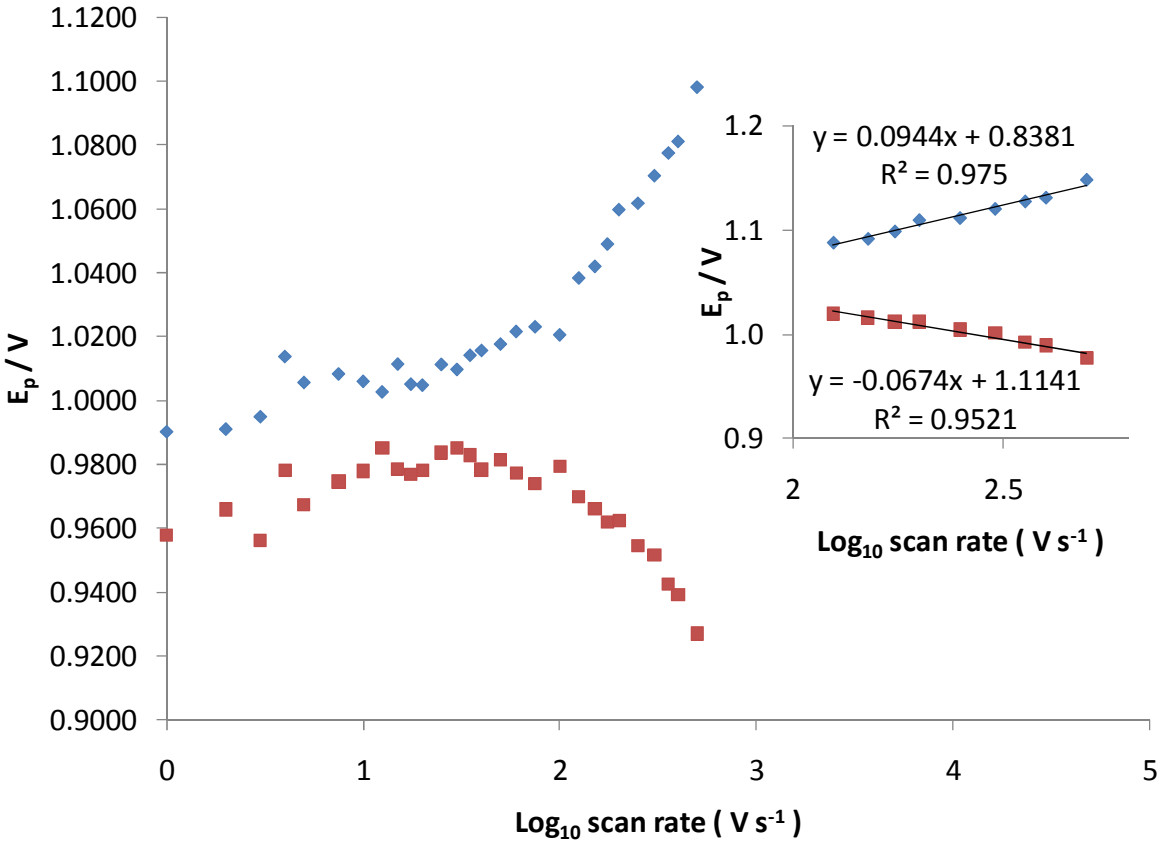


**Fig 3.3.2.7:** Laviron plot showing the dependence of the peak potential on the logarithm of scan rate for a Ru11D monolayer backfilled with 1-undecanethiol on a 3 mm diameter platinum. The inset shows the linear segments of the Laviron plots. All peak potentials were corrected for ohmic drop. All electrochemistry was carried out in ACN with 0.1 mM $TBAClO_4$ as the supporting electrolyte. All potentials are vs. $Ag/AgNO_3$ electrode and corrected against ferrocene. Values for $k^o$ were an average of two separate experiments.

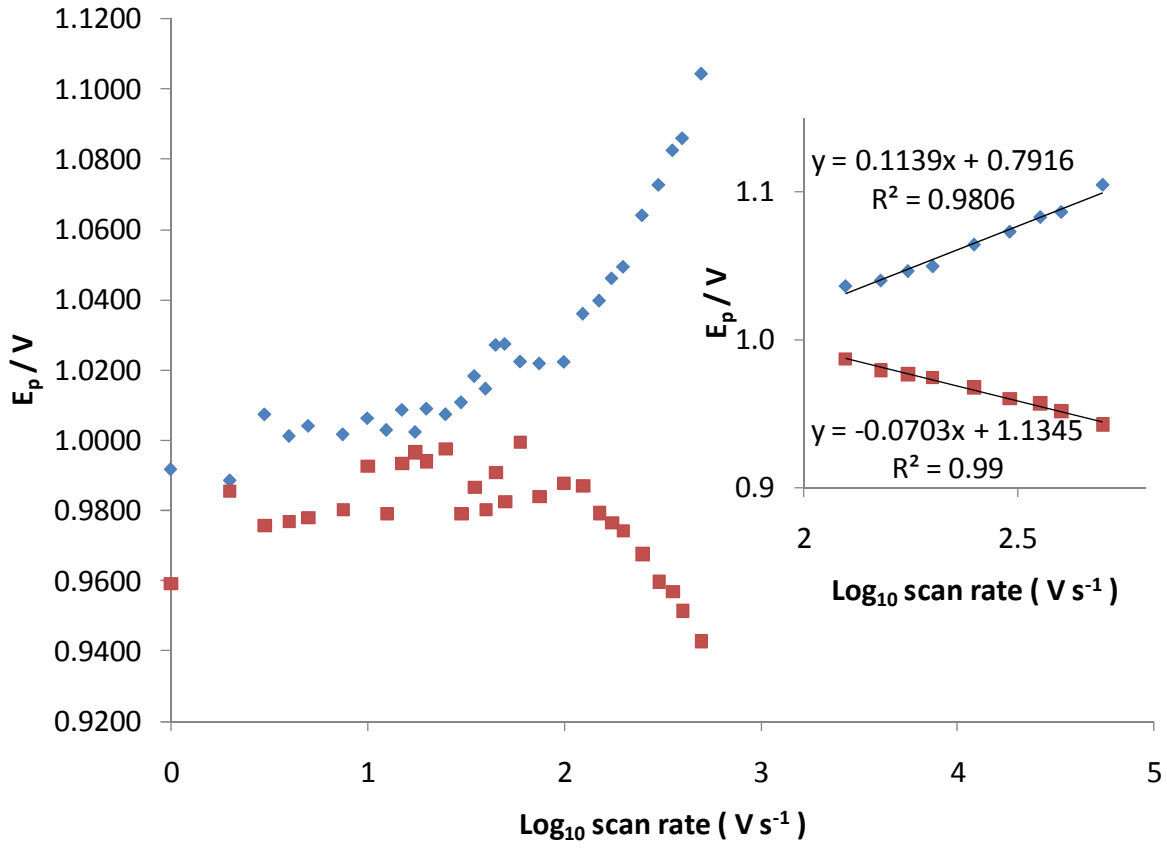


**Fig 3.3.2.8:** Laviron plot showing the dependence of the peak potential on the logarithm of scan rate for a Ru16D monolayer backfilled with 1-hexadecanethiol on a 3 mm diameter platinum. The inset shows the linear segments of the Laviron plots. All peak potentials were corrected for ohmic drop. All electrochemistry was carried out in ACN with 0.1 mM $TBAClO_4$ as the supporting electrolyte. All potentials are vs. $Ag/AgNO_3$ electrode and corrected against ferrocene. Values for $k^o$ were an average of two separate experiments.

| Complex | $E_{1/2}{}^{ox}{}_{Ru}{}^{2+/3+}$ (V) | | Surface Coverage (mol / $cm^2$) | | $k^o$ ($s^{-1}$) | |
|---|---|---|---|---|---|---|
| | Non-backfilled | Backfilled | Non-backfilled | Backfilled | Non-backfilled | Backfilled |
| Ru6D | 0.920 (± 0.010) | 0.945 (± 0.012) | $2.8\ e^{-11}$ (± $2.4\ e^{-12}$) | $1.5\ e^{-11}$ (± $1.5\ e^{-12}$) | 1375 (±239) | 1441 (±157) |
| Ru8D | 0.911 (± 0.009) | 0.940 (± 0.006) | $2.8\ e^{-11}$ (± $3.1\ e^{-12}$) | $2.2\ e^{-11}$ (± $3.2\ e^{-12}$) | 945 (±52) | 1189 (±113) |
| Ru11D | 0.921 (± 0.002) | 0.947 (± 0.012) | $2.9\ e^{-11}$ (± $4.4\ e^{-12}$) | $1.5\ e^{-11}$ (± $1.4\ e^{-12}$) | 1100 (±24) | 1056 (±131) |
| Ru16D | 0.922 (± 0.010) | 0.960 (± 0.008) | $2.9\ e^{-11}$ (± $1.7\ e^{-12}$) | $1.8\ e^{-11}$ (± $1.7\ e^{-12}$) | 1208 (±127) | 1247 (±142) |

| Complex | $\Delta E_p{}^{ox}{}_{Ru}{}^{2+/3+}$ (V) | | $FWHM_{Ru}{}^{2+/3+}$ (V) | |
|---|---|---|---|---|
| | Non-backfilled | Backfilled | Non-backfilled | Backfilled |
| Ru6D | 0.028 (± 0.002) | 0.023 (± 0.002) | 0.096 (± 0.007) | 0.112 (± 0.006) |
| Ru8D | 0.015 (± 0.004) | 0.026 (± 0.003) | 0.110 (± 0.006) | 0.110 (± 0.002) |
| Ru11D | 0.026 (± 0.004) | 0.029 (± 0.002) | 0.106 (± 0.009) | 0.112 (± 0.003) |
| Ru16D | 0.019 (± 0.004) | 0.015 (± 0.004) | 0.098 (±0.009) | 0.110 (± 0.004) |

**Table 3.3.1:** Surface monolayer electrochemical properties of RuxD complexes. All electrochemistry was carried out in ACN with 0.1 mM $TBAClO_4$ as the supporting electrolyte vs. $Ag/AgNO_3$ electrode at 20 V/s with the exception of the $\Delta E_p$ values which were taken at 1 V/s.

### *3.3.3 RuxD Monolayer Stability*

Due to the high formal potential of the ruthenium redox centre in the RuxD complexes all monolayer electrochemistry had to be performed on platinum electrodes with acetonitrile as the solvent although exposure of an alkanethiol monolayer covered electrode to organic solvents can lead to loss of thiolated monolayer from the surface[38]. As a result monolayer stability is poor and there is significant loss of RuxD complex from the monolayer during prolonged experiments, in particular the Laviron plot experiments that required the monolayer to be cycled electrochemically multiple times at varying scan rates. Figures 3.3.3.1 to 3.3.3.4 show the loss of RuxD from both nonbackfilled and backfilled monolayers during repetitive scanning at 0.1 $vs^{-1}$. Backfilling of the monolayers does not protect the monolayer from loss of surface coverage and loses surface coverage at around the same rate as nonbackfilled monolayers.

It is believed that this loss of surface coverage is caused by traces of water in the electrolyte. Monolayer stability is increased when anhydrous electrolyte and solvent is used and the $N_2$ used to purge oxygen from the solution and form a nitrogen blanket is first passed through a drying agent like anhydrous silica beads. Anhydrous electrolyte and dried $N_2$ were used in these experiments but substantial loss of surface coverage was still evident. Trace chloride could also be a factor since it can form a metal chloride with the electrode surface that is oxidised and removed at lower potentials than the metal. Changing the electrolyte to $TBACLO_4$ from $TBATBF_4$ resulted in a slight increase in stability. In tightly packed alkanethiol layers the organic solvent, in this case acetonitrile, can disrupt the close packing of the layer through non-polar interactions or even dissolving the monolayer moieties thus facilitating water or chloride interactions with the metal surface that would otherwise be blocked resulting in the metal surface being stripped away.

Backfilling of the RuxD monolayers should protect the monolayer from surface coverage loss more effectively than nonbackfilled monolayers. However, RuxD surface coverage is lost in the backfilled monolayers at practically the same rate as nonbackfilled monolayers. The RuxD moieties lying down flat on the electrode surface and buried in the

backfilling alkanethiol monolayer are more than likely disrupting the close packing of the alkanethiol layer facilitating interactions of chloride and water with the metal surface. These monolayer stability issues are further explored in the following section, 3.3.4.

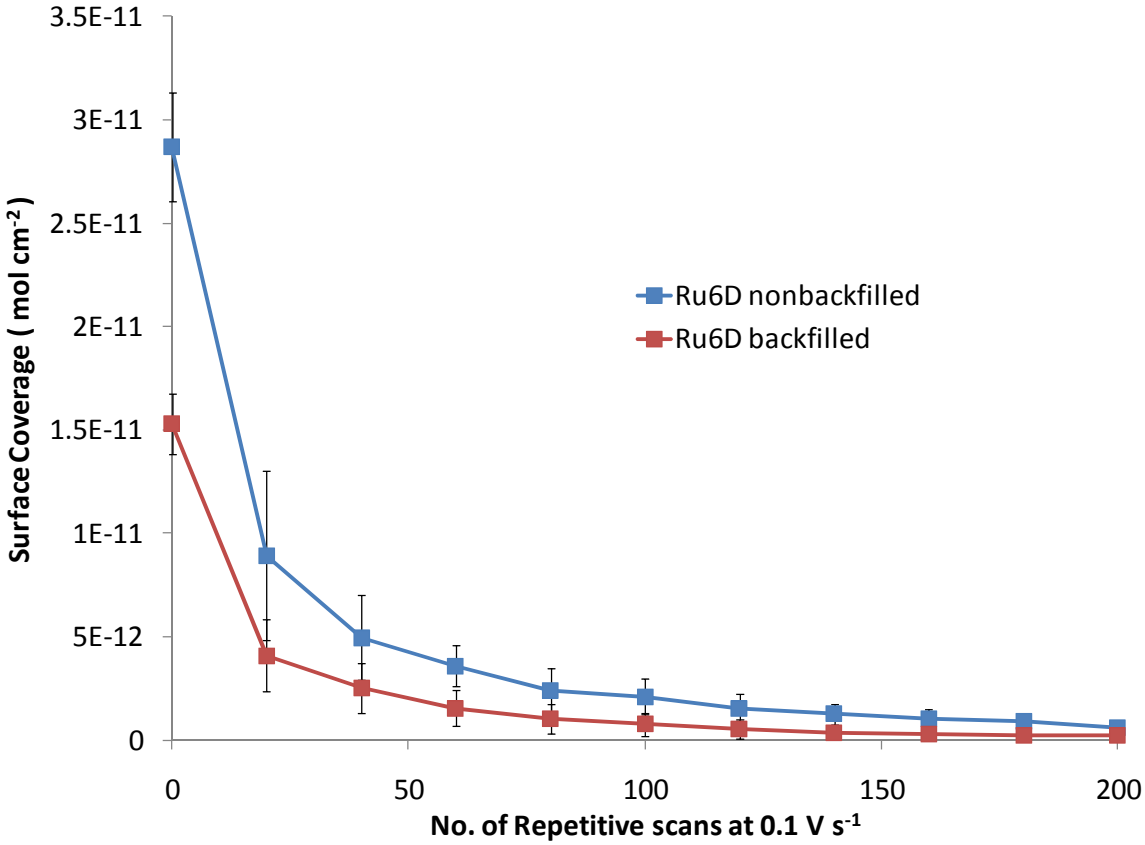


**Figure 3.3.3.1:** Graph comparing the nonbackfilled and backfilled stabilities of Ru6D monolayers on platinum electrodes**.** The monolayers were cycled from 0.5 V to 1.2 V and back again to 0.5 V repetitively at 0.1 $Vs^{-1}$ with Ru6D surface coverage measurements taken every 20 scans. A scanning cycle from 0.5 V to 1.2 V and then back to 0.5 V represents 2 scans. All electrochemistry was carried out in ACN with 0.1 mM TBA $ClO_4$ as the supporting electrolyte.

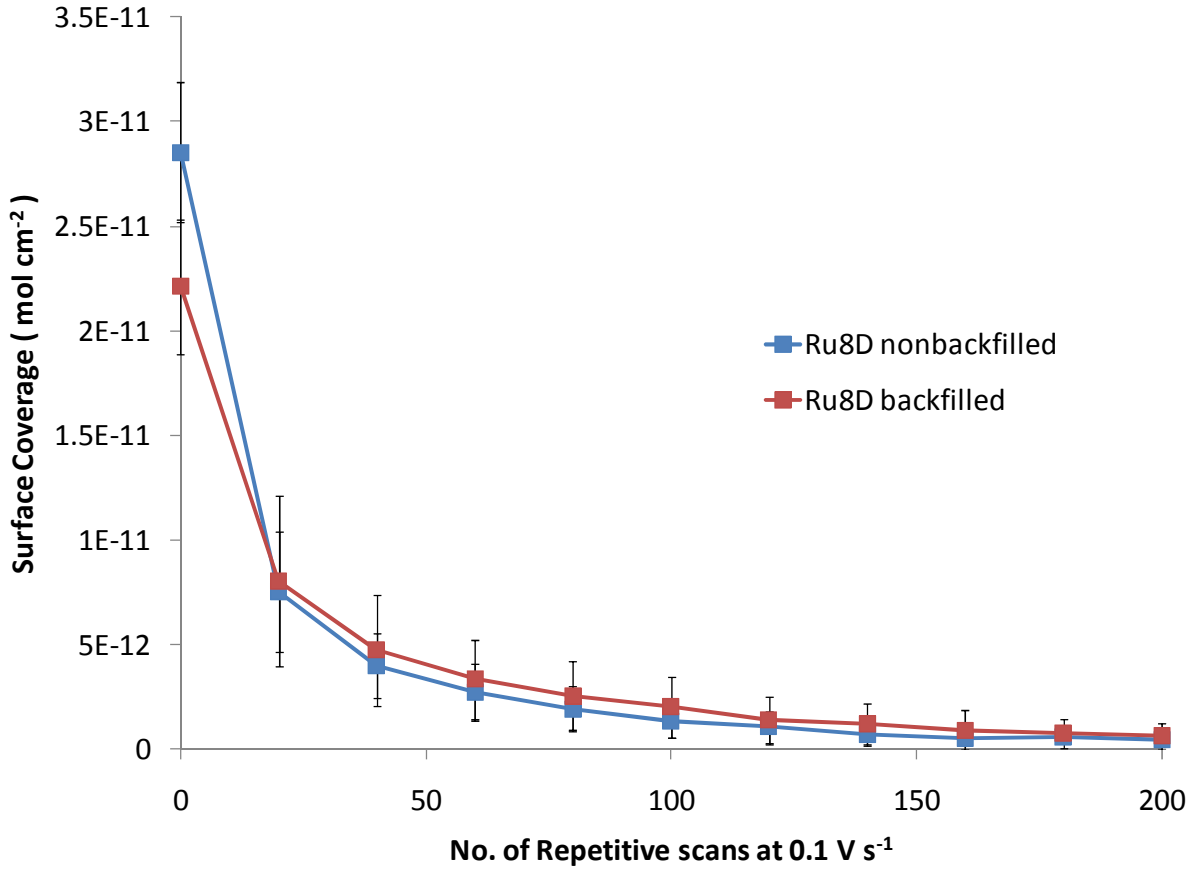


**Figure 3.3.3.2:** Graph comparing the nonbackfilled and backfilled stabilities of Ru8D monolayers on platinum electrodes**.** The monolayers were cycled from 0.5 V to 1.2 V and back again to 0.5 V repetitively at 0.1 $Vs^{-1}$ with Ru8D surface coverage measurements taken every 20 scans. A scanning cycle from 0.5 V to 1.2 V and then back to 0.5 V represents 2 scans. All electrochemistry was carried out in ACN with 0.1 mM TBA $ClO_4$ as the supporting electrolyte.

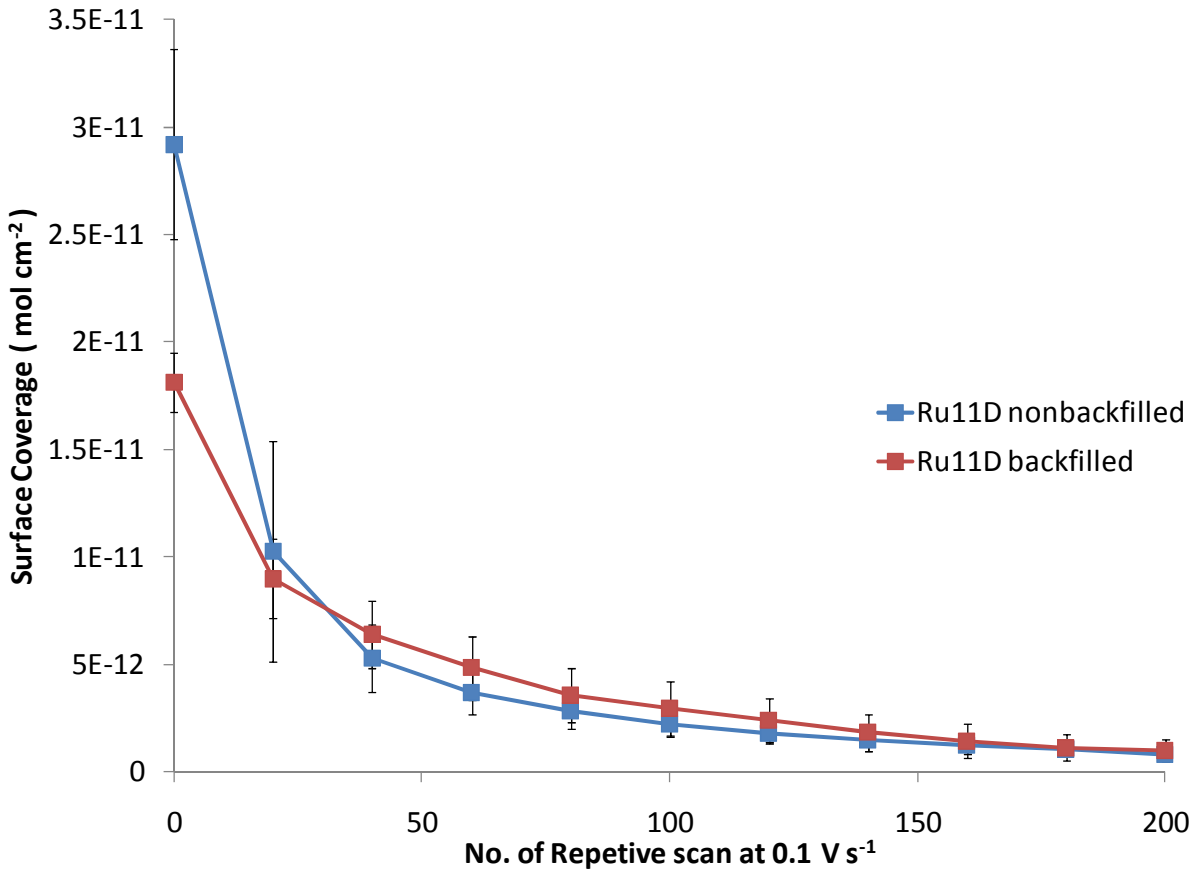


**Figure 3.3.3.3:** Graph comparing the nonbackfilled and backfilled stabilities of Ru11D monolayers on platinum electrodes**.** The monolayers were cycled from 0.5 V to 1.2 V and back again to 0.5 V repetitively at 0.1 $Vs^{-1}$ with Ru11D surface coverage measurements taken every 20 scans. A scanning cycle from 0.5 V to 1.2 V and then back to 0.5 V represents 2 scans. All electrochemistry was carried out in ACN with 0.1 mM TBA $ClO_4$ as the supporting electrolyte.

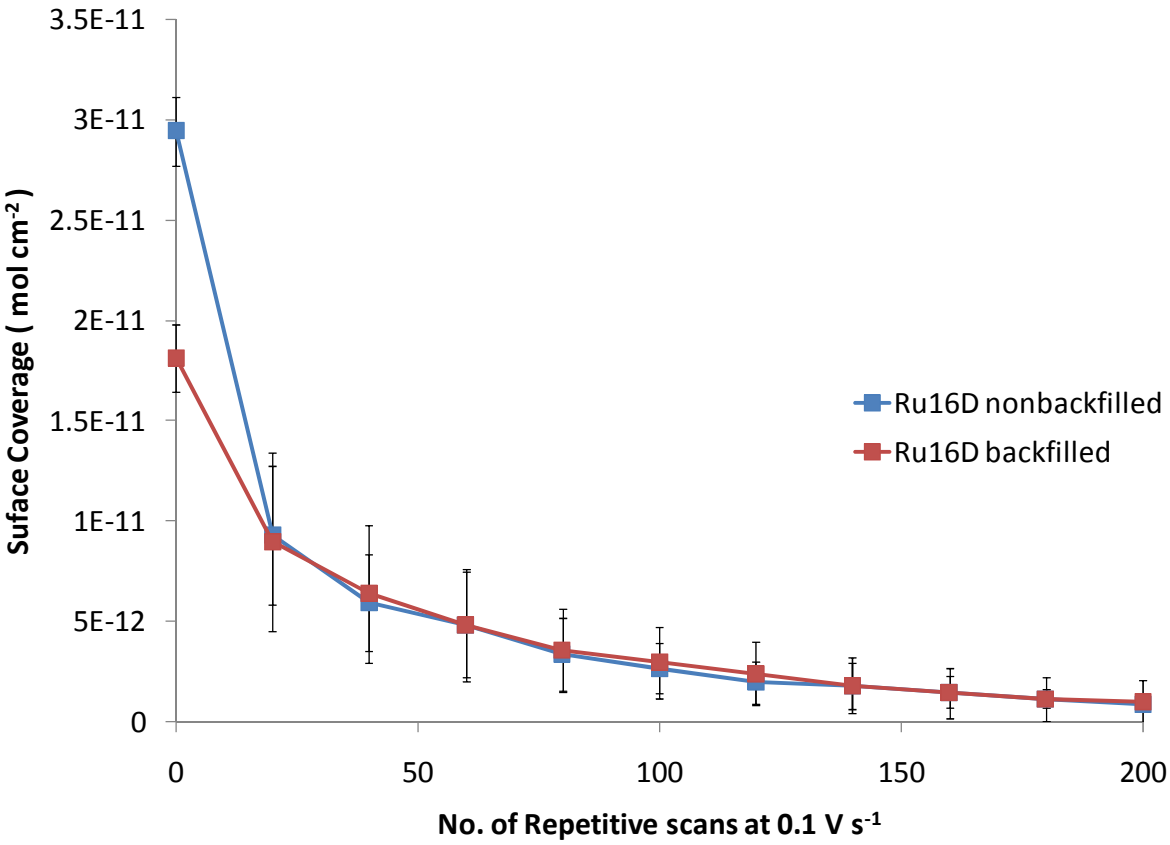


**Figure 3.3.3.4:** Graph comparing the nonbackfilled and backfilled stabilities of Ru16D monolayers on platinum electrodes**.** The monolayers were cycled from 0.5 V to 1.2 V and back again to 0.5 V repetitively at 0.1 $Vs^{-1}$ with Ru16D surface coverage measurements taken every 20 scans. A scanning cycle from 0.5 V to 1.2 V and then back to 0.5 V represents 2 scans. All electrochemistry was carried out in ACN with 0.1 mM TBA $ClO_4$ as the supporting electrolyte.

### *3.3.4 RuxD Monolayers on Gold Surfaces*

All electrochemical analysis of the RuxD complexes had to be carried out on Pt surfaces due to the high anodic $Ru^{2+/3+}$ redox process. Monolayers of RuxD complexes were formed on gold electrodes to confirm that binding of the RuxD complexes to the metal surface is through a metal sulphur M-S bond. Evidence of the assembly of RuxD complexes as monolayers through S-Au bonds on gold electrodes was confirmed by sulphur reductive desorption. Sulphur reductive desorption was only carried out on Ru8D nonbackfilled monolayers. The Ru8D monolayer was scanned from 0 V to -1.3 V at a scan rate of 0.05 $Vs^{-1}$ in 0.1 M TBA $ClO_4$ in ACN. At sufficiently negative potentials the sulphur to gold bonds are reduced and cleaved. Fig 3.3.4.1 shows a cyclic voltagramm of this experiment. Surface coverages were calculated from the charge under the sulphur desorption process and was found to be about $1.5e^{-10}$ mol $cm^{-2}$, a larger surface coverage than the same monolayers on a Pt surface possibly indicating more ordered monolayers on gold surfaces. For alkanethiol monolayers it has been reported that surface coverages are normally similar if slightly higher on platinum surfaces than gold. Petrovykh *et al*.[39] demonstrated by X-ray photoelectron microscopy (XPS) measurements that monolayers of 1-hexanethiol, 1-dodecanethiol and 1-decoctanethiol on platinum have surface coverages of about $9.1e^{-10}$ – $1e^{-10}$ mol $cm^{-2}$. The surface coverage of 1-hexanethiol on gold was calculated to be $7.47e^{-10}$ mol $cm^{-2}$ which was in agreement with previous reported surface coverage calculations. Despite the higher binding energy of Au-S compared to Pt-S, 418 kJ/mol and 234 kJ/mol respectively[39], it would seem that the lower surface coverage of RuxD monolayers on platinum compared to gold is not dependent on these binding energies. Another factor could be the binding of the dpp ligands to the metal surface as discussed in Sections 3.3.1 and 3.3.2. Wieckowski *et al*.[32] calculated the Gibbs free energy of adsorption of pyridine complexes to gold in a horizontal configuration to be 30 kJ/mol, which corresponds to a rather weak physisorbed reaction compared to the binding energy of the Au-S or Pt-S bonds, which are 418 and 234 kJ/mol respectively. As the concentration of pyridine in the deposition solution was increased the pyridine configuration changed to a vertical configuration. Wieckowski *et al*.[33] also reported on pyridine binding to platinum surfaces although no Gibbs free energy of adsorption was calculated for pyridine binding to platinum in the horizontal configuration. At low concentrations pyridine had a horizontal configuration. However, as the concentration of pyridine in the deposition solution was increased vertical orientation of the pyridine layer did

not occur. This could correspond to a much stronger adsorbtion bond between pyridine and platinum than with gold. This could result in the dpp to platinum bonds of the RuxD complexes to be strong enough to resist displacement by Pt-S bonds of an alkanethiol layer.

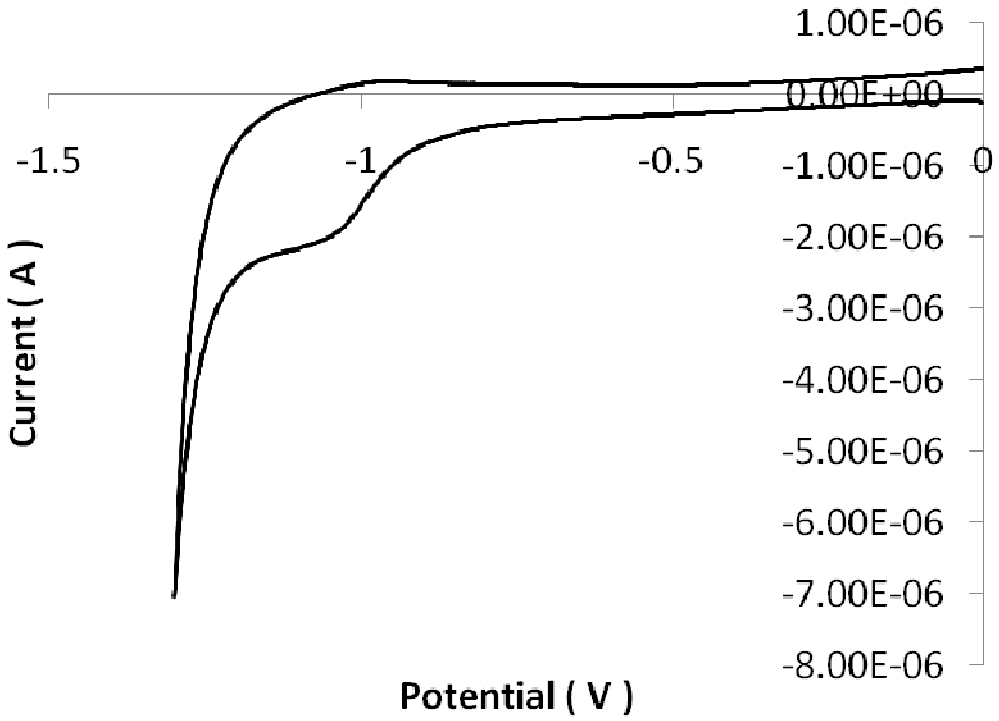


**Fig 3.3.4.1:** Cyclic voltammagram for reductive desorption of a nonbackfilled Ru8D monolayer on a polished Au electrode. All electrochemistry was carried out in ACN with 0.1 mM TBA $ClO_4$ as the supporting electrolyte. Solutions were purged of oxygen with $N_2$. All potentials are vs. $Ag/AgNO_3$ electrode and corrected against ferrocene. A scan rate of 0.05 V $s^{-1}$ was used.

XPS was carried out on backfilled monolayers of Ru6D and Ru16D on silicon wafers sputter coated with smooth gold surfaces. The results are detailed for backfilled Ru6D and Ru16D monolayers on gold in Fig 3.3.4.2 and 3.3.4.3 respectively. More detailed XPS data is available in the Appendix. Of particular note are the Atomic abundance percentage figures. These do not correlate with the results expected from a backfilled monolayer of RuxD on gold. The ratio of ruthenium 3d5 to nitrogen 1s is close to 1:7 which would be expected as it is the same ratio of ruthenium to nitrogen in the chemical formula of the RuxD complexes. However the ratio of nitrogen 1s to oxygen 1s is completely different to the expected value of

7:1. The measured ratio of nitrogen 1s to oxygen 1s is about 3:15 for both the backfilled Ru6D and Ru16D monolayers.

All experiments with RuxD monolayers in this chapter are carried out on freshly prepared monolayers with the exception of these XPS experiments which were carried out on 2 week old samples since the work was carried out in Montpellier Institut Charles Gerhardt. The large O 1s signal is probably due to oxidation of the Au-S bonds to form sulfonates and sulfinates which can lead to loss of monolayer surface coverage. This is confirmed by the presence of a peak at about 167 eV which corresponds to the S 2p electron of oxidised sulphur[39, 40]. This rapid degradation of thiolate monolayers on gold in ambient conditions has been reported by Willey *et al.*[40] who showed the rapid degradation of 1-dodecanethiol monolayers on gold over 24 hours. Using XPS it was shown that the C 1s signal in ambient conditions decreases by around 30% after 24 hours. These samples also show the presence of an oxygen 1s signal at about 531 eV and a sulphur 2p peak at 167 eV, which is characteristic of oxidised sulphur. Both O s1 and oxidised S 2p are not present in the freshly made monolayer samples which due to oxidation of sulphur in the Au-S bonds. The generation of oxidising $O_3$ is thought the primary culprit for oxidising thiol monolayers in this system. Petrovykh *et al.*[39] also reported on the degradation of 1-hexanethiol and 1-octadecanethiol from platinum surfaces. XPS analysis of the monolayers also showed a decrease C 1s peak and an increase in the O 1s peak.

The orientation of the RuxD complexes, which from the electrochemistry of the monolayers, are expected to be lying flat on the metal surface in both backfilled and nonbackfilled monolayers would lead to monolayers with more defect sites than the alkanethiols reported in references 39 and 40. The defective nature of these monolayers will lead to the greater accessibility of the Au-S bonds to oxidising agents such as $O_3$. Even partial oxidisation of the sulphur in the Au-S bond to sulphonites could be responsible for the poor stability of the RuxD monolayers which is exasperated by the defective nature of the monolayers. Freund, Ferguson *et al.*[41] demonstrated that the surface roughness of the metal surface is an important factor in how efficiently the Au-S bonds are oxidised. XPS data showed that for monolayers of 1-dodecanethiol on gold an increase in the surface roughness and, therefore, defects in the monolayer lead to an increase in the oxidation of Au-S to

sulphonite and sulphonate. The destruction of the Ru6D and Ru16D backfilled monolayers over such a short timeframe shows how accessible the Au-S bonds in the monolayers are to oxidative damage and thus how defective these monolayers are.

(a)

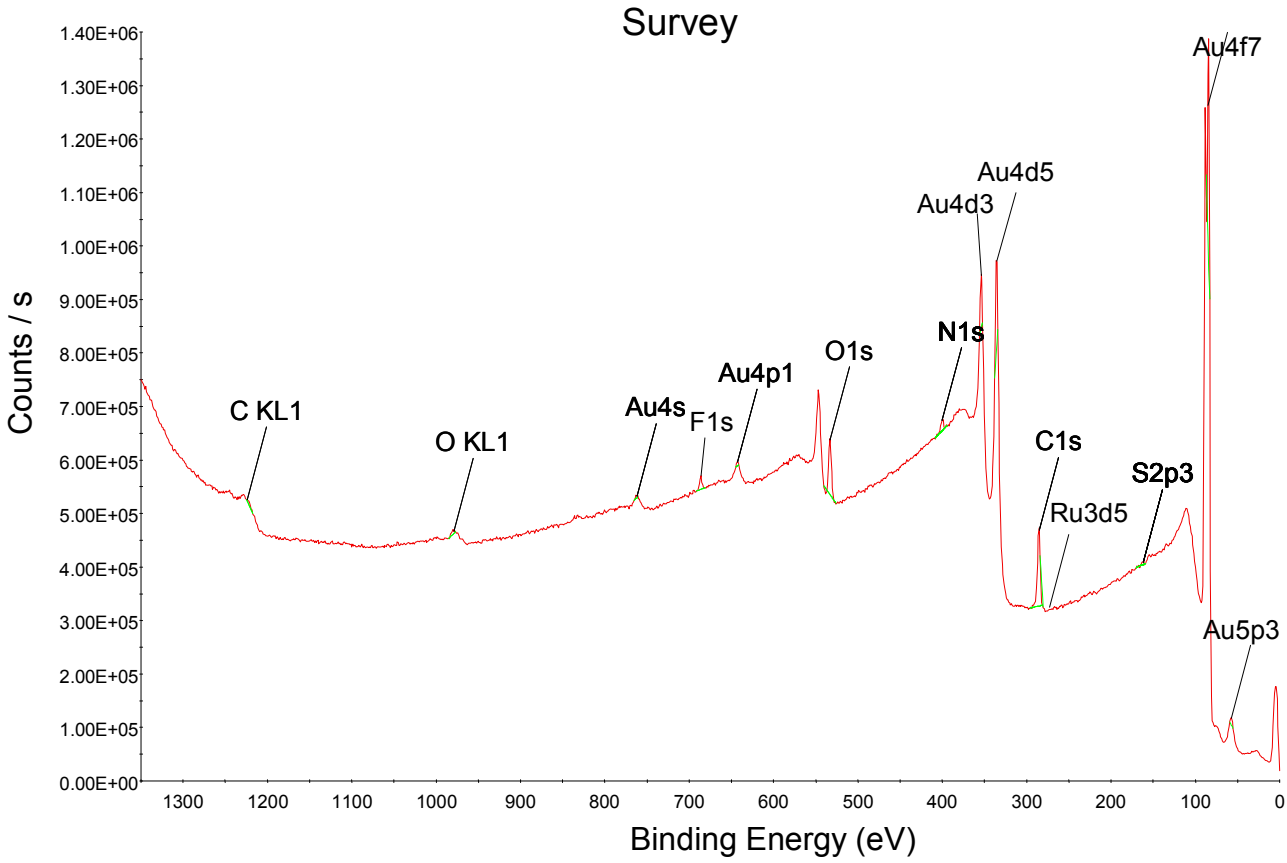


(b)

| Name | Peak BE | Height Counts | FWHM eV | Area (P) CPS.eV | Area (N) | At. % |
|---|---|---|---|---|---|---|
| Au4f | 84.00 | 237738.76 | 0.69 | 351567.80 | 0.47 | 32.95 |
| S2p | 162.11 | 521.90 | 2.28 | 1125.86 | 0.02 | 1.09 |
| Ru3d5 | 281.20 | 1793.60 | 0.92 | 1773.54 | 0.01 | 0.39 |
| C1s | 284.92 | 15828.51 | 1.58 | 29247.91 | 0.67 | 47.56 |
| N1s | 400.20 | 2478.58 | 1.19 | 3419.91 | 0.04 | 3.13 |
| O1s | 533.29 | 9174.95 | 2.96 | 26039.08 | 0.21 | 14.89 |

**Figure 3.3.4.2:** XPS data for a backfilled Ru6D monolayer on a gold surface. (a) Wide Scan XPS spectrum of backfilled Ru6D monolayer on a gold surface. (b) Table of XPS data including atomic abundance values.

(a)

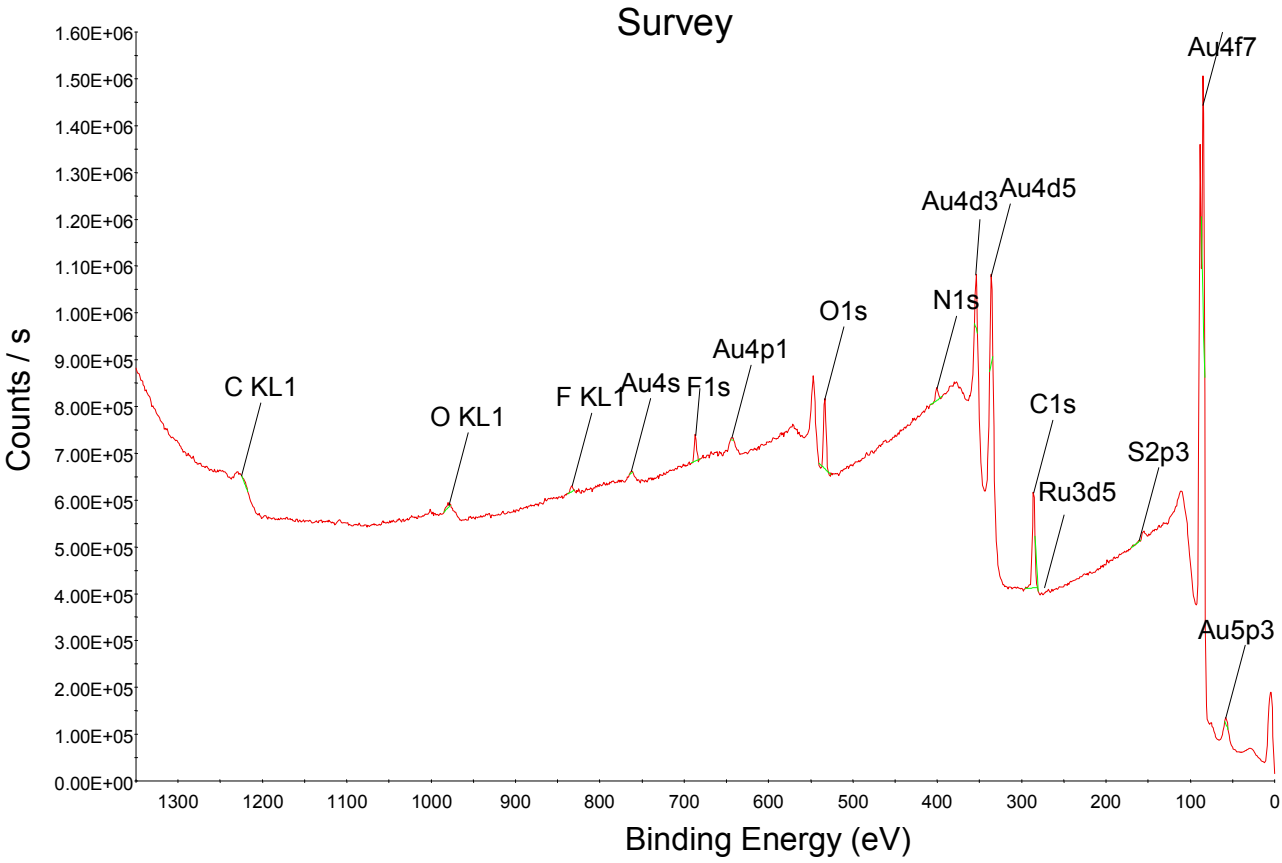


(b)

| Name | Peak BE | Height Counts | FWHM eV | Area (P) CPS.eV | Area (N) | At. % |
|---|---|---|---|---|---|---|
| Au4f | 84.03 | 170541.60 | 0.67 | 249982.01 | 0.33 | 27.44 |
| S2p | 162.10 | 325.43 | 0.64 | 635.99 | 0.01 | 0.72 |
| Ru3d5 | 281.39 | 1427.44 | 0.87 | 1334.38 | 0.00 | 0.34 |
| C1s | 285.06 | 14654.87 | 1.59 | 27221.24 | 0.63 | 51.85 |
| N1s | 400.37 | 2288.63 | 1.23 | 3265.97 | 0.04 | 3.50 |
| O1s | 533.20 | 9871.00 | 2.00 | 24110.79 | 0.20 | 16.14 |

**Figure 3.3.4.3:** XPS data for a backfilled Ru16D monolayer on a gold surface. (a) Wide Scan XPS spectrum of backfilled Ru16D monolayer on a gold surface. (b) Table of XPS data including atomic abundance values.

### *3.3.5 RuxD Monolayers Raman Spectroscopy and Photophysics*

Raman studies of monolayers on RuxD complexes on gold and platinum proved very difficult due to the low surface of the monolayers. Raman spectra on platinum electrodes produced very noisy spectra due to the background reflectance from the platinum surface. This swamped out all Raman signals even when exciting into the MLCT absorption band of the RuxD complexes to achieve a Resonance condition. Due to the high energy plasmon of platinum in the UV region no laser was available with a wavelength of high enough energy to allow SERS spectra to be collected. On gold electrodes using regular Raman and resonance Raman the signal was swamped by the background and reflectance signal of the gold electrode. Even using an excitation wavelength of 632nm from a Helium-Neon laser to excite into the gold Plasmon led to poorly resolved and noisy SERS spectra even on electrochemically roughened gold.

Figure 3.3.5.1 shows the SERS spectrum of a Ru8D monolayer on a roughened gold electrode. Peaks at 579, 1263, 1399, 1448, 1513, 1587 and 1599 $cm^{-1}$ that are also present in the resonance Raman spectra appear in the SERS spectrum with slight red shifting. There is also large broadening and enhancement of the mode located at 579 $cm^{-1}$. This normally corresponds to the ring breathing modes of the RuxD complex. All peaks are poorly defined due to the high background noise and weak signal strength. The SERS peaks are quite broad probably due to the innate broadening of Raman in SERS spectra, explained in more detail in Section 3.3.7. The large enhancement of these ligand modes would suggest that the ligands are located quite close to the gold surface, which is further evidence of the lying down orientation of these complexes.

It was originally thought that a chromophore in close proximity to a metallic surface, as in a monolayer, would experience complete luminescence quenching through fast energy transfer to the surface. However, it has been reported that although there can be significant quenching of the excited luminescence state, luminescence may not be completely quenched by the metallic surface in these assemblies.[42,43] For example Kamat *et* al.[44] recorded luminescence from gold nanoparticles that had been modified with 1-methylaminopyrene on

the surface. Surface enhanced fluorescence effects have also been reported where normally weak luminophores close to metallic surfaces experience enhanced quantum yield and reduced luminescence lifetimes. However, this effect is only significant in normally extremely weakly luminescent molecules such as DNA[45] and as long as some distance is kept between the chromophore and the surface. Figure 3.3.5.2. shows the luminescence of a nonbackfilled Ru8D monolayer on a roughened gold electrode excited at 514nm, the luminescence of the RuxD monolayers is not completely quenched despite the luminophore centres being in close proximity to the metal surface. An excitation wavelength of 514 nm was used since this wavelength allowed a complete luminescence spectrum to be recorded on the Raman spectrometer employed. When 458 nm and 488 nm excitation lines were used the luminescence spectrum was cut off. The $\lambda_{max}$ of emission has significantly red shifted to about 640-650 nm from the $\lambda_{max}$ of emission of the RuxD complexes in solution at 608 nm. A luminescence intensity comparison between different RuxD monolayers proved impossible with the current instrument set up as the intensity of the detected luminescence was very sensitive to the focus of the laser and detector which was manually controlled and the lack of any standard for comparison.

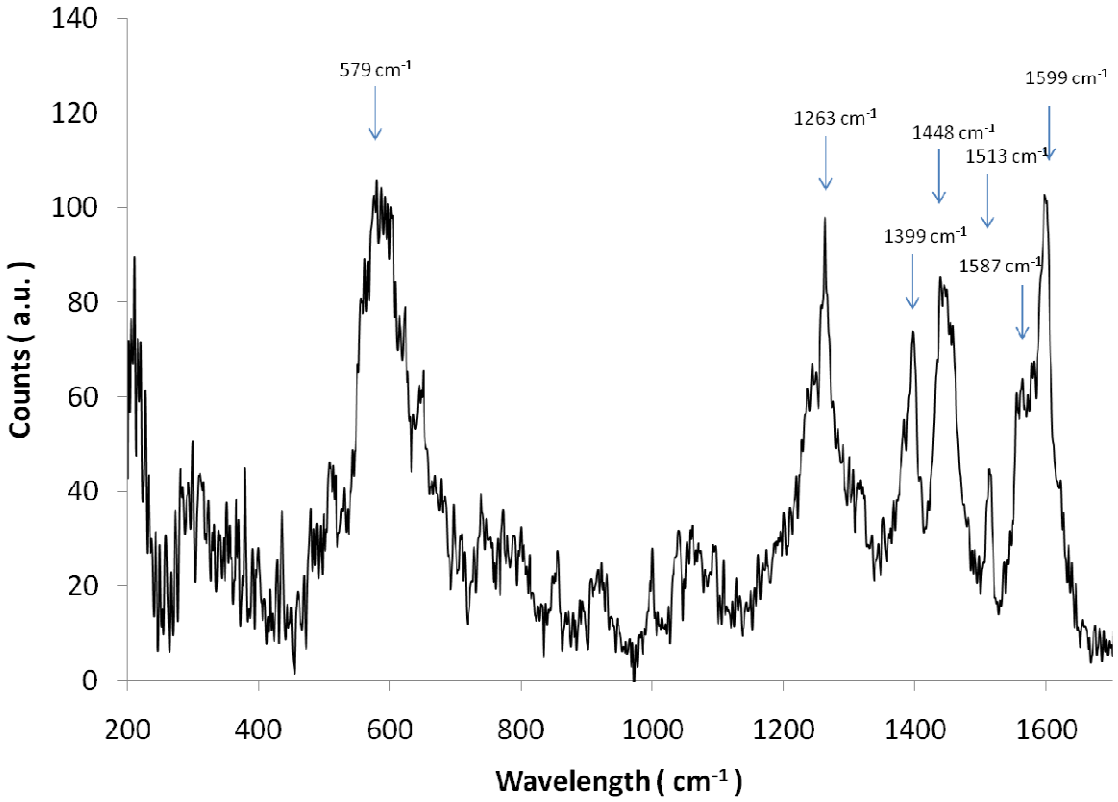


**Figure 3.3.5.1:** SERS spectrum of nonbackfilled Ru8D monolayer on an electrochemically roughened 3 mm gold electrode. An excitation wavelength of 632 nm from a He-Ne laser was used.


**Figure 3.3.5.2:** Emission spectrum of dry Ru8D monolayer on roughened gold electrode. An excitation wavelength of 514 nm was used.

### *3.3.6 Colloidal Suspensions of RuxD Functionalized Nanoparticles*

SERS and luminescence analysis of Au nanoparticles functionalised with RuxD complexes was carried out to assess these functionalised nanoparticles potential as SERS and luminescence cell imaging agents. The UV-vis absorption spectra of all nonbackfilled RuxD functionalised 50 nm Au nanoparticles in colloidal suspension are show in Fig. 3.3.6.1. Samples were not concentration matched or normalised due to the poorly defined UV-vis absorption spectra of these functionalised nanoparticles. All characteristic absorbance bands of the RuxD complexes are dominated by the plasmon absorbance from the nanoparticles, which has been reported in other studies of chromophore functionalized nanoparticles[46]. The plasmon is much broader in the case of the modified nanoparticles compared with their unfunctionalised counterparts and features two absorbance maxima centred at around 610-630 nm and 550 nm. Unfunctionalised nanoparticles have a much narrower absorbance centre

at 530 nm. This is more than likely a longitudinal mode of caused by the combination of absorption spectra of particles of two or more size distributions. Some aggregation of the nanoparticles and a change in nanoparticle size has more than likely occurred during the functionalisation process. There is a visible change in the colour of the colloidal suspension, unfunctionalised nanoparticle suspensions have a red colour while the RuxD functionalised colloidal suspensions have a purple/wine colour. Without a visible characteristic absorption band for the RuxD complexes in the functionalised nanoparticle UV-vis absorption spectra it is difficult to quantify a ratio of RuxD molecules per nanoparticle. Calculation of the concentration of functionalised nanoparticles was also difficult due to the change in the UV-vis absorption band of the nanoparticles upon functionalisation. The change in the surface plasmon suggests a change in the size of the nanoparticles therefore a calculation of nanoparticle concentration using the extinction co-efficient of the unfunctionalised nanoparticles would be an estimate at best. Some agglomeration is also expected to occur and result in a broadening of the absorption spectrum, when left to stand the functionalised nanoparticles will stick to the sides of any container they are in or precipitate out in the presence of high concentrations of $NaSO_4$.

Fig. 3.3.6.2 shows the emission spectrum of the RuxD functionalised nanoparticles in a colloidal suspension. Again samples could not be concentration matched or normalised for the same reasons given. Although the emission intensity is extremely weak it shows that the luminescent excited state of the RuxD complexes is not entirely quenched by their close proximity to the metal nanoparticle. The functionalised nanoparticles were thoroughly washed with 50:50 EtOH:Water (v/v) and sonicating between each washing step to remove unbound any unbound or loosely bound RuxD from the solution, therefore emission is not due to free RuxD in solution. Luminescence lifetime measurements in later in this section confirm this. The concentration of dye molecules on the surface of the Au nanoparticle is expected to be very low which could account for the weak emission signal. Quenching of the luminescent excited state is also expected to largely contribute to the weak emission intensity and is made worse by the orientation of the RuxD complexes lying flat on the surface. Luminescence of RuxD complexes on a metallic surface appears very weak in comparison to monolayers of other Ru(II) complexes. Forster *et al.*[47] showed that monolayers of $[Ru(bpy)_2(Qbpy)]^{2+}$ on a platinum electrode displayed luminescence intensity comparable to a degassed solution of $[Ru(bpy)_2(Qbpy)]^{2+}$ in 4:1 v/v ethanol:methanol when luminescence

intensity is normalised by concentration. The high fluorescence in this case is probably due to a SEF enhancement. RuxD monolayers are too close to the electrode surface and thus luminescence quenching negates any SEF effect.

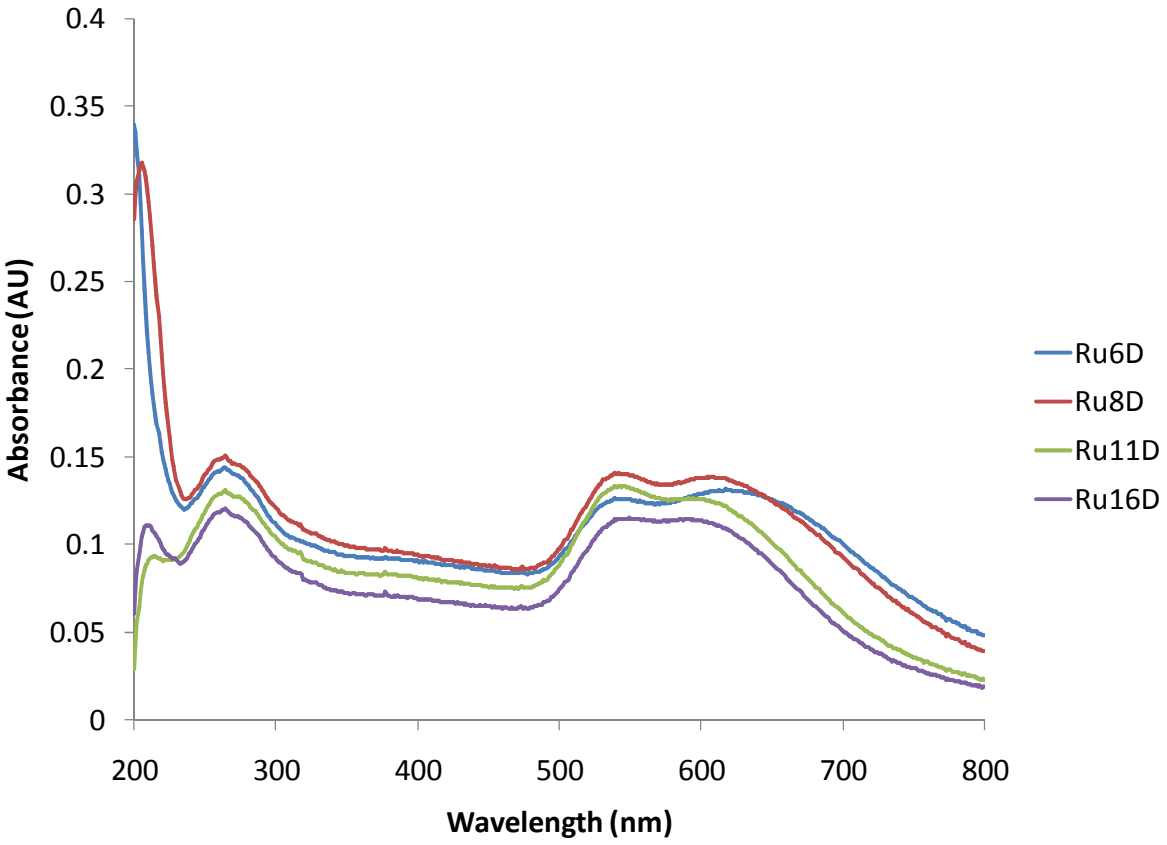


**Figure 3.3.6.1:** UV-vis absorption spectra for nonbackfilled RuxD modified 50 nm Au nanoparticles. All samples are suspended in 50:50 $H_2O$: EtOH v/v.

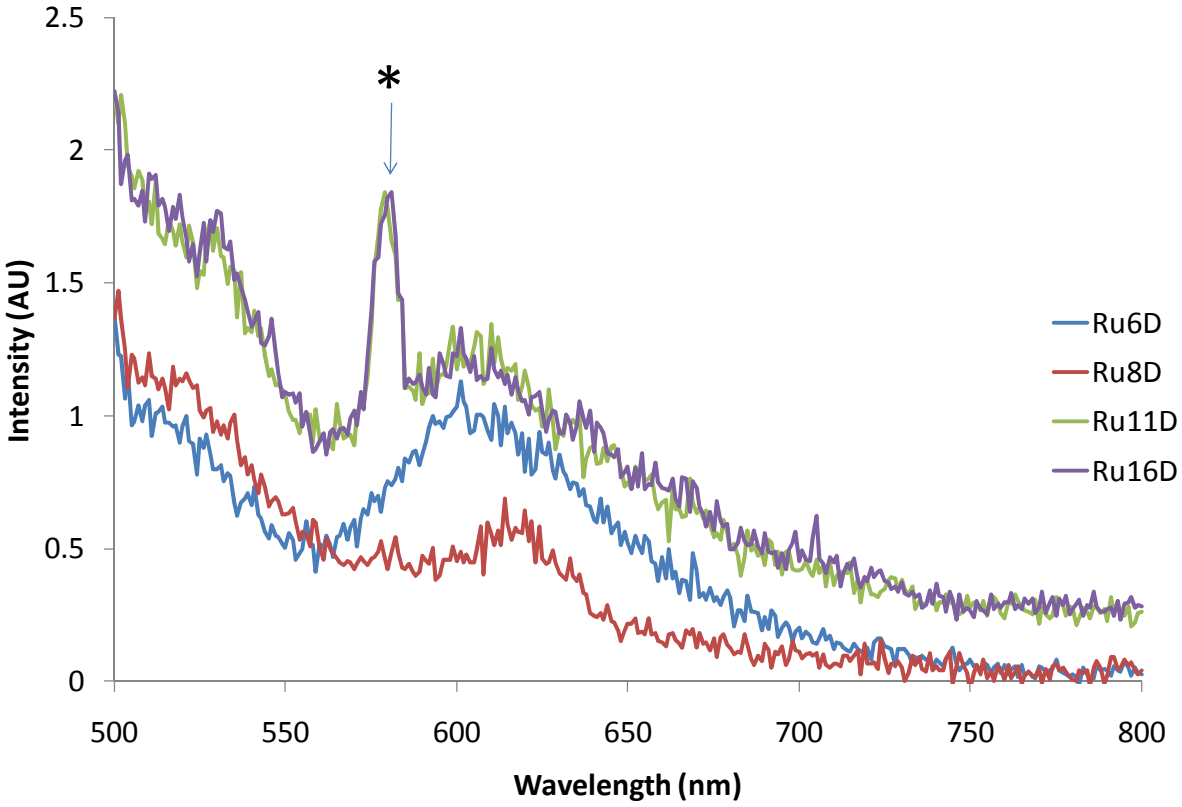


**Figure 3.3.6.2:** Emission spectra of nonbackfilled RuxD modified 50 nm Au nanoparticles. All samples are suspended in 50:50 $H_2O$: EtOH v/v. An excitation wavelength of 454 nm was used. * denotes a water Raman line.

Table 3.3.2 lists the luminescent lifetimes of the colloidal suspensions of the RuxD functionalised 50 nm Au nanoparticles. After reconvoluting with the IRF the collected decay integrates for 3 distinct lifetime decays for all RuxD modified complexes. One lifetime between 4 ns is a background lifetime from the SPC filters and can be discounted. The remaining two lifetime components consist of a short lifetime decay of about 1ns and a much longer lifetime of ~100 ns. The short component of about 1 ns is attributed to the intrinsic fluorescence from the gold nanoparticles which is usually around 1 ns. The remaining long lifetime component is attributed to RuxD bound to the gold nanoparticles. This long lifetime component is too short to be due to emission from RuxD in solution which was found to be ~180 ns in Chapter 2. The distance between RuxD free in solution and the nanoparticle surface would be too great for any quenching process to occur and no affect on the luminescence lifetime would be observed if it was due to RuxD free in solution. There is a trend of increasing luminescent lifetime with chain length for the long lifetime component,

indicating that on gold surfaces the RuxD complex may not be absorbed to the surface as seen with the monolayers of RuxD on platinum electrodes in Sections 3.3.1. and 3.3.2. The decay is also quite long lived if the complex was so close to the surface, for example . Forster, Keyes *et al*[48]. reported on the lifetime of $[Ru(bpy)_2(Qbpy)]^{2+}$ decreasing from 306 ns in solution to less than 20 ns as a monolayer on the surface of gold nanocavities. In a vertical orientation the distance of the metal centre from the metal surface would be much greater for RuxD complexes in comparison to $[Ru(bpy)_2(Qbpy)]^{2+}$.

| | **Ru6D functionalised Au nanoparticles** | | **Ru8D functionalised Au nanoparticles** | | **Ru11D functionalised Au nanoparticles** | | **Ru16D functionalised Au nanoparticles** | |
|---|---|---|---|---|---|---|---|---|
| | Lifetime (ns) | Fractional amplitude | Lifetime (ns) | Fractional amplitude | Lifetime (ns) | Fractional amplitude | Lifetime (ns) | Fractional amplitude |
| (a) | 89.7 (±7.0) | 2.36 % ( ±0.014%) | 113.8 (±1.9 ) | 1.5% (±0.39%) | 126.3 (±6.9 ) | 3.79% (±0.08%) | 164.2 (±0.3) | 1.38% (±0.1%) |
| (b) | 4.4 (±0.28) | 20.29% (±0.26%) | 4.2 (±0.28) | 14.8% (±1.9%) | 5.15 (±0.07) | 22.97% (±2.3%) | 6.15 (±0.07) | 27.0% (±0.01%) |
| (c) | 0.98 (±0.03) | 77.35% (±0.28%) | 0.95 (±0.07) | 83.7 (±2.3%) | 1.19 (±0.014) | 73.25% (±0.21%) | 1.35 (±0.07) | 71.63% (±0.01%) |

**Table 3.3.2:** Table of luminescent lifetimes of RuxD functionalised 50 nm Au nanoparticles. Samples were suspended in 50:50 $H_2O$: EtOH and an excitation wavelength of 450nm was used. (a), (b) and (c) represent the lifetime components from longest to shortest respectively.

### *3.3.7 Particle Size Analysis of RuxD Functionalised Gold Nanoparticles*

The size of the RuxD functionalised nanoparticles were measured by laser diffraction particle sizing, the results of which are detailed below in Table 3.3.3. Example particle size distributions are presented in Fig 3.3.7.1 – 3.3.7.4. The diameter of the RuxD functionalised nanoparticles are about 300 nm, far larger than 50 nm of the initial unfunctionalised nanoparticles. Aggregation of the nanoparticles is thought to cause this increase in particle size. The colloidal functionalised nanoparticle solutions could not be filtered resulting in the large contaminant outlier signals seen is the size distribution charts in Fig 3.3.7.1 – 3.3.7.4. If the RuxD functionalised nanoparticles are filtered the nanoparticles adhere to the filter resulting in total loss of the nanoparticles.

Attempts were made to acquire zeta potentials for the RuxD functionalised nanoparticles. However the results for the zeta potentials varied widely between about 15 mV to -15 mV even when taking repeat measurements on the same samples. This is more than likely due to the samples being unfiltered contaminated with large particulates such as dust. However such low zeta potentials would indicate weak electrostatic repulsion between the nanoparticles leading to aggregation.

| **Diameter of RuxD functionalised nanoparticles (nm)** | | | |
|---|---|---|---|
| Ru6D | Ru8D | Ru11D | Ru16D |
| 304 ( ±19 ) | 287 ( ±26 ) | 364 ( ±25 ) | 288 ( ±58 ) |

**Table 3.3.3:** Diameters of RuxD gold nanoparticles measured by laser diffraction particle sizing. Results are based on the average of 3 samples.

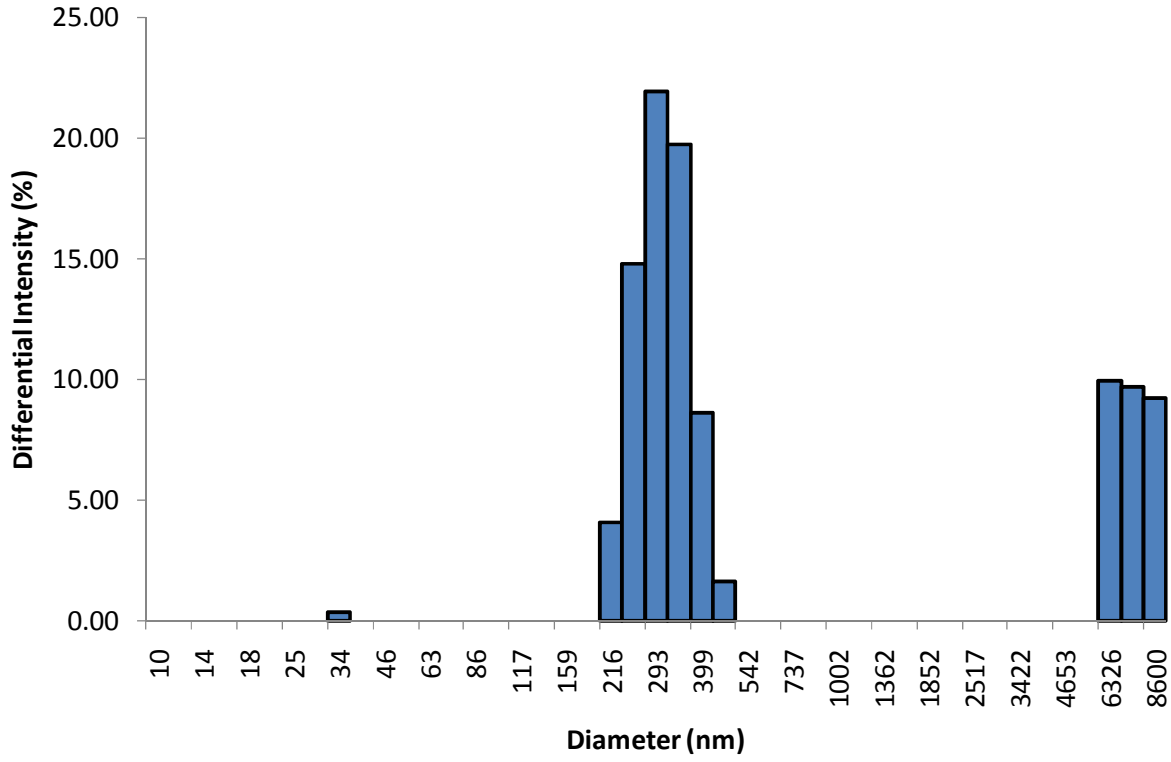


**Figure 3.3.7.1:** Particle size distribution for Ru6D functionalised 50 nm nanoparticles.

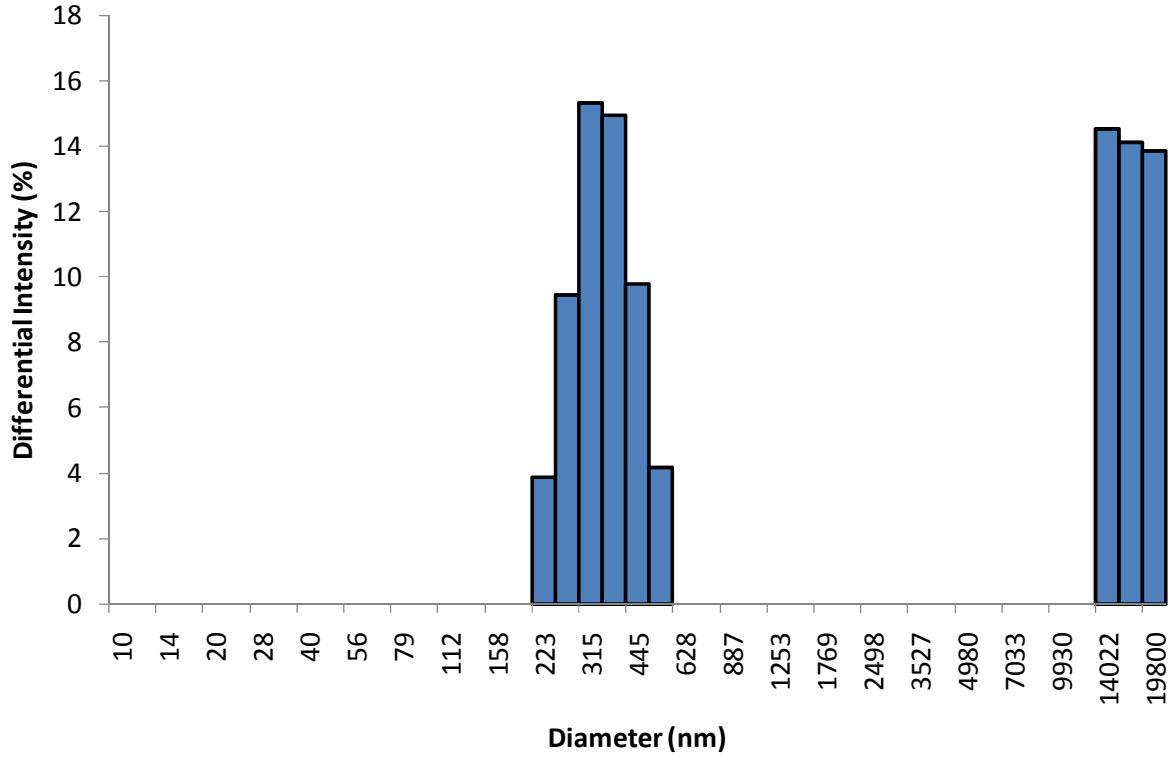


**Figure 3.3.7.2:** Particle size distribution for Ru8D functionalised 50 nm nanoparticles.

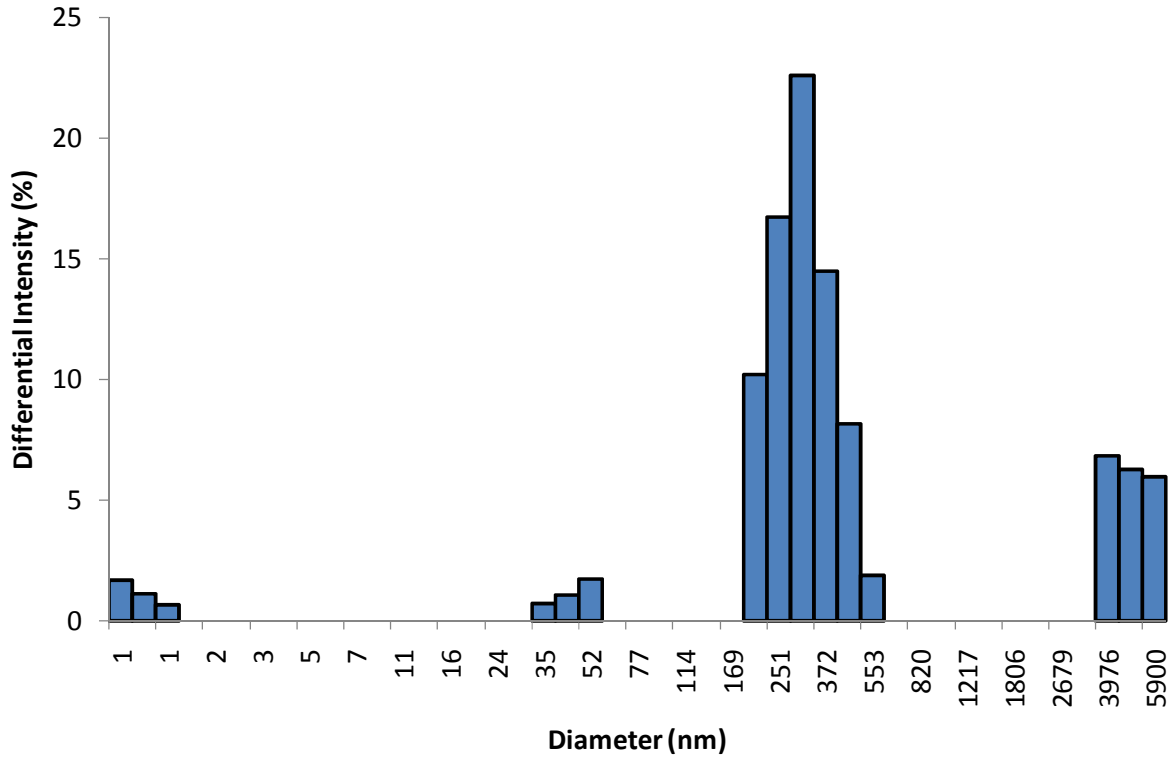


**Figure 3.3.7.3:** Particle size distribution for Ru11D functionalised 50 nm nanoparticles.

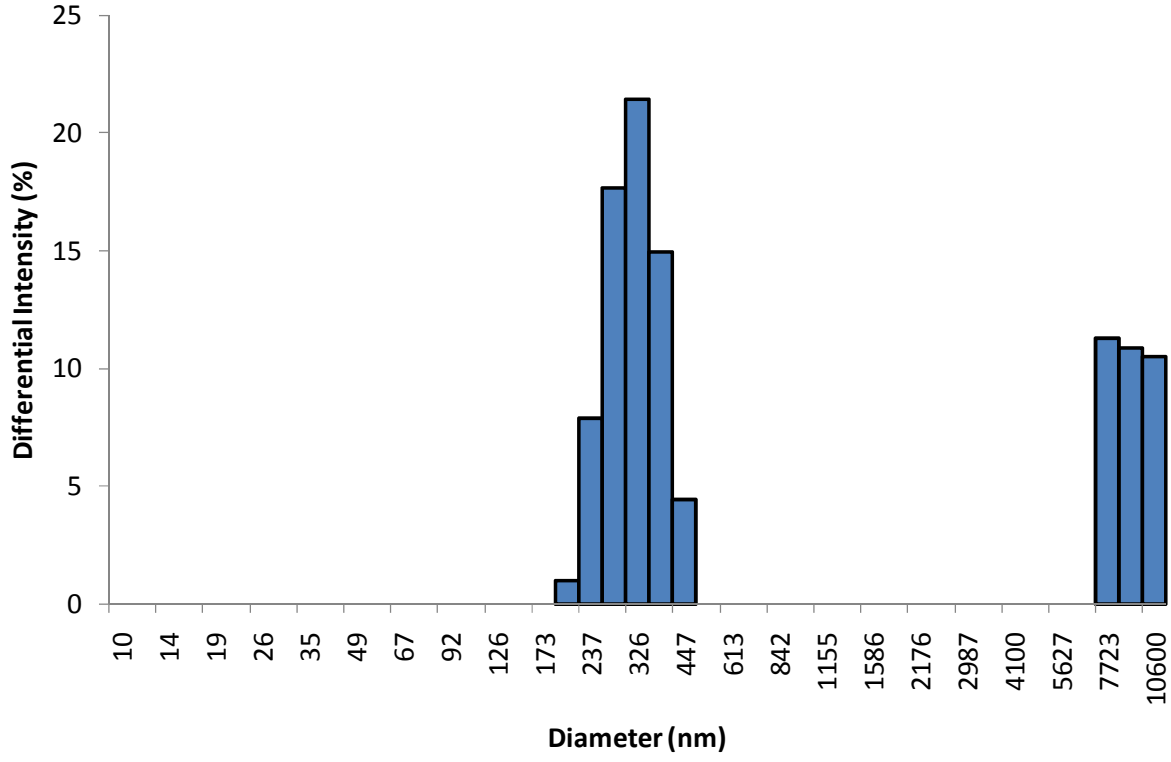


**Figure 3.3.7.4:** Particle size distribution for Ru16D functionalised 50 nm nanoparticles.

### *3.3.8 RuxD Functionalised Isolated Gold Nanoparticles*

RuxD functionalised 50 nm Au nanoparticles which were nonbackfilled were dropcast on to silicon wafers and allowed to dry in air before measurements were created. Figure 3.3.8.1 shows the emission spectra of these dropcast nanoparticles. The emission maximum has red shifted to about 675 nm in each case, a much greater red shift than observed with the monolayers on roughened gold electrodes. The emission is surprisingly intense for a complex so close to the surface of the metal nanoparticles, most likely due to a surface enhancement effect. The greater red shift in emission for these nanoparticles compared to roughened gold is due to greater plasmon coupling of the complex with the metal surface. Surface plasmons are stronger at nanoparticle junctions which will form when the nanoparticles are dropcast in this manner. For example Nie *et al.*[49] reported significant SERS enhancement from nanoparticle aggregates due to increased plasmonic coupling at 'hot-spots' at nanoparticle junctions in at nanoparticle aggregates.

The surface of a smooth gold electrode features a propagating surface plasmon as opposed to a localised surface plasmon of gold nanoparticles (see Section 1.5.3). Localised plasmons have a much smaller wavelength than propagating plasmons, typically of the order of visible light, allowing them to interact with incident visible light. SEF is thought to occur by two co-operative mechanisms, an electric field effect and an induced plasmon effect. In the electric field effect, luminophores in very close proximity (< 10nm) to the metal surface experience increased electric field resulting in an increase in absorption due to an effective increase in molar extinction co-efficient and therefore an enhanced emission quantum yield. Luminescence properties such as lifetime and emission wavelength are retained. The plasmonic effect is when the transient vibrations in the molecule induce equivalent dipole transitions in the metal effectively creating a mirror image of the molecule in the metal. Plasmons can excite both the molecule and the dipole image in the metal. Excitation of the plasmon leads to emission from the molecule and the dipole transition mirror image in the metal. This leads to a reduction in the luminescence lifetime and a red shift in emission.[50] A red shift in emission have been previously reported for monolayers of complexes on gold surfaces that facilitate plasmonic coupling, for example monolayers of $[Ru(bpy)_2(Qbpy)]^{2+}$ on gold nanocavity arrays reported by Forster, Keyes *et al.*[48], which experienced a 20 nm red

shift in emission maximum of the Ru (II) complex. Unfortunately it was impossible to quantify any dependence of emission intensity with chain length due to the lack of an internal standard and the fact that the emission is very dependent on the focus of the detector.

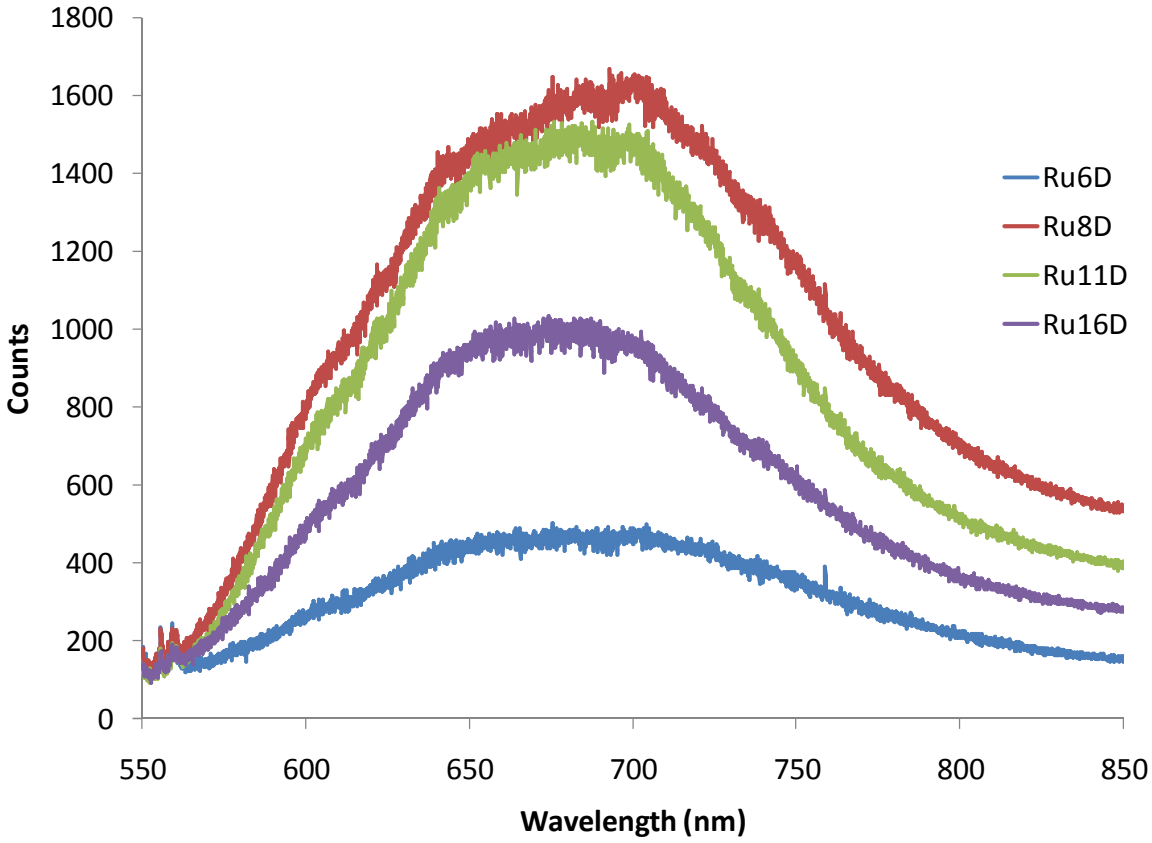


**Figure 3.3.8.1** Fluorescent spectra of nonbackfilled RuxD functionalised 50 nm Au nanoparticles dropcast on a silica wafer. An excitation wavelength of 514 nm was used. Emission intensity is not normalised.

The SERS spectra of these dropcast nanoparticles are shown in Fig. 3.3.8.2. An excitation wavelength of 632 nm from a HeNe laser source was used as it was the closest to the plasmon absorbance of the nanoparticles. These show excellent enhancement of the characteristic RuxD modes located at 576, 854, 881, 1091, 1261, 1299, 1399, 1442, 1514, 1556, 1599 $cm^{-1}$. The Raman enhancement of the nanoparticle aggregates over RuxD monolayers on roughened gold is again due to the presence of plasmon 'hot-spots' at nanoparticle junctions. These modes were also present in the resonance Raman spectrum of

the solid sample with only slight peak shifting and also exhibiting the peak broadening associated with SERS. A slight shoulder is also present at ~1585 and 1320 $cm^{-1}$ correspond to a Raman mode at the same position in the resonance Raman spectra of the RuxD complexes. The massive enhancement of the ligand Raman modes are evidence of the horizontal orientation of the RuxD complexes. The ligand Raman modes would not exhibit such large enhancement in a vertical orientation due to the distance of the ligands from the metal surface. The large enhancement shows strong coupling of the ligands with the surface plasmon indicating the ligands close proximity to the surface. The peaks, however, are poorly defined due to a massive SERS background signal. This unusually large SERS background is caused by the electron withdrawing effect of the positively charged RuxD complexes and the proximity of the charged ruthenium head groups to the metallic surface.

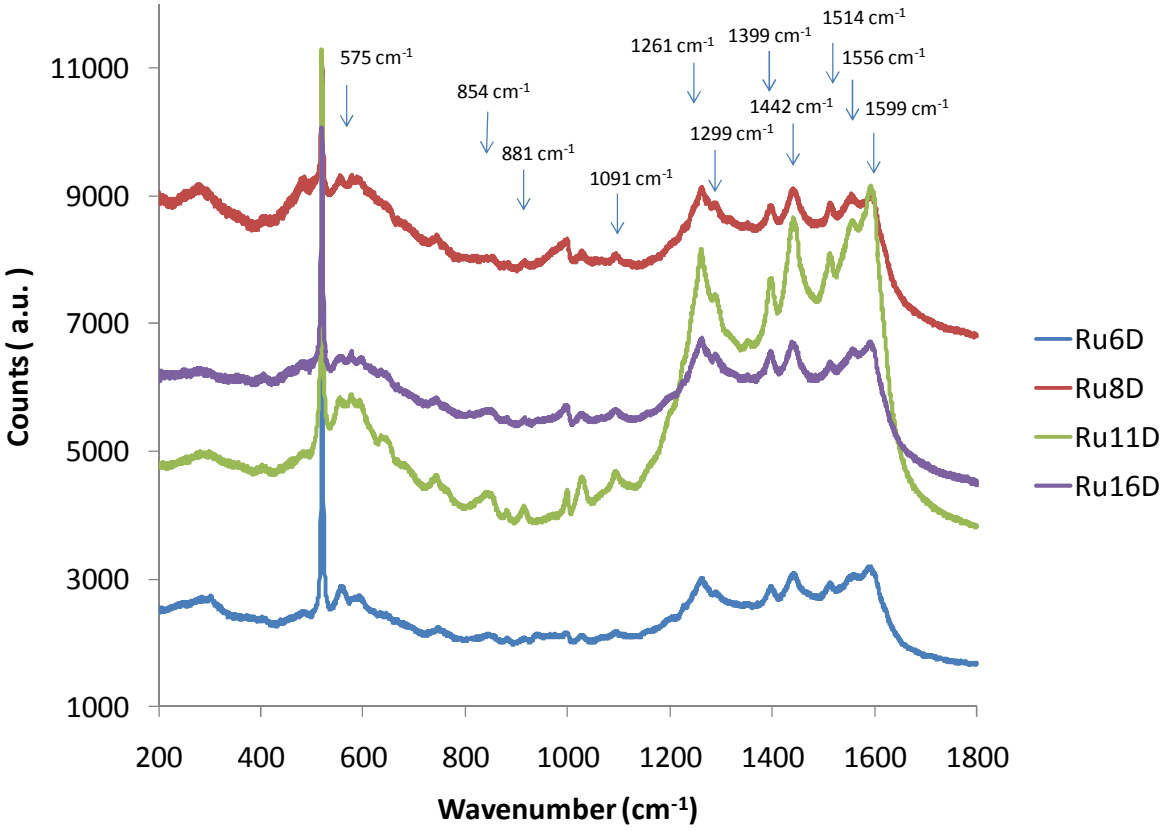


**Figure 3.3.8.2:** Raman spectra of nonbackfilled RuxD modified 50 nm Au nanoparticles dropcast on silicon wafer, An excitation wavelength of 632 nm was used.

Russell, Baumberg, *et al*.[51] showed how the electron withdrawing properties of a complex on the surface of a metal can affect the SERS background. An enhancement factor was impossible to find due to the lack of a Raman mode that could be used as an internal standard. The use of any internal standards that were attempted were swamped by the background noise or poorly defined. Ferquently a SERS spectrum consists of enhanced Raman modes riding on a broad continuum emission background. The transient dipoles created by vibrations in the molecule on the metallic surface create mirrored dipole displacements in the metal through Coulomb-coupled excitation. This effectively creates a mirrored image of the transient dipoles in the metal. Plasmons will excite both the surface molecules and the mirrored image. Plasmon excitation of the surface molecule creates the sharp enhanced peaks of a SERS image with the broadening characteristic of SERS spectra due to Coulombic-coupling with the mirror image. Plasmon excitation of the metal mirror image which gives the equivalent SERS spectrum drastically broadened by coupling with the electronic continuum of the metal leading to the observed background of SERS spectra. A diagram of this effect is displayed in Fig 3.3.8.3.

Russell, Baumberg, *et al*. also showed how the electron withdrawing or donating properties of the complex can affect the observed SERS background. In mixed monolayers of *p*-nitrobenzenethiol and *p*-carboxybenzenethiol (CBT), electron withdrawing and donating species respectively, an increase in the concentration of CBT in the monolayer caused a decrease in observed SERS background and vice versa. It was proposed that electron withdrawing complexes pull electron density from the metal closer to the surface molecules thus reducing the dielectric screening and increasing background emission. This effect is also seen by changing the electronic potential of the surface. Increasing the negative potential of the surface of a benzenethiol monolayer on gold increased the observed SERS background. A more negative potential creates a more positively charged double layer at the metal surface reducing the dielectric screening and increasing the observed background.

The large observed SERS background of the RuxD monolayers on the gold nanoparticles made it impossible to use any of the Raman modes as a standard with which to estimate enhancement factors. The observed large SERS background confirms the horizontal orientation of the RuxD complexes on the gold nanoparticle surfaces. This large SERS

background is caused by the close proximity of the electron withdrawing ruthenium head groups in close proximity to the gold surface. Another contributing factor to the SERS background that needs be considered is that the RuxD complex emits at the wavelengths analysed in the 632 nm Raman spectra. Residual emission would contribute to the observed SERS background.

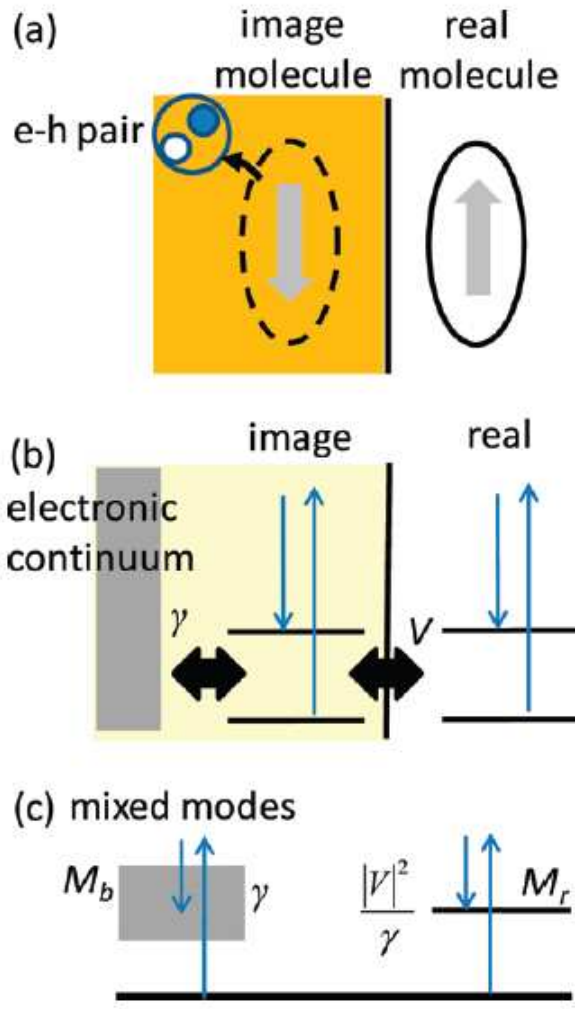


**Figure 3.3.8.3:** Representation of background generation in SERS spectra. (a) Transient vibrations in the molecule generate equivalent dipole transitions in the metal coupled to electron-hole pairs creating a 'mirror image molecule'. (b) Raman transitions of the surface molecule and mirror image are differently coupled to the electronic continuum of the metal. (c) The resulting modes have very different line widths resulting in broadened SERS peaks and the drastically broadened continuum background. Reproduced from Ref[51].

## 3.4 Conclusions

Monolayers of RuxD complexes, which were assembled on planar platinum surfaces alone or backfilled with an alkanethiol of appropriate length, were characterised electrochemically and spectroscopically. The objectives were to examine the distance dependence of $k_{et}$ and the distance dependence of SERS of these RuxD monolayers. These monolayers show nearly ideal surface confined diffusion limited electrochemical behaviour. However, these monolayers show relatively poor stability in organic media with fairly rapid loss of surface coverage when electrochemically cycled in acetonitrile. Electrochemically analysis of the kinetics of these monolayers show that these monolayers exhibit extremely fast electron transfer rates suggesting that the ruthenium redox centres are in close proximity to the metallic surface and these complexes are in 'lying down' and orientation as opposed to a monolayer with the ruthenium head groups exposed on the surface, even in assemblies backfilled with alkanethiols. This orientation was further confirmed wherein no distance dependent β values could be calculated. SERS of these monolayers on roughened gold electrodes gives weakly enhanced Raman signals almost identical to the resonance Raman spectra of the solid RuxD samples. These monolayers however are weakly luminescent and not completely quenched despite close proximity of the ruthenium head group to the metallic surface. It is believed that this horizontal orientation of the RuxD complexes on metal surfaces is due to adsorbtion of the ruthenium head group to the metal surface through interactions between the dpp ligands and the metal surface. To our knowledge this is the first report of a surface active ruthenium complex that behaves in such a manner.

The photophysics of 50 nm Au nanoparticles functionalised with RuxD complexes are also presented in this chapter. SERS analysis of these nanoparticles gives enhanced Raman spectra in solution. Raman spectra were greatly enhanced when these functionalised nanoparticles were deposited as aggregates on silicon. The large enhancement of the ligand Raman bands is evidence of strong plasmon coupling with the ligands due to the ligands being in close proximity to the metal surface. The large SERS continuum background signal from these RuxD nanoparticles makes calculating an enhancement factor impossible. However this large background signal is further evidence of the lying down orientation of the

RuxD units in a monolayer. The RuxD functionalised nanoparticles are strongly luminescent as aggregates due to a strong plasmonic enhancement of the emission at nanoparticle junctions in the aggregates.

# References


[1] Nuzzo, R.G. and Allara, D.L.; *J. Am. Chem. Soc.*, 105, **1983**, 4481-4483

[2] Sagara, T. and Midorikawa; *Langmuir*, 14, **1998**, 3682-3690

[3] Patronea, L.; Palacina, S.; Bourgoina, J.P.; Lagouteb, J.; Zambellib, T. and Gauthierb, S.; *Chem. Phys.,* 281, **2002**, 325–332

[4] Tour, J.M.; Jones II, L.; Pearson, D.L.; Lamba, J.J.S.; Burgin, T.P.; Whitesides, G.M.; Allara, D.L.; Parikh, A.N. and Atr, S.V.; *J. Am. Chem. Soc.,* 117, **1995***,* 9529-9534

[5] Ulman, A.; *Chem. Rev.*, 96, **1996**, 1533-1554

[6] Sellers, H.; Ulman, A.; Shnidman, Y. and Eilers, J.E.; *J. Am. Chem. Soc.*, 115, **1993**, 9389-9401

[7] Ulman, A.; Evans, S. D.; Shnidman, Y.; Sharma, R.; Eilers, J. E. and Chang, J. C.; *J. Am. Chem. Soc.*, 113, **1991**, 1499-1506

[8] Touahir, L.; Chazalviel, J-N.; Sam, S.; Moraillon, A.; Henry de Villeneuve, C.; Allongue, P.; Ozanam, F. and Gouget-Laemmel, A.C.; *J. Chem. Phys. C*, 115, **2011**, 6782-6787

[9] Hossain, M. K. and Ozaki, Y.; *Curr, Sci.*, 97, **2009**, 192-201

[10] Fleischmann, M.; Hendra, P.J. and McQuillan, A.J.; *Chem. Phys. Lett.*, 26, **1974**, 163-166

[11] Jeanmarie, D.L. and Van Duyne, R.P.; *J. Electroanal. Chem.*, 84, **1977**, 1-20

[12] Albrecht, M.G. and Creighton, J.A.; *J. Am, Chem. Soc.*, 99, **1977**, 5215-5217

[13] Kneipp, K.; Y. Kneipp, H.W.; Perelman, L.T.; Itzkan, I.; Dasari, R.R. and Feld, M.S.; *Phys. Rev. Lett,.* 78, **1997**, 1667-1670

[14] Nie, S. and Emory, S.R.; *Science,* 275, **1997**, 1102-1106

[15] Campion, A. and Kambhampati, P.; *Chem. Rev. Soc.,* 27, **1998,** 241-250

[16] Compagnini, G.; De Bonis, A. and Cataliotti, R.S.; *Mater. Sci. Eng. C.*, 15, **2001**, 37-39

[17] De Bonis, A.; Compagnini, G.; Cataliotti, R.S. and Marletta, G.; *J. Raman Spec*, 30, **1999**, 1067-1071

[18] Byrant, M.A. and Pemberton, J.E.; *J. Am. Chem. Soc.*, 113, **1991**, 3629-3637

[19] Ye, Q.; Fang, J. and Sun, L.; *J. Phys. Chem. B*, 101, **1997**, 8221-8224

[20] Fromm, D.P.; Kinkhabwala, A.; Schuk, P.J.; Moerner, W.E.; Sundaramurthy, A. and Kino, G.; *J.Chem. Phys.*, 124, **2006**, 61101-1 – 61101-4

[21] Gersten, J. and Nitzan, A.; *J. Chem. Phys.,*75, **1981**, 1139-1151

[22] Chew, H.; *J. Phys. Chem.*, 87, **1987**, 1355-1359

[23] Weitz, D.A.; Garoff, S.; Gersten, J.I. and Nitzan, A.; *J. Phys. Chem.,* 78, **1983**, 5324-5338

[24] Lakowicz, J.R.; *Plasmonics*, 1, **2006**, 5–33

[25] Jose, B.; Steffen, R.; Neugebauer, U.; Sheridan, E.; Marthi, R.; Forster, R. J. and Keyes, T. E.; *Phys. Chem. Chem. Phys.*, 11, **2009**, 10923-10933

[26] Forster, R. J.; Pellegrin, Y.; Leane, D.; Brennan, J. L. and Keyes, T. E.; *J. Phys. Chem. C.*, 111, **2007**, 2063-2068

[27] Laviron, E.; *J. Electroanal. Chem.*, 101, **1979**, 19-28

[28] Dong, T-Y.; Huang, C.; Chen, C-P. and Lin, M-C.; *J. Organomet. Chem.,* 692, **2007**, 5147-5155

[29] Finklea, H.O. and Hanshew, D.D.; *J. Am. Chem. Soc.*, 114, **1992**, 3173-3181

[30] Finklea, H. O.; Liu, L.; Ravenscroft, M. S. and Punturi,S.; *J. Phys. Chem.*, 100, **1996**, 18852-18858

[31] Forster, R. J. and Faulkner, L. R.; *J. Am. Chem. Soc.*, 116, **1994**, 5444-5452

[32] Zelenay, P.; Rice-Jackson, L. M. and Wieckowski, A.; *Langmuir*, 6, **1990**, 974-979

[33] Krauskopf, E. K.; Rice-Jackson, L. M. and Wieckowski, A.; *Langmuir*, 6, **1990**, 970-973

[34] Rowe, G. K. and Creager, S. E.; *Langmuir*, 7, **1991**, 2307-2312

[35] Rowe, G. K. and Creager, S. E.; *J. Phys. Chem.*, 98, **1994**, 5500-5507

[36] Saavedra, H. M.; Barbu, C. M.; Dameron, A. A.; Mullen, T. J.; Crespi, V. H. and Weiss, P. S.; *J. Am. Chem. Soc.*, 129, **2007**, 10742-10746

[37] Collard, D. M. and Fox, M. A.; *Langmuir*, 7, **1997**, 1192-1197

[38] Rowe, G. K. and Creager, S. E.; *J. Phys. Chem.*, 98, **1994**, 5500-5507

[39] Petrovykh, D.Y.; Kimura-Suda, H.; Opdahl, A.; Richter, L. J.; Tarlov, M. J. and Whitman, L. J.; *Langmuir*, 22, **2006**, 2578-2587

[40] Willey, T. M.; Vance, A. L.; van Buuren, T.; Bostedt, C.; Terminello, L. J. and Fadley, C. S.; *Surface Science*, 576, **2005**, 188-196

[41] Lee, M-T.; Hsueh, C-C.; Freund, M. S. and Ferguson, G. S.; *Langmuir*, 14, **1998**, 6419-6423

[42] Nerambourg, N.; Werts, M.H.V.; Charlot, M. and Blanchard-Desce, M.; *Langmuir,* 23, **2007**, 5563-5570

[43] Thomas, K.G. and Kamat, P.V.; *Acc. Chem. Res.*, 36, **2003**, 888-898

[44] Thomas, K. G. and Kamat, P.V.; *J. Am. Chem. Soc.*, 122, **2000**, 2655-2656

[45] Lakowicz, J.R.; *Anal. Biochem.,* 298, **2001**, 1-24

[46] Kuwahara, Y.; Akiyama, T. and Yamada, S.; *Thin Solid Films,* 393, **2001**, 273-277

[47] Forster, R. J. and Keyes, T. E.; *J. Phys. Chem. B.*, 102, **1998**, 10004-10012

[48] Jose, B.; Steffen, R.; Neugebauer, U.; Sheridan, E.; Marthi, R.; Forster, R. J. and Keyes, T. E.; *Phys. Chem. Chem. Phys.*, 11, **2009**, 10923-10933

[49] Nie, S. and Emory, S.; *Science*, 275, **1997**, 1102-1106

[50] Zhang, Y.; Dragan, A. and Geddes, C. D.; *J. Phys. Chem. C*., 113, **2009**, 12095-12100

[51] Mahajan, S.; Cole, R. M.; Speed, J. D.; Pelfrey, S. H.; Russell, A. E.; Bartlett, P. N.; Barnett, S. M. and Baumberg, J. J.; *J. Phys. Chem. C,* 114, **2010**, 7242-7250

# 4. Interactions of $Ru(dpp)_2(x\text{-}ATAP)$ with Mammalian Cells

## 4.1 Introduction

Optical cell imaging is a very attractive and powerful tool in biological and biomedical applications as it is a minimally invasive approach to imaging living cells and tissue. Fluorescence imaging in particular has become a key technique in biological sciences. Creating contrast in fluorescent mapping techniques can be achieved by a wide range of parameters such as intensity, wavelength, lifetime and polarization[1]. Through Fluorescence Lifetime Imaging (FLIM) the contrast in the image is generated by variations in the lifetime of the sample. A large variety of fluorescence probes for use as FLIM cell imaging agents are available and in the absence of a fluorescence probe the cells inherent autofluorescence has also been used[2,3]. FLIM has many benefits over fluorescence intensity imaging. FLIM is concentration and intensity independent and the probes sensitivity to environmental factors such as $O_2$ concentration or pH can reveal physiological variations within the cell[4,5,6,7,8].

The majority of commercially available fluorescent probes are based on modified organic fluorophores or proteins mutagenically modified with fluorophore and suffer from many similar problems. They have short lifetimes that can overlap temporally with the autofluorescence of the cell. They are easily photobleached, often permanently, making them unsuitable for repeat or long experiments. The small Stokes shifts of these complexes cause an overlap of the excitation and emission spectra that can lead to self quenching and consequently a reduction in sensitivity and distorted spectra[9]. The use of luminescent probes based on ruthenium polypyridyl complexes may lead to significant improvements over organic fluorophores[10]. Ruthenium polypyridyl complexes have very stable luminescent excited states making them suitable for experiments with long run times, such as those that measure kinetic cellular events. Modified organic fluorophores are in general more prone to photobleaching after extended irradiation than ruthenium polypyridyl complexes. These complexes may provide greater sensitivity afforded by their large stokes shifts which reduces self quenching processes. They emit in the red region of the spectrum away from the autofluorescence emission. The long lived luminescent lifetimes also allows autofluorescence to be time gated out leading to less interference. Finally their luminescent lifetime is often highly sensitive to environmental conditions such as pH and $O_2$ concentration[4].

In this chapter we examine the use of the novel RuxD complexes described in previous chapters for use as a luminescence intensity and FLIM cellular imaging probe. It was predicted that the long alkyl chain might allow interaction with the lipid bilayer of the cell, binding to the cell membrane and even possibly facilitating the uptake of RuxD into the cytoplasm. This could lead to the interaction with membrane sub cellular components in the cell. This is explored here and compared to the uptake of the complex by liposomes. The cell membrane of mammalian cells is a bilayer structure consisting mostly of phospholipids. Bilayer liposomes are therefore good model for cell membranes. The interaction of heavy metal $d^6$ polypyridyl complexes with liposomes has been reported in the literature. For example Lo *et al.*[11] demonstrated a series of iridium polypyridyl complexes with pendent alkyl chains that associated with liposomes of DSPC (1,2-distearoyl-*sn*-glycero-3-phosphocholine). The structures of these complexes is given in Fig 4.1.1. Upon association with the DSPC liposomes a red shift in emission was observed while luminescence intensity remained single exponential. It is hoped that the alkyl chains of the RuxD series of complexes will facilitate their associating with lipid bilayers.

Pendant alkyl chains on $d^6$ heavy metal polypyridyl complexes have been shown to facilitate the uptake of these complexes by live cells. One of the previously mentioned iridium polypyridyl complexes reported on by Lo *et al.*[11] was also shown to be taken up into the cytoplasm of live HeLa cells. Fluorescence intensity imaging of HeLa cells that had been incubated with complex 3a (see fig 4.1.1) for 5 hours clearly showed luminescence due to the complex within the cell cytoplasm. Coogan *et al.*[12] reported on a series of rhenium complexes with pendent alkyl chains. After incubation *Spironucleus vortens* cells with the complexes for 2 hours, fluorescence intensity imaging confirmed the presence of the complexes within the cytoplasm by the presence of luminescence due to the complex within the cell. It is hoped that RuxD complexes will diffuse across the cell membrane and into the cytoplasm of live mammalian cells in a similar fashion to other reported heavy metal $d^6$ complexes with pendent alkyl chains.

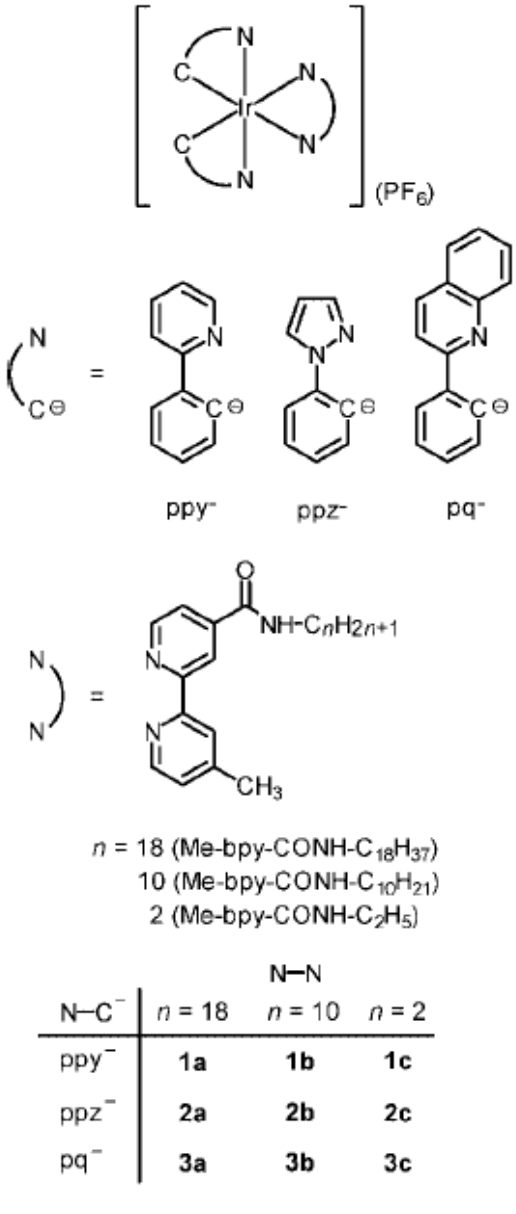


| N–C⁻ | N–N *n* = 18 | *n* = 10 | *n* = 2 |
|---|---|---|---|
| ppy⁻ | **1a** | **1b** | **1c** |
| ppz⁻ | **2a** | **2b** | **2c** |
| pq⁻ | **3a** | **3b** | **3c** |

**Figure 4.1.1**: Structure of the iridium polypyridyl complexes in ref [11].

## 4.2 Experimental

### *4.2.1 Materials*

All reagents and spectroscopic grade solvents were used as received from Sigma-Aldrich. Nanopure water (>18.0 MΩ $cm^{-1}$) was purified using Millipore Milli-Q gradient system was used in all experiments.

### *4.2.2 Preparation of liposomes with membrane probes*

1 mL of a 100:1 mix of DPPC (dipalmitoylphosphatidylcholine) phospholipid and the corresponding RuxD complex was prepared in a glass container. The solvent was stripped with a flow of $N_2$ leaving a thin layer of lipid on the walls of the glass container. The lipid film was resuspended in 1 mL of phosphate buffer (pH 7.4) and sonicated for 10 minutes to ensure the formation of unilamellar vesicles. The liposome solution was then extruded through a 100 nm polycarbonate filter 5 times at $60^{o}$ C using an Avanti Mini-Extruder system to obtain uniform size vesicles.

### *4.2.3 Cell staining with RuxD complexes*

Sterile glass cover slips were seeded in 1mL growth media containing 8 x $10^4$ CHO (Chinese hamster ovarian) cells or Hep G2 carcinoma liver cells. The growth media consists of 89% Dulbecco's Modified Eagles Medium (DMEM), 1% penicillin/streptomycin 5000/5000 mg/mL solution and 10% of Foetal Bovine Serum (FBS). Both of these cell lines are adherent and will adhere to the coverslip over time. To make the RuxD staining solution, 250 µL of PBS buffer solution are added to every 20 µL of a 1.5 x $10^{-4}$ M RuxD solution in DMSO used giving a concentration of 1.2 x $10^{-5}$ M of RuxD. 250 µL of this RuxD solution was added to the cell suspension giving the cell suspension a final concentration of 2.4 x $10^{-6}$ M of RuxD in 0.625% DMSO solution. DMSO was used to solubilise the RuxD complexes which are normally insoluble in aqueous media. DMSO has been used in low concentrations for cell staining procedures and has been reported to be non-toxic to cells in low concentrations. The cells were left to stain for 24 hours in a humidified incubator with 5% $CO_2$ at $37^{o}$ C. Before imaging the glass coverslip was removed and washed with PBS to

remove unbound cells and any RuxD that had not been associated with of internalised by the cells.

### *4.2.4 Cell Fixing*

Cells were fixed with 3.8% paraformaldehyde for 10 minutes at room temperature then washed with PBS buffer solution before imaging. When imaging cells stained with RuxD complexes cells were imaged live then fixed and imaged. No difference was observed in the luminescence images.

### *4.2.5 Co-staining RuxD stained cells*

Cells mounted on coverslips that had been stained with RuxD were permeabilised with 0.1% triton in PBS buffer solution for 10 minutes at room temperature and then blocked with 1% BSA/PBS for 1 hour at room temperature. The cells were then incubated with DiOC6 5 µM in PBS for 30 mins at room temperature followed by 4 µM DRAQ7 in PBS for 15 minutes. The cells mounted coverslip was then mounted on glass slides with Fluoroshield mounting media (Sigma). Slides were stored at $4^{o}$ C until required for imaging.

### *4.2.6 Luminescence Intensity Microscopy*

Luminescence intensity images were recorded with a Zeiss LSM 50 confocal microscope using a 64x oil immersion objective. For the images were the cells were stained solely with RuxD an excitation wavelength of 458 nm was employed at 4% power with a long pass 560 nm filter to remove interference from the excitation source. A HFT 458 dichroic filter was used. For the co-staining experiments of CHO cells stained with RuxD, $DiOC_6$ and DRAQ7 the following parameters were used. The $DiOC_6$ images were collected using an excitation wavelength of 488nm at 0.8% power with a band pass 505-550 nm filter. A HFT 405/488 dichroic filter was used. The DRAQ7 images were collected using an excitation wavelength of 633 nm at 100% power with a long pass 650 nm filter. A HFT 405/488/543/633 dichroic filter was used. The RuxD images were collected using an excitation wavelength of 458 nm at 3% power and long pass 615 nm filter. A HFT 458

dichroic filter was used. Excitation at 458 nm and 488 nm was provided by an argon ion laser. Excitation at 633 nm was provided by a HeNe laser.

### *4.2.7 Fluorescence Imaging Microscopy*

FLIM analysis was carried out using a Microtime 200 FLIM system. A diode laser provided an excitation wavelength of 440 nm with a pulse with of 2.5 µs at 20% power. Samples were mounted and focused using an Olympus IX71 microscope platform and a x60 water immersion objective. Data analysis was carried out using Symphotime analysis software. A 460 long pass filter was used to cut out any interference from the excitation source. A SPAD single photon detector was used as the detector.

## 4.3 Results and Discussion

### *4.3.1 Characterisation of Ru16D in Liposomes*

Every living cell is bound by a phospholipid bilayer based cell membrane. Phospholipids are one of the most important components of cell membranes and their bilayer structure in aqueous environments gives the cell membrane its structure. Phospholipids when present above a critical concentration will spontaneously form liposomes when in an aqueous environment. Liposomes of phospholipids are widely used as a cell membrane mimicking model[11]. Fluorescent membrane probes are often used to measure the dynamics of kinetic events in the cell membrane such as the rate of diffusion to different areas of the membrane. The suitability of RuxD complexes as cell membrane probes was first tested on liposomes of the phospholipid DPPC (1,2-dipalmitoyl-*sn*-glycero-3-phosphocholine). The structure of DPPC is shown in Fig 4.3.1.1 below.

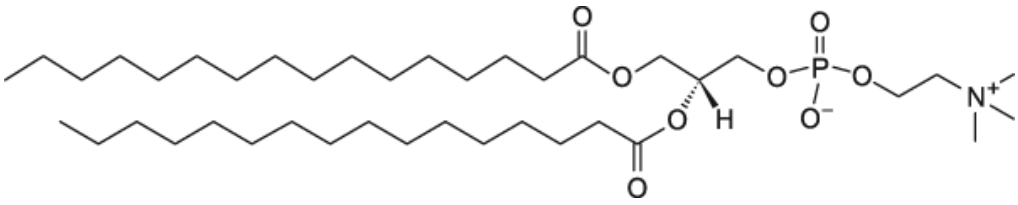

**Figure 4.3.1.1:** Structure of the phospholipid DPPC.

Liposomes containing Ru16D were created as described in Section 4.2.2. For liposome bilayers in aqueous media the outer part of the bilayer acts as a polar solvent while the inner layer acts as a non-polar solvent[13]. Since some membrane probes have different spectral properties when in polar or non-polar solvents this can be used to investigate where in the membrane the luminescence probe sits. The photophysical solvent dependence of Ru16D in various solvents including water has been previously discussed in Chapter 3 in section 3.3.3. Ru16D has a luminescence lifetime of 185 ns when in ACN. In water evidence suggests that Ru16D forms bilayer vesicle structures which exhibit biexponential luminescence lifetimes with a long component of about 920 ns and a short component about 138 ns. When the Ru16D dye is in the liposome it also exhibits biexponential lifetimes with a long component of 1.203 (±0.018) μs and a shorter component of 245 (±2.1) ns. Biexponential luminescence lifetimes for Ru(II) complexes have been observed in micellular or vesicles. De Cola *et al.* reported on a complex based on $[Ru(bpy)_3]^{2+}$ with two pendent alkyl chains that displayed biexponential luminescence lifetimes above the CMC and when integrated in micelles of CTAB, 400 ns and 860 ns in the case of the complex in micellular form and 380 ns and 650 ns when integrated in CTAB micelles. It was postulated that the long lived component was due to the complex in micellular form while the short lifetime component was due to the complex in solution[14]. Here it is postulated that the longer lifetime component is from the Ru16D dye anchored in the liposomes bilayer while the shorter component is from free Ru16D in solution. The increase in lifetime in the liposome membrane is attributed to the extra rigidity and limiting of the molecules rotation by being bound in the liposome structure. In aqueous solution the lifetime of the complex would also be reduced due to the H-O oscillations of water facilitating non-radiative decay processes of the excited state. The longer lifetime of the solvated Ru16D in the liposomes compared to the vesicle structures of just Ru16D, 245 ns compared to 138 ns respectively suggests that it is located inside the liposome complexes rather than outside. The longer lifetime is attributed to

slower rates of oxygen diffusion through the liposome structure. An example of the luminescence decay recorded from the DPPC liposomes containing Ru16D is presented in Fig 4.3.1.2.

The extrusion process seems to ensure that Ru16D is not present outside the liposome structures but only present in the liposome bilayer and solvated in the liposome interior. If solvated Ru16D was present outside the liposomes then the luminescence decay would contain components that matched the luminescence decay of Ru16D solvated in water. In section 3.3.3 the luminescence of Ru16D in water gave a biexponential lifetime with lifetimes of 920 ns and 138 ns, which were assigned to Ru16D in bilayer vesicle form and Ru16D solvated in water respectively. These values are not within experimental error of the two lifetime decays measured for Ru16D in DPPC liposomes. From these results we can conclude that both luminescence decays observed for the Ru16D containing liposomes reside in completely different environments than when Ru16D forms vesicle bilayers in an aquesous environment as reported in section 3.3.3.

These results suggest that Ru16D can interact and associate with biological membranes and has the potential to be a luminescence cellular imaging probe. The presence of Ru16D solvated inside the liposomes suggests that the complex may diffuse across bilayer membranes. This would make the complex capable of diffusing across the cell membrane of mammalian cells or even diffusing across the membranes of sub-cellular organelles.

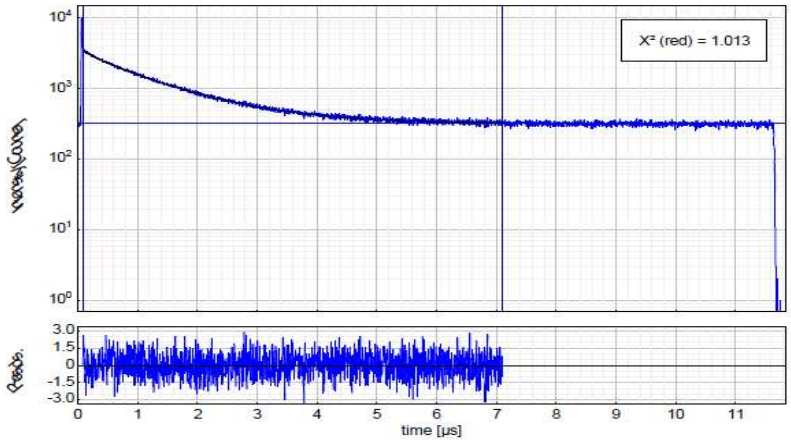


**Figure 4.3.1.2:** Luminescence lifetime measurements for Ru16D in DPPC liposomes. The liposomes are suspended in water and were prepared by extrusion using the method described in section 4.2.2. An excitation wavelength of 450 nm was used.

### 4.3.2 *RuxD as a Luminescence Cell Imaging Probe*

The liposome experiments with Ru16D reported in the previous section 4.3.1 indicated that the RuxD complexes are capable of associating and even crossing lipid bilayer membranes. Here the ability of the RuxD series of complexes to be uptaken by CHO cells (Chinese Hamster Ovary cells) was examined as well as the suitability of the RuxD complexes to act as cellular luminescence imaging probes. A cell line of CHO cells was stained with the RuxD series of complexes as described in section 4.2.3. CHO cells were also stained with the parent ruthenium complex, $[Ru(dpp)_2(NH_2phen)](PF_6)_2$, as a control. Luminescence intensity images of these stained cells were recorded and are presented in Fig 4.3.2.1 to 4.3.2.5. Although it was hoped that the RuxD complexes would diffuse across the cell membrane spontaneously without the need for a membrane permeabilising agent due to their positive charge and long alkyl chains a small amount of DMSO was used in the staining experiments. This was because the RuxD complexes and the parent complex $[Ru(dpp)_2(NH_2phen)](PF_6)_2$ proved to be insoluble in aqueous solutions such as the PBS buffer solution used in these experiments. To solubilise the complexes in PBS a small amount of DMSO was employed. DMSO was chosen since it has been proven to be non toxic to cells during the staining procedure while facilitating cellular uptake by ‘softening’ the cell

membrane[15]. The volume of DMSO was kept as low as possible during the staining procedure, 0.625 % of the total volume during the staining procedure.

Fig 4.3.2.1 shows a luminescence intensity image of CHO cells after incubation with $[Ru(dpp)_2(NH_2phen)](PF_6)_2$ for 24 hours. As can be seen the $[Ru(dpp)_2(NH_2phen)](PF_6)_2$ complex has diffused across the cell membrane and found to be localised around the cell cytoplasm. The circular dark areas within the cells are confirmed later on to be the nucleus. Interestingly, no penetration of the nuclear membrane by $[Ru(dpp)_2(NH_2phen)](PF_6)_2$ is detected. The penetration of the cell membrane by $[Ru(dpp)_2(NH_2phen)](PF_6)_2$ is more than likely down to the presence of 0.625 % DMSO during the staining. Keyes *et al.*[4] demonstrated how a similar Ru(II) complex, $[Ru(bpy)_2(picH_2)]^{2+}$, did not enter human blood platelet cells despite extensive incubation of the complex. In this case no DMSO was used to facilitate diffusion across the cell membrane. In another publication Keyes *et al.* showed that again a similar Ru(II) complex, $[Ru(dppz)_2PIC]^{2+}$ did not cross the membrane of live mouse SP2 myeloma cells. Again DMSO was not employed to facilitate diffusion across the membrane. In comparison Barton *et al.*[16] wrote an article on the transport mechanism of a very similar complex $[Ru(dpp)_2(dppz)]^{2+}$ stating that these complexes enter the HeLa cells through passive and energy dependent transport mechanisms without taking into account that DMSO was present during the staining procedure. In another publication Zhao *et al.*[17] reported on the cellular uptake of a series of Iridium polypyridyl complexes into HeLa cells and based this uptake on the cationic properties of the complexes while again ignoring the fact that the cells were incubated in a 1:49 v/v DMSO/PBS solution. At such concentrations DMSO will play a significant role in cellular uptake of the complex and the complex cannot really be deemed cell permeable without carrying out controls in the absence of DMSO.

As can be seen in Fig 4.3.2.1 $[Ru(dpp)_2(NH_2phen)](PF_6)_2$ distributes non-uniformly within the cytoplasm of the CHO cells. Of particular note is that the complex localises at circular structures with high luminescence intensity. The identity of these structures will be discussed in a later section.

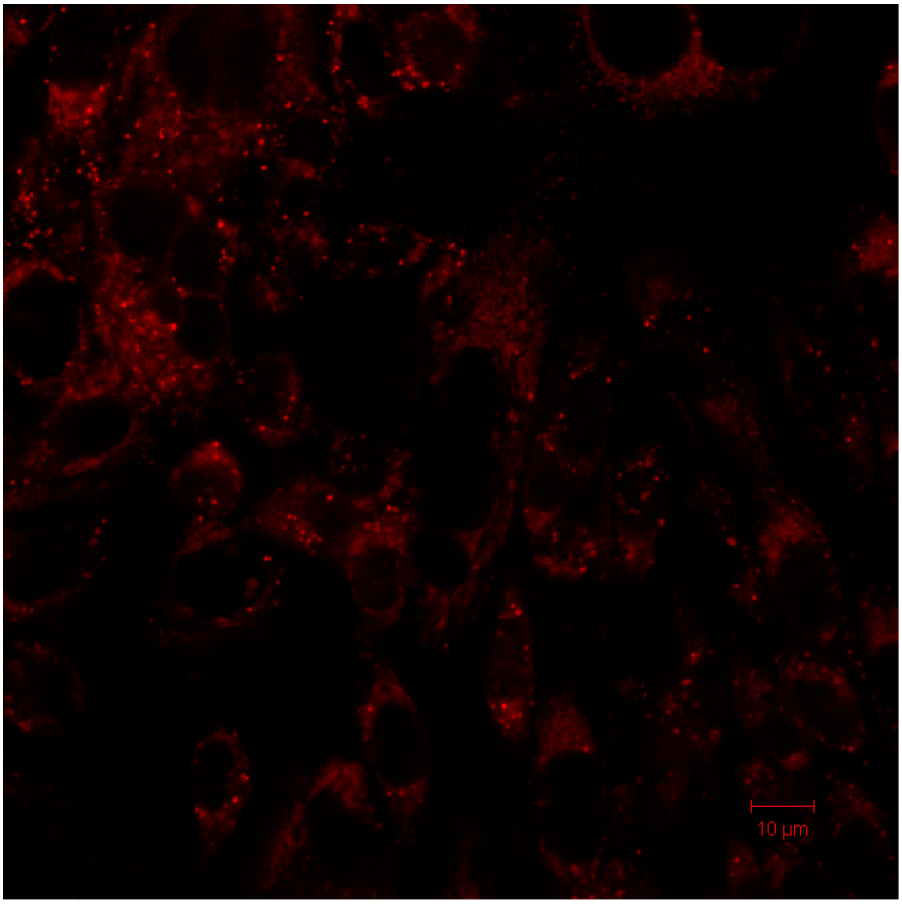


**Figure 4.3.2.1:** Luminescence intensity image of CHO cells after 24 hours staining with $[Ru(dpp)_2(NH_2phen)](PF_6)_2$. An argon ion excitation laser line of 458 nm at 4% power was used. A long pass 560 nm filter was used to reduce interference from the excitation source. A HFT 458 dichroic filter was used.

Fig 4.3.2.2-4.3.2.5 show luminescence intensity images of CHO cells after 24 hours staining with the RuxD series of complexes. All cells were fixed before luminescence imaging according to the procedure described in section 4.2.4. Fixing was deemed necessary due to the sensitivity of the CHO cells to ambient environmental conditions. When the cells are suspended in PBS solution at ambient conditions and not in growth media under the incubation conditions described in section 4.2.3, the morphology of the CHO cells can rapidly change within 30 minutes followed by cell death making them unsuitable for the long experiment times required by the experiments conducted in this section. Fixing of the RuxD

stained CHO cells was shown not to change the luminescence intensity images compared to live RuxD stained CHO cell. Therefore fixing of the CHO cells was deemed suitable for luminescence intensity imaging.

Just as for $[Ru(dpp)_2(NH_2phen)](PF_6)_2$ all RuxD complexes appear to localise in spherical structures throughout the cell that are of high luminescence intensity. Of particular interest in these images is how the RuxD complexes exhibit an alkyl chain length dependence on where they localise within the CHO cell. Ru6D and Ru8D are localised non-uniformly throughout the cytoplasm as well as in the high luminescent intensity spherical structures. However in the Ru11D stained cells the luminescence intensity in the cytoplasm decreases and the complex has become more localised in the highly luminescent spherical structures. For the cells stained with Ru16D the complex has become almost specifically localised within these spherical structures. There also appears to be a chain length dependence on nuclear penetration of the RuxD complexes. Unlike the parent complex $[Ru(dpp)_2(NH_2phen)](PF_6)_2$, luminescence due to Ru6D and Ru8D is clearly visible within the nuclei of the CHO cells that have been incubated with these complexes. Very weak luminescence is observed from the nuclei of the CHO cells incubated with Ru11D while there is no luminescence detected from the nuclei of the CHO cells that have been incubated with Ru16D. Surprisingly despite the lipophilicity of the RuxD complexes no preferential localisation of the RuxD complexes is detected at the cell membrane, particularly for the long chained RuxD complexes. This may be due to the presence of DMSO. The disruption of the cell membrane by DMSO possibly weak the Van Der Waals interactions between the alkyl chains of the RuxD complexes and the alkyl chains of the phospholipids in the cell membrane.

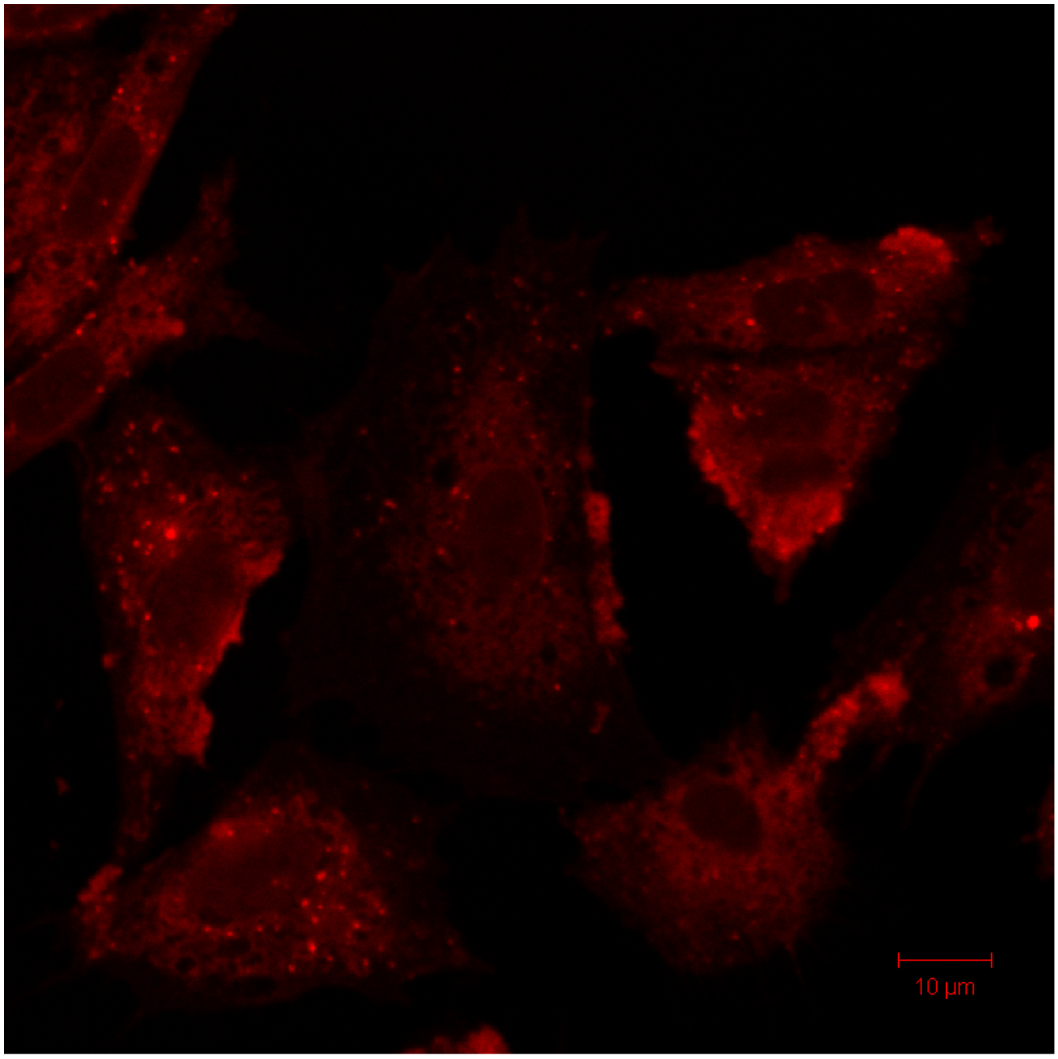


**Figure 4.3.2.2:** Luminescence intensity image of CHO cells after 24 hours staining with Ru6D. An argon ion excitation laser line of 458 nm at 4% power was used. A long pass 560 nm filter was used to reduce interference from the excitation source. A HFT 458 dichroic filter was used.

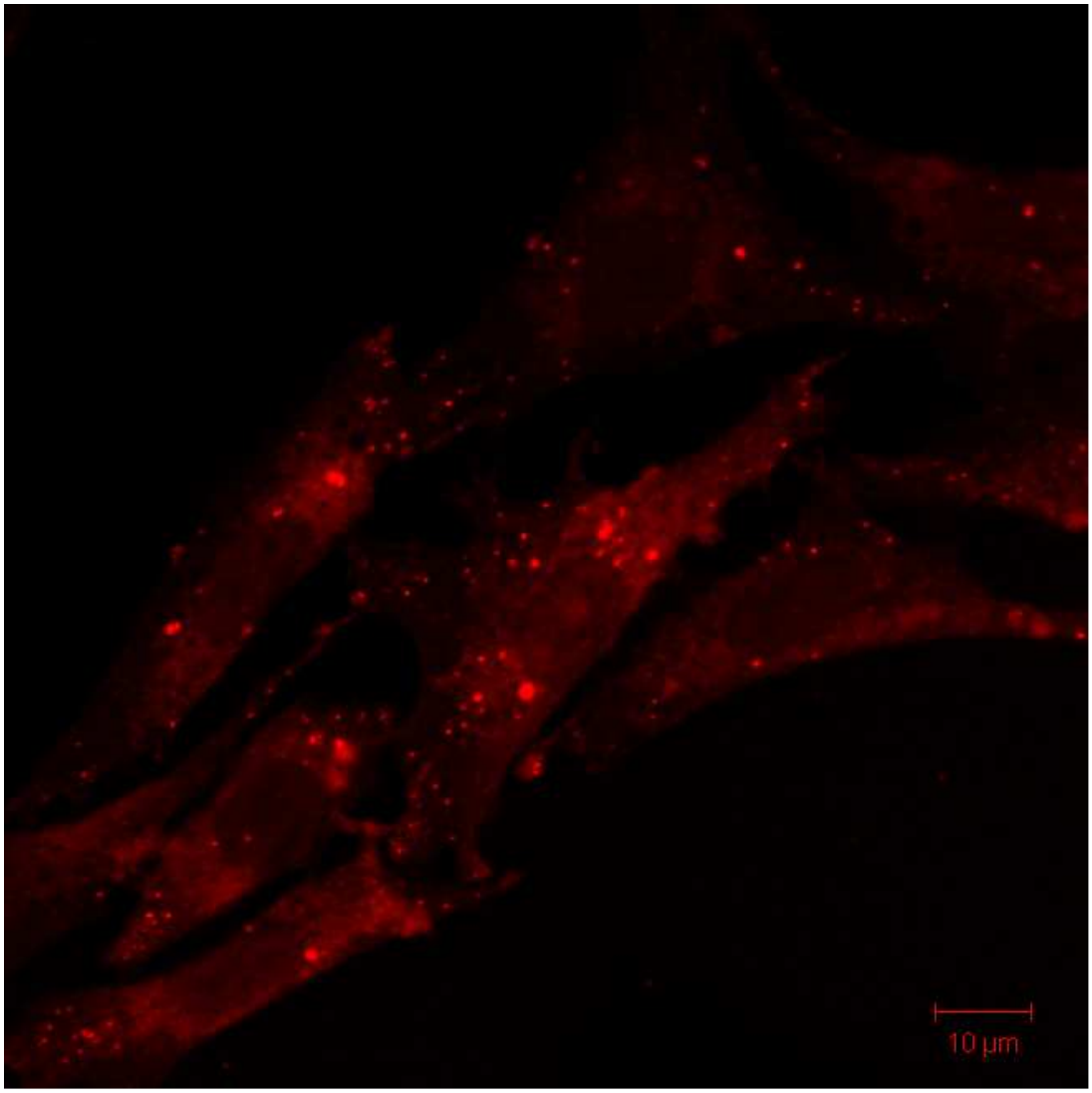


**Figure 4.3.2.3:** Luminescence intensity image of CHO cells after 24 hours staining with Ru8D. An argon ion excitation laser line of 458 nm at 4% power was used. A long pass 560 nm filter was used to reduce interference from the excitation source. A HFT 458 dichroic filter was used.

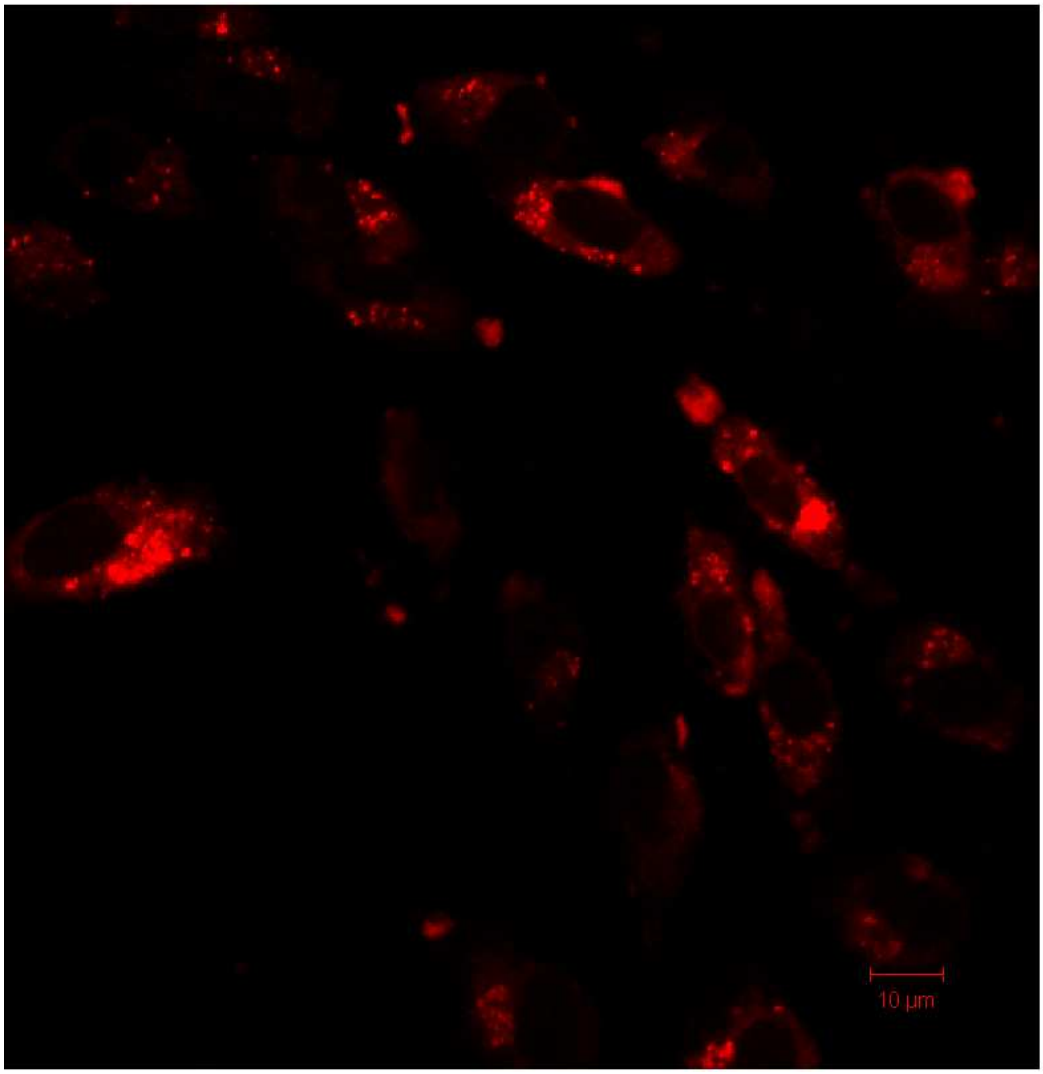


**Figure 4.3.2.4:** Luminescence intensity image of CHO cells after 24 hours staining with Ru11D. An argon ion excitation laser line of 458 nm at 4% power was used. A long pass 560 nm filter was used to reduce interference from the excitation source. A HFT 458 dichroic filter was used.

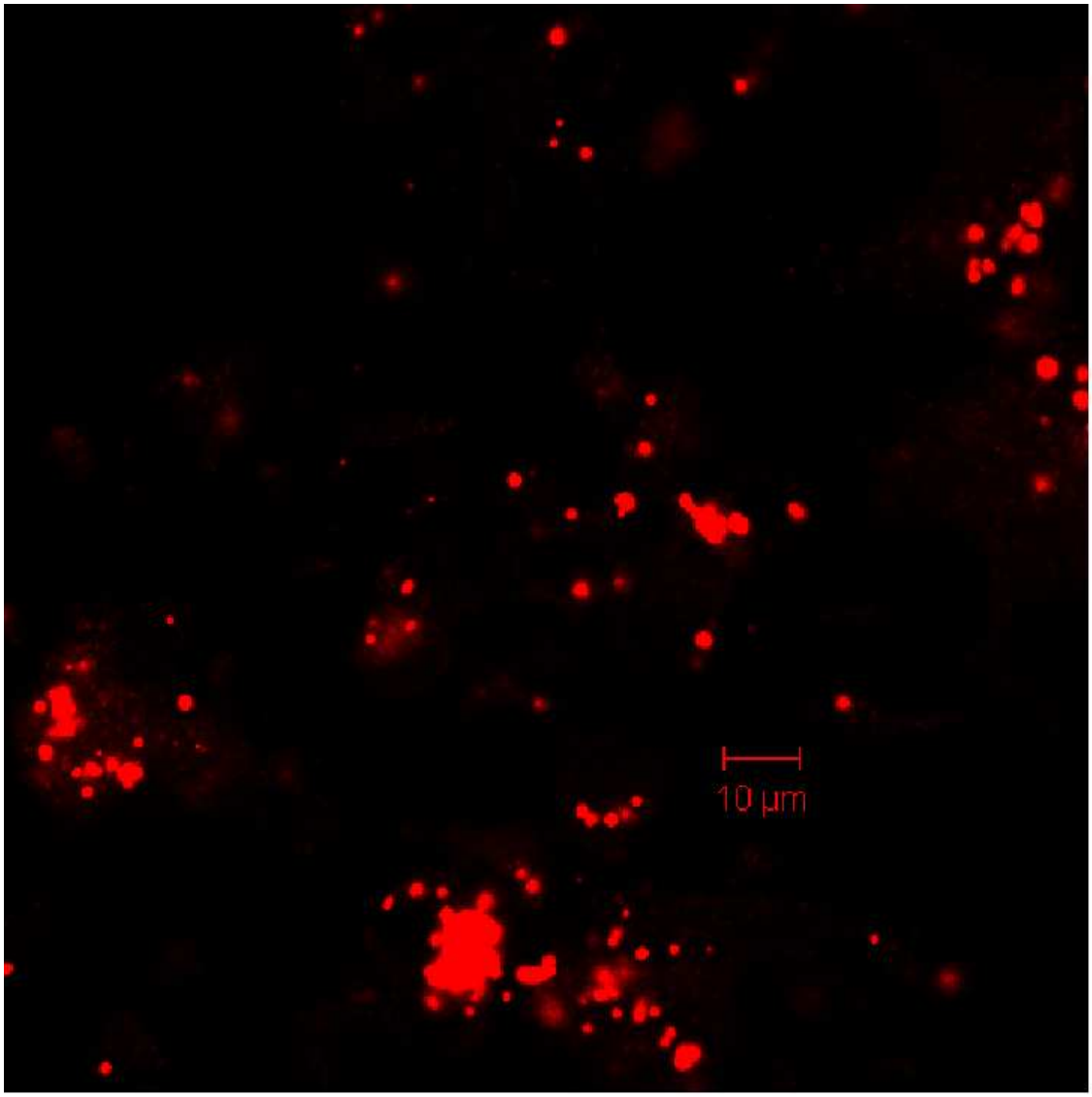


**Figure 4.3.2.5:** Luminescence intensity image of CHO cells after 24 hours staining with Ru16D. An argon ion excitation laser line of 458 nm at 4% power was used. A long pass 560 nm filter was used to reduce interference from the excitation source. A HFT 458 dichroic filter was used.

Fig 4.3.2.6 shows a lambda mode image of an area inside a fixed CHO cell that has been incubated with Ru6D. This area includes one of the high intensity spherical structures that have been mentioned. Lambda mode analysis collects the luminescence intensity of different wavelengths from a defined area. These are combined to form a luminescence emission spectrum of the area under analysis. As can be seen the luminescence spectrum of the Ru6D incubated CHO cell is attributed to luminescence with a $\lambda_{max}$ of about 640 nm, the same $\lambda_{max}$ of the Ru6D complex in solution. This confirms that the luminescence from these stained cells is due to only the RuxD complexes.

(a)

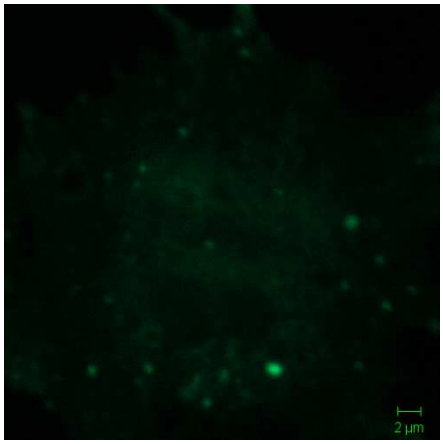


(b)

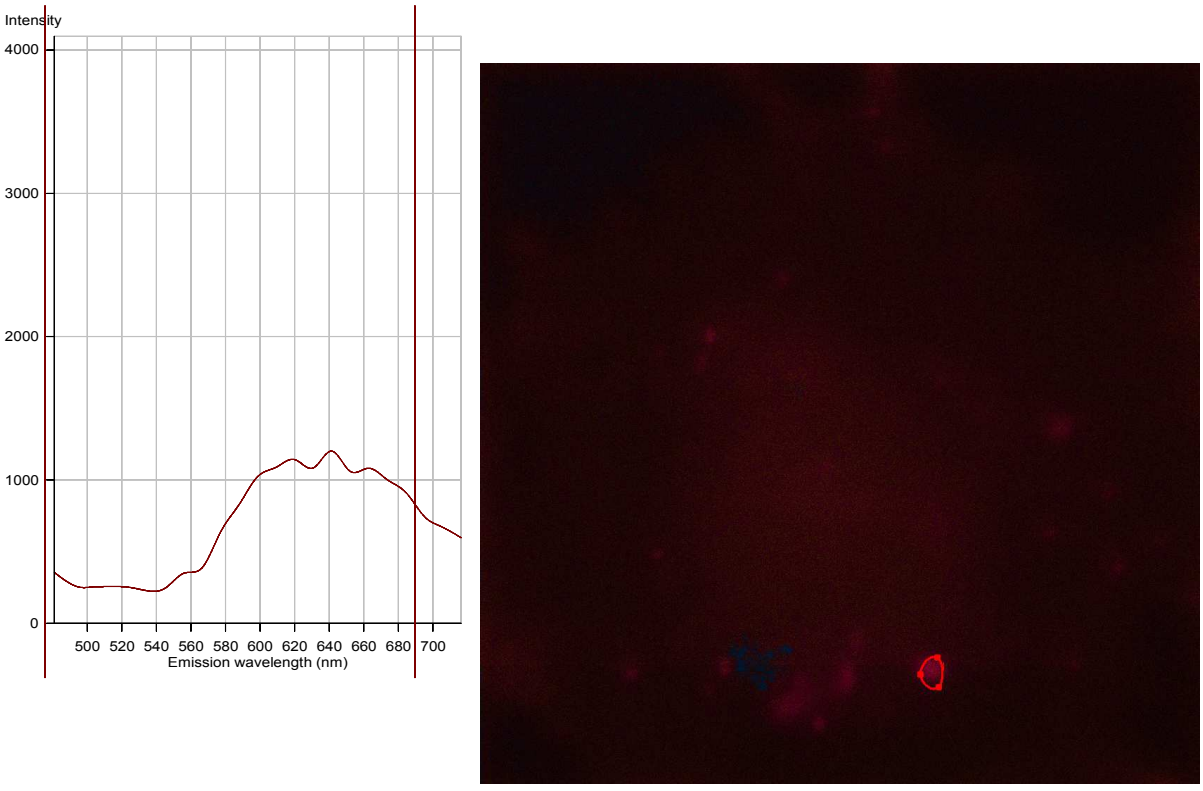


**Figure 4.3.2.6:** Lambda mode luminescence image of CHO cells after 48 hours staining with Ru6D. (a) represents the luminescence intensity image of the CHO cell that has been incubated with Ru6D while (b) represents the same area under lambda mode analysis. The spectrum on the left shows the luminescence spectrum of the area highlighted in the image of the Ru6D stained CHO cell on the right. An argon ion excitation laser line of 458 nm at 4% power was used. A long pass 560 nm filter was used to reduce interference from the excitation source. A HFT 458 dichroic filter was used.

The luminescence image of the unstained CHO cells under the same conditions as the RuxD stained CHO cells was take as a control experiment and is presented in Fig 4.3.2.7 below. As can be seen no luminescence signal is detected from the unstained cells as expected. Therefore under the excitation conditions and emission detection conditions used to collect the luminescence intensity images of the CHO cells incubated with RuxD, autofluorescence does not contribute to the observed signal.

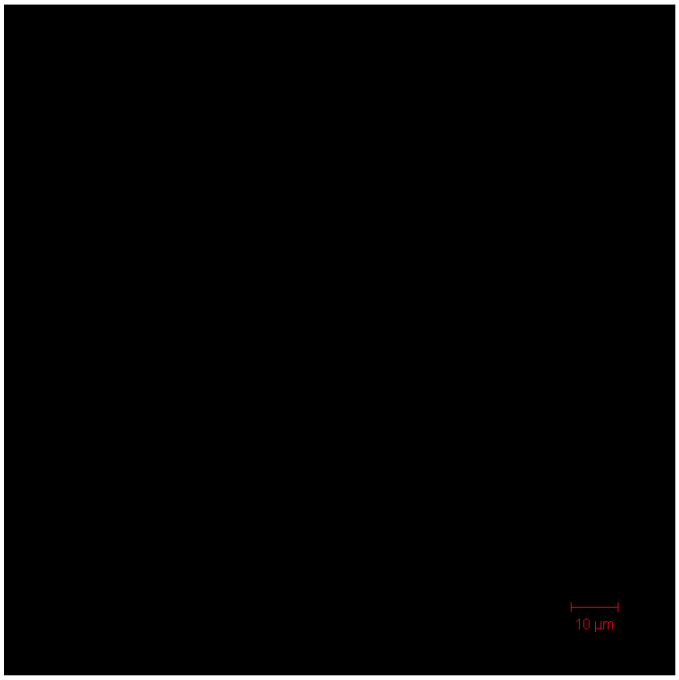


**Figure 4.3.2.7:** Luminescence intensity image of control unstained CHO cells. An argon ion excitation laser line of 458 nm at 4% power was used. A long pass 560 nm filter was used to reduce interference from the excitation source. A HFT 458 dichroic filter was used.

### *4.3.3 Co-staining of RuxD Stained CHO Cells*

Co-staining experiments were performed on the RuxD treated CHO cells to identify the areas were the RuxD dyes localise within the CHO cells. Two commercially available fluorescence dyes were chosen, $DiOC_6$ (3,3' - Dihexyloxacarbocyanine iodide) and DRAQ7 (a proprietary derivative of 1,5-bis{[2-(di-methylamino)ethyl]amino}-4,8-dihydroxyanthracene-9,10-dione). $DiOC_6$ is a commercially available fluorescent dye that selectively localises at the endoplasmic reticulum, mitochondria and nuclear envelope within the cell. It has an excitation wavelength of 484 nm and an emission wavelength of 501 nm. DRAQ7 is another commercially available fluorescent dye that selectively stains the nucleus of cells with compromised cell membranes, such as fixed cells. It has an optimal excitation wavelength of 633 or 647 nm, in this case we used 633 nm, and an emission wavelength of 694 nm when bound to double stranded DNA. There is no overlap of the emission of $DiOC_6$ with the absorbance of DRAQ7 so no quenching of the emission of $DiOC_6$ due to DRAQ7 is expected. A small amount of emission quenching of $DiOC_6$ may be expected due to emission overlapping with the MLCT excitation of the RuxD complexes. Some slight quenching of the RuxD complexes emission is expected due to emission overlap with DRAQ7.

The cells were co-stained as explained in section 4.2.5. The luminescence intensity images obtained from the co-staining experiments for the RuxD complexes are presented in Fig 4.3.3.2-4.3.3.5 while the luminescence intensity images for co-staining experiments involving $[Ru(dpp)_2(NH_2phen)](PF_6)_2$ are presented in Fig 4.3.3.1. To gain the image of the luminescence intensity of only the RuxD inside the co-stained cells an excitation wavelength of 458 nm was used and a LP 560 nm filter was used to cut off emission from $DiOC_6$. For the images of the luminescence intensity from DiOC6 an excitation wavelength of 488 nm was used and a 505-550 nm band pass filter to cut off any emission from the RuxD complexes. For the DRAQ7 images an excitation wavelength of 633 nm was used with a long pass 650 nm filter. The excitation wavelength of 633 nm does not have the energy to excite the either $DiOC_6$ or RuxD to the excited state and the 650 LP filter can filter out any interference from residual luminescence.

Comparison of the DRAQ7 and RuxD treated cells luminescence intensity images confirms that the large circular area seen within the RuxD treated cells is indeed the nucleus.

This confirms the nuclear penetration of the CHO cell nucleus by Ru6D, Ru8D and Ru11D. No nuclear penetration of is observed for Ru16D or the parent complex $[Ru(dpp)_2(NH_2phen)](PF_6)_2$. The spherical structures that display high luminescence intensity seen in the previous luminescence intensity images, Fig 4.3.2.1 – 4.3.2.5 of RuxD and $[Ru(dpp)_2(NH_2phen)](PF_6)_2$ treated cells were thought to be cellular organelles that the RuxD complexes and $[Ru(dpp)_2(NH_2phen)](PF_6)_2$ had selectively bound to. Analysis of the combined RuxD, DioC6 and DRAQ7 treated cells luminescence intensity images reveals that these spherical structures do not co-localise with $DiOC_6$. These spherical structures are, therefore, not mitochondria. The identity of these structures could be either vacuoles, lysosomes, endosomes or another cellular organelle. Another possibility would be the formation of RuxD vesicles within the cytoplasm. These structures are less than 1 µm in diameter. A possibility is the formation of bilayer vesicles of the RuxD complex inside the cell but this does not account for the appearance of these features in the images of the $[Ru(dpp)_2(NH_2phen)](PF_6)_2$ treated CHO cells. It seems likely that the mechanism of RuxD entry into the cell is an endocytotic pathway where RuxD and $[Ru(dpp)_2(NH_2phen)](PF_6)_2$ interact with the cell membrane followed by the formation of an endosome. In the case of RuxD this could due to lipsome fusion with the cell membrane since the aqueous staining solution more than likely contains bilayer vesicle structures of RuxD like those reported on in Chapter 3. Collins *et al*[18]. have reported on CHO cells that were incubated with liposomes of DOTAP/DC-CHOL, where DOTAP is dioleoyltrimethylammonium propane and DC-CHOL is *3~8-(N-(N',N'-dimeth*ylaminoethane)carbamoyl)cholesterol. These liposomes were labelled with FPE, fluorescein labelled 1,2-Bis(diphenylphosphino)ethane. Fluorescence intensity imaging of these CHO cells after imaging showed a similar punctuated staining with high luminescence intensity spherical structures as observed with RuxD and $[Ru(dpp)_2(NH_2phen)](PF_6)_2$ treated CHO cells. It was proposed that these spherical structures were endosomes and that the FPE had entered the cell through an endosomic pathway after liposome fusion with the cell membrane. An image of a CHO cell stained with the FPE containging DOTAP/DC-CHOL liposomes is shown in Figure 4.3.3.6. Further co-staining studies are required to elucidate the identity of these structures.

For the Ru6D, Ru8D, Ru11D and $[Ru(dpp)_2(NH_2phen)](PF_6)_2$ treated cells the complexes are also distributed outside of the spherical structures although at a lower concentration than in the spherical structures. Comparison of the luminescence intensity

images of these Ru(II) complexes in the cells and the same cells $DiOC_6$ luminescence intensity images shows that outside of the spherical structures these ruthenium complexes localise in the regions that $DiOC_6$ localises indicating that these complexes are interacting with the mitochondria and endoplasmic reticulum of the cells, possibly through interactions with the membranes of these structures. These structures are too small to distinguish with the level of magnification in available.

(a) (b)

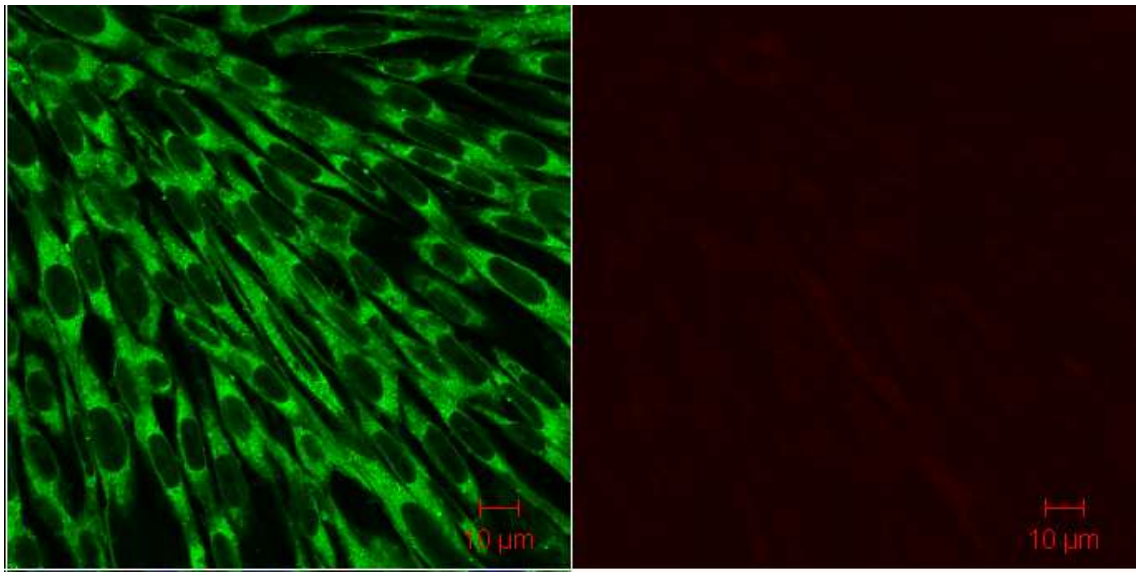


(c) (d)

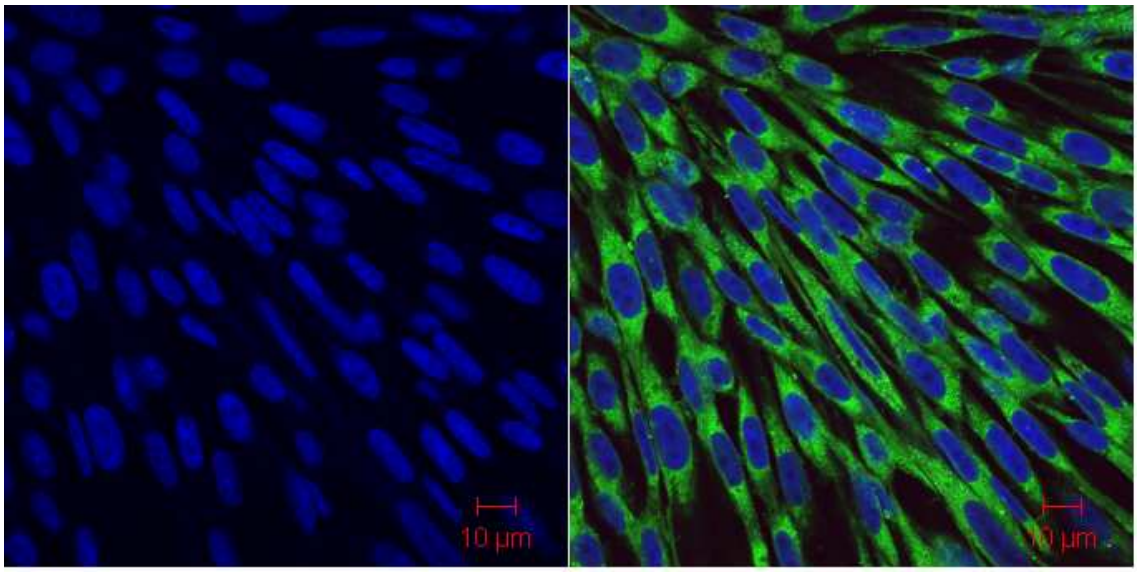


**Figure 4.3.3.1:** Co-staining experiment carried out on $[Ru(dpp)_2(NH_2phen)](PF_6)_2$ stained CHO cells. The co-stains used are Dioc6, which selectively stains the mitochondria and endoplasmic reticulum and vesicle membranes, and DRAQ7, which selectively stains the nucleus. (a) represents the areas stained Dioc6, (b) stained with $[Ru(dpp)_2(NH_2phen)](PF_6)_2$, (c) stained with DRAQ7 and (d) a combined image of the areas stained with all three.

(a) (b)

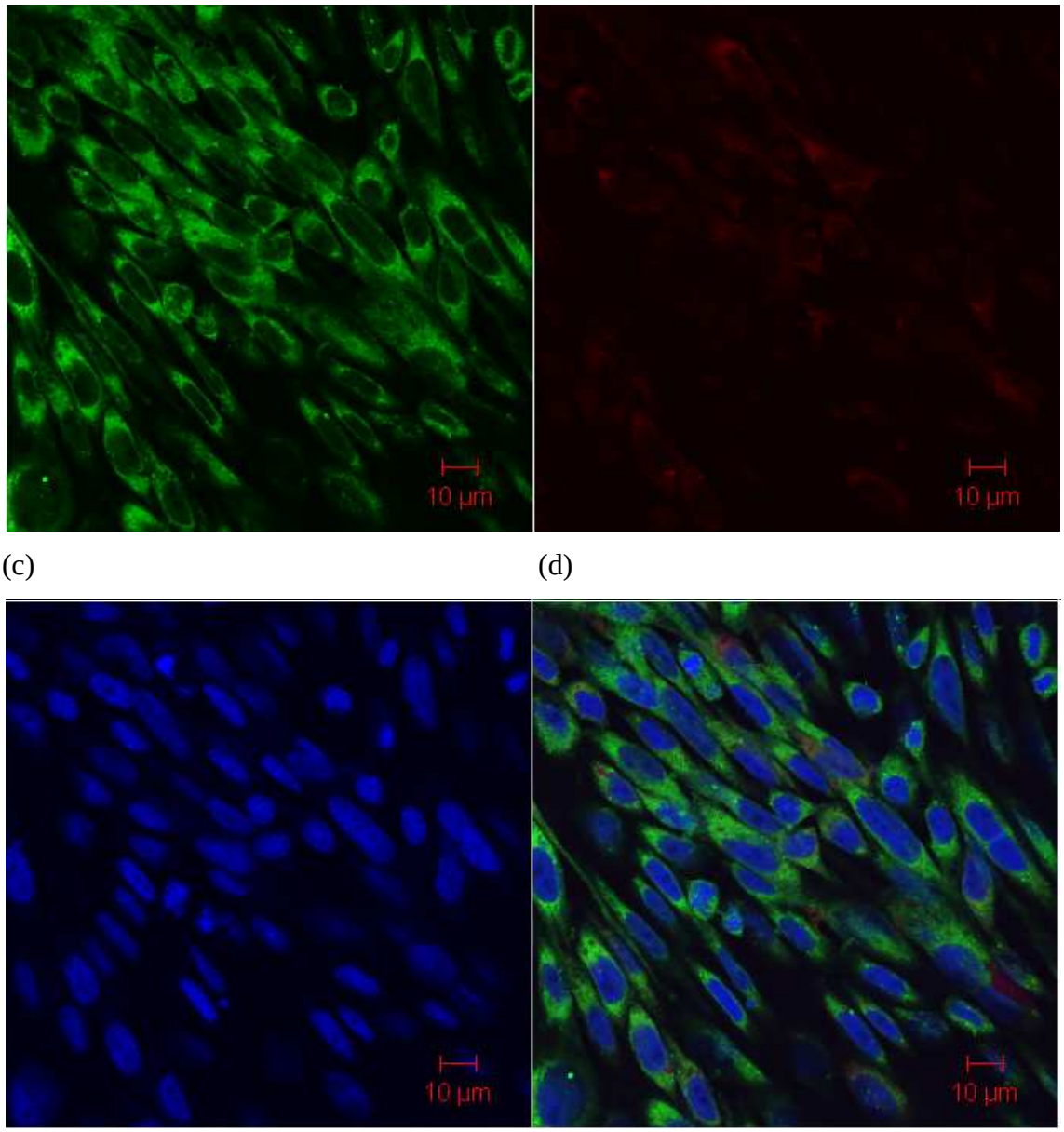


(c) (d)

**Figure 4.3.3.2:** Co-staining experiment carried out on Ru6D stained CHO cells. The co-stains used are Dioc6, which selectively stains the mitochondria and endoplasmic reticulum and vesicle membranes, and DRAQ7, which selectively stains the nucleus. (a) represents the areas stained Dioc6, (b) stained with Ru6D, (c) stained with DRAQ7 and (d) a combined image of the areas stained with all three.

(a) (b)

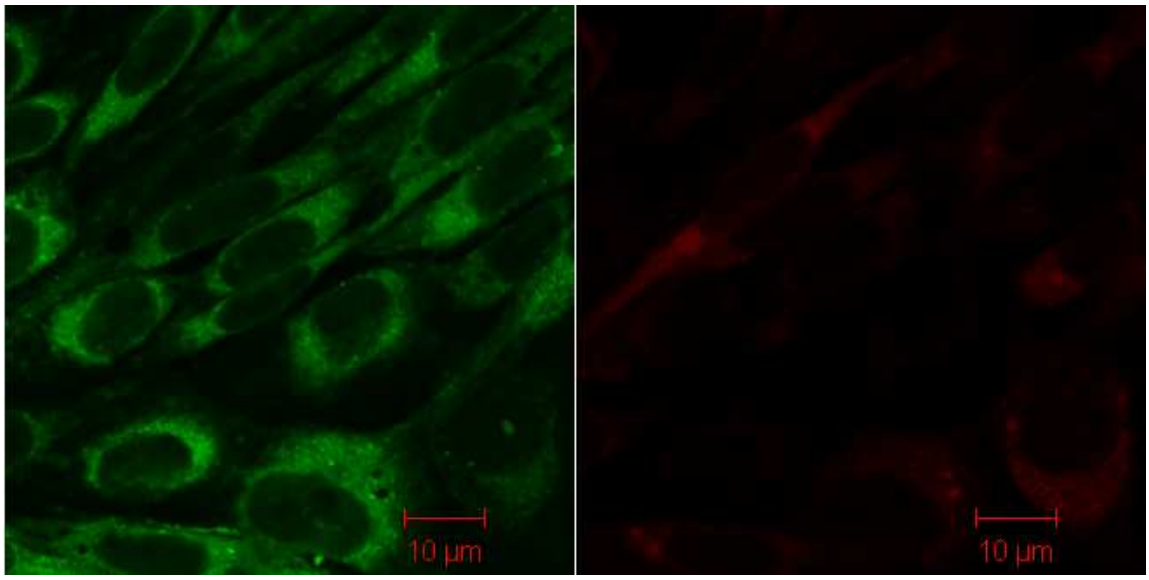


(c) (d)

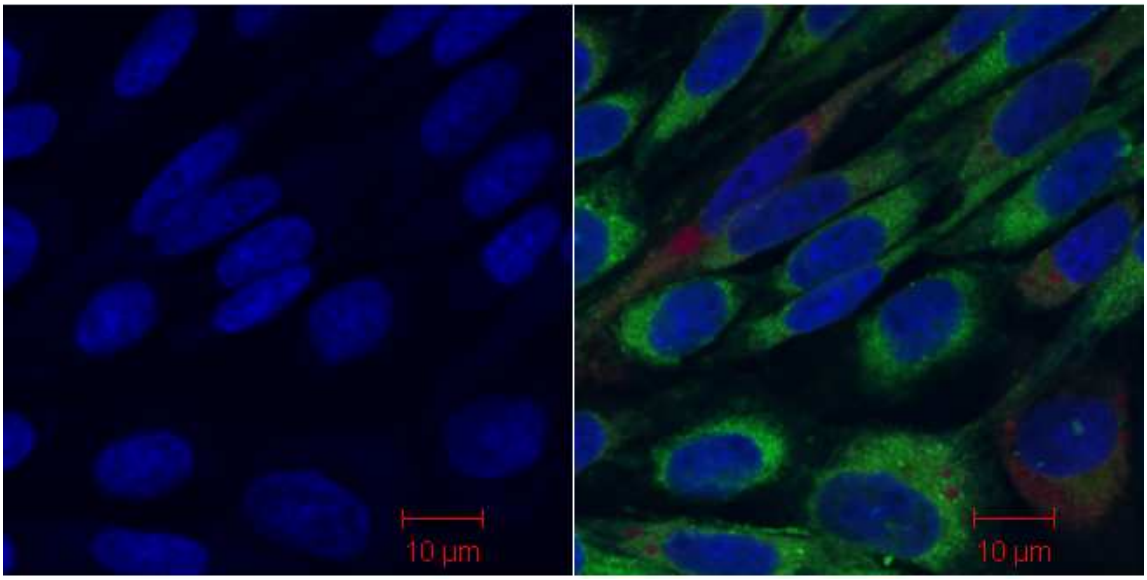


**Figure 4.3.3.3:** Co-staining experiment carried out on Ru8D stained CHO cells. The co-stains used are Dioc6, which selectively stains the mitochondria and endoplasmic reticulum and vesicle membranes, and DRAQ7, which selectively stains the nucleus. (a) represents the areas stained Dioc6, (b) stained with Ru8D, (c) stained with DRAQ7 and (d) a combined image of the areas stained with all three dyes.

(a) (b)

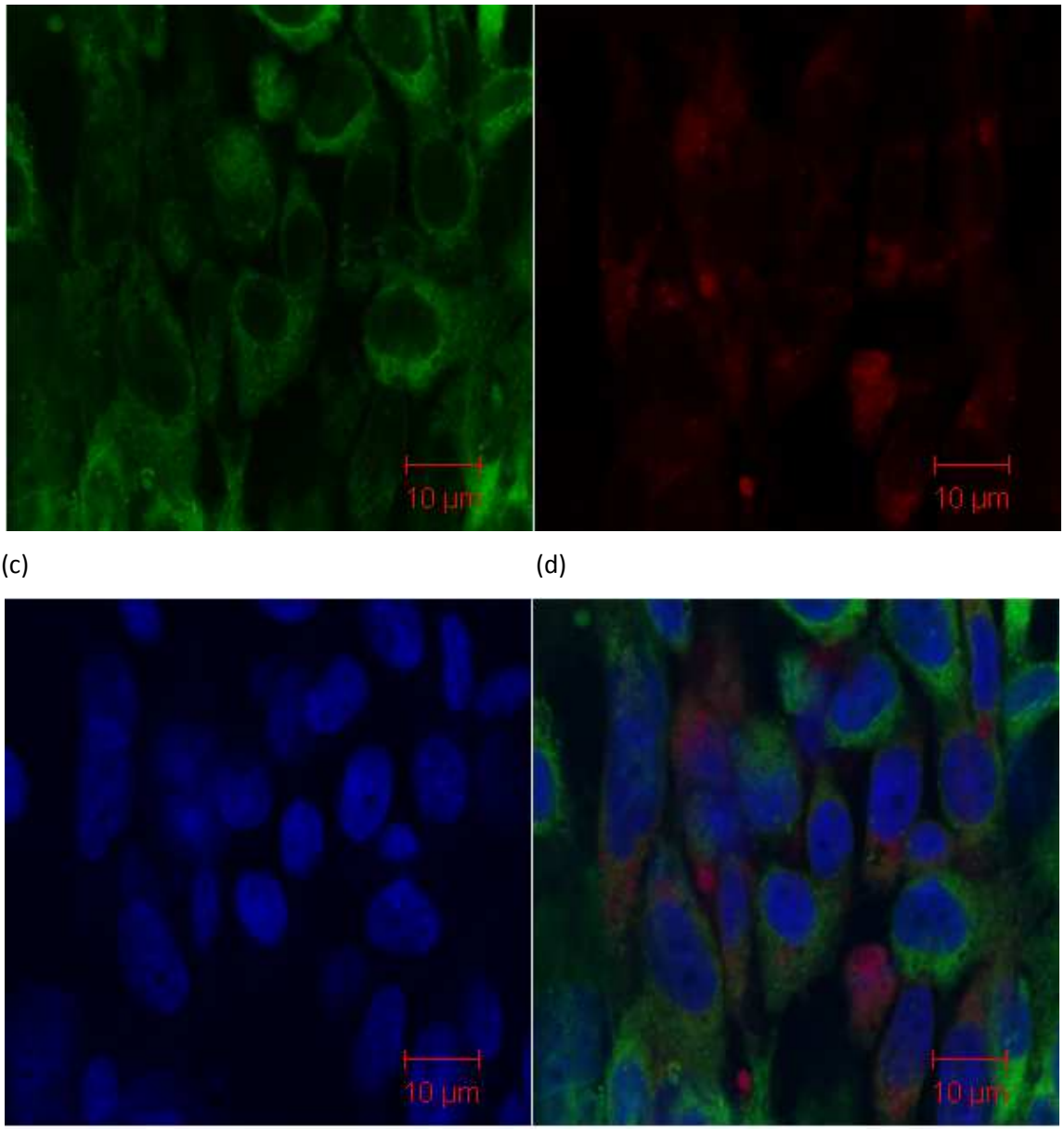


(c) (d)

**Figure 4.3.3.4:** Co-staining experiment carried out on Ru11D stained CHO cells. The co-stains used are Dioc6, which selectively stains the mitochondria and endoplasmic reticulum and vesicle membranes, and DRAQ7, which selectively stains the nucleus. (a) represents the areas stained Dioc6, (b) stained with Ru11D, (c) stained with DRAQ7 and (d) a combined image of the areas stained with all three.

(a) (b)

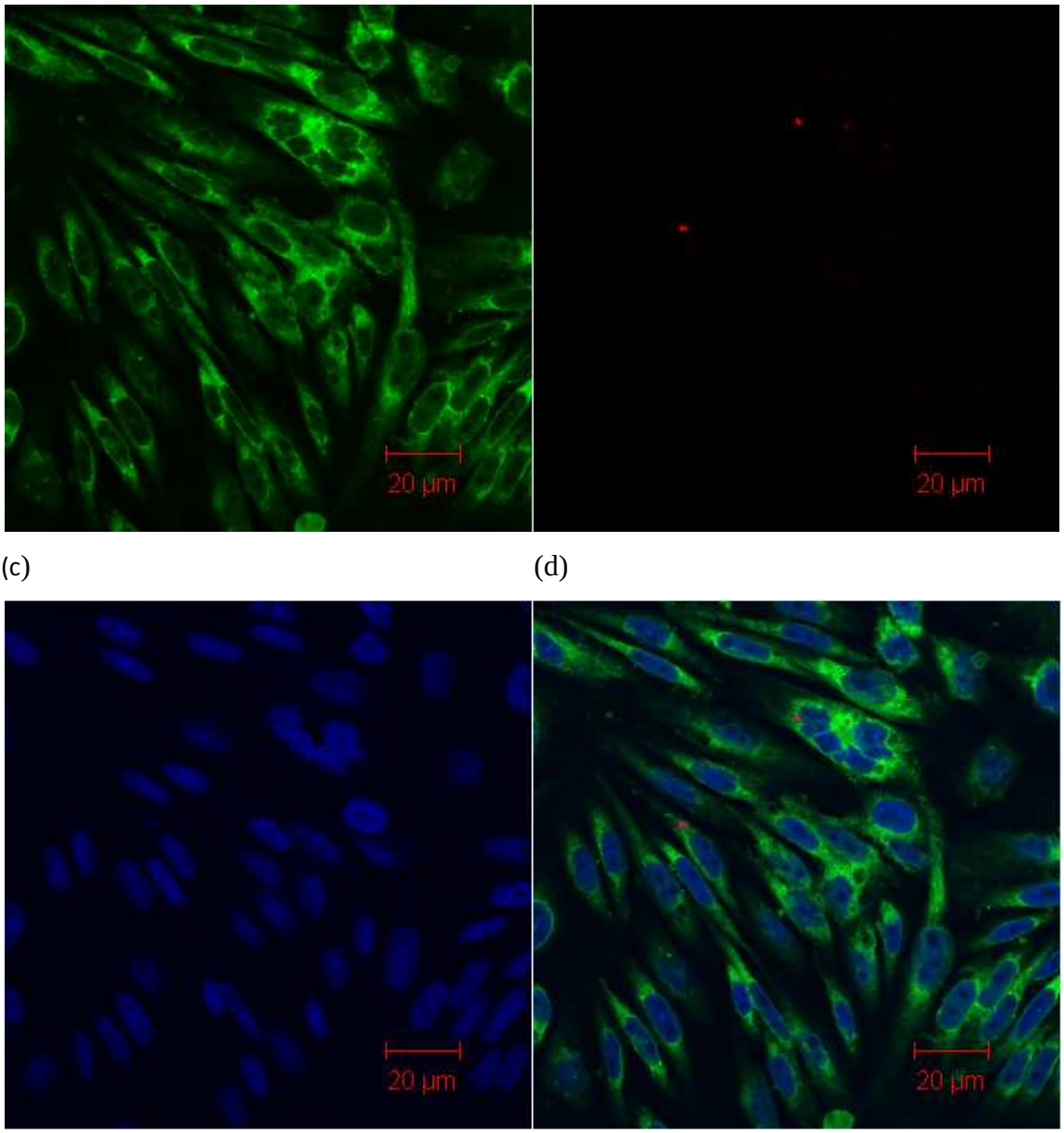


(c) (d)

**Figure 4.3.3.5:** Co-staining experiment carried out on Ru16D stained CHO cells. The co-stains used are Dioc6, which selectively stains the mitochondria and endoplasmic reticulum and vesicle membranes, and DRAQ7, which selectively stains the nucleus. (a) represents the areas stained Dioc6, (b) stained with Ru16D, (c) stained with DRAQ7 and (d) a combined image of the areas stained with all three.

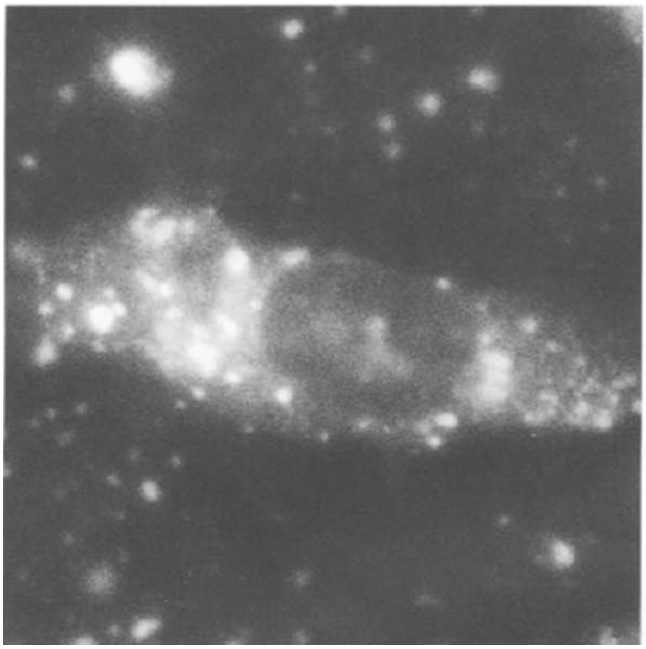

**Figure 4.3.3.6:** Fluorescence intensity image of a CHO cell incubated with DOPE/DC-CHOL liposomes containing 5% FPE. The CHO cells were incubated on a coverslip for 30 minutes with the liposomes. The cells were then washed and fixed before the image was collected. Image reproduced from ref[18].

### *4.3.4 FLIM Imaging of RuxD Treated Cells*

As the RuxD complexes have long lived luminescence lifetimes they are particularly suitable to FLIM imaging. The luminescence lifetimes of these RuxD complexes are also expected to be strongly affected by their environment, as demonstrated in Chapter 3 where the RuxD complexes luminescence lifetime was shown to be sensitive to the solvent environment and to quenching by oxygen. Confocal FLIM mapping was carried out on the CHO cells treated with RuxD and the resulting FLIM images are displayed in Fig 4.3.4.1 – 4.3.4.4. Confocal FLIM mapping was also carried out on $[Ru(dpp)_2(NH_2phen)](PF_6)_2$ treated CHO cells and the resulting FLIM image is presented in Fig 4.3.4.5. All FLIM imaging experiments were preformed on live cells and which were not fixed with paraformaldehyde.

The FLIM experiments were deemed fast enough that no cell fixing was required. The FLIM maps for all the RuxD and $[Ru(dpp)_2(NH_2phen)](PF_6)_2$ treated cells are consistent with the luminescence intensity images in section 4.3.2. All FLIM maps show the complexes are distributed non-uniformly throughout the cell punctuated with spherical structures. The exception to this is the Ru16D treated CHO cells wherein the complex is almost uniformly localised within these spherical structures, indicating again that there is dependence on the localisation of the complexes within the cell with alkyl chain length. The average lifetime for all the RuxD and the $[Ru(dpp)_2(NH_2phen)](PF_6)_2$ treated cells is about ~740 ns with the exception of Ru16D treated cells which displays a significantly lower average lifetime of ~570 ns. These lifetimes are very long compared to the complex in solution but are comparable to the complexes in liposomes and in vesicle structures and seem to indicate that the complex resides in lipophilic regions in the cell, most likely within membrane structures within the cells.

For $[Ru(dpp)_2(NH_2phen)](PF_6)_2$ treated CHO cell and for RuxD treated CHO cells, excluding Ru16D treated cells, the areas where the complex is localised outside of the spherical structures tends to have a lifetime close to the observed average lifetime. The spherical structures in all treated cells however display lifetimes that vary from structure to structure. In particular the Ru16D treated CHO cells display some spherical structures with exceptionally long lived lifetimes of about 800 ns. The lifetime distribution histograms of the Ru6D, Ru8D, Ru11D and $[Ru(dpp)_2(NH_2phen)](PF_6)_2$ are bell shaped curves with spanning luminescence lifetimes from about 400 ns to 1000 ns. This wide variety of luminescence lifetimes is due to the observed variety of luminescence lifetimes of the spherical structures observed in the cell after staining. For Ru16D treated cells the lifetime histogram spans lifetimes from about 300 ns to 700 ns with a long tail spanning from about 700 ns to 900 ns. Again the wide variety of observed luminescence lifetimes is due to the observed spherical structures. The long lived luminescence tail is accounted for by the presence of the very long lived luminescence spherical structures observed in the Ru16D treated CHO cells.

Due to the variance in the observed lifetimes of these spherical structures it is safe to say that they are not caused by the formation of RuxD bilayer vesicles inside the cytoplasm. This would lead to structures that had very stable environments and therefore there would be little change in luminescence lifetime from structure to structure. These structures are also

much bigger than the size of the liposomes of RuxD complexes reported on in Chapter 3, which have sizes of around 130 – 180 nm in diameter, while the structures observed in the cell are < 1 µm. A possible explanation for the identity of these spherical structures is that these spherical structures are endosomes and lysosomes and represent the mechanism by which the RuxD and $[Ru(dpp)_2(NH_2phen)](PF_6)_2$ complexes enter the cell. The initial formation of the endosome represents the structures with high luminescence lifetime due to the lipophilic environment experience by the complexes residing in the endosome lipid bilayer. As the endosome becomes a lysosome the lifetime of the complex within it is reduced due to the harsh acidic environment experienced within the lysosome.

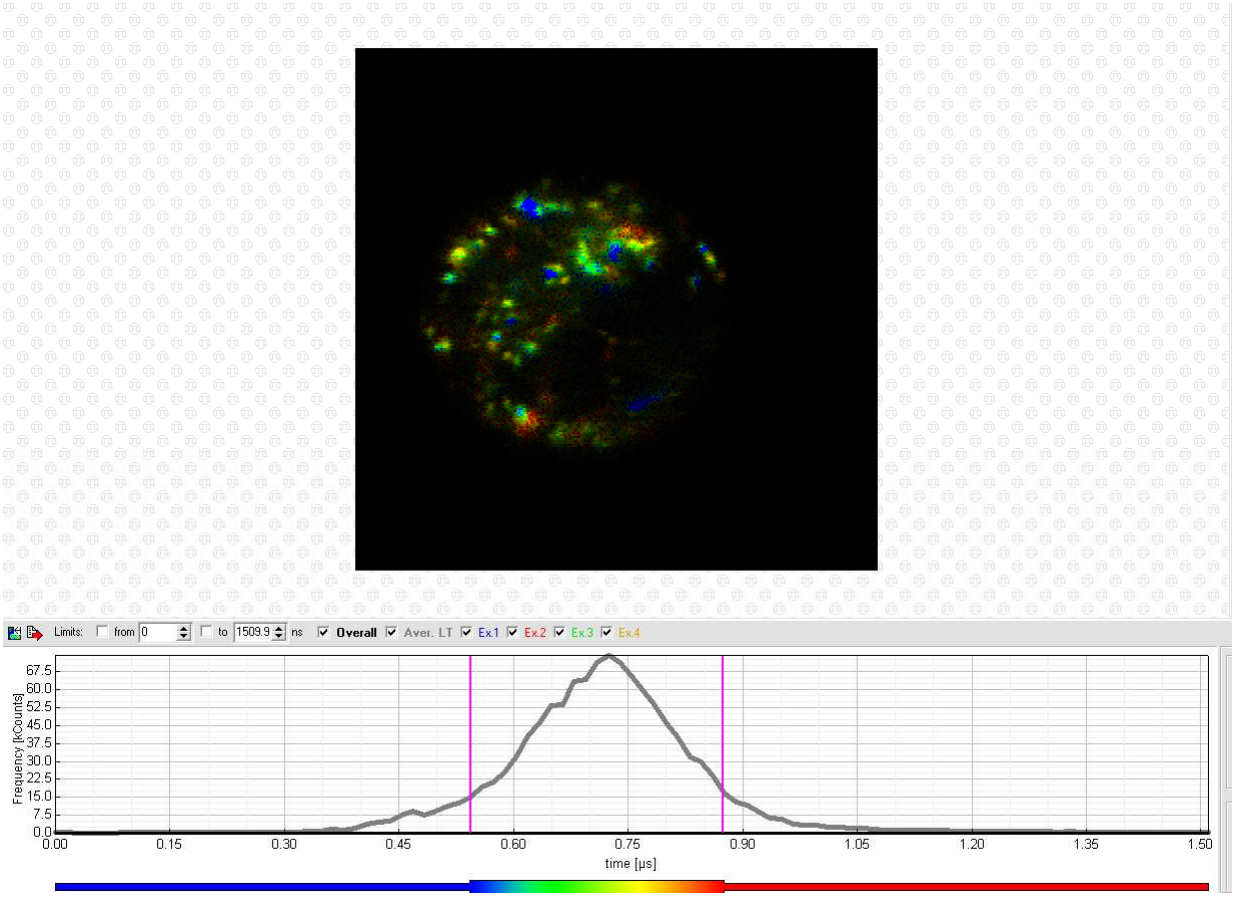


**Figure 4.3.4.1:** Confocal average luminescence lifetime maps of Ru6D treated CHO cells with lifetime histogram. CHO cells were adhered to a glass slide and kept hydrated with PBS buffer solution. An excitation wavelength of 440 nm was used with a 460 nm long pass filter to reduce interference from the excitation source. A SPAD single photon detector was used as the detector.

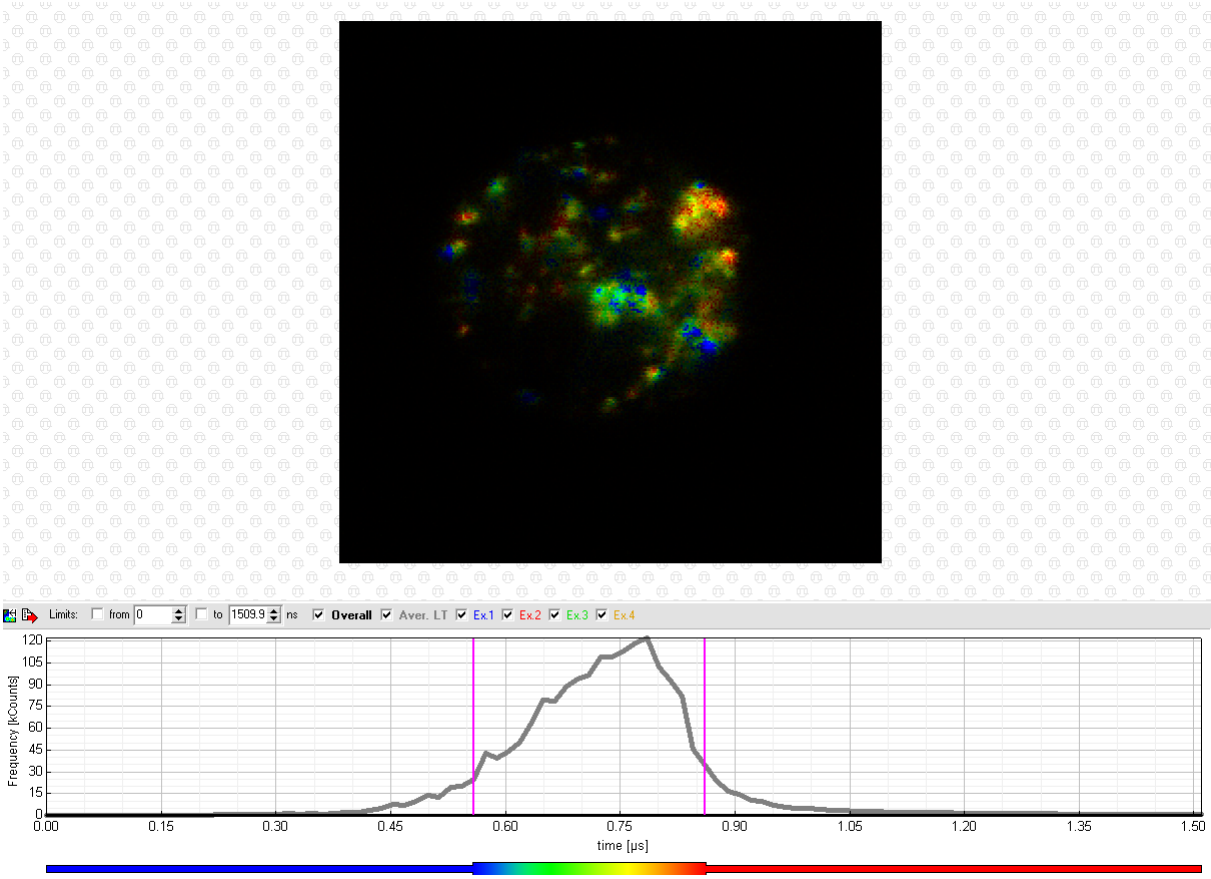


**Figure 4.3.4.2:** Confocal average luminescence lifetime maps of Ru8D treated CHO cells with lifetime histogram. CHO cells were adhered to a glass slide and kept hydrated with PBS buffer solution. An excitation wavelength of 440 nm was used with a 460 nm long pass filter to reduce interference from the excitation source. A SPAD single photon detector was used as the detector.

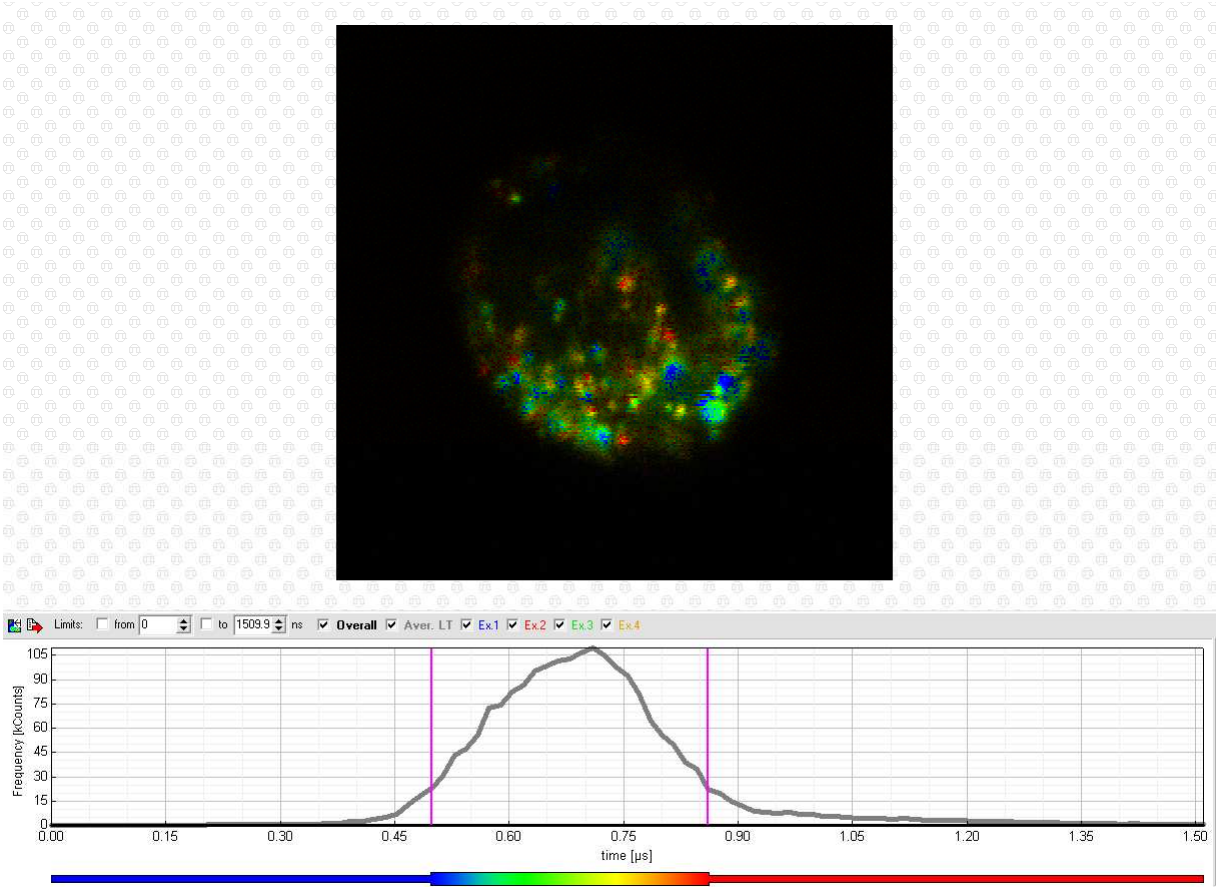


**Figure 4.3.4.3:** Confocal average luminescence lifetime maps of Ru11D treated CHO cells with lifetime histogram. CHO cells were adhered to a glass slide and kept hydrated with PBS buffer solution. An excitation wavelength of 440 nm was used with a 460 nm long pass filter to reduce interference from the excitation source. A SPAD single photon detector was used as the detector.

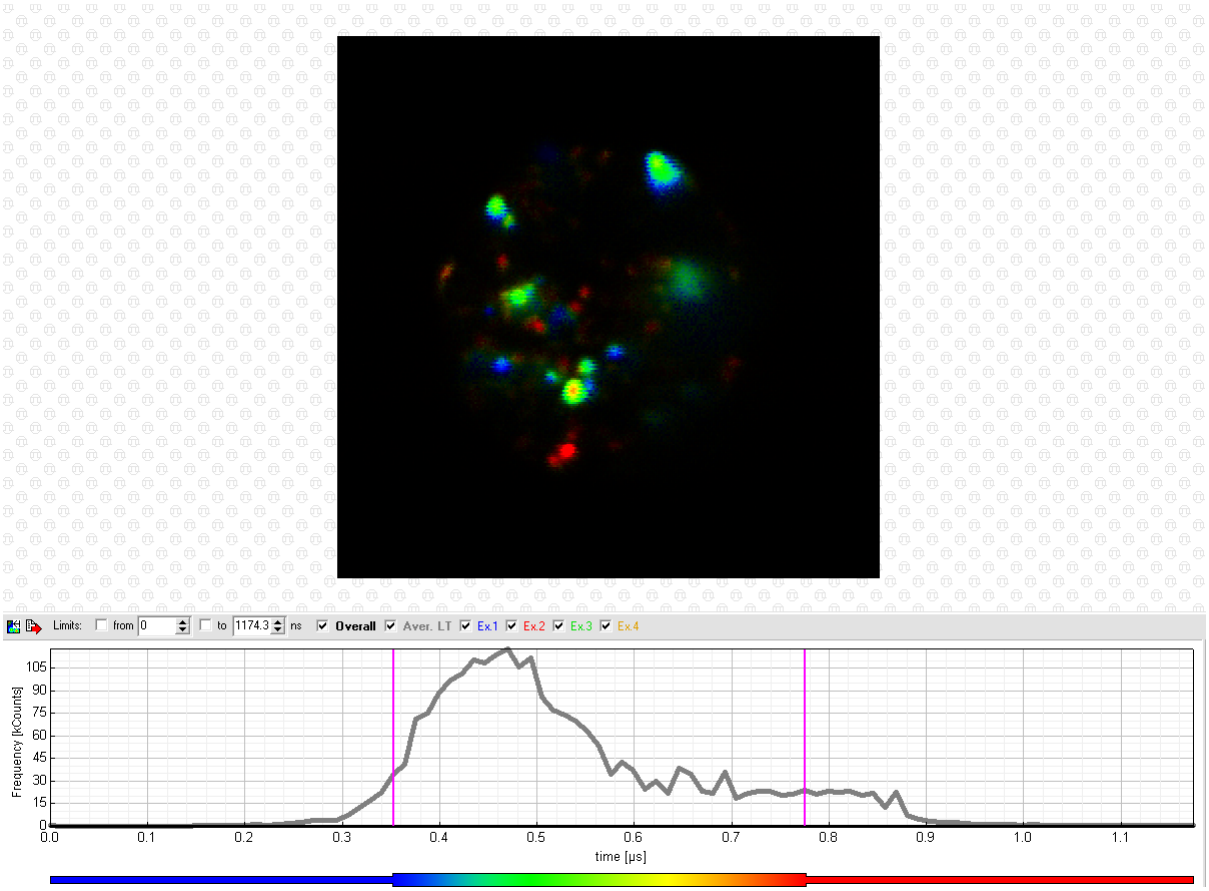


**Figure 4.3.4.4:** Confocal average luminescence lifetime maps of Ru16D treated CHO cells with lifetime histogram. CHO cells were adhered to a glass slide and kept hydrated with PBS buffer solution. An excitation wavelength of 440 nm was used with a 460 nm long pass filter to reduce interference from the excitation source. A SPAD single photon detector was used as the detector.

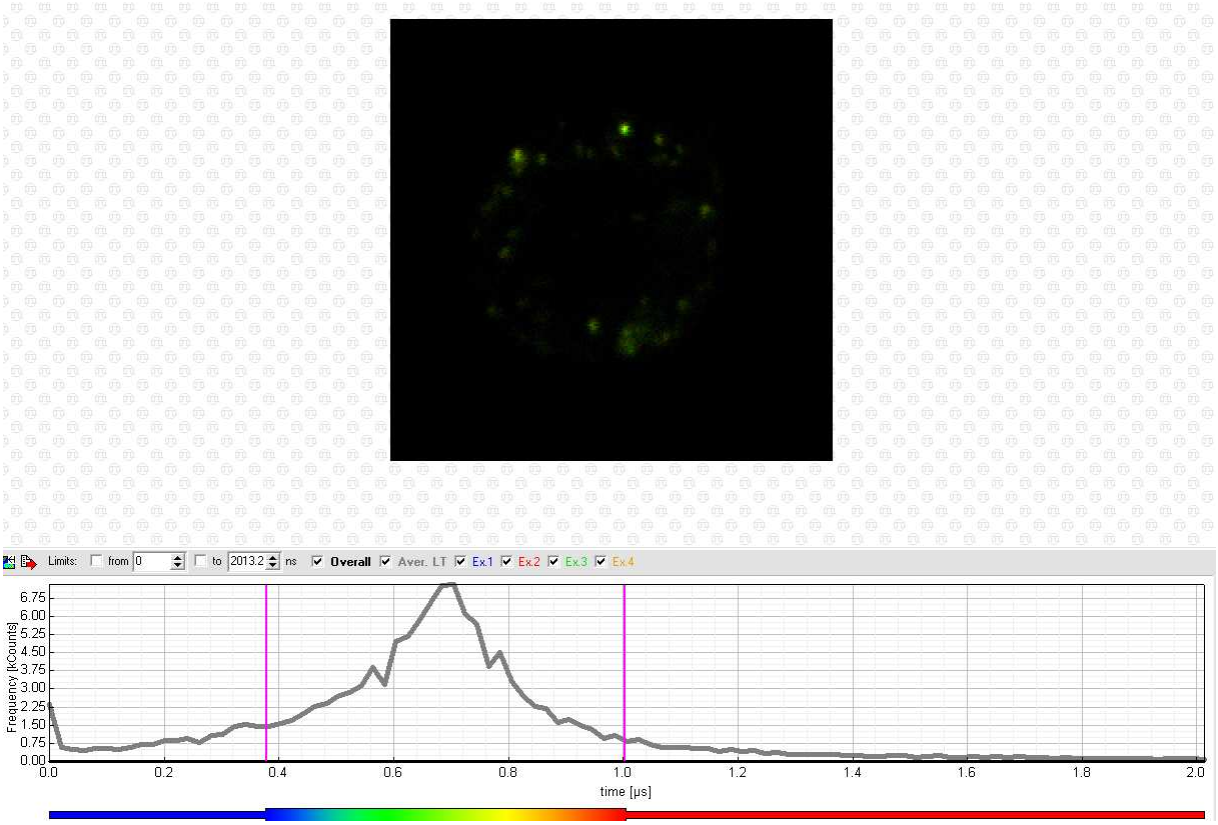


**Figure 4.3.4.5:** Confocal average luminescence lifetime maps of $[Ru(dpp)_2(NH_2phen)](PF_6)_2$ treated CHO cells with lifetime histogram. CHO cells were adhered to a glass slide and kept hydrated with PBS buffer solution. An excitation wavelength of 440 nm was used with a 460 nm long pass filter to reduce interference from the excitation source. A SPAD single photon detector was used as the detector.

Untreated CHO cells were also imaged by FLIM mapping under the same conditions as the RuxD treated CHO cells as a control to identify any contributions from cellular autofluorescence to the observed luminescence of the RuxD treated CHO cells. A FLIM map of an untreated CHO cell is shown below in Fig 4.3.4.6. Luminescence intensity is very weak and the only observed average fluorescent lifetimes are extremely short and probably due to cellular autofluorescence.

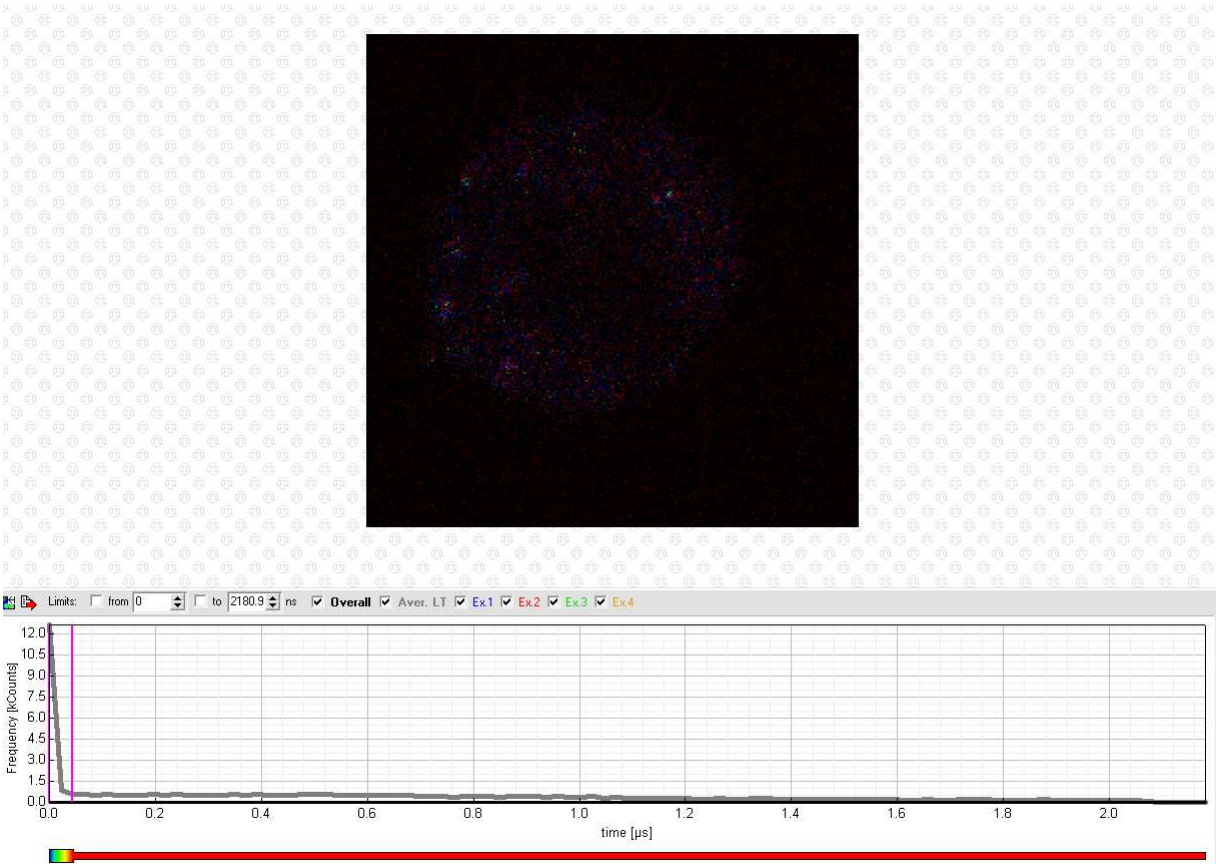


**Figure 4.3.4.6:** Confocal average luminescence lifetime maps of untreated CHO cells with lifetime histogram. CHO cells were adhered to a glass slide and kept hydrated with PBS buffer solution. An excitation wavelength of 440 nm was used with a 460 nm long pass filter to reduce interference from the excitation source. A SPAD single photon detector was used as the detector.

In order to examine the distribution of the RuxD dyes and the structures they occupy in more detail 3D z-stack FLIM images of the CHO cells treatedwith the RuxD complexes were obtained. These 3D z-stacks of the RuxD treated CHO cells and are presented in Fig 4.3.4.7 – 4.3.4.10. These z-stack images confirm distribution of Ru6D, Ru8D and Ru11D throughout the cytoplasm. Some dark areas are evident in the 3D z-stack images and are probably due to the nucleus where the RuxD complexes only show weak localisation. Distribution of the spherical structures is evident throughout the cell cytoplasm. Ru16D again appears to only localise in these spherical structures and not throughout the cytoplasm.

(a)

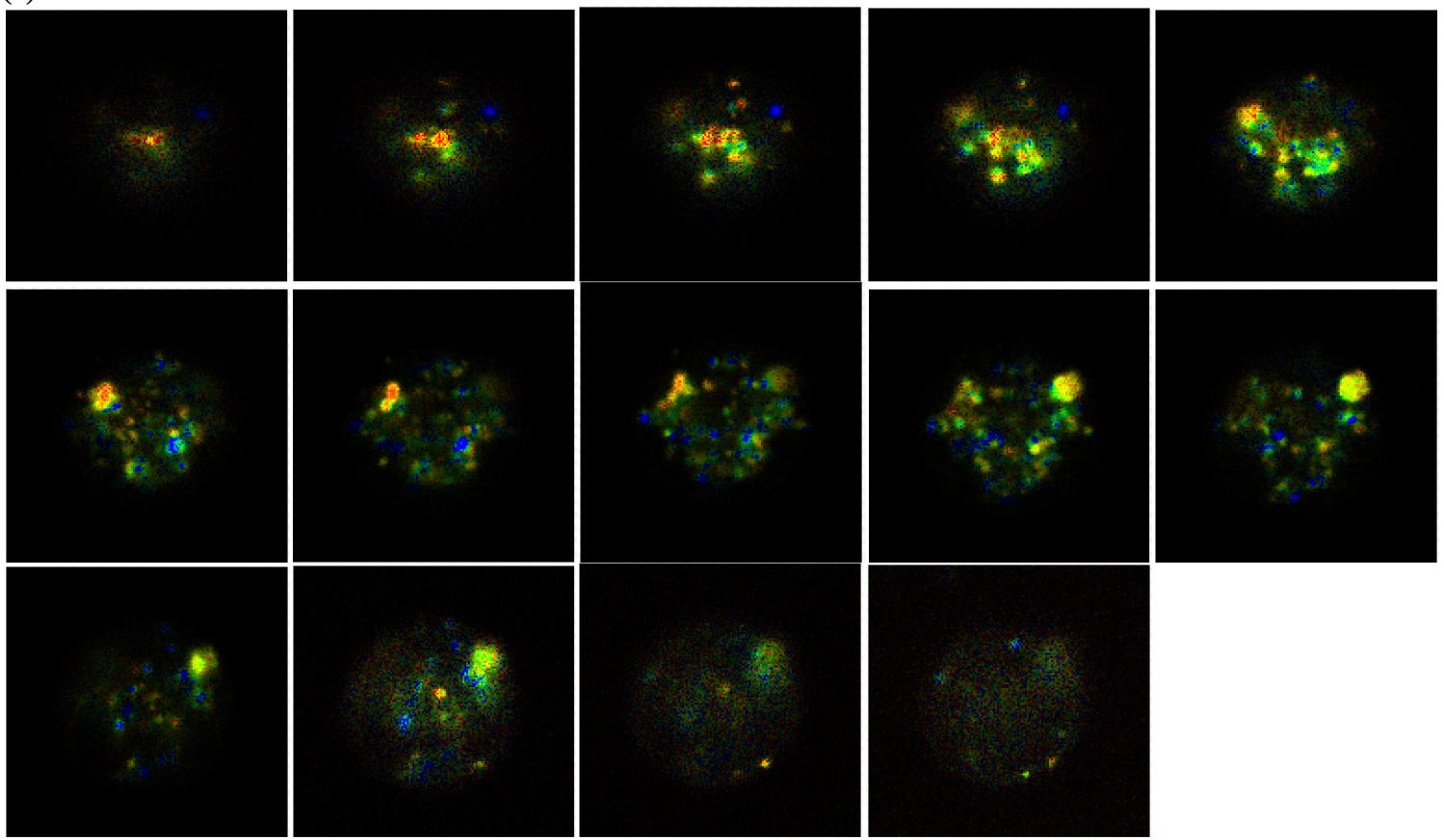

(b)

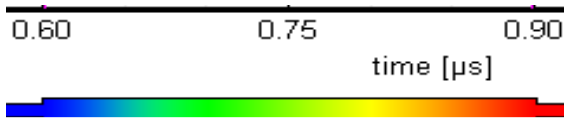


**Figure 4.3.4.7:** (a) 3D z-stack false colour FLIM mapping image of Ru6D treated CHO cell. Each image represents a step in the z-axis of 1 µm. (b) Luminescence lifetime histogram for these image

(a)

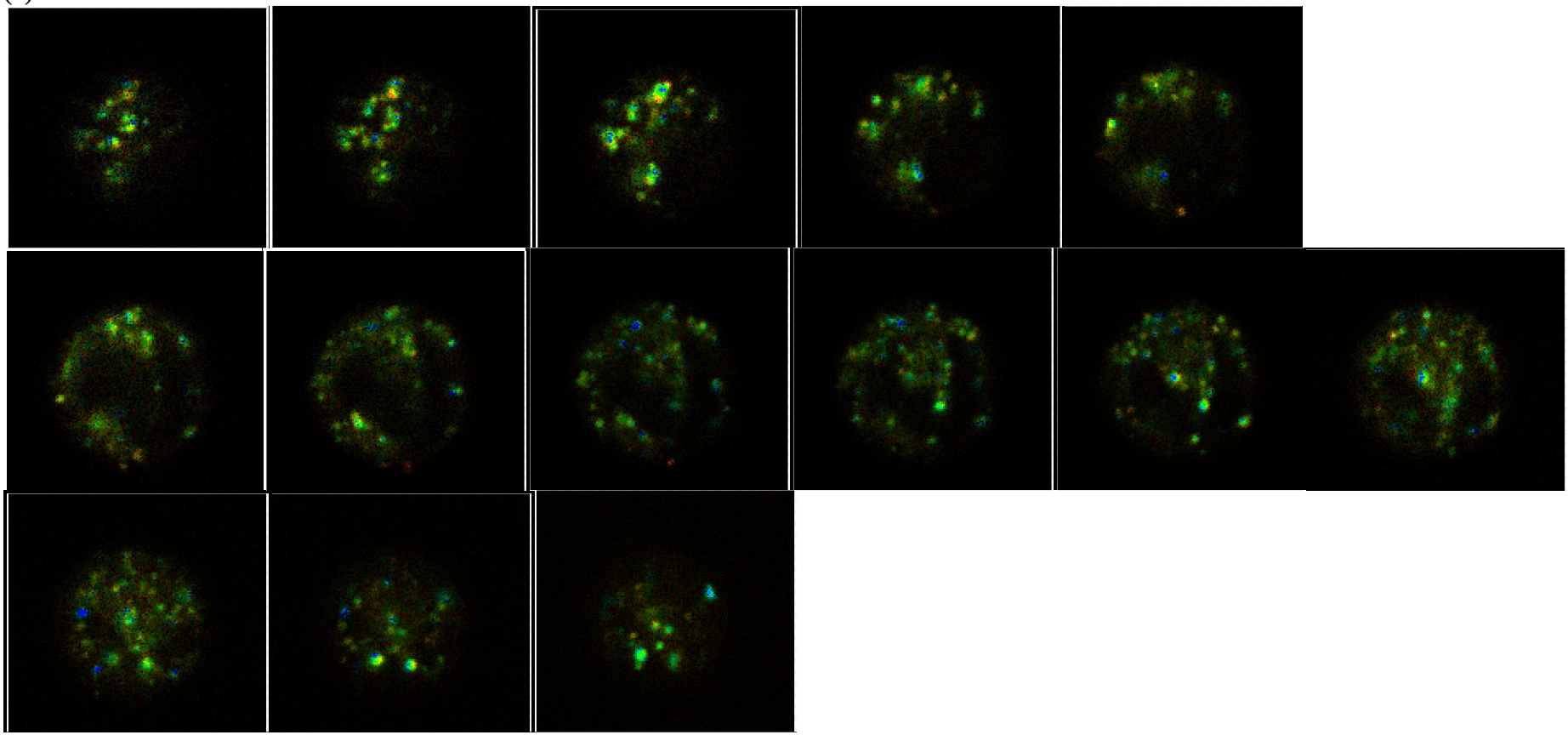

(b)

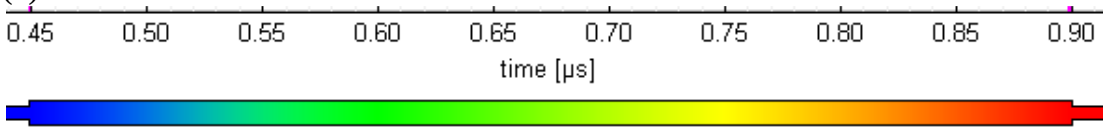


**Figure 4.3.4.8:** (a) 3D z-stack false colour FLIM mapping image of Ru8D treated CHO cell. Each image represents a step in the z-axis of 1 µm. (b) Luminescence lifetime histogram for these images

(a)

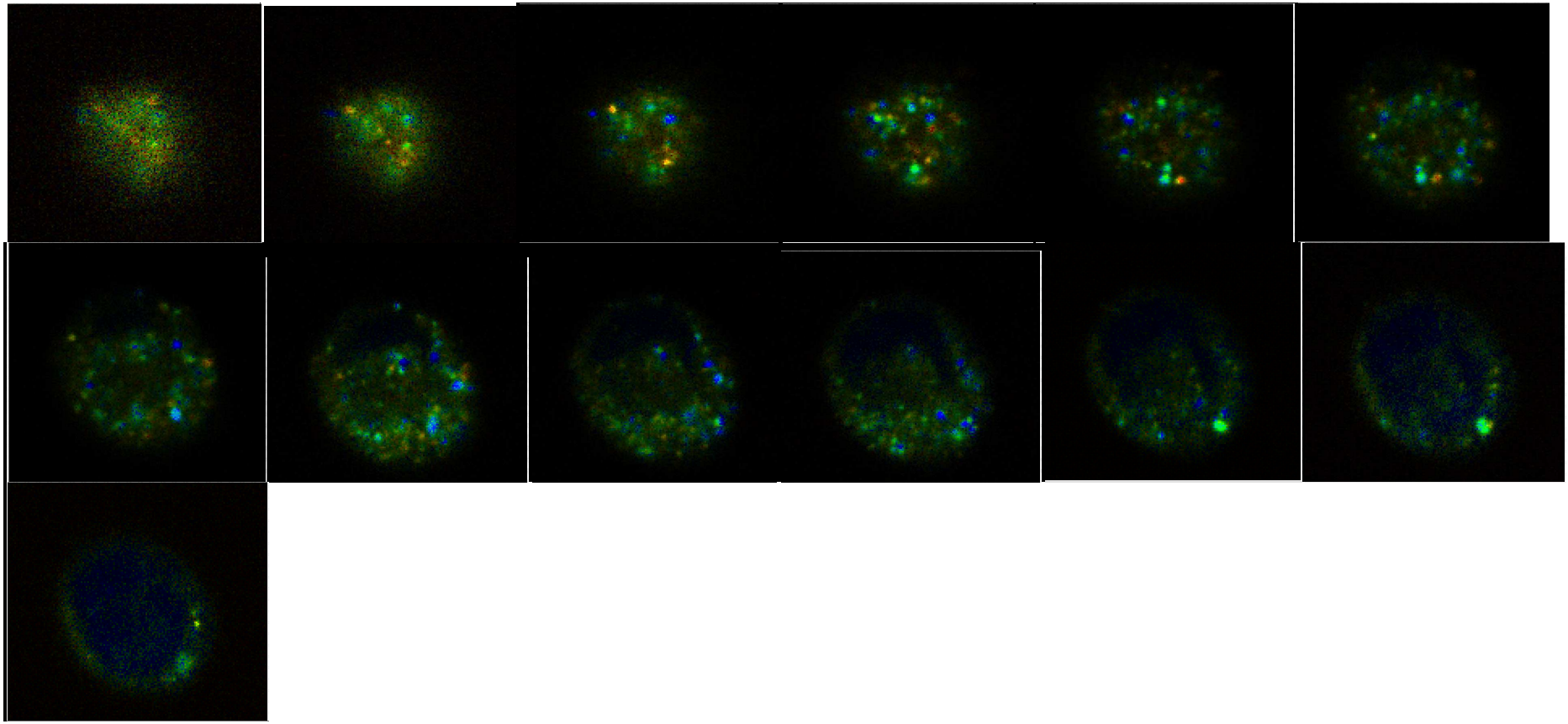

(b)


**Figure 4.3.4.9:** 3D z-stack false colour FLIM mapping image of Ru11D treated CHO cell. Each image represents a step in the z-axis of 1 µm. (b) Luminescence lifetime histogram for these images

(a)

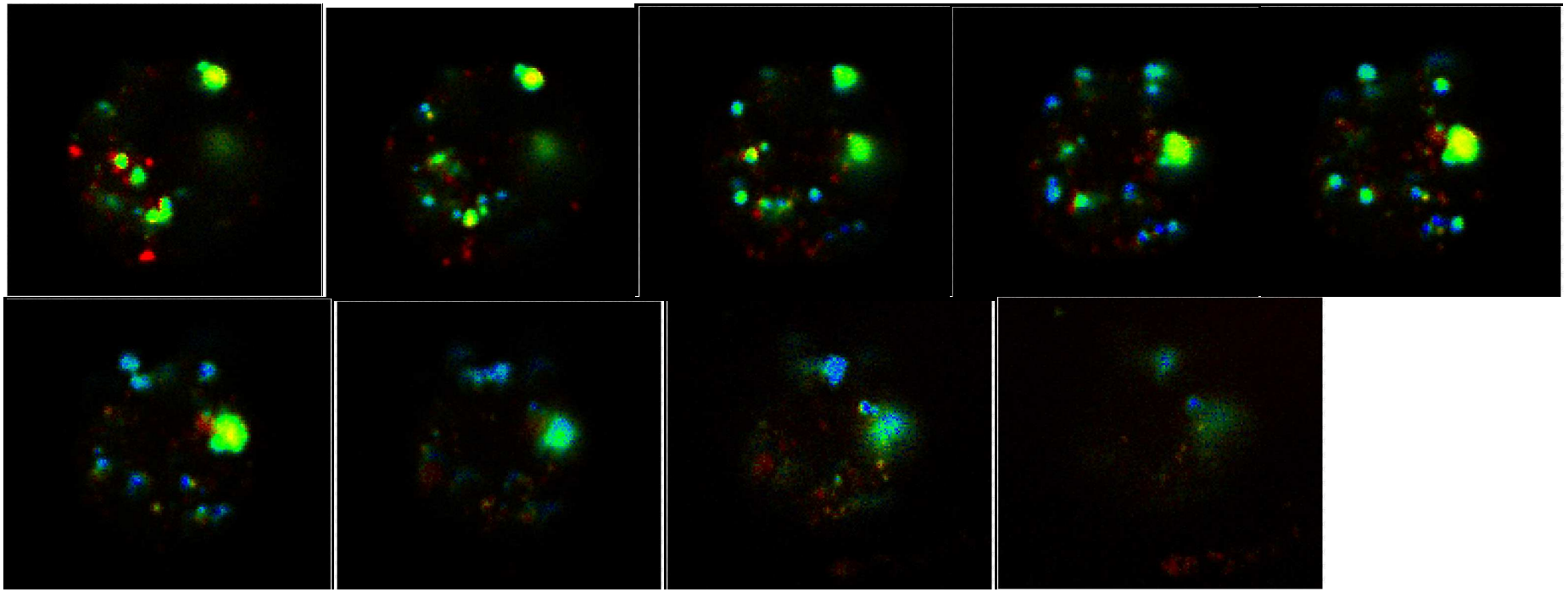

(b)

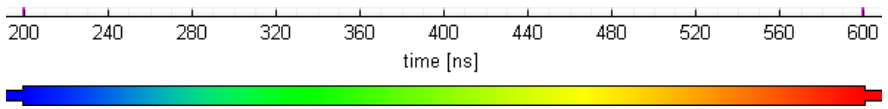


**Figure 4.3.4.10:** 3D z-stack false colour FLIM mapping image of Ru16D treated CHO cell. Each image represents a step in the z-axis of 1 µm. (b) Luminescence lifetime histogram for these images.

## 4.4 Conclusions

In this chapter the ability of the RuxD series of complexes to function as cell imaging agents in mammalian cells was explored. A CHO cell line was treated with the RuxD series of complexes and the parent complex $[Ru(dpp)_2(NH_2phen)](PF_6)_2$. It was found that all four RuxD complexes diffused through the cell membrane into the cytoplasm. It was also found that the parent complex $[Ru(dpp)_2(NH_2phen)](PF_6)_2$ diffused across the cell membrane into the cytoplasm despite the lack of an alkyl chain. This was attributed to the presence the 0.625% DMSO solution that the cells are immersed in during the staining procedure. Despite the low volume of DMSO $[Ru(dpp)_2(NH_2phen)](PF_6)_2$ still crossed the cell membrane showing that DMSO could not be discounted from the mechanism of uptake. However the hydrophobicity of the complex cannot be discounted as a contributing fact to cellular uptake either.

The RuxD complexes showed interesting alkyl chain length dependence on the localisation of the complex within the cell. All RuxD complexes localised within small spherical structures within the cell in high concentrations, but Ru16D was barely detected outside of these structures. For Ru6D, Ru8D and Ru11D the luminescence intensity of the complex outside these structures decreased with increasing alkyl chain length. Co-staining experiments were carried out to with DiOC6 and DARQ7 to elucidate where the RuxD complexes localised. Co-staining with DARQ7 confirmed that there was little nuclear penetration by the RuxD complexes. However luminescence intensity imaging clearly shows staining of the nucleus by all RuxD complexes except Ru16D. DiOC6 did not co-localise with the high luminescence intensity spherical structures, identifying that they were not mitochondria. Co-localisation of the RuxD complexes with other areas that DiOC6 stains, such as lipid membrane structures in the cytoplasm, was observed.

FLIM mapping of the RuxD treated CHO cells was in agreement with the luminescence intensity images. FLIM mapping showed distribution of Ru6D, Ru8D, Ru11D throughout the cell cytoplasm and again confirmed localisation within spherical structures throughout the cytoplasm. Ru16D uniformly localised in these spherical structures. The average luminescence lifetime of the treat CHO cells was ~740 ns except for Ru16D treated cells where it was ~540 ns. The luminescence lifetime of these spherical structures varied

throughout the cell. Ru16D showed a higher proportion of very long lived spherical structures. Due to the variety of lifetimes of these structures it was proposed that these structures and endosomes and liposomes. Future co-staining experiments will be carried out to confirm this.

# References


[1] Levitt, J.A.; Matthews, D.R.; Ameer-Beg, S.M. and Suhling, K.; *Curr. Opin. Biotech.*, 20, **2009**, 28-36

[2] Schneckburger, H.; Wagner, M.; Weber, P.; Strauss, W.S.L. and Sailer, R.; *J. Flour.,* 14, **2004**, 649-654

[3] Ghukasyan, V.V. and Kao, F.J.; *J. Phys. Chem. C.*, 113, **2009**, 11532-11540

[4] Neugebauer, U.; Pellegrin, Devocelle, M.; Forster, R.J.; Signac, W.; Moran, N. and Keyes, T.E.; *Chem. Comm.,* **2008**, 5305-5309

[5] Zhong, W.; Urayama, P. and Mycek, M.A.; *J. Phys. D.: Appl. Phys.*, 36, **2003**, 1689-1695

[6] Ji, J.; Rosenzweig, N.; Jones, I. and Rosenzweig, Z.; *J. Biomed. Optics*, 7, **2002**, 404-409

[7] Lin, H. J., Herman, P. and Lakowicz, J.R.; *Cytometry Part A*, 52A, **2003**, 77-89

[8] Carlsson, K.; Liljebourg, A.; Andersson, R.M. and Brismar, H.; *J. Microsp.*, 199, **2000**, 106-114

[9] Margineanu,A.; Hotta, J.; Van der Auweraer, M.; Ameloot, M.; Stefan, A.; Beljonne, D.; Engelborghs, Y.; Herrmann, A.; Mullen, K.; De Schryver, F.C. and Hofkens, J.; *Biopys. J.*, 93, **2007**, 2877-2891

[10] Margineanu, A.; Hotta, J.; Van der Auweraer, M.; Ameloot, M.; Stefan, A.; Beljonne, D.; Engelborghs, Y.; Herrmann, A.; Mullen, K.; De Schryver, F.C. and Hofkens, J.; *Biophys. J.*, 93, **2007**, 2877-2891

[11] Lo, K. K-W.; Lee, P-K. and Lau, J. S-Y.; *Organometallics*, 27, **2008**, 2998-3006

[12] Amoroso, A. J.; Coogan, M. P.; Dunne, J. E.; Fernandez-Moreira, V.; Hess, J. B.; Hayes, A. J.; Llyod, D.; Millet, C.; Pope, S. J. A. and Williams, C.; *Chem. Comm.*, **2007**, 3066-3068

[13] Pratt, L.R. and Pohorille, A.; *Chem. Rev.*, 102, **2002**, 2671-2692

[14] Guerrero-Martinz, A.; Vida, Y.; Dominguez-Gutierrez, D.; Alburquerque, R. Q. and De Cola, L.; *Inorg. Chem.*, 47, **2008**, 9131-9133

[15] Notman, R.; Noro, M.; O'Malley, B. and Anwar, J.; *J. Am. Chem. Soc.*, 128, **2006**, 31982-13983

[16] Puckett, C. A. and Barton, J. K.; *Biochem.*, 47, **2008**, 11711-11716

[17] Zhao, Q.; Yu, M.; Shi, L.; Liu, S.; Li, C.; Shi, M.; Zhou, Z.; Huang, C. and Li, F.; O*rganometallics*, 29, **2010**, 1085-1091

[18] Wrobel, I. and Collins, D.; *Biochim. Biophys, Acta.*, 1235, **1995**, 296-304

# 5. Characterisation of $Ru^{II}(L_{Ket})_2$: A Novel Ruthenium(II)-Polypyridine Complex Exhibiting Remarkably High Quantum Yields under Ambient Conditions

## 5.1 Introduction

The unique photophysical properties of ruthenium (II) polypyridyl complexes has led to increased interest in their use in a variety of light driven devices and photophysical applications. However the photophysical performance of ruthenium (II) polypyridyl complexes in terms of their quantum yield of emission at ambient conditions tends to be rather poor because they are prone to quenching. The quantum yields and luminescence lifetimes of ruthenium (II) polypyridyl complexes tend to be very high in $O_2$ purged environments and at low temperatures. However in ambient conditions quantum yields and luminescence lifetimes are vastly reduced. Along with vibrational relaxation, the ease of de-excitation of the metal to ligand charge transfer excited state by $O_2$ is mostly responsible for the poor photophysical performance at ambient conditions. For example the RuxD complexes described in previous chapters exhibit low quantum yields and lifetimes at ambient conditions, lower than even $[Ru(bpy)_3]^{2+}$, while in $O_2$ purged solutions and at low temperatures quantum yields and lifetimes are vastly increased, surpassing the photophysical performance of $[Ru(bpy)_3]^{2+}$. This poor performance at ambient conditions is holding back the use of ruthenium (II) polypyridyl complexes in sensors or devices that need to be robust enough for ambient conditions.

$[Ru^{II}(tpy)_2]^{2+}$ and its analogues have garnered a lot of interest as candidates for use in supramolecular systems and self assembling systems, where tpy is 2,2':6'2''-terpyridine. Unlike ruthenium polypyridyl complexes with bidentate ligands, the formation of multiple diastereomers are prevented due to the $D_{2h}$ symmetry of $[Ru^{II}(tpy)_2]^{2+}$ type complexes. In comparison Ruthenium polypyridyl complexes with bidentate ligands, such as bpy derivatives, offer no control over diastereomer formation [1]. Rod like supramolecular assemblies can be created through substitution in the 4'position of the tpy ligand [2]. For example Barrigelletti, Constable *et al.*[3] demonstrated a complex consisting of $[Ru(tpy)_2]^{2+}$ and $[Os(tpy)_2]^{2+}$ type units linked by a number of phenyl spacers at the 4' position of the

terpyridine ligands of both complexes. The absorption spectra of the complexes show clear electronic interaction between the two metal centres, with a decrease in electronic interaction detected going from 0 phenyl ring spacers to two phenyl ring spacers. The structure of these complexes is shown in Fig 5.1.1.

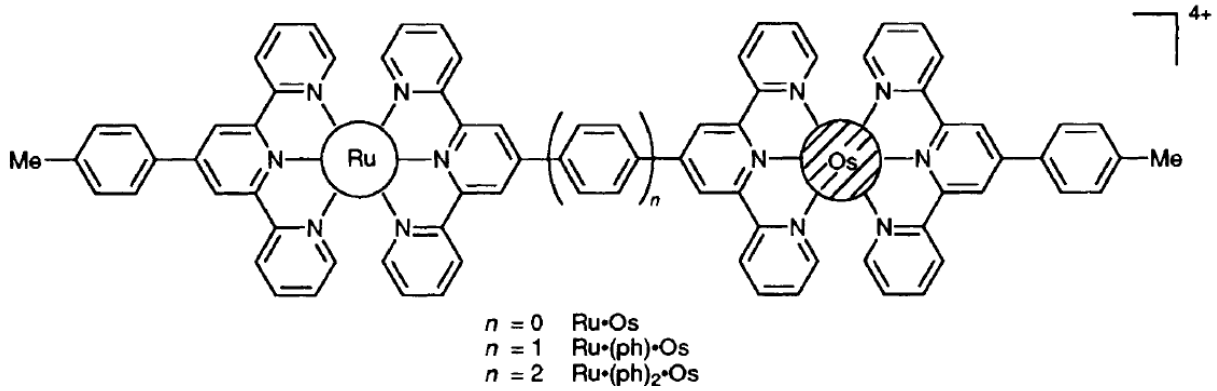


**Figure 5.1.1:** Structure of the binuclear Ru(II) and Os(II) rod like supramolecular assemblies from ref[3].

A disadvantage of using $[Ru^{II}(tpy)_2]^{2+}$ and its analogues is the poor photophysical performance of these complexes in ambient conditions. This class of complex exhibits very large quantum yields and long lifetimes at low temperatures. However photophysical performance is drastically reduced at room temperature and they exhibit short lifetimes and very low quantum yields [4, 5]. In ambient conditions $[Ru^{II}(tpy)_2]^{2+}$ is practically non luminescent with a lifetime in the picosecond range[6]. Ruthenium polypyridyl complexes with tridentate ligands exhibiting stable and excellent photophysics at room temperature are therefore of major interest.

The poor photophysical performance of $[Ru^{II}(tpy)_2]^{2+}$ at ambient conditions is due to the complex having far from perfect octahedral coordination. The bite angle of terpyridine in this complex [bite angle defined as the angle from N(terminal ring) – Ru – N (terminal ring)] was calculated to be 158.3$^o$ from X-Ray crystallography, far from the 180$^o$ degree bite angle expected for perfect octahedral coordination[7]. This distorted $O_h$ geometry leads to mixing of the $d\sigma^*(eg)$ and $d\pi^*(t_2g)$ orbitals. This stabilises some of the *d-d* excited states relative to low

lying $^3$MLCT states. This lowering of the energy gap between low lying $^3$MLCT and d-d excited states is thought to contribute to more efficient thermally activated transitions from $^3$MLCT states to a low lying *d-d* state. Once populated the *d-d* state undergoes rapid non-radiative decay to the ground state or can result in photochemical ligand loss all of which dramatically reduce luminescent lifetime and quantum yield[8,9,1].

Enlarging the coordination cage compared to $[Ru^{II}(tpy)_2]^{2+}$ to give geometry closer to $O_h$ symmetry should destabilise the non-emissive d-d excited states, extending lifetimes and increasing quantum yields. Some ruthenium complexes with tridentate ligands based on 2,2':6'2''-terpryidine that enlarge the coordination sphere have been reported on and exhibit substantial increases in room temperature luminescence lifetimes and quantum yields compared to the $[Ru^{II}(tpy)_2]^{2+}$ complex under the same conditions [9,10]. Sun, Hammarström *et al.*[11] synthesised a $[Ru^{II}(tpy)_2]^{2+}$ type complex where a single mehtylene group bridged two of the pyridine groups of the terpyridine in both of the complexes ligands to increase the ligand bite angle. The structure of the complex is shown in Fig 5.1.2. This had the effect of increasing the luminescence lifetime to 15 ns in deareated conditions compared to the lifetime of $[Ru^{II}(tpy)_2]^{2+}$ of 0.25 ns in deaerated conditions. The measured bite angles of the ligand were 168.3$^o$ (N1–N3), 168.4$^o$ (N4–N6) and 173.06$^o$ (N2–N5) making it closer to ideal octahedral symmetry than $[Ru^{II}(tpy)_2]^{2+}$, which has measured ligand bite angles of 158$^o$ (N1–N3), 158$^o$ (N4–N6) and 178$^o$ (N2–N5). Another $[Ru^{II}(tpy)_2]^{2+}$ type complex was synthesised by Hammarström *et al.*[12], where the terpyridine ligands are replaced with bpq ligands, where bpq is 2,6-bis(8'-quinolinyl)pyridine. The structure of this complex is shown in Fig 5.1.3 below. The N1 – Ru – N3 bite angle in this complex was found to be 179.6$^o$ compared to 158.4$^o$ in $[Ru^{II}(tpy)_2]^{2+}$. In deaerated conditions the luminescence lifetime was dramatically increased to 3 µs.

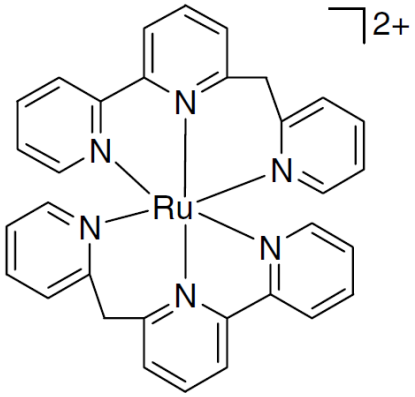


**Figure 5.1.2:** Structure of ruthenium (II) complex from ref[11].

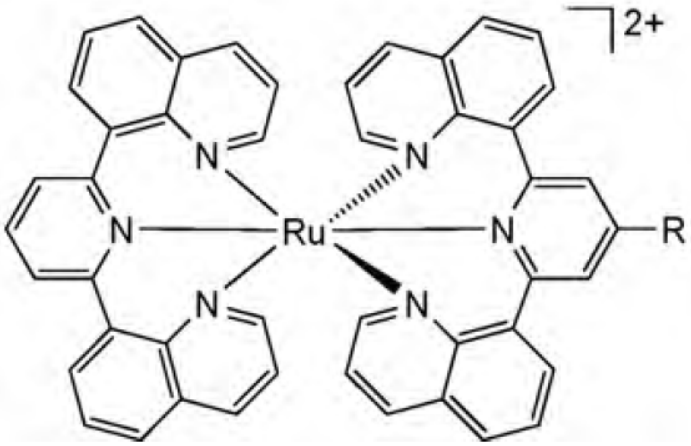


**Figure 5.1.3:** Structure of ruthenium (II) complex from ref[12], where R = H.

In this chapter a novel ruthenium (II) bis(terpyridyl) type complex, $[Ru^{II}(L_{Ket})_2](PF_6)_2$ whose structure is shown below in Fig 5.1.4, is characterised photophysically and electrochemically and is shown to display extremely high quantum yields and long lived lifetimes even at ambient conditions. By inserting additional carbon bridges between the aromatic pyridine rings the coordination cage is extended leading to a structure closer to true octahedral symmetry whilst maintaining a terpyridine like structure with the possibility of linear extension. The synthesis of this complex was achieved by first synthesising a methylene elongated terpyridine type complex, L, by the same method in reference[13]. The ligand was then reacted at 100° C with $Ru^{II}(DMSO)_4Cl_2$. This leads to coordination of two L ligands to one $Ru^{II}$ metal ion accompanied by simultaneous oxidation of the metylene groups of the L ligand to carbonyl groups forming $L_{KET}$. The structure of these ligands and the reaction scheme are shown in Fig 5.1.5. The methylene groups were converted to electron

withdrawing carbonyl groups to give the $L_{Ket}$ ligand which is a much stronger π-acceptor characteristics than the base 2,2':6'2''terpyridine ligand.

A copy of the paper published based on the data in this chapter can be found in the appendix.

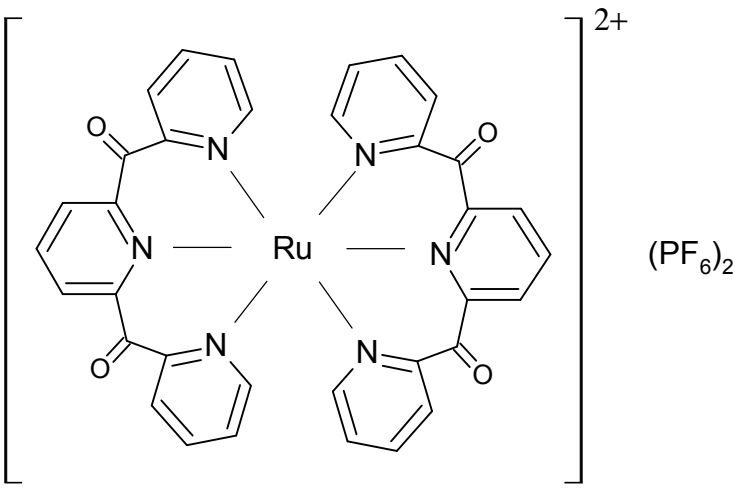


**Figure 5.1.4:** Structure of $[Ru^{II}(L_{Ket})_2](PF_6)_2$ complex

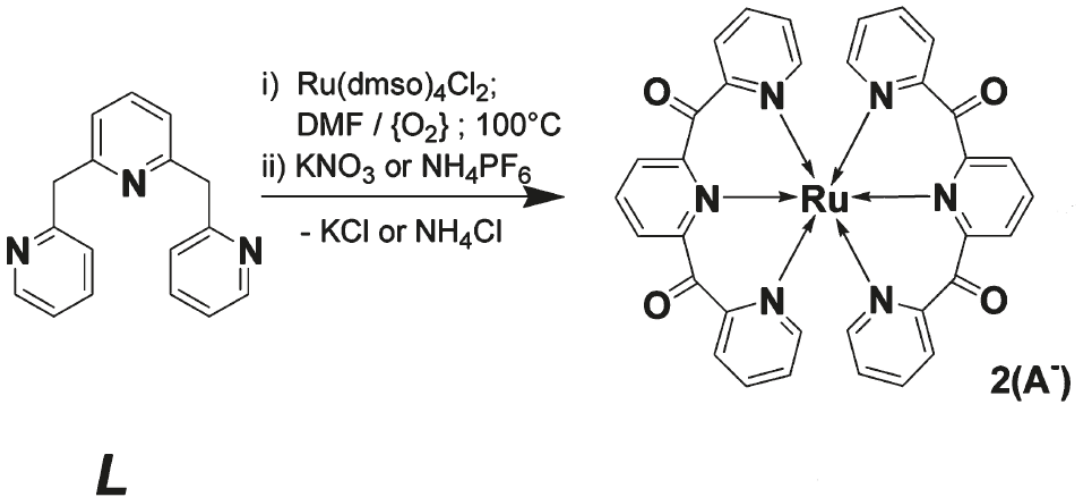


**Figure 5.1.5:** Reaction scheme for $[Ru^{II}(L_{Ket})_2](PF_6)_2$, where A = $PF_6$. Reproduced from ref[14].

## 5.2 Instruments and Methods

Synthesis of the $[Ru^{II}(L_{Ket})_2](PF_6)_2$ was carried out by Dr. Frank Schramm in Prof. Mario Ruben's group according to the procedure in ref [14] and was used as received.

UV-vis absorption spectroscopy experiments were carried out on a Varian Cary 50 scan UV-vis spectrometer. Room temperature emission experiments were recorded on a Varian Cary Eclipse luminescence spectrometer. Luminescence lifetime and 77K emission experiments were recorded using the third harmonic (355 nm, 30 mJ / pulse) of a continuum Surelite Q-switched Nd:YAG Laser as the excitation source. Emission was detected using an Anchor model M20 grated intensified CCD coupled to an Oriel model MS125 spectrograph in a right angled configuration to the laser. The gate width was never more than 5% of the excited state lifetime. Step size was around 5% of the excited state half-life. 77K experiments were carried out by dissolving the analyte in a porpionitrile : butryonitrile (4:5 v/v) which forms a glass at a low temperatures. Resonance Raman spectroscopy was carried out on a Horiba Jobin Yvon HR Labram microscope with an argon ion laser source for excitation at 458 nm, 488 nm and 514 nm. KBr pressed discs consisting of 1% w/w $[Ru^{II}(L_{Ket})_2](PF_6)_2$ in KBr was used for the Raman studies.

Cyclic Voltammetry was carried out using a CHI 660 potentiostat. A conventional three electrode cell was employed with a platinum wire was used as the counter electrode, a 2mm diameter platinum as the working electrode and an $Ag/AgNO_3$ nonaqueous reference electrode was used. The working electrode was electrochemically cleaned and polished with 0.05 mm alumina before use. Samples were dissolved in Acetonitrile with 0.1 M TBA TBF as the supporting electrolyte. All solutions were degassed with $N_2$ gas for 20 minutes and a $N_2$ blanket was maintained above the solution during the experiments.

Frank Condon analysis was carried out by Prof. Tia Keyes.

## 5.3 Results and Discussion

### *5.3.1 Absorption and Emission Spectroscopy*

The photophysical properties of the $[Ru^{II}(L_{Ket})_2](PF_6)_2$ complex are presented in Table 5.1. The electronic absorption spectrum of $[Ru^{II}(L_{Ket})_2](PF_6)_2$ is shown in Fig 5.3.1.1. The electronic absorption spectrum of $[Ru^{II}(tpy)_2]^{2+}$ is shown in Fig 5.3.1.2 for comparison. The addition of the carbonyl bridging units to the base terpyridine complex has a substantial bathochromatic effect on the MLCT absorption compared to $[Ru^{II}(tpy)_2]^{2+}$. This is expected for ligands with greater π-acceptor properties, in this case the addition of the carbonyl electron withdrawing groups give $L_{Ket}$ greater π-acceptor properties than terpyridine. The electron withdrawing groups can stabilise the excited state due to greater delocalisation of the charge in the ligand compared to tpy ligands. The MLCT absorption maximum of $[Ru^{II}(L_{Ket})_2](PF_6)_2$ appears at 522 nm, a substantial red shifted from the $[Ru^{II}(tpy)_2]^{2+}$ MLCT $\lambda_{max}$ of 473 nm[15]. For $[Ru^{II}(L_{Ket})_2](PF_6)_2$ the absorption band at 522 nm has two shoulders at 562 nm and 500 nm and also a well defined absorption band centred at 432 nm all of which are attributed to $^1$MLCT d-$\pi^*$ transitions[14].

A strong absorption peak centred at 266 nm has been attributed to a LC $\pi$-$\pi^*$ transition. This transition has been red shifted substantially from $[Ru^{II}(tpy)_2]^{2+}$ which has a corresponding LC $\pi$-$\pi^*$ transition centred at 304 nm. $[Ru^{II}(tpy)_2]^{2+}$ has another LC $\pi$-$\pi^*$ transition centred at 226 nm. The corresponding $[Ru^{II}(tpy)_2]^{2+}$ LC $\pi$-$\pi^*$ transition seems to be centred below 200 nm out of the spectral range studied. The hypsochromic shift of the LC $\pi$-$\pi^*$ transitions in $[Ru^{II}(L_{Ket})_2](PF_6)_2$ is likely due to the electron withdrawing carbonyl bridge structures drawing electron density away from the phenyl rings and increasing the excitation energy required for the LC $\pi$-$\pi^*$ transtitions compared to $[Ru^{II}(tpy)_2]^{2+}$. The weak absorption band centred at 331 nm is likely due to MC *d-d* transitions. The molar extinction coefficient of the $[Ru^{II}(L_{Ket})_2](PF_6)_2$ MLCT band was calculated to be 17570 $L^{-1}$ $cm^{-1}$ comparable to the molar extinction coefficient of the $[Ru^{II}(tpy)_2]^{2+}$ MLCT which is 18000 in ACN.[9]

The aerated and deaerated emission spectra at 298 K of $[Ru^{II}(L_{Ket})_2](PF_6)_2$ are presented in Fig 5.3.1.3 below. Unlike $[Ru^{II}(tpy)_2]^{2+}$ which is practically non-emissive at room temperature, $[Ru^{II}(L_{Ket})_2](PF_6)_2$ shows intense luminescence centred at 608 nm in both aerated and deaerated solutions, a red shift compared with the luminescence of $[Ru^{II}(tpy)_2]^{2+}$ which is observed at around 629 nm. In oxygen purged ACN the quantum yield of $[Ru^{II}(L_{Ket})_2](PF_6)_2$ more than doubles from 0.13 to 0.3, as expected, with no change in the $\lambda_{max}$ of emission. These quantum yields are huge compared to $[Ru^{II}(tpy)_2]^{2+}$ which has a quantum yield of $< 5\ e^{-6}$ in deaerated ACN and is immeasurably small in aerated conditions[16]. The quantum yield of $[Ru^{II}(L_{Ket})_2](PF_6)_2$ is remarkably high for a ruthenium polypyridyl complex and comparable to some tris-1,10-phenanthroline ruthenium complexes. For example in deaerated ACN $[Ru^{II}(bpy)_3]^{2+}$ has a quantum yield of 0.06 while the RuxD complexes of the previous chapters have a quantum yield of 0.011 in aerated ACN and ~ 0.08 in deaerated ACN [17]. Also some tris-1,10-phenanthroline ruthenium complexes have comparable deaerated quantum yields, such as $[Ru(dpp)_3]^{2+}$ which has a deaerated quantum yield of 0.366 in 4:1 EtOH:MeOH.[18] The stokes shift was calculated to be 86 nm, quite small for this class of complex. $[Ru^{II}(tpy)_2]^{2+}$ has a stokes shift of 155 nm.[17]

The room temperature lifetime of the excited state under aerated conditions was calculated to be 1.36 µs, which, to our knowledge, is the longest measured excited state lifetime for a ruthenium polypyridyl complex in aerated conditions at room temperature. Under deaerated conditions the lifetime of the excited state increases to 3.3 µs, putting it on par with some Ruthenium tris-phenantrholine type complexes[18]. This is in stark contrast to the measured lifetime of $[Ru^{II}(tpy)_2]^{2+}$ in deaerated conditions which was measured to be 250 ps[6]. The room temperature aerated and deaerated luminescence decay profiles are presented in Fig. 5.3.1.4 and 5.3.1.5 respectively.

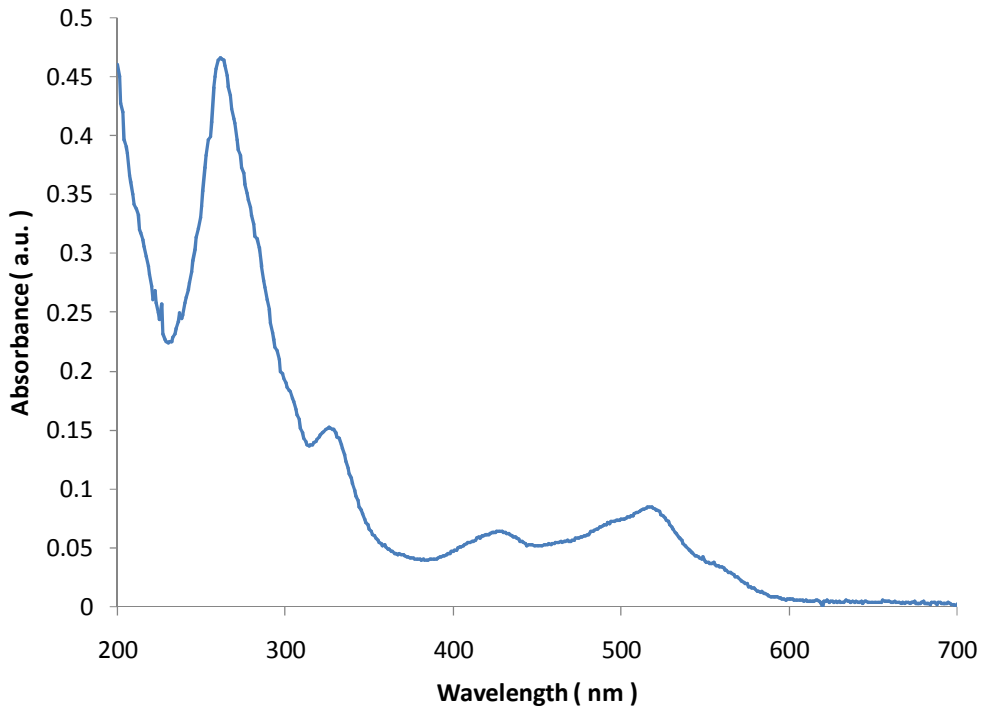


**Figure 5.3.1.1:** Uv-vis absorption spectrum of $[Ru^{II}(L_{Ket})_2](PF_6)_2$. Spectrum was taken from a $1.3e^{-5}$ M soln of $[Ru^{II}(L_{Ket})_2](PF_6)_2$ in ACN.

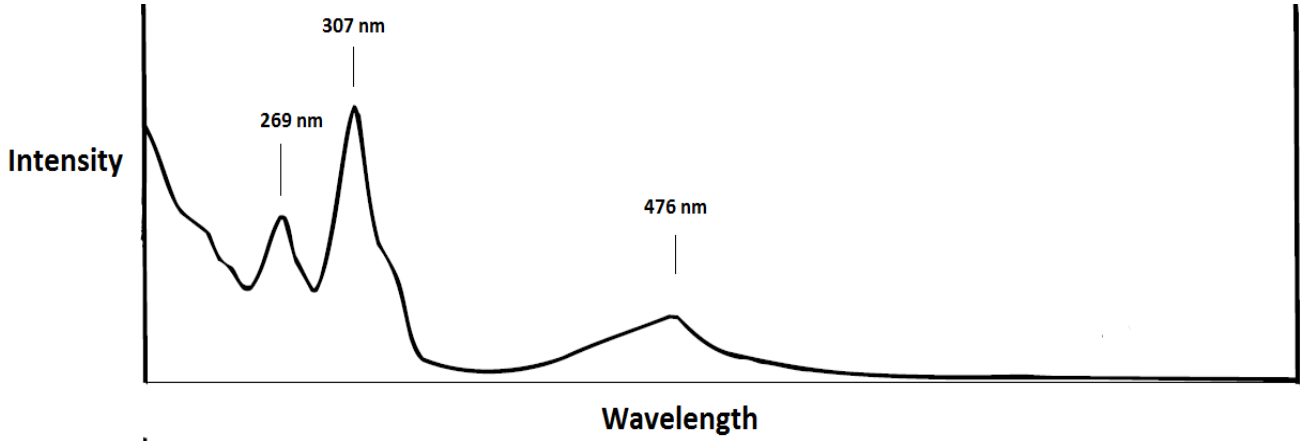


**Figure 5.3.1.2:** UV-vis absorption spectrum of $[Ru^{II}(tpy)_2]^{2+}$ in acetonitrile. Spectrum was reproduced from ref[19].

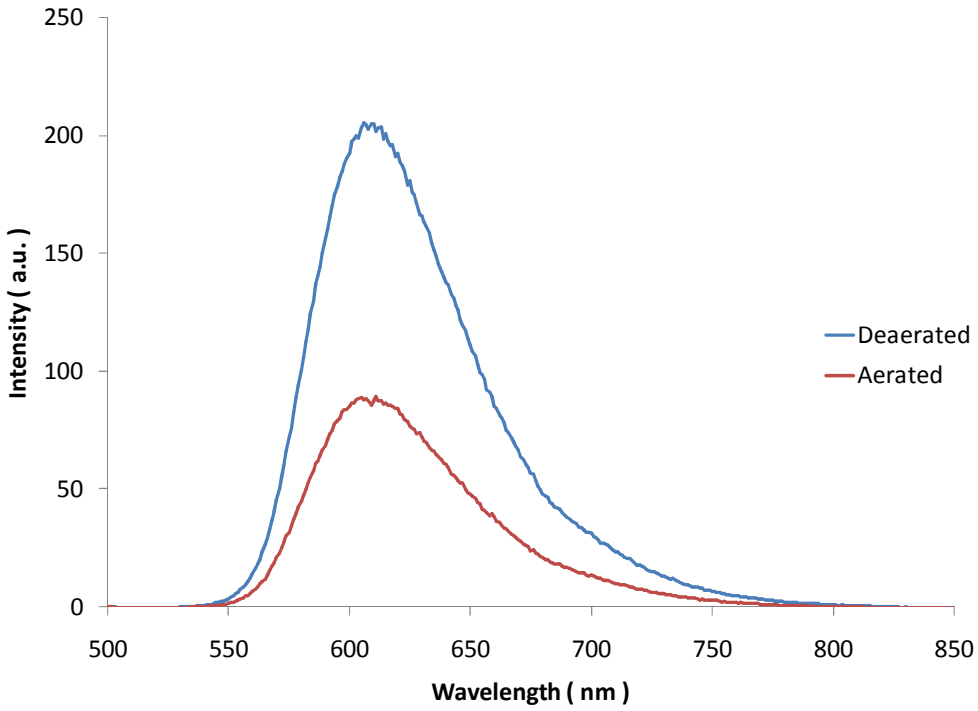


**Figure 5.3.1.3:** Room temperature Emission spectra of aerated and deaerated $[Ru^{II}(L_{Ket})_2](PF_6)_2$. Both samples were absorbance matched and were taken from ~$1.3e^{-5}$ M solns of $[Ru^{II}(L_{Ket})_2](PF_6)_2$ in ACN. An excitation wavelength of 522 nm was used.

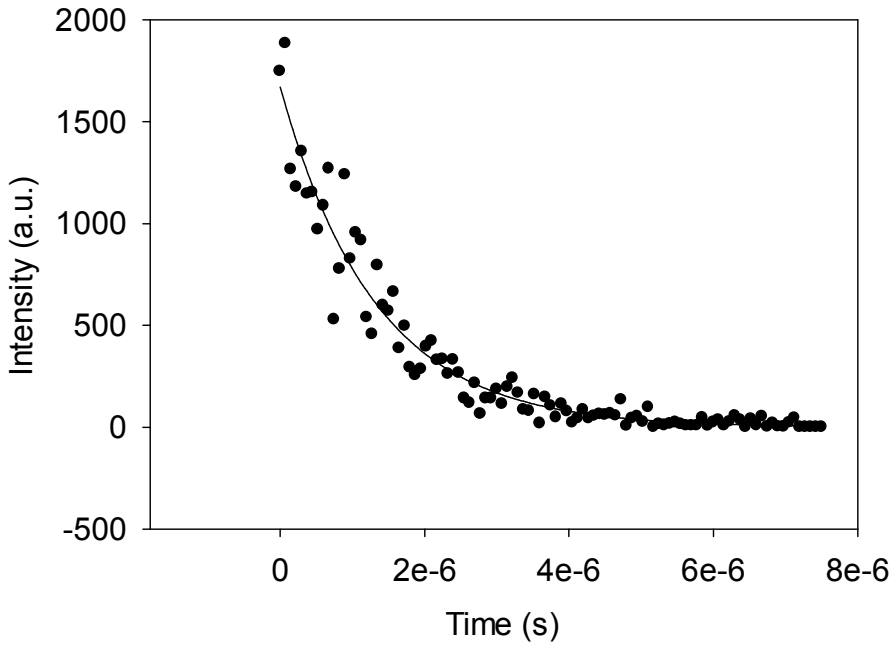


**Figure 5.3.1.4:** Room temperature emission decay profile of $1.3e^{-5}$ M $[Ru^{II}(L_{Ket})_2](PF_6)_2$ in aerated ACN. An excitation wavelength of 355 nm was used.

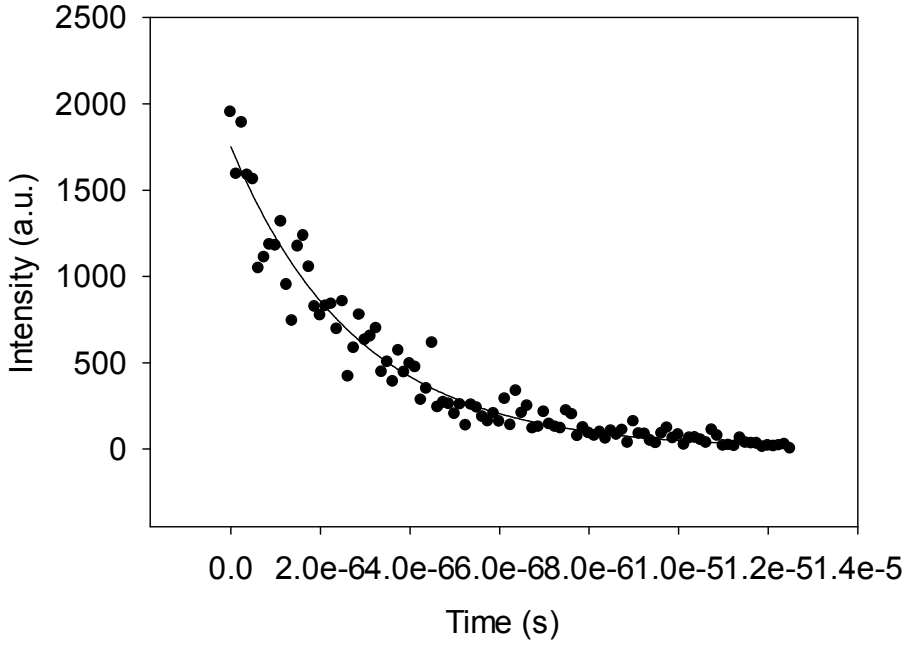


**Figure 5.3.1.5:** Room temperature emission decay profile of $1.3e^{-5}$ M $[Ru^{II}(L_{Ket})_2](PF_6)_2$ in deaerated ACN. An excitation wavelength of 355 nm was used.

The emission spectrum of $[Ru^{II}(L_{Ket})_2](PF_6)_2$ in propionitrile : butyronitrile (4:5 v/v) glass at 77 K is shown in Fig 5.3.1.6. Extra vibrational fine structure due to ν (ligand) framework vibrations can be seen in the spectrum from about 650 nm onwards although notably it is not as pronounced as in other ruthenium polypyridyl complexes. $\lambda_{max}$ of emission at 77 K is at 613 nm which is unchanged from the $\lambda_{max}$ of emission at 298 K within experimental error. Although unusual some ruthenium (II) complexes exhibiting small changes in $\lambda_{max}$ of emission at 77 K have been reported[20,21]. The quantum yield greatly increases at 77 K, displaying a quantum yield of 0.41 in aerated solution and 0.43 in deaerated, which is unchanged from aerated within experimental error ( ± 0.06 ). These Quantum yields are comparable to $[Ru^{II}(tpy)_2]^{2+}$ which displays a quantum yield of 0.48 in aerated alcohol glass at 77 K [5]. Higher 77 K quantum yields have been reported for tridentate ruthenium polypyridyl complexes, such as $[Ru(dpp)_3]^{2+}$ which has a luminescence lifetime of 0.682 at 77 K in 4:1 MeOH:EtOH, as well as the RuxD series which has a quantum yield of about 0.6 in propionitrile : butyronitrile at 77 K.

The luminescence lifetime in porpionitrile : butryonitrile (4:5 v/v) glass at 77 K increases to 6.17 µs in aerated conditions and 6.34 µs in deaerated conditions. Although much shorter lived than $[Ru^{II}(tpy)_2]^{2+}$ at 77 K, which has an excited state lifetime at 77 K in alcohol glass of about 10 µs, the excited state lifetime of $[Ru^{II}(L_{Ket})_2](PF_6)_2$ is still remarkably high under these conditions. 77 K photphysical performance is however also disappointing compared to some tridentate ruthenium polypyridyl complexes such as the RuxD series which have excited state lifetimes of around 10 µs.

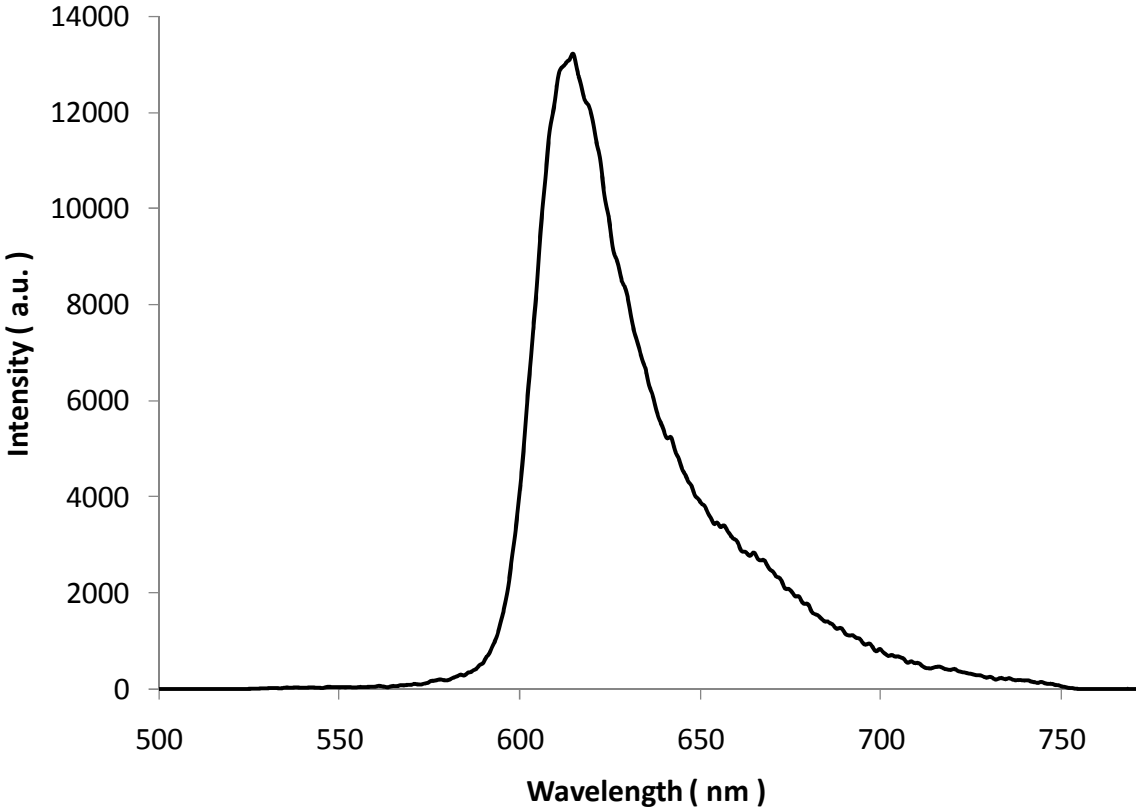


**Figure 5.3.1.6:** 77K emission spectrum of $[Ru^{II}(L_{Ket})_2](PF_6)_2$ in porpionitrile : butryonitrile (4:5 v/v) glass. An excitation wavelength of 355 nm was used.

The radiative and nonradiative rate constants $k_r$ and $k_{nr}$ were calculated and are presented in Table 5.2 using the same methods of calculation in Chapter 3. The presence of oxygen at 298 K has surprisingly little effect on the emission lifetime and quantum as already detailed. As expected the presence of $O_2$ at 298 K increases the rate of non radiative decay although not to the extent as expected. In comparison the $k_r$ and $k_{nr}$ values of $[Ru(tpy\text{-}py)_2]^{2+}$,

where tpy-py = 4'-(4-pyridyl)-2,2':6',2''-terpyridine) in ambient conditions are 1.33x $10^4$ $s^{-1}$ and 3.3 x $10^8$ $s^{-1}$ respectively[22]. In the case of $[Ru^{II}(L_{Ket})_2](PF_6)_2$ $k_r$ is nearly an order of magnitude faster while $k_{nr}$ is 3 orders of magnitude slower. It is commonly accepted that luminescence of ruthenium (II) complexes occurs from an MLCT triplet state except in complexes with other lower lying ligand based transitions. The weak luminescence oxygen dependence of the $[Ru^{II}(L_{Ket})_2](PF_6)_2$ could be evidence of a contribution $^3$LC type emission. TDDFT (time-dependent density functional theory) calculations were carried out by Prof. Rubens group to generate a theoretical UV-vis absorption spectrum[14]. Analysis of the triplet spectrum determined that the seven lowest energy transitions between 2.20 and 2.78 eV were $^3$MLCT in nature. Additional calculations were preformed on the same system but replacing the ruthenium centre with $Mg^{2+}$, $Zn^{2+}$ and $Ir^{2+}$. In the case of the $Mg^{2+}$ compound no d-electrons can interact with the ligands and pure triplet ligand to ligand transitions are observed at 2.8 eV. For the $Zn^{2+}$ and $Ir^{2+}$ systems the lowest energy triplet excitations were dominated by ligand to ligand transitions and found in the same energy range at about 2.7 eV. With this knowledge the TDDFT triplet spectrum was revised and excitations at about 2.8 eV were identified as $^3$LC in nature. This could correspond to an observed absorption process in the electronic absorption spectrum of $[Ru^{II}(L_{Ket})_2](PF_6)_2$ centred at 432 nm which corresponds to 2.87 eV. The computational data shows that the emission is $^3$MLCT in nature due to the lowest energy triplet excitations being $^3$MLCT in nature and how well this data agrees with the observed emission of $[Ru^{II}(L_{Ket})_2](PF_6)_2$ at 2.04 eV. However the relative $[O_2]$ insensitivity is unusual and a contribution to the emission from $^3$LC excitations cannot be completely ruled out.

Frank-Condon analysis of the low temperature emission was carried out by Prof. Keyes. The results of which are presented in table 5.3. The low frequency ($\nu_L$) and high frequency acceptor ($\nu_M$) modes were calculated[14] and were estimated to be 1407 $cm^{-1}$ and 590 $cm^{-1}$ for the high frequency and low frequency acceptor modes respectively. Huang-Rhys values for the low and high frequency acceptor modes, $S_L$ and $S_M$ were calculated for $[Ru^{II}(L_{Ket})_2](PF_6)_2$ and were found to be 0.55 and 0.26 respectively. These were considerably smaller than the calculated $[Ru^{II}(tpy)_2]^{2+}$ which has $S_L$ and $S_L$ values of 1.2 and 0.70 (values taken from ref)[23]. Huang-Rhys factors are a measure of the distortion of the excited state compared to the ground state, the higher the Huang-Rhys factor the higher the distortion. There is therefore less distortion between the excited state and the ground state of

$[Ru^{II}(L_{Ket})_2](PF_6)_2$ compared to $[Ru^{II}(tpy)_2]^{2+}$. This suggests that the influence of vibrational coupling on the photochemistry is small and further supports the possibility of $^3$LC contributions to the emission.

| | $[Ru^{II}(L_{Ket})_2](PF_6)_2$ | $[Ru^{II}(tpy)_2]^{2+}$ | $[Ru(bpy)_3]^{2+}$ |
|---|---|---|---|
| $\varepsilon_{522nm}$ ($mol^{-1}$ $cm^{-1}$) | 17570 (± 190) | 18000 | 13000 |
| λ max aerated @ 298 K (nm) | 608 | | |
| λ max deaerated @ 298 K (nm) | 608 | 628 | 609 |
| $\phi_{em}$ aerated @298 K | 0.13 (±0.02) | | |
| $\phi_{em}$ deaerated @ 298 K | 0.3 (±0.03) | <0.005 | 0.062 |
| $\tau_{em}$ aerated @ 298 K (μs) | 1.36 (±0.06) | | |
| $\tau_{em}$ deaerated @ 298 K (μs) | 3.30 (±0.08) | 0.00025 | 0.89 |
| λ max @ 77 K (nm) | 613 | 599 | 582 |
| $\phi_{em}$ aerated @ 77 K | 0.41 (±0.06) | 0.48 | 0.328 |
| $\phi_{em}$ deaerated @ 77 K | 0.43 (±0.06) | | |
| $\tau_{em}$ aerated @ 77 K (μs) | 6.17 (±0.12) | 11 | 5.1 |
| $\tau_{em}$ deaerated @ 77 K (μs) | 6.43 (±0.11) | | |

**Table 5.1:** Photophysical properties of $[Ru^{II}(L_{Ket})_2](PF_6)_2$. Deaerated samples were purged with $N_2$ for 20 minutes before measurements were taken. 298 K experiments were recorded in ACN. 298 K emission experiments were excited at 522 nm. 298 K emission lifetime experiments were excited at 355 nm. 77 K experiments were recorded in propionitrile : butyronitrile 4:5 glass and excited at 355 nm. Values for $[Ru^{II}(tpy)_2]^{2+}$ and $[Ru(bpy)_3]^{2+}$ are included for comparison and are taken from ref[17]. $[Ru(bpy)_3]^{2+}$ values at 298 K are from acetonitrile solutions while 77 K values are in MeOH:EtOH glass. $[Ru^{II}(tpy)_2]^{2+}$ values are from MeOH:EtOH solutions.

| | $k_r$ @298 K ($s^{-1}$) | $k_{nr}$ @298 K($s^{-1}$) | $k_r$ @77 K ($s^{-1}$) | $k_{nr}$ @77 K ($s^{-1}$) |
|---|---|---|---|---|
| aerated | $9.6 \times 10^4$ ($\pm 1.53 \times 10^4$) | $6.4 \times 10^5$ ($1.53 \times 10^4$) | $6.65 \times 10^4$ ($\pm 9.8 \times 10^3$) | $9.6 \times 10^4$ ($\pm 9.8 \times 10^3$) |
| deaerated | $9.1 \times 10^4$ ($\pm 9.4 \times 10^3$) | $2.1 \times 10^5$ ($\pm 9.4 \times 10^3$) | $6.65 \times 10^4$ ($\pm 9.4 \times 10^3$) | $8.9 \times 10^4$ ($\pm 9.4 \times 10^3$) |

**Table 5.2:** Table of radiative and non radiative rate constants of $[Ru^{II}(L_{Ket})_2](PF_6)_2$. Deaerated samples were purged with $N_2$ for 20 minutes before measurements were taken. 298 K experiments were recorded in ACN. 298 K emission experiments were excited at 522 nm. 298 K emission lifetime experiments were excited at 355 nm. 77 K experiments were recorded in propionitrile : butyronitrile 4:5 glass and excited at 355 nm.

| Complex | $E_{00}/cm^{-1}$ | $S_L$ | $S_M$ | $\nu_M/cm^{-1}$ | $\nu_L/cm^{-1}$ | fwhm/$cm^{-1}$ |
|---|---|---|---|---|---|---|
| $[Ru^{II}(L_{Ket})_2](PF_6)_2$ [a] | 16574 | 0.26 | 0.55 | 1407 | 591 | 642 |
| $[Ru^{II}(tpy)_2]^{2+}$ [b] | 16820 | 0.7 | 1.2 | 1250 | 350 | 575 |

**Table 5.3:** Parameters obtained from Franck-Condon analysis of emission at 77K. [a] Obtained at 77K in propionitrile : butyronitrile 4:5 glass at an excitation wavelength of 355 nm. [b] Determined at 77 K in MeOH:EtOH 4:1 and taken from ref[23].

### *5.3.2 Resonance Raman spectroscopy of solid $[Ru^{II}(L_{Ket})_2](PF_6)_2$*

In order to investigate the origin of the optical transition and elucidate contributions to vibrational changes in the excited state, resonance Raman of the $[Ru^{II}(L_{Ket})_2](PF_6)_2$ complex was conducted. Fig 5.3.2.1 – 5.3.2.3 represents a resonance Raman spectrum of a powder sample of $[Ru^{II}(L_{Ket})_2](PF_6)_2$ dispersed in a KBr disc (1% w/w) excited at 488, 458 and 514 nm respectively. Fig 5.3.2.4 represents the resonance raman spectrum of $[Ru(tpy)_2]^{2+}$ in acetonitrile excited at 467.5 nm for comparison. Table 5.4 lists the band energies of the

$[Ru^{II}(L_{Ket})_2](PF_6)_2$ resonance Raman spectrum. The resonance Raman band energies of $[Ru(tpy)_2](PF_6)_2$ are also included for comparison. The resonance Raman spectrum shows enhanced Raman bands in the region from 1000 – 1700 $cm^{-1}$ which are ligand based. As expected these bands are enhanced due to the excited state lying residing on the ligands. The $[Ru^{II}(L_{Ket})_2](PF_6)_2$ spectrum contains most of the vibrational bands of the $[Ru(tpy)_2](PF_6)_2$ complex with the exception of a band at 1549 which is unique to the $[Ru(tpy)_2](PF_6)_2$ - complex. The $[Ru^{II}(L_{Ket})_2](PF_6)_2$ complex has unique bands at 1678, 1472, 1456, 1435, 1410, 1255 and 1068 $cm^{-1}$. Based on the normal coordination analysis of $[Ru(tpy)_2](PF_6)_2$ published by Jensen *et al.*[24] the vibrations involved in the resonance Raman spectrum of $[Ru^{II}(L_{Ket})_2](PF_6)_2$ were assigned. Raman modes from 1678 to 1435 $cm^{-1}$ were assigned to ring stretching vibrations. Raman modes from 1410 to 1321 $cm^{-1}$ were assigned to C-H bends. The Raman modes at 1290 and 1255 $cm^{-1}$ are more than likely due to ring stretching vibrations. Raman modes from 1192 to 1068 $cm^{-1}$ are due to C-H bends. The Raman mode at 1026 $cm^{-1}$ was assigned to a ring stretching vibration. Raman modes from 719 to 654 $cm^{-1}$ were assigned to ring deformations. Very little variation in peak position was observed between Raman bands when excited at 458 nm, 488 nm or 514 nm. The Ru-N stretching vibrations at 598 nm were much more pronounced when excited at 514 nm.

The low frequency and high frequency acceptor modes were calculated from the Franck-Condon analysis of the low temperature emission carried out by Prof. Keyes. The low frequency and high frequency acceptor modes refer to the deactivating Ru-N and ν(ligand) ring stretches respectively. These were calculated to be 1407 $cm^{-1}$ and 590 $cm^{-1}$ for the high frequency and low frequency acceptor modes respectively. These correspond to Raman modes in the resonance Raman spectrum of $[Ru^{II}(L_{Ket})_2](PF_6)_2$. Comparison to normal mode coordinate analysis of $[Ru(tpy)_2](PF_6)_2$ from ref[24] suggests that high frequency mode is a C-C ring stretch and the low frequency mode is a ring deformation mode. The Raman mode at 601 $cm^{-1}$ has been designated as a Ru-N stretch since it is the closest to the calculated low frequency acceptor mode Ru-N stretch.

| $[Ru(tpy)_2](PF_6)_2$ [a] $\lambda_{ex}$ 457 nm | Corresponding vibration | $[Ru^{II}(L_{Ket})_2](PF_6)_2$ $\lambda_{ex}$ 488 nm | $[Ru^{II}(L_{Ket})_2](PF_6)_2$ $\lambda_{ex}$ 458 nm | $[Ru^{II}(L_{Ket})_2](PF_6)_2$ $\lambda_{ex}$ 514 nm |
|---|---|---|---|---|
| | | 1678 | 1676 | 1675 |
| 1604 | Ring stretch | 1594 | 1594 | 1592 |
| 1561 | Ring stretch | 1567 | 1564 | 1565 |
| 1552 | Ring stretch | | | |
| 1494 | Ring stretch | 1499 | | 1498 |
| 1472 | Ring stretch | 1472 | 1471 | 1472 |
| | | 1456 | | 1458 |
| | | 1435 | 1439 | 1436 |
| 1392 | C-H bend | 1410 | | 1412 |
| 1331 | C-H bend | 1321 | 1322 | 1322 |
| 1302 | C-H bend | | | |
| 1287 | Ring stretch | 1290 | 1291 | 1288 |
| | | 1255 | 1255 | 1257 |
| 1186 | C-H bend | 1192 | 1192 | 1191 |
| 1166 | C-H bend | 1162 | | |
| 1135 | C-H bend | | | |
| 1102 | C-H bend | 1101 | 1099 | 1100 |
| | | 1068 | 1063 | 1068 |
| 1017 | Ring stretch | 1026 | 1024 | 1026 |
| 729 | Ring bend | 719 | 715 | 720 |
| 674 | Ring bend | 665 | 669 | |
| 647 | Ring bend | 654 | 651 | 654 |
| | Ru-N stretch | 601 | | 598 |

**Table 5.4:** Resonance raman band energies ($cm^{-1}$) for $[Ru(tpy)_2](PF_6)_2$ and $[Ru^{II}(L_{Ket})_2](PF_6)_2$ at room temperature. [a] taken from Ref[24]. The $[Ru(tpy)_2](PF_6)_2$ spectrum was acquired in acetonitrile while the $[Ru^{II}(L_{Ket})_2](PF_6)_2$ spectrum was acquired from a $[Ru^{II}(L_{Ket})_2](PF_6)_2$ solid sample in KBr disc (1% w/w).

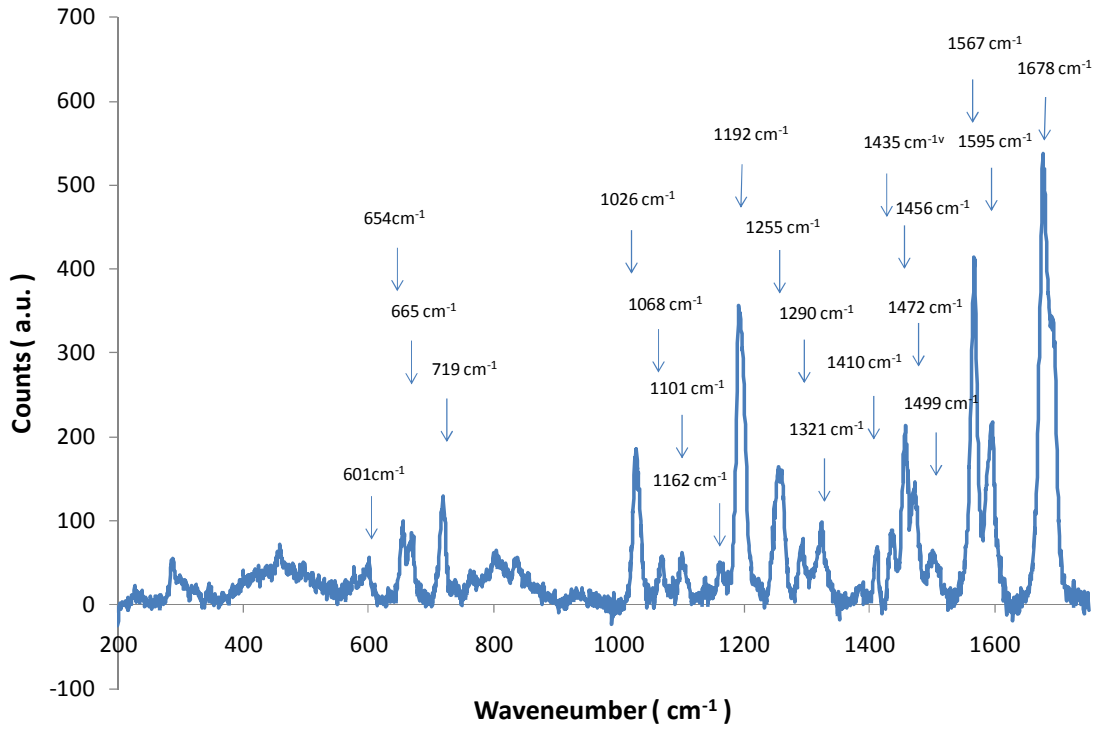


**Figure 5.3.2.1:** Resonance Raman spectrum of $[Ru^{II}(L_{Ket})_2](PF_6)_2$ solid sample in KBr disc (1% w/w). An excitation wavelength of 488 nm was used.

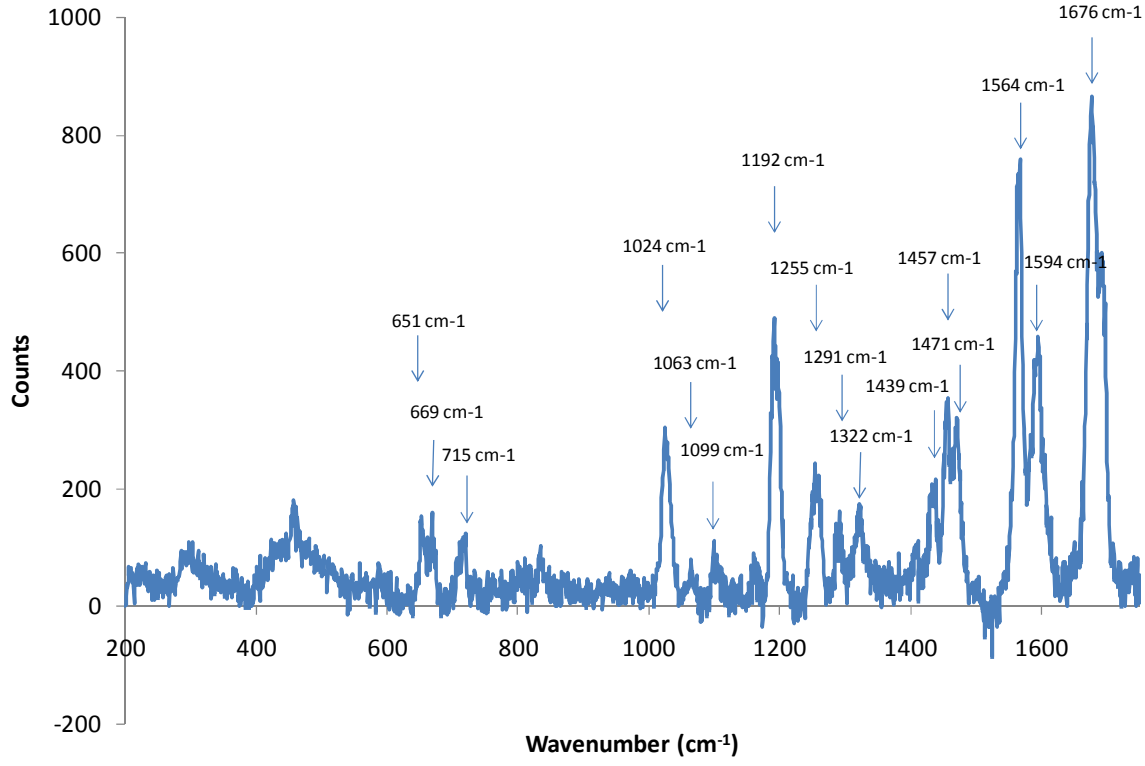


**Figure 5.3.2.2:** Resonance Raman spectrum of $[Ru^{II}(L_{Ket})_2](PF_6)_2$ solid sample in KBr disc (1% w/w). An excitation wavelength of 458 nm was used.

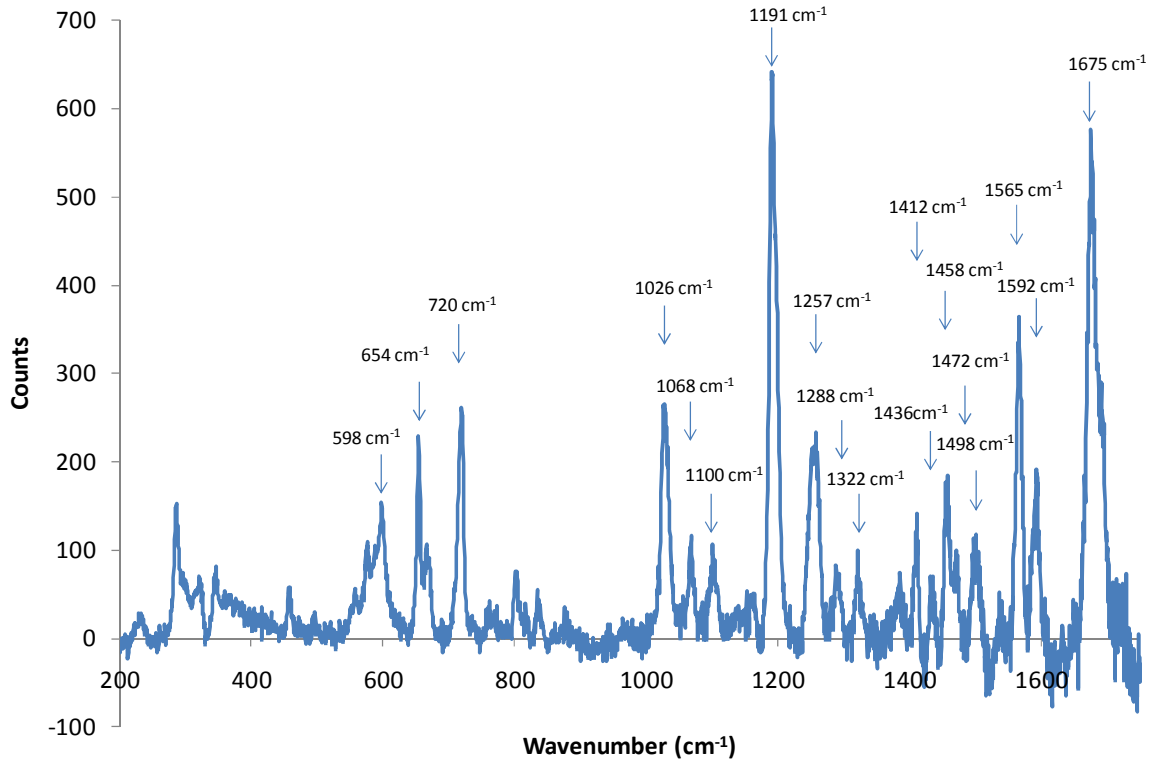


**Figure 5.3.2.3:** Resonance Raman spectrum of $[Ru^{II}(L_{Ket})_2](PF_6)_2$ solid sample in KBr disc (1% w/w). An excitation wavelength of 514 nm was used.

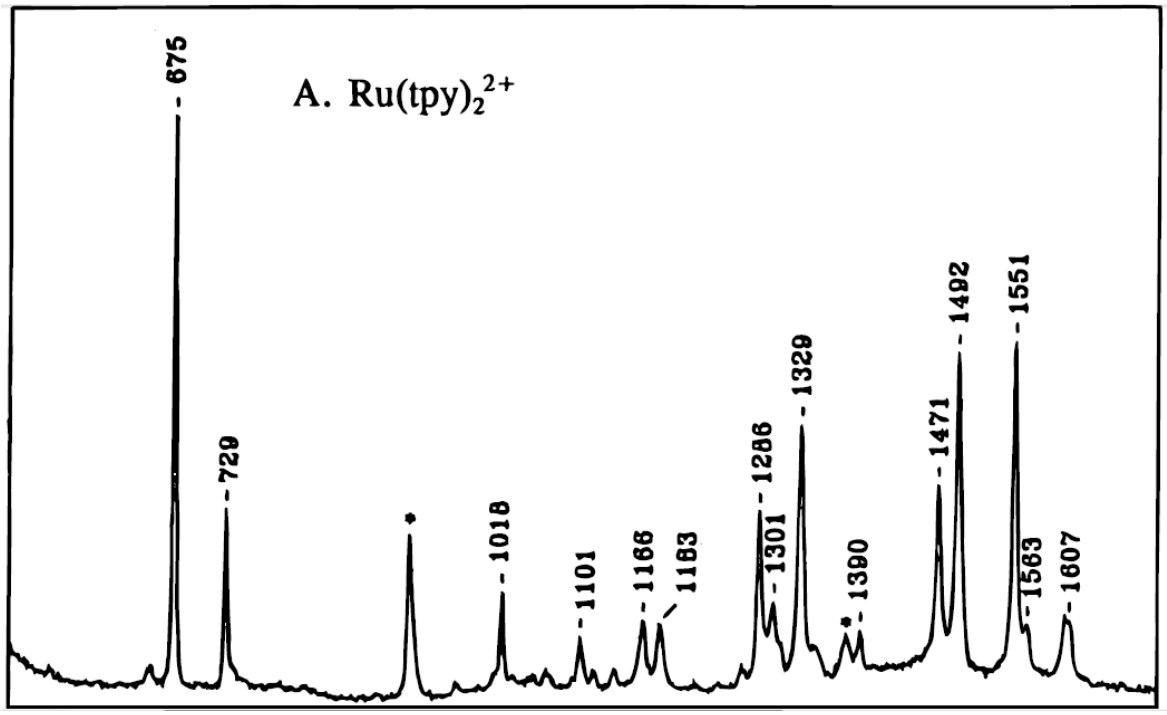


**Figure 5.3.2.4:** Resonance Raman spectrum of $[Ru(tpy)_2]^{2+}$ in Acetonitrile. An excitation wavelength of 476.5 nm was used. Image reproduced from ref[19].

### *5.3.3 Solution phase electrochemistry of $[Ru^{II}(L_{Ket})_2](PF_6)_2$*

In order to understand the molecular orbital levels and redox behaviour of $[Ru^{II}(L_{Ket})_2](PF_6)_2$, solution phase cyclic voltammetry was carried out on the complex. A cyclic voltammagram of the $[Ru^{II}(L_{Ket})_2](PF_6)_2$ complex in ACN is shown in Fig 5.3.3.1. Table 5.5 gives details the potentials of each redox process the present in the cyclic voltammetry of $[Ru^{II}(L_{Ket})_2](PF_6)_2$ complex in ACN with the potentials of the $[Ru(tpy)_2]^{2+}$ redox processes included as a comparison. The $Ru^{2+/3+}$ oxidation appears at +1.525 V, about 0.255 V higher than the same oxidation potential in $[Ru(tpy)_2]^{2+}$ which appears at +1.3 V. The addition of the electron withdrawing carbonyl bridging units to the $L_{Ket}$ ligand have given it greater π-acceptor properties than 2,2':6'2''-terpyridine. As a result the metal centre is much more difficult to oxidise than in $[Ru(tpy)_2]^{2+}$. The ligand based reductions undergo an anodic shift, the first ligand based reduction appears at -0.91 V, 0.33 V more positive in comparison to -1.24 V for the first ligand reduction of $[Ru(tpy)_2]^{2+}$. A total of four ligand based reductions are observed at -0.908, -1.084, -1.407 and -1.657 V, all of which are fully reversible. The electron withdrawing carbonyl bridging groups facilitate the reduction of the ligands in comparison to $[Ru(tpy)_2]^{2+}$.

The electrochemical results are in agreement with the observed red shift of the MLCT absorption of $[Ru^{II}(L_{Ket})_2](PF_6)_2$ compared to $[Ru(tpy)_2]^{2+}$. The difference between the first ligand reduction and the metal oxidation is 2.43 eV for $[Ru^{II}(L_{Ket})_2](PF_6)_2$ compared to 2.54 eV for $[Ru(tpy)_2]^{2+}$.This corresponds to a wavelength of 510 nm, in close agreement to the $\lambda_{max}$ of absorption of $[Ru^{II}(L_{Ket})_2](PF_6)_2$ at 522 nm.

| | $E_{1/2}^{ox}$ $Ru^{2+/3+}$ (V) | $E_{1/2}^{red}$ ligand (V) | | | |
|---|---|---|---|---|---|
| $[Ru^{II}(L_{Ket})_2](PF_6)_2$ | +1.525 | -0.908 | -1.084 | -1.407 | -1.657 |
| $[Ru(tpy)_2]^{2+}$ [a] | +1.3 | -1.24 | -1.49 | | |

**Table 5.5** Electrochemical oxidation and reduction potentials for a $1e^{-3}$ M solution of $[Ru^{II}(L_{Ket})_2](PF_6)_2$ in 0.1M TBATBF in ACN. [a] Values for the oxidation and reduction potential of $[Ru(tpy)_2]^{2+}$ were taken from Ref[25]. All potentials are vs. a non-aqueous $Ag/AgNO_3$ reference electrode.

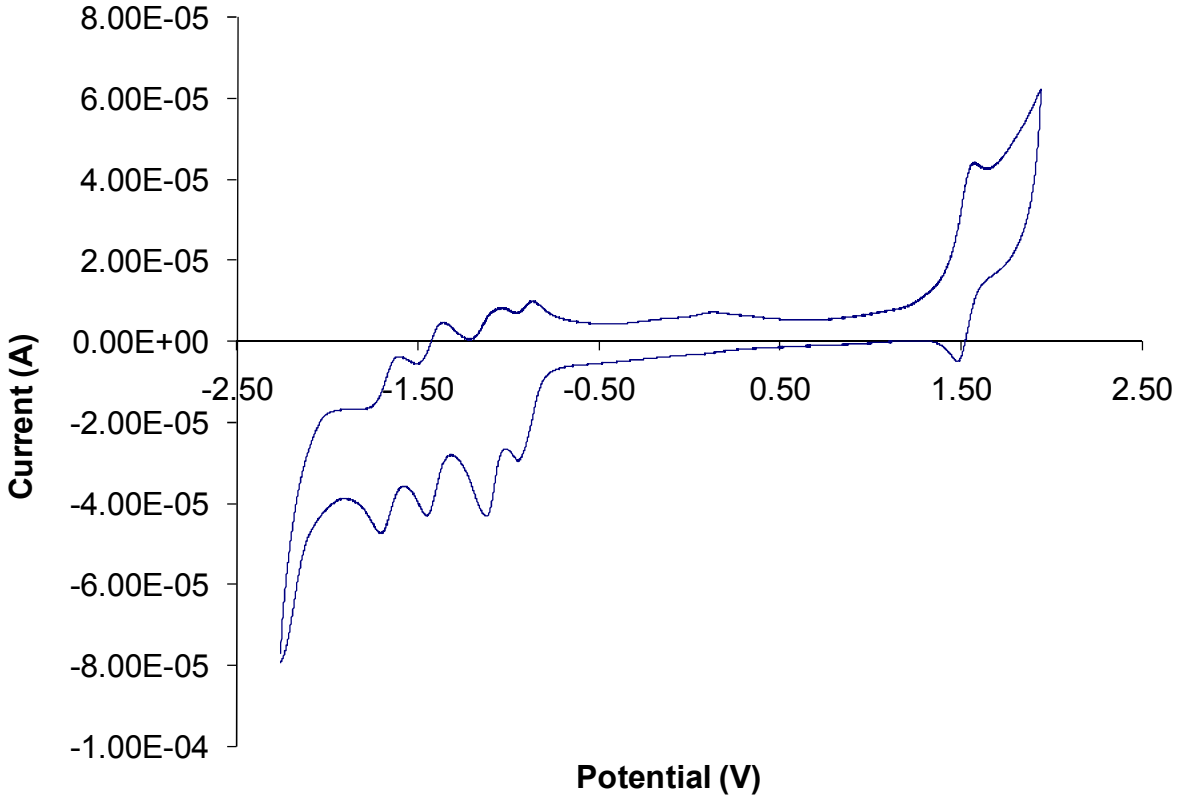


**Figure 5.3.3.1:** Cyclic voltammogram of $[Ru^{II}(L_{Ket})_2](PF_6)_2$ in solution. Electrochemistry was carried out with a 1mM solution of the complex in ACN with 0.1 mM $TBATBF_4$ as the supporting electrolyte and a platinum electrode as the working electrode. All potentials are vs $Ag/AgNO_3$ electrode.

## 5.4 Conclusions

In this chapter the photophysical and redox properties of a novel Ru (II) complex was explored. This complex had two tridentate tpy type ligands with bridging carbonyl groups to extend the coordination cage. Extension of the coordination cage of tridentate ruthenium polypyridyl complexes to bring their structure closer to perfect octahedral symmetry is an excellent method for overcoming their poor photophysical performance in ambient conditions. The complex $[Ru^{II}(L_{Ket})_2](PF_6)_2$, using this principle, was shown to have long luminescence lifetimes and large quantum yields at room temperature in aerated and deaerated conditions. This is in stark contrast to the base complex $[Ru(tpy)_2]^{2+}$ which is barely luminescent at 298 K. The luminescence lifetime at room temperature under aerated conditions of 1.36 µs is particularly impressive and to our knowledge is the longest reported for a ruthenium polypyridyl complex luminescence lifetime for a ruthenium polypyridyl complex at 298 K in aerated conditions. 77 K photophysical performance is excellent with comparable luminescence lifetimes to $[Ru(tpy)_2]^{2+}$ and some ruthenium tris-phenanthroline type complexes. The complex was characterised by resonance Raman spectroscopy and was in close agreement with calculated acceptor modes from Frank-Condon analysis of the 77 K emission. There was evidence that the luminescence of $[Ru^{II}(L_{Ket})_2](PF_6)_2$ contains some $^3$LC contributions due to how weakly dependent the $k_{nr}$ is on $[O_2]$ and also the lack of distortion in the excited state compared to the ground state. Although luminescence is certainly $^3$MLCT in nature it was not possible to fully rule out $^3$LC contributions to the excited state. TDDFT calculations showed evidence of the possibility triplet ligand to ligand excitations at higher energy than $^3$MLCT excitations.

This new method of molecular design for ruthenium polypyridyl complexes could lead to the development of new complexes with high performance photophysical properties for use in light driven devices in ambient conditions. In particular these complexes open up new avenues for light driven devices for biological applications such as cell imaging. These devices and imaging agents must be able to perform in an oxygen rich environment at 37$^o$ C. Bringing the complex closer to octahedral symmetry has the effect of making the low lying metal *d-d* excited state less accessible. Population for this state from the $^3$MLCT excited state

can cause irreversible bleaching of the complex by photodissociation of the ligand. Decreasing the accessibility of the metal *d-d* excited state will increase the stability of the complex when under illumination from an excitation source and make it more suitable for experiments that require long irradiation times. For example the z-stacking cell imaging experiments in Chapter 5 require long illumination times and a luminescent dye that is resistant to photobleaching. Future work includes functionalising the 4' position of the $L_{KET}$ ligand with alkyl chains for use in cell imaging experiments.

# References


[1] Sauvage, J-P.; Collin, J-P.; Chambron, J-C.; Guillerez, S.; Coudret, C.; Balzani, V.; Barigelletti, F.; De Cola, L. and Flamigni, L.; *Chem. Rev.*, 94, **1994**, 993-1019

[2] Constable, E. C.; *Coord. Chem. Rev.*, 252, **2008**, 842-855

[3] Barigelletti, F.; Flamigni, L.; Balzani, V.; Collins, J-P.; Sauvage, J-P.; Sour, A.; Constable, E. C. and Thompson, A. M. W. C.; *J. Chem. Soc., Chem Comm.*, 11, **1993**, 942-944

[4] Maestri, M.; Armaroli, N.; Balzani, V.; Constable, E. C. and Thompson, A. M. W. C.; *Inorg. Chem.*, 34, **1995**, 2759-2767

[5] Demas, J. N. and Crosby, G. A.; *J. Am. Chem. Soc.*, 93, **1971**, 2841-2847

[6] Winkler, J. R.; Netzel, T. L.; Creutz, C. and Sutin, N. J.; *J. Am. Chem. Soc.*, 109, **1987**, 2381-2392

[7] Bessel, C. A.; See, R. F.; Jameson, D. L.; Churchill, M. R. and Takeuchi, K. J.; *J. Chem. Soc. Dalton Trans.*, **1992**, 3223-3228

[8] Calvert, J. M.; Caspar, J. V.; Binstead, R. A.; Westmoreland, T. D. and Meyer, T. J.; *J. Am. Chem. Soc.*, 104, **1982**, 6620-6627

[9] Wolpher, H.; Johansson, O.; Abrahamsson, M.; Kritikos, M.; Sun, L. and Akermark, B.; *Inorg. Chem. Comm.,* 7, **2004**, 337-340

[10] Hammarstrom, L. and Johansson, O.; *Coord. Chem. Rev.*; 254, **2010**, 2546-2559

[11] Wolpher, H.; Johansson, O.; Abrahamsson, M.; Kritikos, M.; Sun, L. and Akermark, B.; *Inorg. Chem. Comm.*, 7, **2004**, 337-340

[12] Abrahamsson, M.; Jager, M.; Osterman, T.; Eriksson. L.; Persson, P.; Becker, H-C.; Johansson, O. and Hammarstrom, L.; *J. Am. Chem. Soc.*, 128, **2006**, 12616-12617

[13] Dyker, G.; and Muth, O.; *Eur. J. Org. Chem.*, 21, **2004**, 4319-4322

[14] Schram. F.; Meded, V.; Fliegl, H.; Fink, K.; Fuhr, O.; Qu. Z.; Klopper, W.; Finn. S.; Keyes, T. E. and Ruben, M.; *Inorg. Chem.*, 48, **2009**, 5677-5684

[15] Miller, J. D. and Prince, R. H.; *J. Chem. Soc. (A)*, **1966**, 1048-1052

[16] Maestri, M..; Armaroli, N.; Balzani, V.; Constable, E. C. and Thompson, A. M. W. C.; *Inorg. Chem.*, 34, **1995**, 2759-2767

[17] Juris. A. and Balzani, V.; *Coord. Chem. Rev.*, 85, **1988**, 85-277

[18] Alford, P. C.; Cook, M. J.; Lewis, A. P.; McAuliffe, G. S. G.; Skarda, V. and Thomsom, A. J.; *J. Chem. Soc. Perkin Trans. II*, **1985**, 705-709

[19] Bhuiyan, A. A. and Kincaid, J. R.; *Inorg. Chem.*, 37, **1998**, 2525-2530

[20] Benniston, A. C.; Harriman, A.; Li, P.; Patel, P. V.; Rostron, J. P. and Sams, C. A.; *J. Phys. Chem. A.*,110, **2006**, 9880-9886

[21] Benniston, A. C.; Chapman, G. M.; Harriman, A. and Sams, C. A.; *Inorg. Chim. Acta.*, 359, **2006**, 753-758

[22] Constable, E. C.; Housecroft, C. E.; Thompson, A. C.; Passaniti, P.; Silvi, S.; Maestri, M. and Credi, A.; *Inorg. Chim. Acta.*, 360, **2007**, 1102-1110

[23] Coe, B. J.; Thompson, D. W.; Culbertson, C. T.; Schoonover, J. R. and Meyer, T. J.; Inorg. Chem., 34, **1995**, 3385-3395

[24] Hansen, P. W. and Jensen, P. W.; *Spectrochimica Acta.*, 50A, **1994**, 169-183

[25] Beley, M.; Collin, J-P.; Sauvage, J-P.; Sugihara, H.; Heisel, F. and Miehe, A.; *J. Chem. Soc. Dalton Trans.*, **1991**, 3157-3159

# 6. Conclusions and Future Work

A series of novel Ruthenium (II) polypyridyl complexes with pendent alkyl chains of varying length with an acetylthio headgroup were successfully synthesised. These complexes were characterised by electrochemicalistry and spectroscopy and the photophysical properties were explored. The luminescence quantum yield and lifetime of this series of complexes are very sensitive to oxygen. Luminescence quantum yields and lifetime are also very sensitive to solvent polarity, both increase greatly in the non-polar solvent dichloromethane compared to the more polar acetonitrile. All complexes in the series were capable of forming bilayer liposome structures when solvated in water. The luminescence lifetime increased dramatically to ~800ns. Liposome dimensions were confirmed by light scattering experiments to be 130 nm and 190 nm in diameter for Ru6D and Ru16D liposomes respectively.

The RuxD series of complexes are surface active due to the acetylthio headgroup and formed monolayers on metal surfaces. Monolayers of the RuxD complexes were formed on platinum electrodes and characterised electrochemically. These monolayers proved to be quite unstable and surface coverage was rapidly reduced during electrochemical experiments in acetonitrile, even when backfilled with alkanethiols. The rate of electron transfer was calculated to be about 1000-1400 $s^{-1}$ for all RuxD complexes monolayers which was much faster than would be expected for a monolayer with a ruthenium polypyridyl headgroup separated from the metal surface by an alkanethiol layer.. The energy of the $Ru^{2+}/Ru^{3+}$ redox potential increased with longer backfilling alkanethiols. This suggests that the RuxD complexes are lying flat on the metal surface as opposed to forming a monolayer with the head groups held above the electrode surface. 50 nm gold nanoparticles were also functionalised with RuxD monolayers. Despite the close proximity of the ruthenium centre to the metal surface these monolayers were luminescent. A strong SERs signals was observed from these nanoparticles but was unfortunately obscured by a high background signal, which was further evidence of the proximity of the ruthenium head group to the metal surface. The greatly enhanced ligand Raman modes also show evidence of strong coupling of the ligand vibrations to the surface plasmon due to the close proximity of the ligands to the metal surface. It was theorised that the ligands are adsorbed to the metal surface through interactions between the aromatic dpp ligands and the metal, similar to the interactions of

pyridine in low concentrations at a gold or platinum surface forming monolayers in a horizontal orientation. This is the first report of a surface active ruthenium (II) polypyridyl complex that behaves in this manner.

RuxD was used to stain CHO cells and the cells luminescence intensity images and FLIM maps were taken of the treated cells. It was found that not only did the RuxD complexes cross the cell membrane but so did the parent complex, $[Ru(dpp)_2(NH_2phen)](PF_6)_2$. This was attributed to the presence of DMSO during cell treatment. It was found that staining of the CHO cells was chain length dependent, with Ru6D, Ru8D, Ru11D staining non-uniformly throughout the cytoplasm and also localising within spherical structures within the cytoplasm. Ru16D localised selectively in the spherical structures. Nuclear penetration was detected for the Ru6D, Ru8D and Ru11D compexes but not for Ru16D. The identity of the spherical structures is still unknown although the possibility of the being mitochondria was eliminated through counter staining experiments with Dioc6. It was postulated that these structures are endosomes and lysosomes due to the fact that their luminescence lifetimes varied from 450 ns to upwards of 850 ns. 3D z-stack FLIM images of the CHO cells stained treated with RuxD were also obtained.

Finally a new class of $[Ru(tpy)_3]^{2+}$ type complex, $[Ru(L_{Ket})_3]^{2+}$ was characterised photophysically and electrochemically. By extending the coordination cage of the tpy ligand with carbonyl bridges the coordination cage in the $[Ru(L_{Ket})_3]^{2+}$ complex was brought closer to perfect octahedral symmetry thus increasing the energy gap between the $\pi - \pi^*$ and d – d orbitals responsible for non-radiative decay. $[Ru(L_{Ket})_3]^{2+}$ has the highest luminescent lifetime of any ruthenium (II) polypyridyl complex in aerated ambient conditions, 1.36 µs, reported to our knowledge and quantum yields close to that of $[Ru(phen)_3]^{2+}$ class complexes. This is in stark contrast to $[Ru(tpy)_3]^{2+}$ which displays no measureable luminescence is aerated conditions at 298 K.

Future work involves functionalising the $[Ru(L_{Ket})_3]^{2+}$ complex at the 4' position with COOH groups to facilitate further functionalisation through the formation of amide bond. The $[Ru(L_{Ket})_3]^{2+}$ complex will be functionalised with alkyl and peptide chains to facilitate

the penetration of cell membranes for cell luminescence intensity and lifetime imaging experiments.

# Appendix

## Display Report



**Analysis Info**

| | | | |
|---|---|---|---|
| FileName | D:\Data\Damo\sf0213a.d\Analysis.yep | | |
| Acquisition Date | Monday, 02/13/06, 16:04:56 UTC | Print Date | Monday, 13.February.2006, 16:25 |
| Method | maurice.MS | Operator | Administrator |
| Comment | sf mw= 345.51 in methanol/acn<br>sf mw= 345.51 in methanol/acn | Instrument | Esquire-LC 00050 |

**Acquisition Parameter**

| | | | | | |
|---|---|---|---|---|---|
| Ion Source Type | ESI | Ion Polarity | Positive | Alternating Ion Polarity | |
| Mass Range Mode | Std/Normal | Scan Begin | 100.00 m/z | Scan End | 500.00 m/z |
| Skim 1 | 35.3 Volt | Cap Exit Offset | 73.4 Volt | Trap Drive | 33.2 |
| Accumulation Time | 4505 µs | Averages | 10 Spectra | Auto MS/MS | Off |

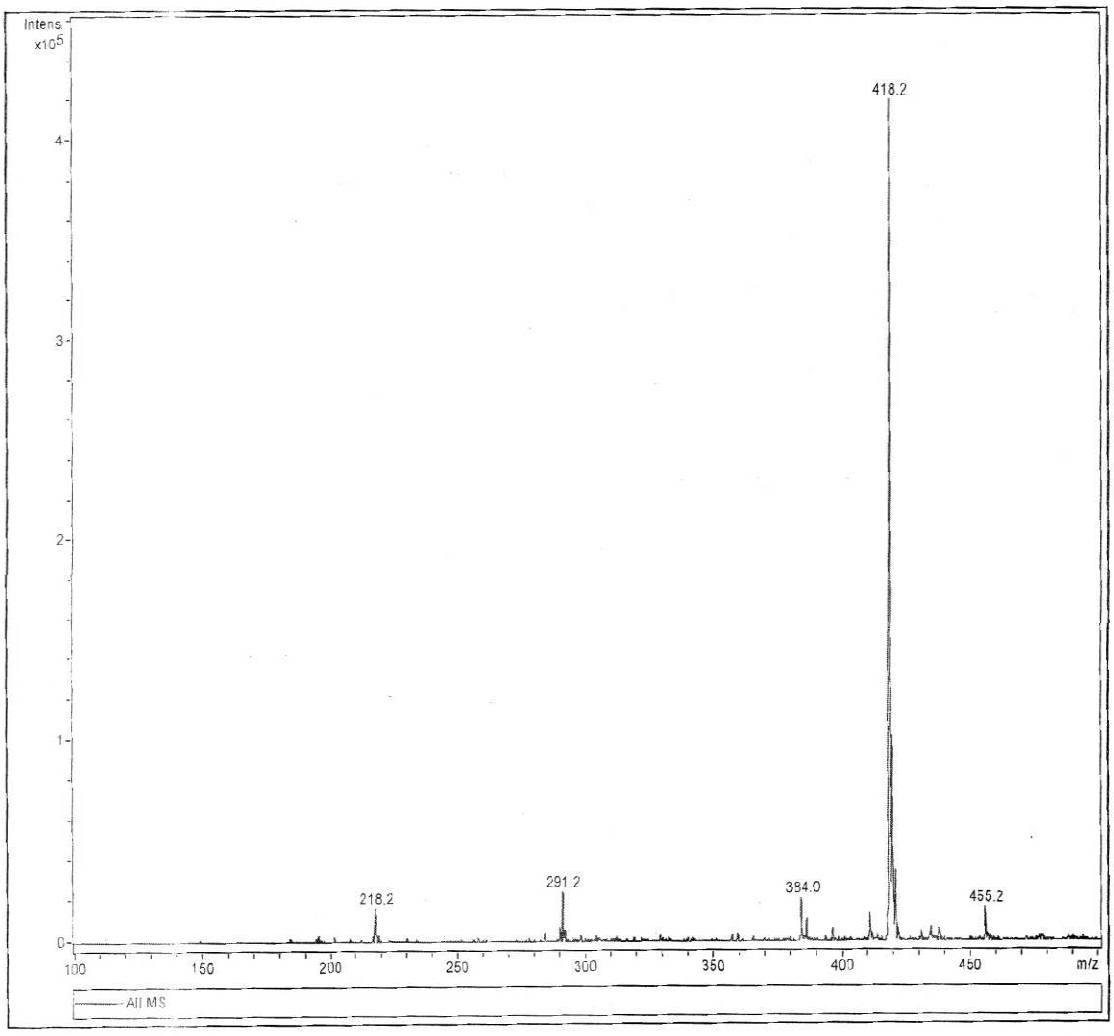


Bruker Daltonics DataAnalysis 2.0

**Figure A-1:** MS data for Amidophenanthroline-8-(acetylthio)-octanyl

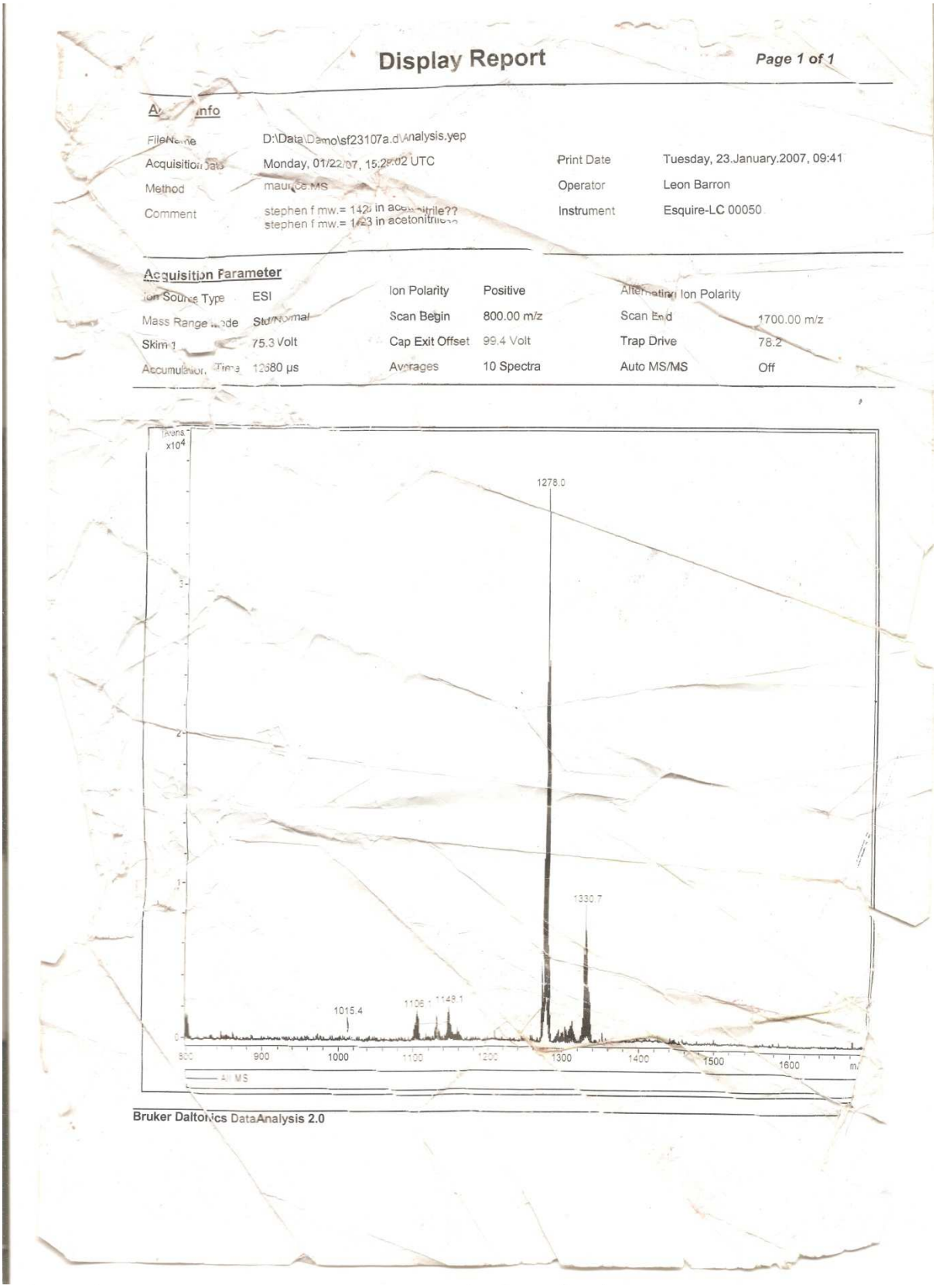


**Figure A-2:** MS data for $[Ru(dpp)_2(AmidoPhen\text{-}6\text{-}(acetylthio)\text{-}hexanyl)(PF_6)_2]^{2+}$

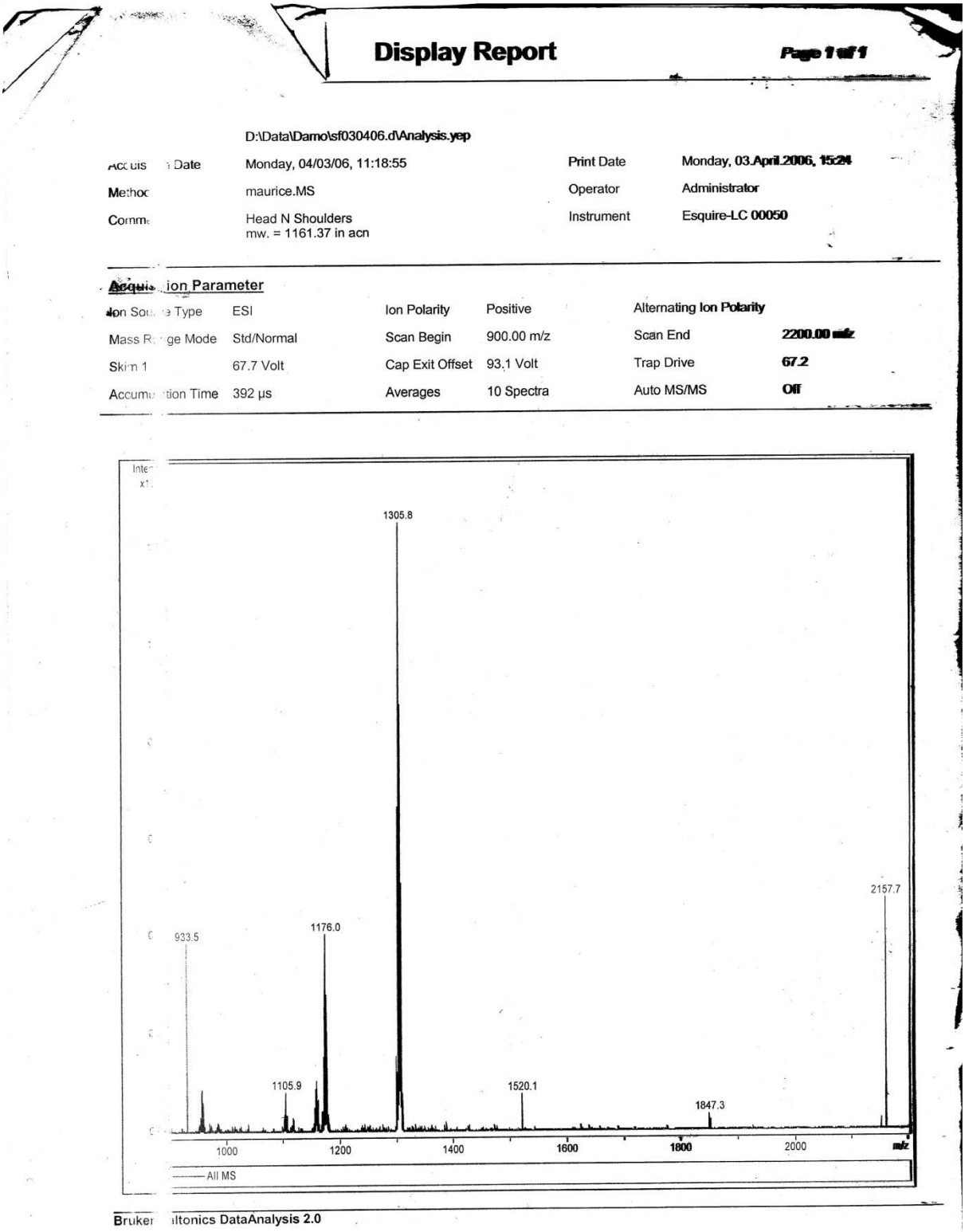


**Figure A-3:** MS data for $[Ru(dpp)_2(AmidoPhen\text{-}8\text{-}(acetylthio)\text{-}octanyl)(PF_6)_2]^{2+}$

# Display Report



**Analysis Info**

| | | | |
|---|---|---|---|
| FileName | D:\Data\Damo\sf23107b.d\Analysis.yep | | |
| Acquisition Date | Monday, 01/22/07, 15:32:12 UTC | Print Date | Tuesday, 23.January.2007, 09:43 |
| Method | maurice.MS | Operator | Leon Barron |
| Comment | stephen f mw.= 1401 in acetonitrile??<br>stephen f mw.= 1451 in acetonitrile?? | Instrument | Esquire-LC 00050 |

**Acquisition Parameter**

| | | | | | |
|---|---|---|---|---|---|
| Ion Source Type | ESI | Ion Polarity | Positive | Alternating Ion Polarity | |
| Mass Range Mode | Std/Normal | Scan Begin | 800.00 m/z | Scan End | 1700.00 m/z |
| Skim 1 | 75.3 Volt | Cap Exit Offset | 99.4 Volt | Trap Drive | 78.2 |
| Accumulation Time | 2014 µs | Averages | 10 Spectra | Auto MS/MS | Off |

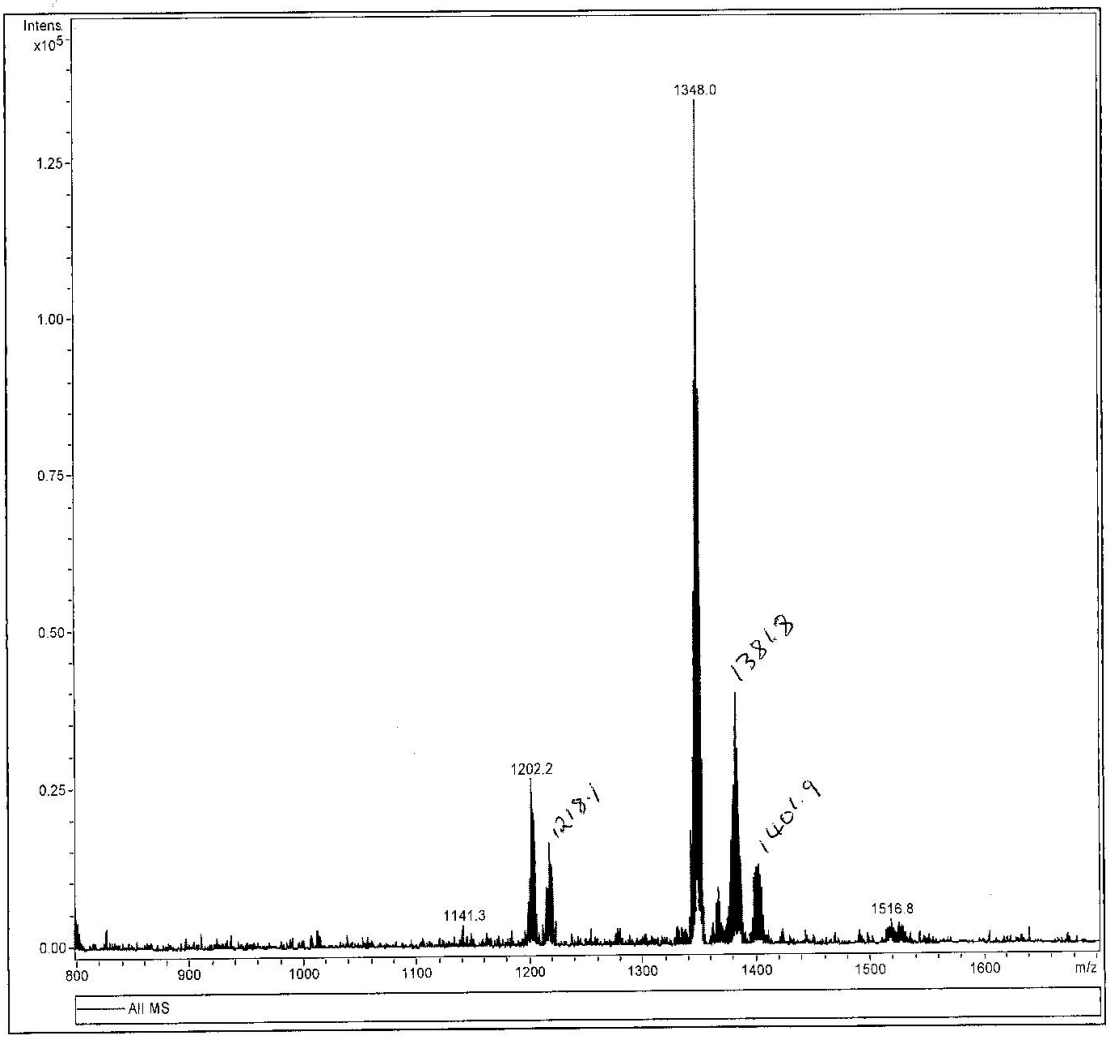


Bruker Daltonics DataAnalysis 2.0

**Figure A-4:** MS data for $[Ru(dpp)_2(AmidoPhen\text{-}11\text{-}(acetylthio)\text{-}undecanyl)(PF_6)_2]^{2+}$

# Display Report



**Analysis Info**

| | | | |
|---|---|---|---|
| FileName | D:\Data\Damo\sf23107c.d\Analysis.yep | | |
| Acquisition Date | Monday, 01/22/07, 15:34:35 UTC | Print Date | Tuesday, 23.January.2007, 09:44 |
| Method | maurice.MS | Operator | Leon Barron |
| Comment | stephen f mw.= 1563 in acetonitrile??<br>stephen f mw.= 1563 in acetonitrile?? | Instrument | Esquire-LC 00050 |

**Acquisition Parameter**

| | | | | | |
|---|---|---|---|---|---|
| Ion Source Type | ESI | Ion Polarity | Positive | Alternating Ion Polarity | |
| Mass Range Mode | Std/Normal | Scan Begin | 800.00 m/z | Scan End | 1700.00 m/z |
| Skim 1 | 79.1 Volt | Cap Exit Offset | 102.8 Volt | Trap Drive | 84.0 |
| Accumulation Time | 493 µs | Averages | 10 Spectra | Auto MS/MS | Off |

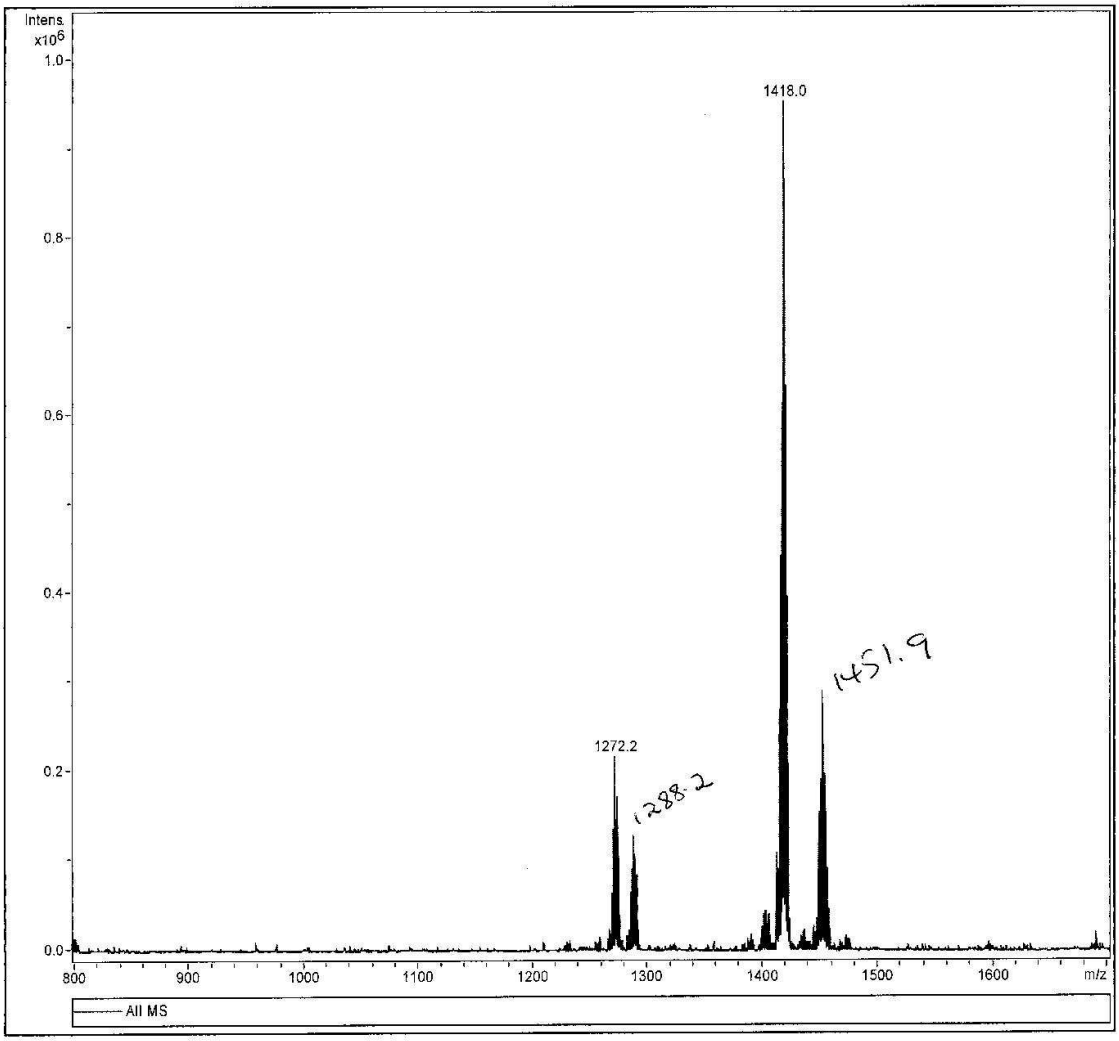


Bruker Daltonics DataAnalysis 2.0

**Figure A-5:** MS data for $[Ru(dpp)_2(AmidoPhen\text{-}16\text{-}(acetylthio)\text{-}hexadecanyl)(PF_6)_2]^{2+}$

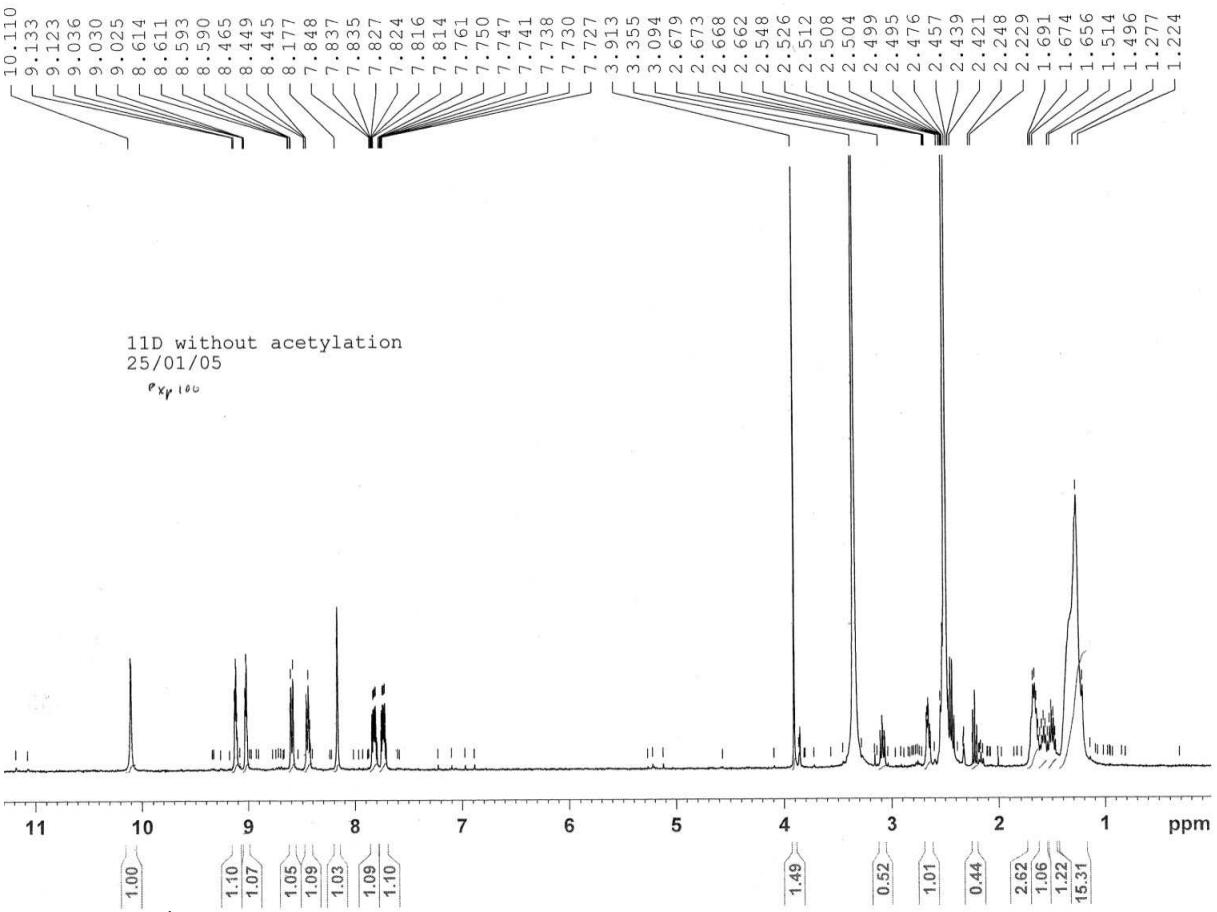


**Figure A-6:** $^{1}$H NMR of unpurified Amidophenanthroline-11-(thio)-undecanyl in $(CD_3)_2SO$. (Amidophenanthroline-11-(acetylthio)-undecanyl reaction without acetyl thio protection step)

Inorganic Chemistry
Article

*Inorg. Chem.* **2009**, *48*, 5677–5684 **5677**
DOI: 10.1021/ic802040v

# Expanding the Coordination Cage: A Ruthenium(II)−Polypyridine Complex Exhibiting High Quantum Yields under Ambient Conditions

**Frank Schramm,[†] Velimir Meded,[†] Heike Fliegl,*[,†] Karin Fink,[†] Olaf Fuhr,[†] Zhirong Qu,[†] Wim Klopper,[‡] Stephen Finn,[§] Tia E. Keyes,*[,§] and Mario Ruben*[,†]**

[†]*Institute of Nanotechnology, Forschungszentrum Karlsruhe, Karlsruhe, Germany,* [‡]*Institute of Physical Chemistry, Universität Karlsruhe (TH), Karlsruhe, Germany, and* [§]*School of Chemical Sciences, Dublin City University, Dublin, Ireland*

Received October 23, 2008



 Published on Web 06/09/2009 